Adaptive beam control and analysis in fluorescence microscopy

THOMAS JAMES MITCHELL

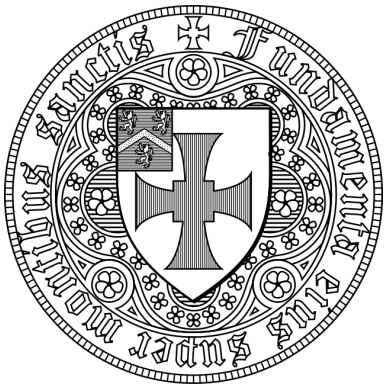

University of Durham
Department of Physics

Adaptive beam control and analysis in fluorescence microscopy

Doctoral Dissertation of:
Thomas J. Mitchell

Supervisors:
Prof. Gordon Love
&
Prof. John Girkin

November 18, 2015

Title
Adaptive beam control and analysis in fluorescence microscopy

Author
Thomas J. Mitchell

Abstract

This thesis details three novel advances in instrumentation that are each related to performance improvement in wide-field visible-spectrum imaging systems. In each case our solution concerns the assessment and improvement of optical imaging quality. The three instruments are as follows: The first is a portable transmission microscope which is able to correct for artificially induced aberrations using adaptive optics (AO). The specimens and the method of introducing aberrations into the optical system can be altered to simulate the performance of AO-correction in both astronomical and biological imaging. We present the design and construction of the system alongside before-and-after AO-correction images for simulated astronomical and biological images. The second instrument is a miniature endoscope camera sensor we re-purposed for use as a quantitative beam analysis probe using a custom high dynamic range (HDR) imaging and reconstruction procedure. This allowed us to produce quantitative flux maps of the illumination beam intensity profile within several operational fluorescence microscope systems. The third and final project in this thesis was concerned with an adaptive modification to the light sheet illumination beam used in light sheet microscopy, specifically for a single plane illumination microscope (SPIM), embracing the trade-off between the thickness of the light sheet and its extent across the detection field-of-view. The focal region of the beam was made as small as possible and then matched to the shape of curved features within a biological specimen by using a spatial light modulator (SLM) to alter the light sheet focal length throughout the vertical span of the sheet. We used the HDR beam profiling camera probe mentioned earlier to assess the focal shape and quality of the beam. The resulting illumination beam may in the future be used in a modified SPIM system to produce fluorescence microscope images with enhanced optical sectioning of specific curved features. [295 words]

Declaration

The work presented in this thesis is based on research carried out at the Centre for Advanced Instrumentation (CfAI), the Department of Physics, University of Durham, England. No part of this thesis has been submitted elsewhere for any other degree or qualification and it is the sole work of the author apart from the following exceptions:

- The AO system control software described in Section 4.2.3 was written by Christopher D. Saunter and Cyril Bourgenot at the CfAI.
- The physical design of the beam profiling camera probe described in Section 5.3.1 is the work of William O'Nions, Christopher D. Saunter, Jonathan Taylor, and John M. Girkin and was created as part of William O'Nions' Mphys project at Durham University. The acrylic rod that the sensor was mounted into was machined by the Mechanical Workshop within the Department of Physics; construction of the probe was completed by Graham Murray.

Some of the work presented in Chapters 5 & 6 of this thesis has been published, the relevant publications are listed below.

1. Mitchell, T. J., Saunter, C. D., O'Nions, W., Girkin, J. M., & Love, G. D. (2014). Quantitative high dynamic range beam profiling for fluorescence microscopy, *Review of Scientific Instruments*, 85(10), 103713. doi:10.1063/1.4899208
2. Mitchell, T. J., Saunter, C. D., O'Nions, W., Girkin, J. M., & Love, G. D. (2015). Adaptive optimisation of illumination beam profiles in fluorescence microscopy, *Proc. SPIE*, 9335(0), 93350B-93350B-6. doi:10.1117/12.2080310

Acknowledgments

First and foremost I gratefully acknowledge the generosity of the Engineering and Physical Sciences Research Council (EPSRC) as the main funding body behind the work presented within, and my life outside of, this thesis. Were it not for my supervisors, Gordon Love and John Girkin, and their belief that I was up to the task then the last three and a half years would simply not have happened. The very earliest and latest stages of this PhD, and everywhere in-between, would have been orders of magnitude more difficult and less enjoyable were it not for the guidance, expertise, camaraderie, and general excellence of (in alphabetical order of surnames) Urban Bitenc, Cyril Bourgenot, Tim Butterley, Mark Corrigan, Paul Clark, Nigel Dipper, Rob Harris, Fiona Kenny, Penny Lawton, Bart Lomanowski, Amrit Lotay, Tim Morris, Graham Murray, James Osborn, Jared Parnell, Saavi Perera, Andrew Reeves, Chris Saunter, Scott Silburn, Jonny Taylor, Matt Townson, Luke Tyas, Claire Whitehill, and Laura Young. I am sure that nearly every member of the CfAI both past and present has helped me with these projects at some point within this time period which is a testament to the remarkable good nature and ample enthusiasm present within our research group. I couldn't possibly have met a kinder, cleverer, crazier, or more welcoming bunch of friends, let alone colleagues. Long may we all continue to score highly on whatever test we set ourselves.

For M & D, and the Idas.

Contents

List of Figures

List of Acronyms

1-D one-dimensional 119

2-D two-dimensional 81

3-D three-dimensional 3

ADC analog-to-digital converter 28

ADRI adaptive dynamic range imaging 33

ADU analog-to-digital unit 42

AO adaptive optics 1

A-SPIM adaptively-curved SPIM 119

AVT Allied Vision Technologies 66

BFP back focal plane 17

BNS Boulder Non-linear Systems 127

BPP beam parameter product 23

CAO conjugate adaptive optics 62

CCD charge-coupled device 24

CDS correlated-double-sampling 41

CMOS complementary metal oxide semiconductor 28

CoM centre-of-mass 135

CPSM confocal point-scanning microscopy 5

CTM confocal theta microscopy 6

DCNU dark current non-uniformity 44

DM deformable mirror 52

Introduction 1

1.1 Thesis motivation

The two main instruments of observation used to explore the intricate structures in the universe around us are, arguably, the microscope and the telescope. Both have extended mankind's knowledge of that which is too small to see using the naked eye; from individual cells for the former, to galactic structures for the latter. Much of the technological advancement of both instruments that has occurred throughout the 20th century was provoked by the advent of efficient photographic methods, evolving both systems from mere ocular appendages informing the observations of a single user into high-performance digital documentation devices adding to mankind's collective knowledge-base directly and accurately.

In both of these systems light which has been emitted, transmitted, or reflected from the object of interest is reflected, focused and filtered by a multitude of precision optics in order to form an image at a camera sensor. The bandwidth of light which can be manipulated in this fashion ranges from the infrared and through the visible regions of the electromagnetic spectrum. Though this ease of manipulation causes the propagation of light within this electromagnetic bandwidth to become heavily affected by unintentional optical effects, it also allows for its correction by using additional optical components. A technology which provides an optical compensation in this fashion goes by the name of adaptive optics (AO) and has over the last 25 years been gradually implemented in ground-based telescopes to reduce the effects of the Earth's atmosphere [1] and in the last 15 years been implemented throughout microscopy to reduce the effects of imaging through biological tissue [2]. This technology is an on-going area of research in both astronomical and biological imaging and yet relatively few researchers outside of the instrumentation or optics community understand or have seen how it works, let alone members of the general public. As such the first piece of work within this thesis was conducted in order to address this: Chapter 4 presents an interactive AO system to demonstrate the technology in simulated astronomical and biological imaging environments to a wider audience.

The remainder of the work presented in this thesis is concerned with the performance of microscope systems away from AO; fluorescence microscope systems to be precise. In a fluorescence microscope system the light emitted by cellular components of a specimen that have been stained or otherwise modified using a fluorescent protein is collected and imaged. This allows distinct cellular features to be imaged separately from other less important structures since the fluorescent proteins can be bound to specific cells. However, the image quality in a fluorescence microscope suffers if out-of-focus regions of the sample are illuminated. In linear fluorescence, emission at a particular wavelength is caused by an excitation of the fluorescent protein by illumination at a shorter wavelength; the number of emitted photons are directly proportional to the illumination intensity. Thus many different fluorescence microscope techniques have been developed which use a specific illumination beam intensity profile in order to illuminate, or collect the emission from, in-focus regions of the sample only. The process of removing light from out-of-focus regions of a sample by optical means rather than mechanical means is known as 'optical sectioning', leaving the sample intact to allow the imaging of living biological specimens.

The majority of this thesis is thusly concerned with quantifying and altering the shape of the illumination beam in a form of fluorescence microscopy that is widely adopted in biological imaging, light sheet microscopy (LSM), in order to analyse and optimise the imaging capability of the microscope system. More specifically, the LSM technique which is the primary topic of discussion is that of the single/selective plane illumination microscope (SPIM): SPIM is the simplest to implement of all LSM techniques and has been overlooked in many of the recent developments in the field. The main questions being addressed are these: Is it possible to see the exact shape of a microscopic illumination laser beam? If this is indeed possible then can we use this newfound ability to assess and enhance the optical performance of the system? In order to directly image the shape of the fluorescence microscope's illumination beam we developed a miniature camera probe that could be placed directly into the beam path, removing the need for additional relay optics. The device was constructed using a highly-compact CMOS sensor to keep the dimensions as small as possible. However, such miniaturised sensor technology often comes at the expense of imaging performance: our particular sensor exhibited non-uniform noise behaviour and correspondingly low signal headroom. Thus we developed a high dynamic range (HDR) imaging and post-processing procedure that extended the limited dynamic range of this camera sensor to allow the full range of intensity within an illumination beam to be quantitatively recorded. The final piece of work in this thesis uses this newly-developed HDR camera probe to investigate the success of coupling adaptive optics with the illumination beam in a SPIM. This novel implementation of SPIM has future potential in realising feature-specific optical sectioning of curved cellular regions within biological specimens, combined with the SPIM-specific benefits of rapid image acquisition and low photo-toxicity.

1.2 Thesis synopsis

The contents of the remaining chapters of this thesis are as follows:

- Chapter 2 presents the history of LSM and a discussion of the popular illumination beam geometries. Following this, we concern ourselves with potential methods which can be used to quantitatively record a beam shape in order to determine its quality: Previously used beam profiling techniques high dynamic range (HDR) imaging procedures are introduced and discussed, as a novel device combining the two is developed later in Chapter 5 in order to quantify the full intensity range of a focused laser illumination beam.

- Chapter 3 introduces the concept of AO and discusses the incorporation of the technique into microscopy, predominantly addressing recent advances in the inclusion of AO in SPIM systems. Each of the AO-specific optical components used in the AO demonstrator system of the following chapter are discussed from the standpoint of general closed-loop AO system operation.

- Chapter 4 presents a portable AO system that was designed to demonstrate AO in simulated astronomical and microscope imaging in a simple-to-understand manner for the general public. Images of the AO correction in both simulations are presented alongside questionnaire feedback from a participating group of school children. Additional materials used in the public demonstration of the system are presented in Appendix A.

- Chapter 5 presents a miniature camera probe that is operated using a HDR imaging and reconstruction procedure in order to accurately quantify the three-dimensional (3-D) intensity profile of illumination beams within fluorescence microscopes.

- Chapter 6 presents a modification to the illumination beam of a SPIM that produces a non-planar light sheet illumination beam that promises improved optical sectioning when imaging curved cellular features within biological specimens. Here the beam profiling device developed in the previous chapter is used to investigate the modified illumination shape.

- Chapter 7 is the final chapter of this theses, in which the work presented in Chapters 4, 5, and 6 is summarised and final conclusions are drawn.

Quantification of illumination beam quality in light sheet microscopy 2

2.1 Introduction

This chapter serves as a literature review for the work presented later in Chapters 5 & 6 and concerns light sheet microscopy (LSM), laser beam profiling, and high dynamic range (HDR) imaging. The initial portion of this theory chapter is concerned with the development, limitations, and advancement of LSM. Then the important differences between several LSM methods are discussed to demonstrate the breadth of LSM applications in modern biological imaging. Each LSM approach exploits either Gaussian or 'exotic' (non-Gaussian) optical behaviour to generate a range of different illumination beams, each one providing fluorescent excitation in a distinctly different way with different benefits. As the Gaussian illumination beam of a an LSM is the primary subject for the investigations presented in Chapters 5 and 6 a mathematical description of Gaussian beam propagation in the context of LSM is provided.

To examine the shape of any illumination beam within a working microscope a method of recording the beam intensity directly is required. The creation of such a recording, referred to in this thesis as a *beam profile*, is therefore the topic underpinning the latter portion of this chapter. We begin by describing the presently-adopted beam profiling methods and note their limitations when imaging the illumination beam of a fluorescence microscope. These current limitations can be largely addressed by using a miniature camera probe which is scanned along the beam to create 3-D beam profiles which until recently has been technologically impossible due to lack of miniaturised camera devices. The hardware limitations of the camera probe implemented later in Chapter 5 caused us to develop a custom HDR imaging procedure in order to improve its imaging capability. Thus HDR imaging, a photographic procedure developed to enhance the imaging capabilities of photographic equipment, and its development form the final section of this chapter.

2.2 Light sheet microscopy

2.2.1 An abridged history of light sheet microscopy

The origin of the LSM harks back to that of Richard Zsigmondy and Heinrich Siedentopf's 'Ultramikroskop' [3]. Whilst working at Carl Zeiss at the beginning of the 20th century they created a darkfield microscope to record the light scattered by nanometer-scale gold particles. Their optical setup used sunlight to provide a collimated illumination source which was passed through a horizontal slit to produce a thin sheet of illumination within the gold particle colloid solution. The scattered light was viewed at 90 degrees to the illumination optical axis. Zsigmondy's further development of the immersion ultramikroskop and his subsequent demonstration of the heterogenous nature of colloid solutions [4] led to him being awarded the Nobel Prize in Chemistry in 1925 [5].

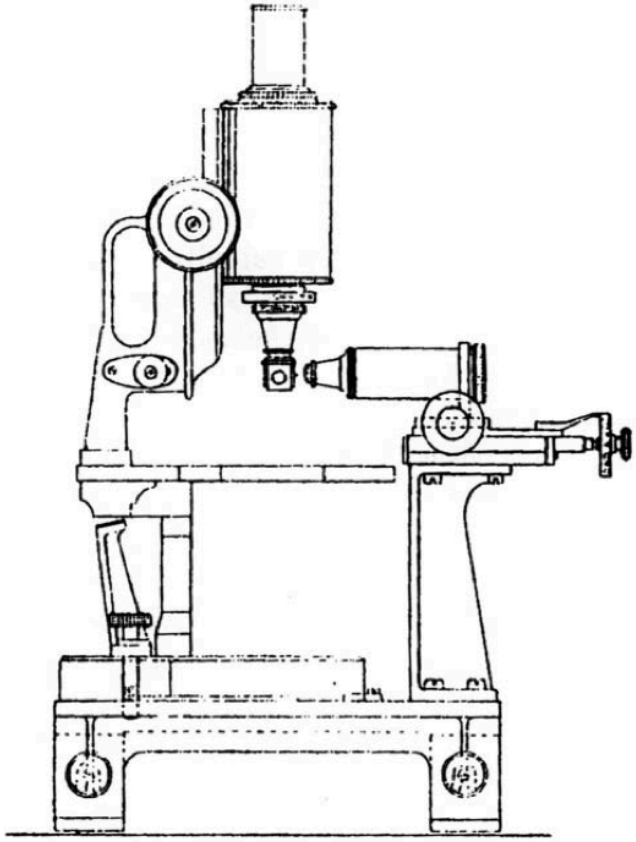

FIGURE 2.1: Siedentopf and Zsigmondy's Ultramikroskop: Figure 3 from their initial paper, the first concerning an orthogonal illumination microscope [3] as reproduced in Peter Santi's 2011 review of LSM [6]. The specimen holder appears to be mounted onto the nose of an upright microscope; at 90° to this there is an illumination objective. The sunlight collector and slit aperture forming the light sheet illumination are not pictured.

From 1977 onwards confocal point-scanning microscopy (CPSM) became the most popular microscopy technique for high resolution 3-D biological imaging [7, 8, 9], building up an

image of the sample point-by-point for each imaged 2-D plane in a 3-D volume. It wasn't until the early 1990s that orthogonal illumination microscopy techniques underwent a further development by Ernst Stelzer and colleagues in an attempt to improve the elongated axial resolution of CPSM [10] by rotating the axis of observation away from the axis of illumination. This technique, known as confocal theta microscopy (CTM), demonstrated an improvement in the observation axial resolution due to the overlap of the illumination and observation point spread function (PSF) volumes [11]. Concurrently to this development, wide-field illumination was implemented by Voie *et al* in an orthogonal fluorescence imaging system developed to investigate 3-D cochlear structure with the intention of improving cochlear implants [12]. The system contained a major number of the optical components now found in LSM systems and rapidly-acquired optical sections of a guinea pig cochlea were published. The technique was termed orthogonal plane fluorescence optical sectioning (OPFOS) and perhaps represents the strongest link between Zsigmondy's original instrument and modern LSM as Stelzer's CTM technique was fundamentally an adaptation of point-scanning CPSM. Unfortunately the development of further orthogonal imaging techniques lay dormant for another decade.

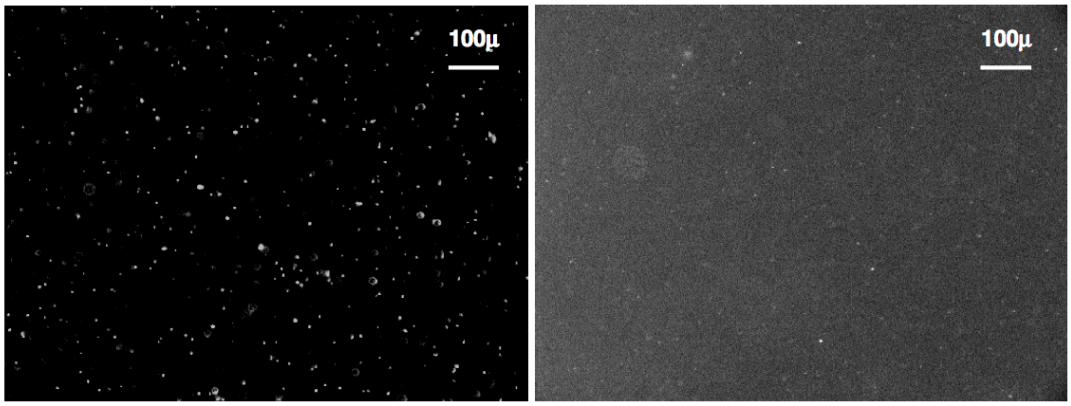

FIGURE 2.2: Imaging oceanic microbes with a thin laser light sheet from Fuchs *et al* 2002 paper [13]. Microbes in a large seawater specimen become optically sectioned from the background when using a side-introduced thin laser light sheet (left) rather than traditional transmission (right) illumination.

Interest in the application of orthogonal imaging techniques was briefly revived in 2002 with Fuchs *et al*'s implementation of a thin laser light sheet to image microbes with reduced background illumination for oceanography [13]. However it wasn't until 2004 that the system was fully embraced by the biological imaging community following the seminal paper by Huisken *et al* in which the authors demonstrated new biological insights into embryogenesis using their now-widely-adopted implementation of LSM [14]. Figure 2.3A presents their sample illumination schematic. Their system, given the name single/selective plane illumination microscope (SPIM), realised the benefit over CPSM of a high-speed and high-resolution 3-D fluorescence imaging system that kept photo-damage to a minimum whilst maximising the detected photonic yield from within *in vitro* and *in toto* samples. The

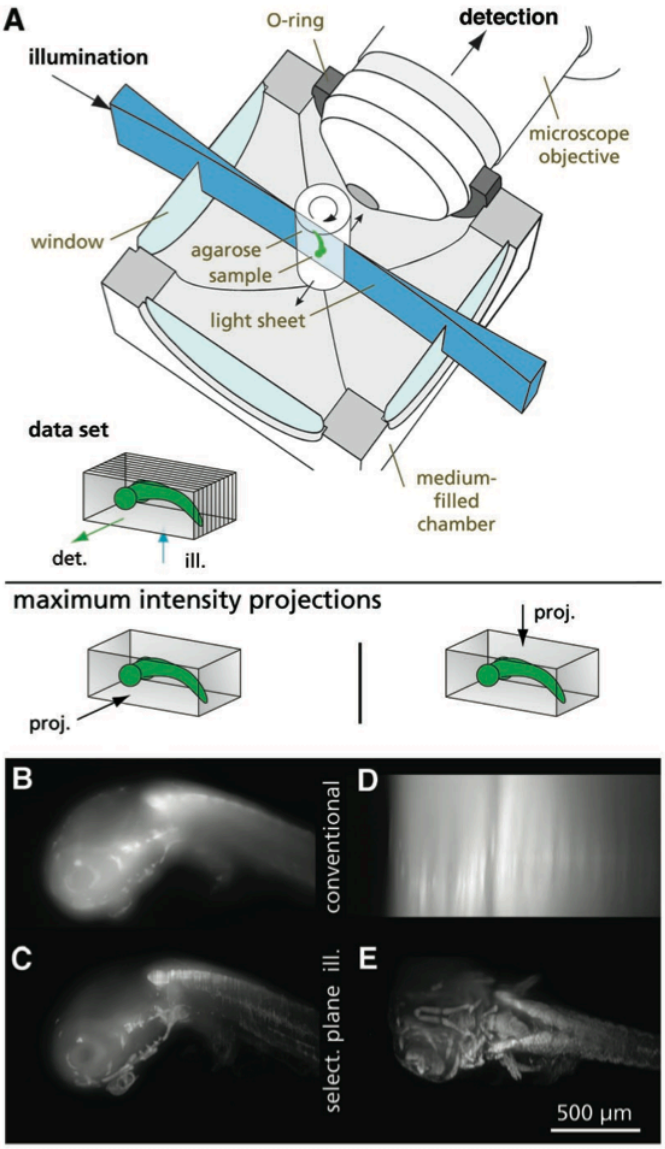

Figure 2.3: The first modern SPIM sample illumination schematic published by Huisken *et al* in 2004 [14]. Here the laser light sheet illumination is introduced into a water-filled specimen chamber through a glass wall, illuminating a whole zebrafish embryo at once (A). For smaller regions of interest many later publications introduced the illumination beam via an objective lens mounted into the chamber wall in the same way as the detection objective. By scanning the sample through with respect to the detection optical axis microscope images can be compiled into a stack to allow 3-D visualisation. For traditional transmission illumination the compiled 3-D stack exhibits a noisy background (B & D). For the optical sections taken using light sheet illumination this background is greatly reduced and the 3-D visualisation is much clearer (C & E).

relative advantages of LSM over CPSM are illustrated in Figure 2.4. Figure 2.5 presents one of their ground-breaking results: sequential images from a SPIM-recorded 3-D time-lapse of a developing *Drosphila* (fruit fly) embryo.

Since then LSM has undergone rapid development and become an important tool in wider applications; including, but not limited to, particle tracking [16], cell imaging [17], and neuronal imaging [18], though the area in which LSM is of tremendous importance remains to be developmental biology, of which there are several excellent in-depth reviews [6, 15, 19, 20, 21]. The wide-spread success of LSM has caused it to become the new *de facto* standard in non-destructive biological imaging, overtaking the popularity of CPSM for many applications due to the higher photo-damage and limited imaging speed preset in the latter [22].

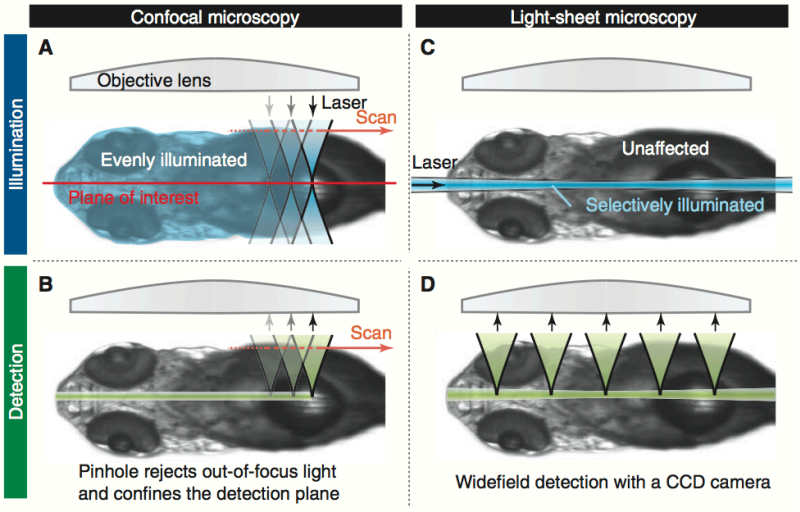

Figure 2.4: Comparision of CPSM with LSM [15]. Only the focal plane of interest is illuminated in LSM (C) and all emission from across the sample is detected at once (D), thus reducing photobleaching and making the imaging process much faster compared to CPSM (A & B).

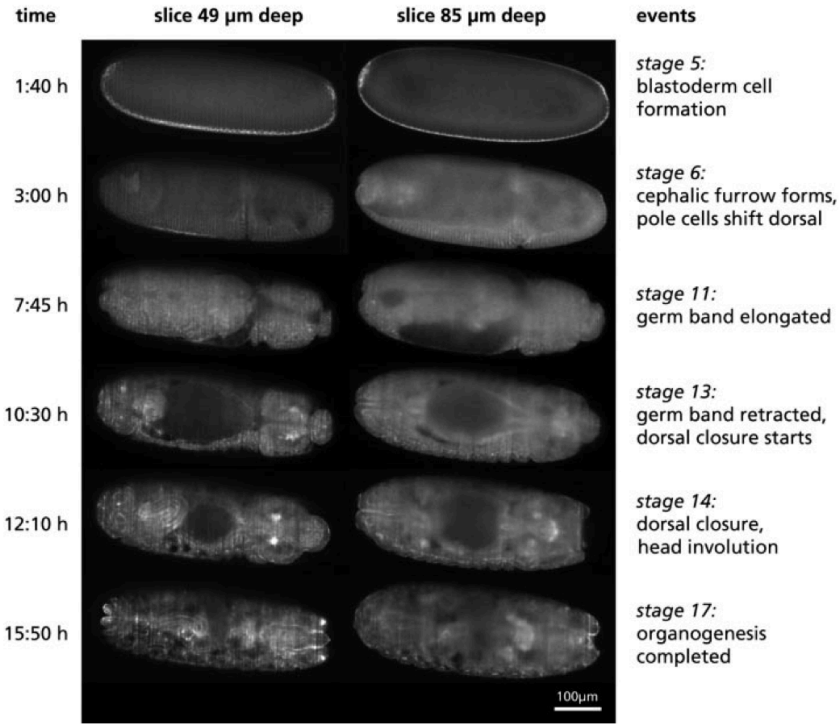

FIGURE 2.5: The seminal Huisken *et al* 2004 paper was the first to demonstrate the benefits of SPIM for *in-vivo* embryonic imaging; at present *embyrogenesis* imaging is the most advanced and most popular biological application of LSM. Here we reproduce their original time-lapse images (3-D stack maximum intensity projections) of a developing *Drosphila* embryo [14]. A video of this time-lapse can be found at `http://www.sciencemag.org/content/suppl/2004/08/11/305.5686.1007.DC1/1100035s5.mov`.

2.2.2 LSM illumination beam optics

We begin this section by discussing perhaps one of the most important optical components within a microscope: the objective lens. Since Chapters 5 & 6 contain analysis of the illumination beam quality within several LSM configurations, each of which produces an illumination beam using this popular optical component, our discussion of the objective lens is primarily concerned with its use within the illumination optical train. We will derive the equations necessary for describing the propagation behaviour of a Gaussian beam focused by an objective lens. Gaussian beam equations are integral to our understanding of both SPIM and digitally-scanned laser light sheet microscopy (DSLSM) illumination beam characteristics. Following this, we move on to discussing the technical aspects and applications of the most popular LSM illumination beam geometries: a static Gaussian light sheet produced by a cylindrical lens as used in SPIM; a digitally-scanned Gaussian light sheet as used in DSLSM; and digitally-scanned laser light sheets using 'exotic' non-Gaussian beams. From the latter category of illumination beams we pay particular attention to Bessel and Airy beam geometries due to their interesting propagation properties that have caused a great deal of recent attention in the LSM community. Figure 2.6 illustrates the light sheets formed by static and scanned illumination beams.

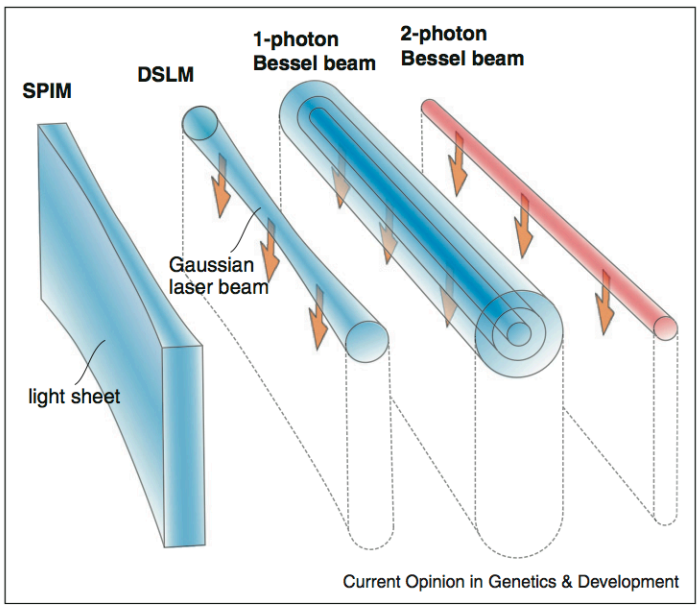

Figure 2.6: Static and scanned light sheet illumination from Weber & Huisken's 2011 LSM review [19]. Dedicated cylindrical optics create the static Gaussian light sheet, whereas the scanned light sheets are formed by rapidly scanning a beam vertically across the height of the specimen during an observation exposure. The acronym DSLM refers to DSLSM in the main text.

2.2.2.1 Microscope objective lenses and Numerical Aperture

The design of microscope objective lenses has come a long way since the 19th century. Objective lenses now typically consist of several component optics within the lens barrel which have been optimised for a specific imaging method. Older objective lenses were designed to form an intermediate image at a specific distance behind the rear aperture of the lens, typically 160 mm. In modern objective lenses this design has been altered such that this intermediate

image is effectively formed at infinity so that an additional lens, a 'tube' lens, is required to form the image at a finite position. All objective lenses used in this thesis are of the latter design and so we limit ourselves to a description of these 'infinity-corrected' objective lenses. A schematic describing the operation of an example infinity-corrected objective lens is shown in Figure 2.7.

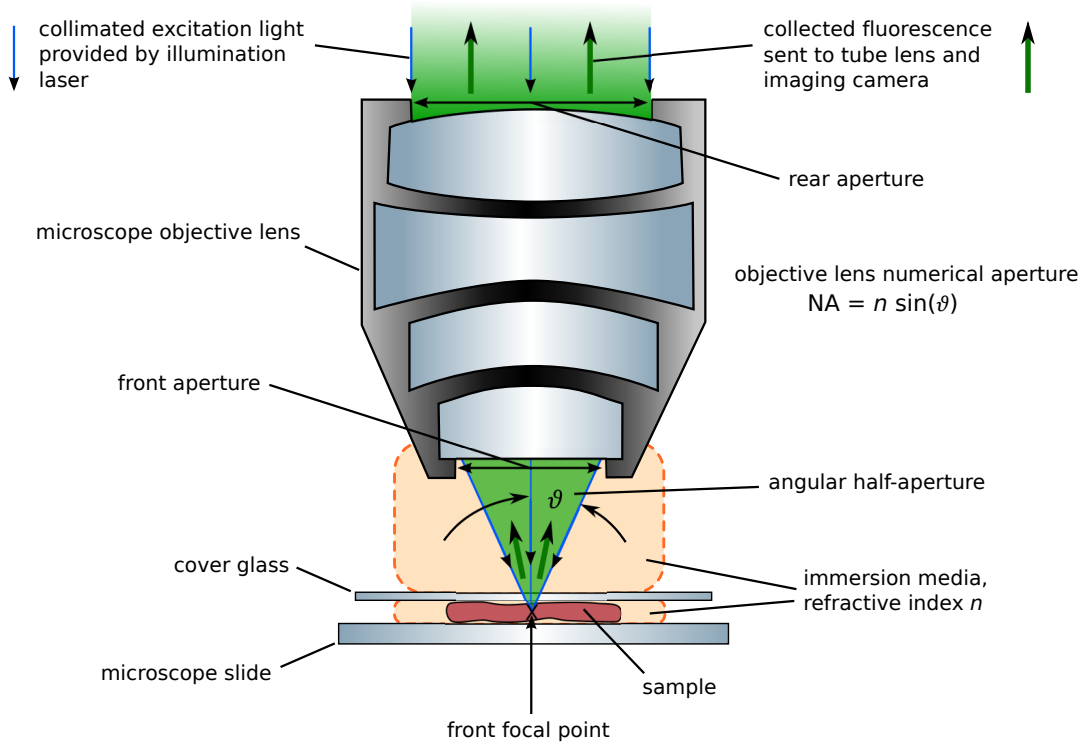

FIGURE 2.7: Schematic of a microscope objective lens operating in an epi-fluorescence configuration. In such a configuration the excitation beam is focused into the sample using the same objective lens that collects the emitted sample fluorescence. The NA of the lens depends on the half-aperture angle ϑ and the refractive index of the immersion mounting media n.

The typically large number of optical components within a single objective lens means that there is no simple position from which the effective focal length can be measured, as would be the case when concerning a thin lens or a similar simple lens system. Instead the focal power of an objective lens is determined by a parameter known as the numerical aperture (NA). According to geometric optics the parallel rays of a collimated beam which enter the rear aperture of the objective lens will emerge from the front aperture of the objective lens as a converging cone of rays. The position at which the apex of this cone occurs is known as the front focal point of the lens. It is between this front focal point and the edge of the front aperture of the objective lens that the half-aperture angle ϑ refers to. The NA of the objective lens is then given by

$$\mathrm{NA} = n \sin(\vartheta) \,, \tag{2.1}$$

where n is the refractive index of the medium between the front aperture and the front focal

point. Parallel rays entering the objective lens rear aperture at various angles to the objective lens optical axis all converge to points within a plane that passes through the front focal point and is orthogonal to the optical axis. This is known as the front focal plane. Similarly there is a back focal point for the objective lens from which a diverging bundle of rays will enter the rear aperture of the lens and exit the front aperture of the lens parallel to one another.

When using the objective lens for imaging the NA determines the light-gathering capability of the imaging system and thus the system's imaging resolution. Many objective lenses have corrective optical components within them that optimise the optical performance of the lens for specific thicknesses of cover glass and immersion media between the lens and the sample. The NA of an objective lens can vary from as low as 0.025 for a low magnification, low correction, achromat lens up to as much as 1.4 for a high magnification, high correction, plan apochromat lens designed for oil-immersion imaging.

The method of projection between a planar wavefront entering the pupil of an objective lens and the focus is largely controlled by the lens NA. For high NA lenses the wavefront propagation has to be treated vectorially and a planar wavefront entering the lens is projected onto a 3-D spherical cap at the lens pupil containing the phase and polarization information [23]. This approach becomes necessary for NA>0.6. For the objective lenses used in this thesis, where NA<0.6, the scalar approximation can be used to relate the NA to the f-number of the lens: A simple lens of diameter D and focal length f has an associated f-number, $\#_f$, which is given by

$$\#_f = \frac{f}{D} \,. \tag{2.2}$$

The angular half-aperture of the lens is given by

$$\tan(\vartheta) = \frac{D/2}{f} = \frac{1}{2\#_f} \,, \tag{2.3}$$

and so the numerical aperture (in air) can be written as

$$\mathrm{NA}_{\mathrm{air}} = n_{\mathrm{m}} \sin(\vartheta) = n_{\mathrm{m}} \sin\left[\arctan\left(\frac{1}{2\#_f}\right)\right] \,, \tag{2.4}$$

which for small angles gives

$$\mathrm{NA}_{\mathrm{air}} \simeq n_{\mathrm{m}} \vartheta = \frac{n_{\mathrm{m}}}{2\#_f} \,, \tag{2.5}$$

where ϑ is measured in radians. Summarily, for an objective lens that is designed for use with a medium of refractive index n_{m} and has the numerical aperture specified within that medium as NA<0.6 we can relate the angular half-aperture to the NA through

$$\mathrm{NA} \simeq \vartheta = \frac{1}{2\#_f} \,. \tag{2.6}$$

2.2.2.2 Propagation of Gaussian beams

In the orthogonal imaging system geometry of LSM the NA of the illumination objective lens plays an important part in the optical sectioning achieved during imaging. We will

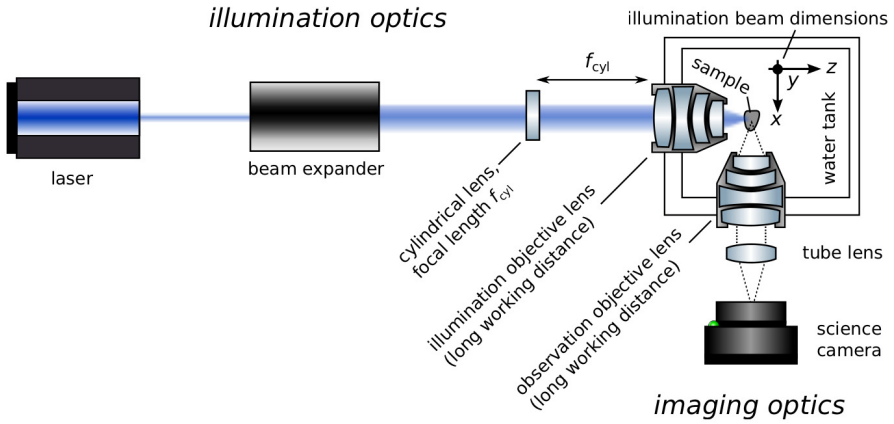

FIGURE 2.8: A typical SPIM optical layout. The line focus formed by a cylindrical lens is conjugated to the back focal plane of an illumination objective lens. This produces a line focus along the opposite axis to that formed by the cylindrical lens by the light exiting the illumination objective. The position of the light sheet in relation to the observation objective lens can be altered by the addition of a tip/tilt mirror at the line focus formed by the cylindrical lens and a 4-*f* relay between this mirror and the illumination objective.

first determine the focusing behaviour of the illumination beam in both SPIM and DSLSM systems; top-down schematics of these microscope systems are shown in Figures 2.8 and 2.9 respectively. In both of these systems illumination is provided by the Gaussian beam output of a monochromatic laser source. Such beams are produced with an electric field amplitude, and thus an intensity profile, that varies according to a Gaussian function. The diffraction of such beams is extremely convenient to describe using Fourier optics. In this section we give a succinct account of Gaussian beam propagation and demonstrate the dependence of a Gaussian beam's focal dimensions on the objective lens NA. Full derivations of the Fourier optical propagation of a Gaussian beam can be found in several optics texts, two of which are [24] and [25], so here we will simply give an account of the most important steps and state the important consequences. Specifically, we describe two important parameters called the 'beam waist' and the 'radius of curvature' which can be used to define the form of a Gaussian beam at any point in space. We begin by describing a Gaussian beam that is radially symmetric about the optical axis of propagation. Simply switching this radial coordinate for a lateral one takes us from a DSLSM beam to a SPIM beam.

According to Fourier optics, a propagating monochromatic plane wave which encounters an aperture will initially represent the 'shadow' of the aperture, bordered by faint interference fringes which evolve with propagation distance. This region is known as the 'Fresnel' regime and the intensity at each plane within this region is a Fresnel diffraction pattern of the aperture. Once the wave has propagated far enough a transition occurs and the wave can then be represented by the Fourier transform of the aperture. This distance marks the transition into a region known as the 'Fraunhofer', or far-field, regime and the intensity of the wave here is thus termed the 'Fraunhofer diffraction pattern' of the aperture. A transition into the far-field

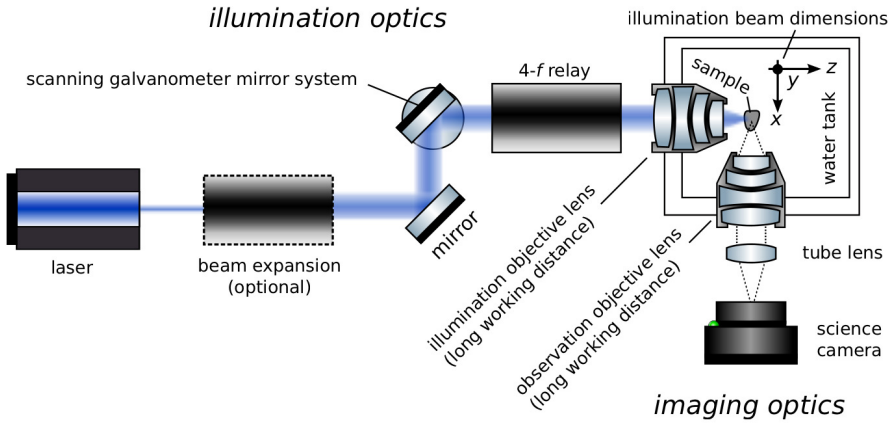

FIGURE 2.9: DSLSM optical layout. A scanning galvanometer mirror pair is used to control the position of the illumination beam as it exits the illumination objective lens. Alterations in the beam angle in the y-z plane perform the vertical scan of the collimated Gaussian pencil beam across the height of the overall observation field-of-view, forming the composite light sheet illumination, whereas alterations in the beam angle in the x-z plane control the proximity of these beam-scanned light sheets to the observation objective lens.

regime can be assumed when

$$d^2/z\lambda \ll 1 \tag{2.7}$$

where d is the longest dimension of the aperture opening, λ is the wavelength of the monochromatic plane wave, and z is the propagation distance from the aperture. If a lens with a spherical curvature is placed at the aperture then the Fourier transform of the aperture is produced at the focal length of the lens, rather than at distances greater than the Rayleigh distance from the aperture.

Where a plane wave has a uniform electric field distribution, a Gaussian wave has an electric field that varies according to a Gaussian function. Conveniently, the Fourier transform of a Gaussian function is also a Gaussian function [24]. This means that a Gaussian beam which is focused by a lens produces a Gaussian beam at the lens focus. In fact, the beam remains Gaussian throughout this simple optical system. Provided the beam profile is not attenuated by small apertures the light from a Gaussian source remains Gaussian throughout the entire optical system. To briefly demonstrate the properties of a propagating Gaussian beam we will state the standard form for the scalar electric field amplitude of a monochromatic beam with a Gaussian distribution and then show this in a more convenient form that describes the beam shape more clearly.

For a radially-symmetric Gaussian beam propagating in the $\pm z$ direction, centered on the z-axis, the scalar electric field amplitude is given by

$$E(z,r) = E_0 \mathrm{e}^{i(kz-\nu t)} \frac{\exp(ikr^2/2q)}{q}\,, \tag{2.8}$$

where $q = z - z_{\mathrm{waist}} - iz_{\mathrm{R}}$ and is called the 'complex radius' of the beam, k is the wavevector

of the beam, related to the wavelength λ by $k = 2\pi/\lambda$, ν is the angular frequency of the wave, and r is the radial distance from the z-axis. The complex radius is an important quantity that allows us to 'unlock' the shape of the beam which is not obvious in this form for E. z_{waist} and z_{R} are real constants that describe the form of q and thus have an important influence on the shape of the beam.

By shifting the origin of z to z_{waist} the complex radius becomes $q = z - iz_{\text{R}}$. Both the exponent $(ikr^2/2q)$ and the factor $1/q$ can then be rearranged by using this form of q, multiplying out using the complex conjugate $q^* = z + iz_{\text{R}}$, and then separating the real and imaginary terms. Starting with the exponent,

$$\begin{aligned} \frac{ikr^2}{2q} = \frac{ikr^2(z+iz_{\text{R}})}{(z-iz_{\text{R}})(z+iz_{\text{R}})} &= \frac{ikr^2}{2}\left(\frac{z}{z^2+z_{\text{R}}^2}\right) - \frac{kz_{\text{R}}r^2}{2(z^2+z_{\text{R}}^2)} \\ &\equiv \frac{ikr^2}{2R(z)} - \frac{r^2}{w^2(z)}\,, \end{aligned} \tag{2.9}$$

where

$$R(z) = \frac{z^2+z_{\text{R}}^2}{z}\,, \text{ and } w^2(z) = \frac{2(z^2+z_{\text{R}}^2)}{kz_{\text{R}}}\,, \tag{2.10}$$

giving us two exponential factors in our field amplitude equation: The first $\exp(ikr^2/2R(z))$ has a complex argument and describes $R(z)$ as the radius of curvature of the wavefront; the second, $\exp(r^2/w^2(z))$, has a real argument and describes a Gaussian amplitude profile. The form of the radius of curvature in Equation 2.10 shows that as z increases from negative to positive $R(z)$ starts out finite and negative, varying as z where $z \ll -z_{\text{R}}$, then tends to infinity in the $-z_{\text{R}} \leq z \leq +z_{\text{R}}$ region (becoming infinite at $z = 0$ and undergoing a change in sign either side of this), and finally becomes finite again, varying with z where $z \gg +z_{\text{R}}$. The minimum radius of $R(z) = 2z_{\text{R}}$ occurs at $z = \pm z_{\text{R}}$. The expression for $w^2(z)$ can written as

$$w^2(z) = \frac{w_0^2(z^2+z_{\text{R}}^2)}{z_{\text{R}}^2} \tag{2.11}$$

$$\Rightarrow w(z) = w_0\sqrt{1+\left(\frac{z}{z_{\text{R}}}\right)^2}\,, \tag{2.12}$$

using

$$w_0^2 = 2z_{\text{R}}/k\,, \quad \text{or rather} \quad z_{\text{R}} = kw_0^2/2\,, \tag{2.13}$$

which in terms of the wavelength, λ, is

$$z_{\text{R}} = \frac{\pi w_0^2}{\lambda}\,. \tag{2.14}$$

At $z = 0$, $w(z)$ takes its minimum value: w_0. This is the point at which the Gaussian amplitude profile has the narrowest radial extent and is referred to as the beam waist.

A similar treatment of the $1/q$ factor in Equation 2.8 (multiplying out by q^*/q^*) and making use of both Euler's formula[1] and Equation 2.11 gives us

$$\frac{1}{q} \equiv i\frac{w_0}{w(z)}\frac{\mathrm{e}^{-i\zeta(z)}}{z_\mathrm{R}}\,, \tag{2.15}$$

where $\tan(\zeta(z)) = z/z_\mathrm{R}$. The first factor in this expression tells us that the overall amplitude of the beam reduces during propagation as the beam waist expands and the second factor is termed the Gouy phase and is a global phase delay that the beam undergoes whilst propagating. The Gouy phase tells us that an additional phase shift of π is picked up during focusing, *i.e.* during propagation from $-z_\mathrm{R}$ to $+z_\mathrm{R}$. Neither of these factors affect the overall shape of the beam.

Putting this all together we then have a description of the scalar electric field with separable real and imaginary factors and a dependence on only z and r:

$$E(z,r) = \frac{iE_0}{z_\mathrm{R}}\frac{w_0}{w(z)}\mathrm{e}^{i(kz-\nu t)}\exp\left(\frac{ikr^2}{zR(z)}\right)\exp\left(\frac{-r^2}{w^2(z)}\right)\,. \tag{2.16}$$

Thus, the intensity of this beam at any point is

$$I(z,r) = |E^*(z,r)E(z,r)| = \left(\frac{E_0}{z_\mathrm{R}}\frac{w_0}{w(z)}\right)^2\exp\left(\frac{-2r^2}{w^2(z)}\right)\,, \tag{2.17}$$

and the beam waist $w(z)$ is shown to be the radius at which the beam intensity has dropped to $1/\mathrm{e}^2$ of the on axis value, *i.e.* $I(z, r = w(z)) = I(z, r = 0)/\mathrm{e}^2$. This expression also shows us that the axial intensity is half of its value at the beam waist when at $z = \pm z_\mathrm{R}$.

The Gaussian beam intensity profile and wavefront shape described by $w(z)$ and $R(z)$ respectively in Equations 2.16 & 2.17 is illustrated in Figure 2.10. When the beam is focused by a lens the beam waist appears at the lens focus.[2] The beam is symmetric about the focus and for $|z| \gg z_\mathrm{R}$ the beam waist asymptotically follows a conic profile having an angular opening, which is double the angular half-aperture given by

$$\tan(\vartheta) = \frac{w(z)}{z}\,. \tag{2.18}$$

Equation 2.12 in the $|z| \gg z_\mathrm{R}$ limit gives us $w(z) = w_0 z/z_\mathrm{R}$ and thus

$$\tan(\vartheta) = \frac{w_0}{z_\mathrm{R}} = \frac{\lambda}{\pi w_0}\,, \tag{2.19}$$

using Equation 2.14 for z_R. Applying the small angle approximation of Equations 2.3 & 2.6 for lenses with NA<0.6 we infer

$$\mathrm{NA} = \frac{\lambda}{\pi w_0}\,, \quad \text{and thus} \quad w_0 = \frac{\lambda}{\pi \mathrm{NA}}\,. \tag{2.20}$$

[1] $\mathrm{e}^{i\alpha} = \cos\alpha + i\sin\alpha = a + ib$ where $\tan(\alpha) = \sin\alpha/\cos\alpha = b/a$

[2] There is actually always a small discrepancy between the the position of the beam waist and the paraxial focal length for Gaussian beams, the beam waist being slightly closer to the focusing lens, but the magnitude of this shift is negligible compared to the focal length: For a beam with an initial collimated waist of 1 mm and wavelength 500 nm, focused by a lens of focal length 50 mm, the waist-focus shift is only 3.2 μm [25].

Combining this with Equation 2.14 we obtain an expression for the Rayleigh length of the Gaussian beam in terms of the lens NA,

$$z_{\mathrm{R}} = \frac{\lambda}{\pi \mathrm{NA}^2} \,. \tag{2.21}$$

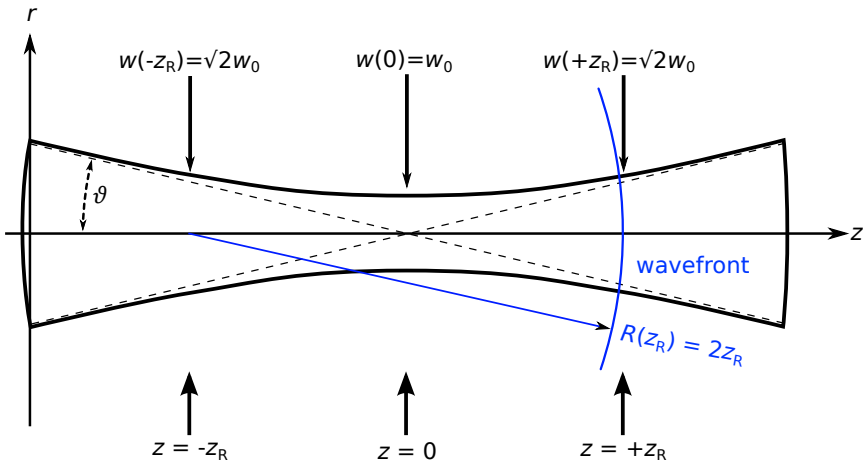

FIGURE 2.10: Propagation of a Gaussian beam. The angular half-aperture of the converging beam is given by ϑ. The waist of a beam, $w(z)$, is measured radially outwards from the optical axis of propagation to where the beam intensity has dropped to $1/e^2$ of the axial peak value. At the narrowest point of the beam along the optical axis the beam waist is given by w_0. The propagation coordinate at this point is given by $z = 0$ and the wavefront radius of curvature is $R(z) = \infty$. As z increases in magnitude away from this point the beam expands and the wavefront radius of curvature becomes finite, reducing with z. The distance from this origin at which the beam waist has increased to $\sqrt{2}w_0$ is known as the Rayleigh length, z_{R}. Here the wavefront radius of curvature reaches a minimum value, $R(z_{\mathrm{R}})$, and then begins to increase linearly with z. Both the beam waist and the Rayleigh length can be related to the NA of a lens causing the focus and the wavelength of the beam and are given in Equation 2.20 & 2.21.

Now we have expressions that define the focal volume for a lens with a given NA. In the case of a Gaussian illumination beam that has been focused by an objective lens the 'length' of the focal volume along z is given by $2z_{\mathrm{R}}$ and the radial 'width', or 'thickness' in terms of a 1-D light sheet, takes a minimum of $2w_0$ at the beam waist ($z = 0$) and expands to $2\sqrt{2}w_0$ at $z = \pm z_{\mathrm{R}}$. When concerning an objective lens used for imaging rather than illumination the length of the focal volume is an appropriate description for the depth-of-focus (DoF), *e.g.* the depth within a sample which is imaged with optimum contrast and resolution. If the focal volume beam width formed by the illumination objective lens is smaller than the orthogonal DoF of the observation objective lens then images recorded in SPIM or DSLSM are optical sections with an axial resolution that is better than that of the imaging optics alone. Thus, to build an optimum LSM setup the observation objective should be selected first, to obtain the desired field-of-view (FoV) and lateral imaging resolution for a specific sample, and the DoF of this objective should then be used to determine the minimum illumination NA that produces the optically-sectioning light sheet. Clearly there is a trade-off between the thickness and length of the light sheet as they are proportional to NA^{-1} and NA^{-2} respectively.

The longer the sheet's span across the observation FoV, the thicker the light sheet becomes. Though the work presented later in Chapter 6 is concerned with the case where the light sheet is made as thin as possible at the expense of its length, in many imaging applications the primary concern is obtaining light sheet illumination over as wide a FoV as possible. This desire has partially led to the development of non-Gaussian beam light sheet illumination, two examples of which are explained in the following section.

An additional caveat exists in the above description of beam dimensions when applied to SPIM specifically, rather than DSLSM. In SPIM two different beam widths may be desired for the focusing and collimated axes of the illumination light sheet, in order to set the sheet NA and its height across the detection FoV separately. Despite the recently published development of a cylindrical zoom lens that maintains the Gaussian beam profile in both axes independently [26] the beam NA is typically controlled using a rectangular aperture [27]. This attenuates the Gaussian beam profile along one axis and thus for low NA light sheets with a longer length and a thicker width the Gaussian beam dimensions above become more of an approximation. Additionally the use of an attenuating rectangular aperture reduces the overall beam power and can introduce fringed distortions in the beam profile.

2.2.2.3 Propagation of non-Gaussian beams

In this section two non-Gaussian beam geometries that have recently been successfully incorporated into LSM are discussed: Bessel and Airy illumination beams. In Chapter 5 Bessel beam geometry is briefly re-visited as we use our HDR beam profiling camera probe to demonstrate the extended focal length of a Bessel beam using a large-volume beam profile. As such, here we present a brief account of how Bessel beams are formed and the necessary additional component processes required to incorporate them as the illumination beam in a DSLSM. Airy beams, however, do not feature later in this thesis. But, since there is a great deal of recent interest in their application to LSM and due to their similar properties and important differences with regards to Bessel beams, we give a similarly brief description of how they are formed and give an account of the drawbacks encountered when attempting to use them in DSLSMs. A general optical schematic of an exotic beam DSLSM setup is shown in Figure 2.11.

For Bessel and Airy beams the distribution of wavevectors in the the objective lens back focal plane (BFP) is altered in order to change the propagation of the beam intensity profile downstream of the lens. Bessel beams rely on a cylindrically-symmetric redistribution of wavevectors that can be generated using annular slits [28, 29] or axicon phase elements (see Figure 2.12), the latter of which can be either a static glass block [30] or a spatial light modulator [31]. Consequently Bessel beams are cylindrically symmetric about the optical axis of propagation. Airy beams, however, are non-symmetric and are generated using a cubic phase map either in one or two dimensions, again using either static glass optics [32], a spatial light modulator [33], or diffraction gratings [34]. Figure 2.13 shows an example of the phase masks required to produce Airy beams. Due to their asymmetry Airy beams appear to curve with regards to the optical axis of propagation, though the centroid of intensity

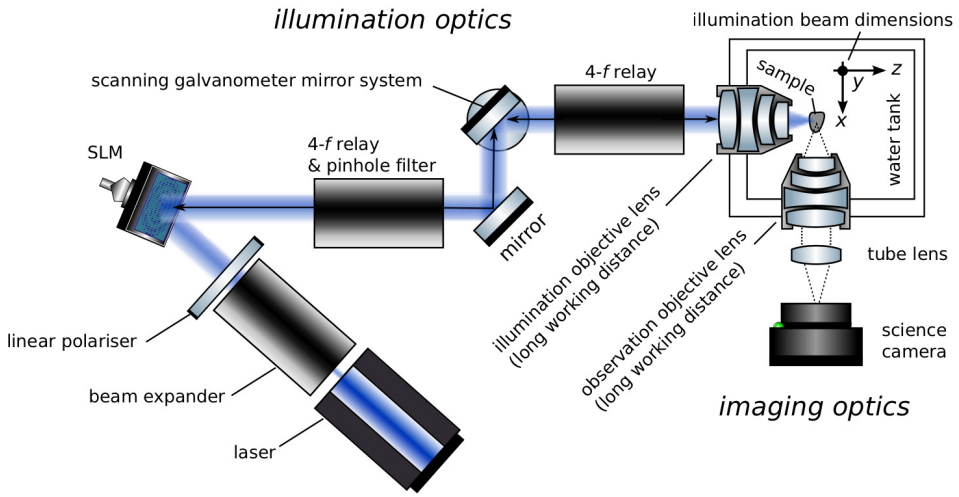

FIGURE 2.11: Optical layout for beam-scanned LSM with exotic beams. A phase or intensity map, in this case represented by a SLM, is conjugated to the BFP of the illumination objective lens in order to produced the desired 'exotic' illumination beam geometry. As with the DSLSM optical layout in Figure 2.9, a scanning galvanometer mirror pair is used to control the position of the illumination beam exiting the illumination objective lens.

continues along a straight line: The continuous cubic variation in phase, coupled with the transformation imposed by the lens orientation, causes the wavevectors of the propagating beam to be incident upon one other at different distances from the lens; This results in the peak intensity of the beam undergoing a lateral translation that varies with propagation distance [35], as shown in Figure 2.14.

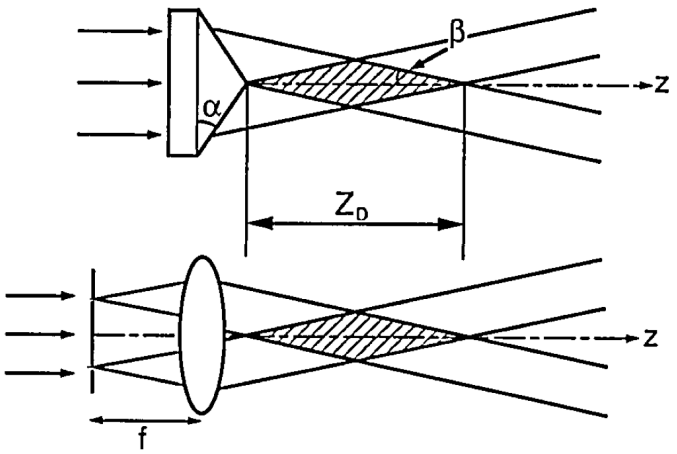

FIGURE 2.12: A Bessel beam can be generated by either an axicon phase element (shown here as a glass block) or an annular slit at the focal length of a lens. From [30].

In both Bessel and Airy cases the redistribution of wavevectors causes an extended

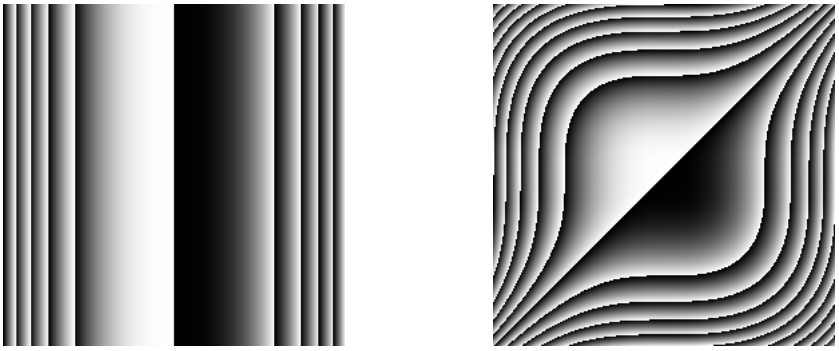

(a) 1-D Airy beam phase mask (b) 2-D Airy beam phase mask

FIGURE 2.13: Cubic phase maps generate 1-D (a) and 2-D (b) Airy beams when conjugate to the BFP of a lens. The phase masks pictured are 2π wrapped: black represents a phase of 0; white represents a phase of 2π.

focal depth much larger than that of a Gaussian beam with additional 'self-healing', or 'self-reconstructing', properties, *i.e.* when a portion of the beam's peak intensity is blocked or diverted by a highly scattering obstacle the peak intensity is re-formed some distance behind the obstacle by other non-obstructed wavevectors [36]. Self-healing of a Bessel beam is shown in Figure 2.15. This property has driven the desire to successfully implement both beams in DSLSM configurations to improve the imaging of strongly scattering specimens, first demonstrated experimentally by [37, 38] and [39, 40] for Bessel and Airy beams respectively.

Both beams are often referred to as 'non-diffracting' since their theoretical form showcases an infinite focal depth [41]. However, it is worth noting that the finite objective aperture size present in real systems causes the extent of this focal depth to be reduced to finite dimensions, despite remaining much longer than that of Gaussian beams [42]. Figure 2.14 shows how the main intensity lobe of an Airy beam becomes attenuated once the input beam extent becomes finite. A discussion of various other experimental applications of Bessel beams is given in [43]. A book chapter on non-diffracting beams principally concerned with the generation of Airy beams is [44].

Unfortunately the benefits in terms of propagation stability and penetration depth brought by these beam geometries is balanced by unwanted fluorescent excitation outside of the central light sheet which is caused by the additional intensity side lobes. This latter effect reduces the imaging contrast and sectioning capability of the microscope. To combat this several different additional measures are required in order to match the imaging performance of an 'exotic' beam DSLSM to that of a regular Gaussian beam DSLSM, all of which increase either the photon dose to the sample, the amount of post-processing required, the overall cost of the system, or all of the above. For Bessel beams the central peak intensity is surrounded by a concentric ring system of lower intensity; for Airy beams side lobes are caused by the cubic distribution of wavevectors away from the main intensity peak. Two efforts to reduce the emission caused by these lobes have been successfully demonstrated thus far: The first is an alteration of the illumination beam using either structured illumination and/or two-photon

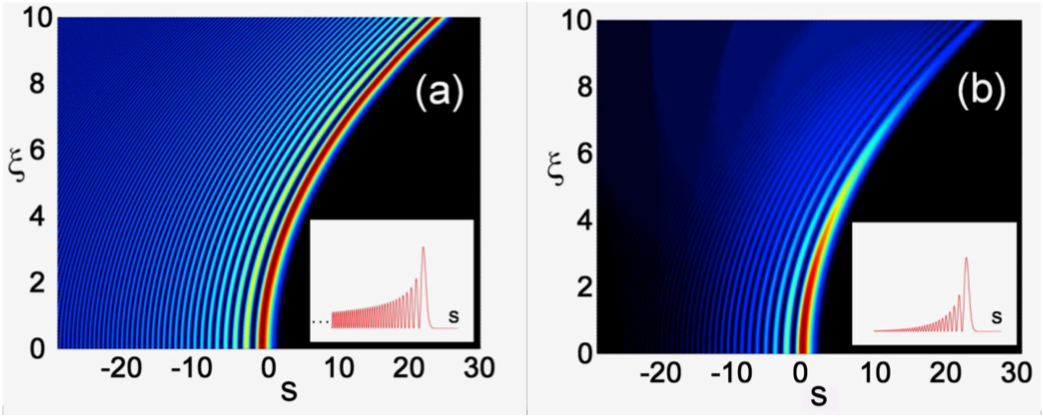

FIGURE 2.14: Propagation dynamics for 1-D infinite (a) and finite (b) energy Airy beams [42]. The inset shows a lateral profile of the input intensity. In this figure ξ and s correspond to the propagation and lateral dimensions respectively.

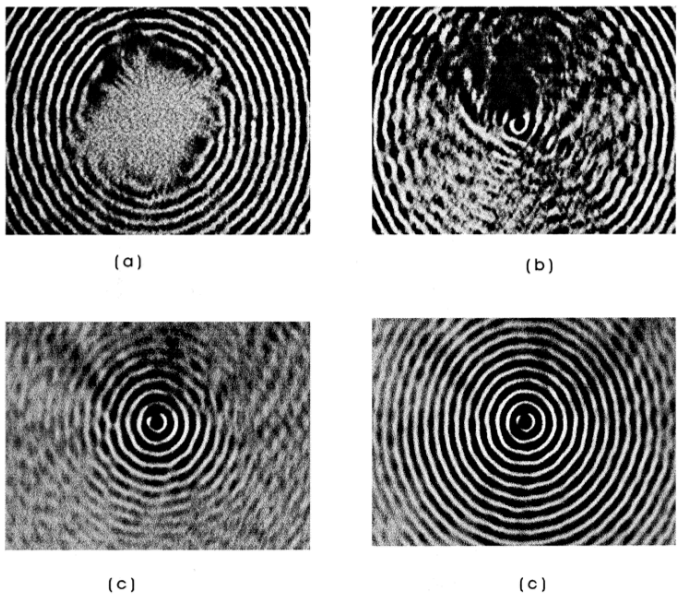

Figure 2.15: The self healing properties of a Bessel beam allow it to reconstruct following obstruction by a scattering object [45]. Images of a Bessel beam at four equally spaced locations along the propagation axis. A rectangular obstacle placed in the centre of a propagating Bessel beam causes scattering (top left). The beam however starts to 'self-heal' and re-build its intensity structure as the wavevectors surround the obstacle and begin to overlap again (top right, bottom left). Finally, the full structure of the Bessel beam heals completely (bottom right).

fluorescence with pulsed lasers [17]. The second is the physical exclusion of this excitation in the detection optics. Each approach has its benefits and drawbacks, an account of which is given below.

Structured illumination increases both the photon dose to the sample (by at least three-fold) and requires post-processing to compute a composite final image with the background computationally removed [46, 47]. Conversely, a two-photon beam causes fluorescent excitation only in the main intensity lobe but requires a high repetition rate ultrafast pulsed laser light source, typically a Ti:Saphirre or Nd:YLF source [48], which immediately increases the cost of the microscope system. The optical complexity of the setup is additionally increased since a visible laser light source remains a requirement for alignment purposes. Expense aside,

line-scanned two-photon Bessel beam DSLSM has been shown to result in better imaging contrast over a wider FoV than that which is achievable using a scanned two-photon Gaussian beam in a DSLSM [49]. The alternative approach, that of physically obscuring the excitation caused by the concentric ring system, is that of confocal slit detection [50]. Similarly to the detection geometry of a confocal microscope, confocal slit detection uses a horizontal slit which is conjugate to both the image plane and the scanned beam in the sample. The horizontal slit can take a number of forms: a combination of de-scanning mirrors and a static physical slit [51, 52]; by masking a full exposure on the imaging camera with a 1-D Gaussian shape for each beam scan position line-by-line and then combining all images in post-processing to compose a 2-D image [50]; or by rapidly recording the image line-by-line using a 'rolling shutter' at the camera using directly-addressable CMOS sensor technology rather than CCD [53]. The latter method was shown to aid the reduction of the striping artifacts which tend to be present in all confocal slit detection methods [53]. Combining confocal slit detection with line-scanned two-photon Bessel beam illumination has been shown to improve both the penetration depth and overall image quality in thick, highly-scattering samples [54]. Unfortunately the inherent asymmetry of Airy beams causes confocal slit detection to be far less effective as the apparent curve of the maximum intensity lobe does not line up well with the slit. Instead, the effect of the side lobes in both Airy and Bessel beam illumination can be reduced computationally using deconvolution [40], though this adds further post-processing time onto the imaging duration. A theoretical and experimental demonstration of the advantages of deconvolved Bessel and Airy beams over Gaussian beam DSLSM when obtaining wide FoV images is given in [39]. The authors noted improved contrast in the case of the Airy beam illumination images over those produced with the Bessel beam illumination.

The choice between whether to use Gaussian or non-Gaussian illumination beams comes down to the scale and opacity of the image being sampled, alongside considerations regarding optical sectioning, imaging resolution and FoV, duration, and photon dosage or potential phototoxicity caused by excess illumination in areas of the sample which are not being imaged. Indeed, the added optical complexity, imaging duration, and high photon dosage of exotic beam illumination means that there are many cases where a simple SPIM system is the most appropriate option. A recent paper suggested a simple procedure for selecting the optimum LSM components and illumination geometry and is as follows [55]:

1. Select the excitation and detection objective lenses according to the sample size and the desired spatial resolution;

2. Choose to use a beam-scanned or static light sheet based on the region-of-interest (RoI) extent within the sample and the desired axial resolution;

3. Find the optimum balance between spatial resolution, sectioning capability, and the level of sample scattering to overcome by selecting the appropriate Gaussian or non-Gaussian optical beam geometry.

Even after selecting the optimum optical imaging system components performance may still be compromised due to the non-scattering refractive index structure of the mounted specimen. These effects and their correction via AO are described in the next chapter. In the remainder of this chapter we continue to discuss LSM illumination beams: in particular how beam quality is currently measured; a proposed device which may overcome some of the shortcomings of the current methods; and how a photographic technique called HDR imaging might aid us in regard to a new device.

2.3 Beam profiling

In Chapter 5 of this thesis we present the development of what we refer to as a 'beam profiling' device. The intended outcome of our device is to obtain a 3-D measurement of the intensity distribution of a fluorescence microscope illumination beam, from directly within a working microscope system. This will provide direct assessment of the optical quality of the illumination beam, of any particular beam geometry, allowing us to register the presence of unwanted optical artifacts and visualise the distribution of fluorophores within a sample that would undergo excitation. The terms 'beam profiling' and 'beam quality' have however been previously applied to assess laser output, comparing the laser beam with an ideal Gaussian beam, outside of the context of fluorescence microscopy. As such, the purpose of this section is threefold: to give some context to beam profiling outside of fluorescence microscopy; to describe how the assessment of fluorescence microscope illumination beams is currently achieved; and to discuss the limitations of these current methods.

2.3.1 Current beam profiling measures

2.3.1.1 Measurement of M^2 to determine laser beam quality

Outside of the microscope the most frequently adopted measure of a laser beam's quality is the 'M^2 parameter'. In order to avoid confusion with the M used within this thesis to denote magnification we hereafter typeset this quality parameter as M^2. This parameter is obtained by comparing the dimensions of the laser beam when focused with those belonging to an ideal Gaussian beam [56]. By placing a lens of known focal length into the laser beam and measuring both the half-aperture of the beam's full angular divergence and the beam waist at the focus, the beam can be compared with a focused Gaussian laser beam having an equivalent waist size. A parameter known as the beam parameter product (BPP) corresponds to the product of half the beam's full angular divergence with the waist size, *i.e.* BPP = ϑw_0 where ϑ is the angular half aperture introduced earlier. The M^2 parameter is the ratio of this measured BPP with that of an ideal Gaussian laser beam with the same waist size. For an ideal Gaussian laser beam with a waist of w_0 after being focused by a lens the beam parameter product is given by

$$\mathrm{BPP} = \vartheta w_0 \simeq \mathrm{NA} \cdot \frac{\lambda}{\pi \mathrm{NA}} = \frac{\lambda}{\pi} \,, \tag{2.22}$$

where we have made use of Equations 2.6 & 2.20 assuming ϑ is measured in radians and the lens is slow enough for the paraxial (small angle) approximation to hold true. Thus by measuring the beam waist and the far-field angular divergence we can obtain the M^2 parameter:

$$\mathsf{M}^2 = \frac{\mathrm{BPP_m}}{\mathrm{BPP_G}} \simeq \frac{\pi \vartheta_\mathrm{m}}{\lambda w_0} \,, \tag{2.23}$$

where the subscripts m and G denote measurements and ideal Gaussian values respectively. Alternatively this can be written as

$$\mathsf{M}^2 = \frac{\vartheta_\mathrm{m}}{\vartheta_\mathrm{G}} \simeq \frac{\vartheta_\mathrm{m}}{\mathrm{NA}} \,, \tag{2.24}$$

where the equivalence of the beam waists in BPP_m and BPP_G causes them to cancel. Whichever way it is decided to calculate M^2 it is clear that the beam divergence has to be measured somehow. The angle of divergence, ϑ_m, can be extracted from w_0 measurements via curve fitting or through the use of $ABCD$ optical matrices and the calculation of second-order beam moments. A simplification of this is illustrated for a simple beam in Figure 2.16. The recommended standard method to measure the angular divergence of the beam is to take ten 2-D intensity profiles either side of the beam waist [57, 58, 59].

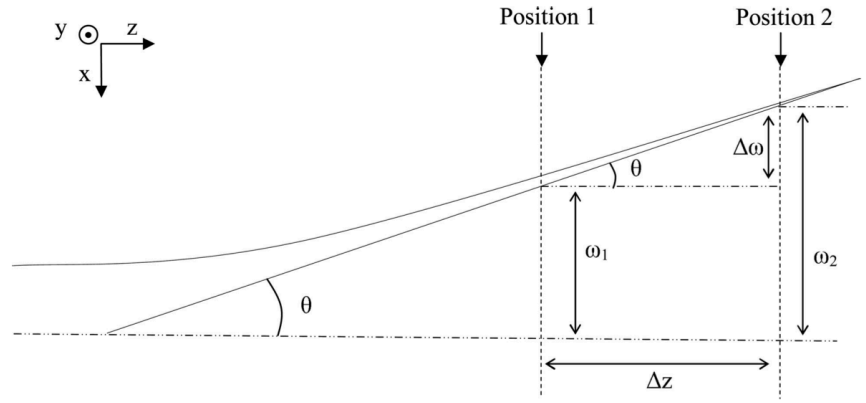

FIGURE 2.16: The angular divergence of a beam, shown here as θ, can be calculated in the simplest case by measuring the difference in the beam waist at several positions along the propagation length [60].

The techniques and corresponding devices that have been devised to directly record the intensity distributions and propagation characteristics of laser beams have taken a number of different forms over the years due to the wide-range of available laser beam powers and the gradual advancement of both imaging sensors and dynamic optical components [61, 62]. Early spatial profiling harnessed the heating power of the beam to induce currents in pyroelectric devices [63] in conjunction with beam choppers and 'moving optics'; either mechanically-scanned knife edges [64], pinholes or variable apertures. These early pyroelectric techniques suffered from long acquisition times and low spatial resolution, high thermal current drifts and low sensitivity, while the moving optics diverted beam power via diffraction and increased the size of devices. Also, these early devices used fixed lenses and required manual placement at each beam waist analysis position. A traditional laser beam profiling setup is shown in Figure 2.17.

Moving optics beam profilers remained popular during the advent of affordable charge-coupled device (CCD)s for high-resolution scanning [65] until the development of dynamic optical element technologies in the early 2000s spurred major technological advancements. Beam profiling devices using these technologies, liquid crystal dislay (LCD) spatial light modulators (SLMs) [66], digital micro-mirror devices (DMDs) [67, 60, 68], and electrically-tunable liquid lenses [69, 70, 71], have allowed beam profiling devices to measure the M^2 parameter of a beam directly and in real time with few or no moving parts. It is worth noting

that in each of these devices the beam profile is still recorded 'indirectly' because the beam is re-imaged in order to be assessed. An example of a modern beam profiling device which uses both an electrically-tunable liquid lenses and a DMD is shown in Figure 2.18.

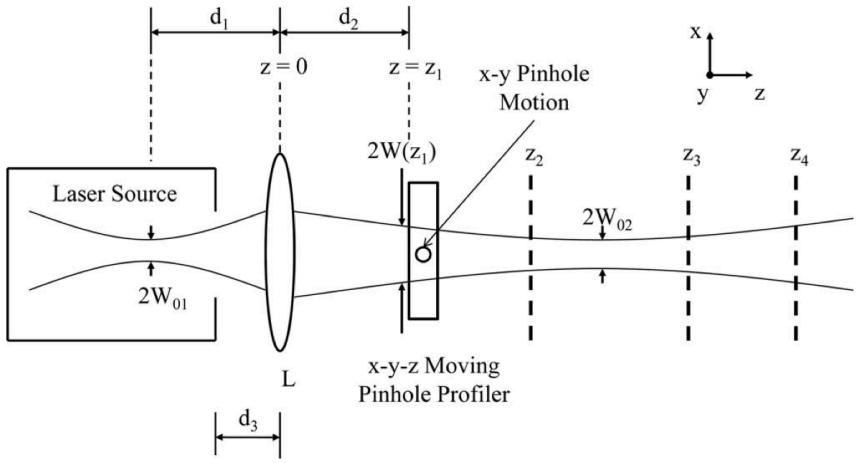

FIGURE 2.17: A traditional M^2 beam profiling procedure [70]. A lens of known focal length (L) is used to bring the laser beam in question to a focus. A moving pinhole aperture with a detector downstream of it is then placed at a number of planes at the z_i positions along the propagation axis z. The beam waists are measured by recording the detected beam power as the pinhole is mechanically-scanned in 2-D across the beam at each plane position.

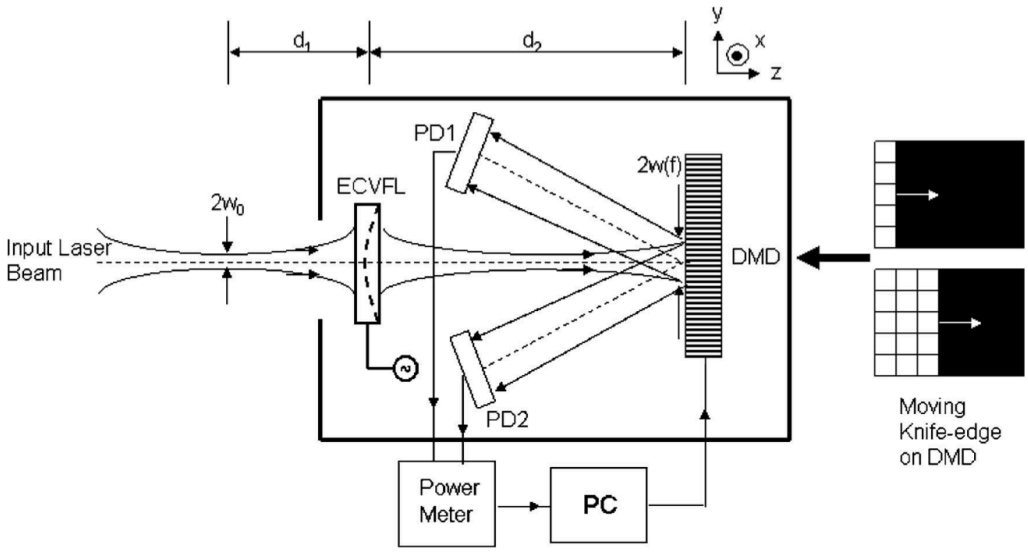

FIGURE 2.18: A modern M^2 beam analyser with no moving parts [69]. An electrically-controlled variable focal length lens (ECVFL) is used to control the position of the beam waist whilst a DMD knife-scans the beam, dividing power between two photodiodes, PD1 and PD2.

These modern beam profiling devices are typically only utilised for the assessment of collimated beams, such as a laser cavity output, rather than focal regions. A primary factor

restricting the usage of these devices elsewhere within a laser optical setup is their size, though a beamsplitter may be used at the entrance aperture in order to analyse a diverted percentage of the overall beam power, allowing the remainder of the beam to continue propagating [66]. In the rest of this chapter, and indeed this thesis, we relax the specificity of the terms 'beam profiling' and 'beam quality' from determination of the M^2 parameter to instead broadly refer to a beam's 3-D intensity profile, as this is perhaps the most important feature of illumination beams used in fluorescence excitation, whether Gaussian or not.

2.3.1.2 Beam profiling of fluorescence microscope illumination beams

Until now the most common method of obtaining the 3-D intensity profile of the illumination beam within a fluorescence microscope was to record the fluorescent excitation caused by the beam. This typically involves using the system in its usual imaging configuration and recording a featureless fluorescent image. This featureless fluorescent image can either be obtained by raster-scanning fluorescent beads, with dimensions below the diffraction limit of the imaging system, through the illumination beam [72, 73, 74, 75], or by sending the illumination beam into a fluorescent sea [16, 76], *e.g.* a solution of Fluorescin and water, where the concentration is high enough to appear uniform but low enough to avoid attenuation of the beam. With this method it is important to note that the recorded illumination beam profile is not purely an image of the illumination beam alone, but is in fact the illumination beam profile modulated by the observation optics of the system. It is also important to note that this method is only effective when the excited fluorescence is linear: non-linear absorption effects may occur at the intense focal region of a high power beam thus altering how well the recorded emission represents the illumination beam profile. This places an upper limit on the intensity range that can be recorded. The FoV and the DoF of the imaging optics set the observation volume and thus limit the extent over which the illumination beam is imaged with optimum contrast and resolution. Whilst the illumination beam profile within the observation volume directly corresponds to the fluorescence imaging efficiency of the microscope system, the ability to see features outside of this constrained region may prove useful in other aspects such as detecting stray diffraction artifacts caused by poor alignment or a misguided choice of optical components in the illumination arm. This is discussed further in Chapters 5 & 6. One major advantage of this method of beam profiling is that the microscope system remains in its intact operational form.

A more radical approach to microscope illumination beam profiling that we will mention here requires the use of an additional objective and tube lens relay, or other re-imaging optics, which are downstream of the illumination beam focus. This relay then images the illumination beam focus onto a camera detector; scanning of this entire system allows a 3-D intensity map of the illumination beam focus to be compiled from the recorded 2-D images slice-by-slice. Clearly, if these relay optics are not already a constituent part of the microscope system then the setup requires some re-configuration. This can become problematic in the case of a system such as a LSM where a water immersion tank is already used to hold the illumination and observation objective lenses in place. A pair of example beam profiles taken

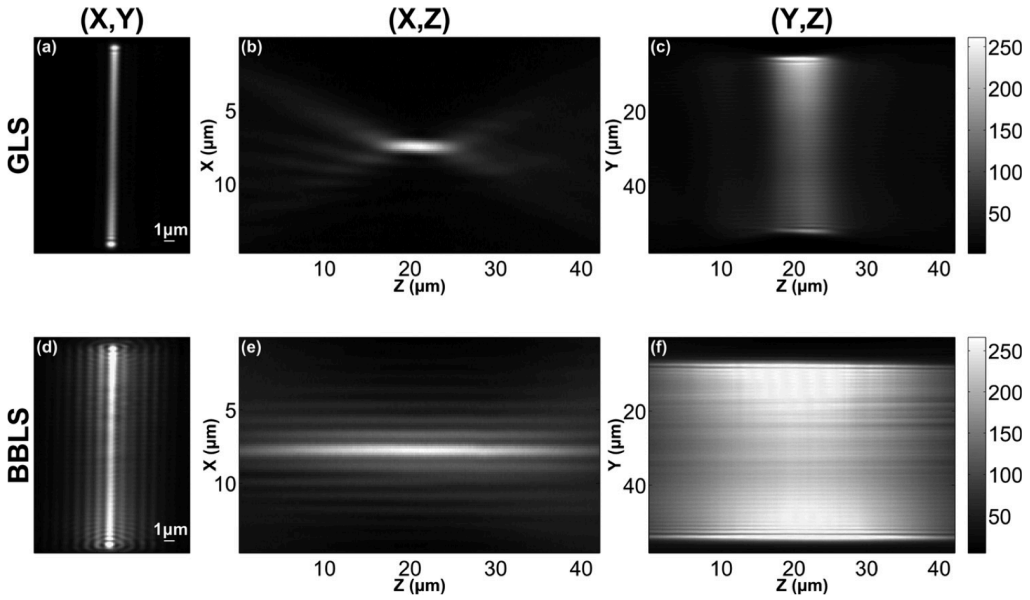

FIGURE 2.19: Indirectly-acquired DSLSM Gaussian (GLS) and Bessel (BBLS) beam profiles, acquired by *z*-stacking a re-imaged *en-face* beam focus. From [77].

with this method are shown in Figure 2.19.

In all of these indirect profiling methods—the M^2 profiling devices, the re-imaging method, and the fluorescence mapping method mentioned described earlier—there is the potential for aberrations to be introduced in the imaging optics. This can clearly distort the recorded image of the beam and thus provide us with a erroneous 3-D map of the illumination beam. This is why the approach taken later in Chapter 5 of this thesis concerns the recording of beam profiles directly, by placing a camera sensor directly within the illumination beam. The mechanics and optics of our approach are much simplified because of this: we only have to record 2-D intensity maps at a range of axial positions throughout the illumination beam in order to produce the 3-D beam profile. This has only been made possible by the recent advances in imaging sensor miniaturisation. There are, however, other significant technological limitations encountered as a direct consequence of the miniaturised sensor technology selected. Our method for overcoming these limitations was integral to our beam profiling approach and required the development of a custom high dynamic range (HDR) imaging and reconstruction procedure to record the full range of brightness in the illumination beam. In the next section we present some of the limitations surrounding the use of digital imaging sensors as well as the general theory behind, and the development of, HDR imaging.

2.4 Extended dynamic range in digital imaging

The ratio of the highest to the lowest brightness or signal level of a scene, image, or imaging device is referred to here as the 'dynamic range'. The variation in brightness of a scene in the real world can be extremely large, and yet typical human vision allows us to perceive objects under little illumination (inside an unlit room for example) simultaneously to those that are illuminated much more brightly (perhaps by daylight, seen through a window in one wall of the aforementioned room) [78].

Unfortunately, the ability to photographically capture such a wide range of illumination levels is limited by the dynamic range of the equipment employed. For digital cameras the dynamic range is limited by the sensor technology just as for traditional film cameras the dynamic range is limited by the film's chemical response to incident light. Both digital and analog photographic techniques often result in images where the dynamic range of the equipment is smaller than that contained within the illuminated scene (the *intra-scene* dynamic range); the features in some regions will be impossible to image because they are either too dark to be discernible from the noise level present or too bright to be measured.

The two primary choices of digital imaging sensors used today are solid-state circuits which operate using either charge-coupled device (CCD) or complementary metal oxide semiconductor (CMOS) technology. Both of these types of device harness the photoelectric effect to sense incident light, though each can be distinguished by the way in which the subsequent electronic information is stored and read out. The electronic components used within both types of sensor directly affect various aspects of the imaging sensor performance, which in turn leads to certain limitations being placed on the overall dynamic range of the camera.

Ultimately the dynamic range of each chip can be defined by the sensor's maximal signal-to-noise ratio (SNR). The upper limit on the measurable signal is set by the depth of the potential well used to store the charge generated by the photoelectric effect at each pixel. This storage capacity is referred to as the *well depth*. Through appropriate signal amplification the full well depth (also known as the pixel saturation level) should align with the maximum signal level available via the output analog-to-digital converter (ADC). The overall noise level is contributed to by noise sources present during the operation of the sensor circuitry alongside statistical errors associated with the counting of discrete photon and electron packets. Thus, all noise contributors combine to produce a noise floor of statistical uncertainty and signal offset in the output signal. The behaviour of the noise floor is discussed towards the end of this section.

Between the offset and the saturation level all voltages which reach the ADC are sampled by the bit-depth spacing of the ADC and are converted into measurable digital output signals; these measurable output levels are termed the *"useable bits"* of the sensor. The greater the number of useable bits, the greater the accuracy of signal digitisation by the ADC. However, an increase in the bit depth of a sensor alone does not necessarily change the *inter-scene* dynamic range that can be recorded by the sensor's useable bits. In fact, access to a camera device with a higher bit-depth may be impossible, something which is especially true in the

case of miniaturised camera sensors. In order to access a wider inter-scene dynamic range the overall light sensitivity of the sensor must be altered by adjusting the light level at which saturation is caused. The techniques used to achieve this dynamic range extension all fall under the umbrella term of high dynamic range (HDR) imaging, the development of which is reviewed in the following section. At the end of this chapter dynamic range expressions are derived and evaluated for the HDR technique applied when using our beam profiling camera probe in Chapter 5.

2.4.1 Review of HDR imaging techniques

Whilst our specific approach to HDR imaging is described later in Chapter 5, here we describe the driving force behind the advancement of HDR imaging, the development of the technique, its general application, and recent applications of HDR in research literature. HDR imaging arose in the pursuit of adequately recording, or reproducing, the wide range of brightness levels in the world around us.

2.4.1.1 Analog HDR photography

The simplest and most popular version of HDR imaging is referred to as multiple or sequential exposure HDR imaging. In the 1960s the first published attempt to improve the dynamic range of a film camera was pioneered through the use of special photographic film containing 3 different emulsion layers with the same panchromatic spectral response but distinctly different photosensitivities [79]. The film was termed "XR" for extended range and was developed by Charles Wyckoff at EG&G Inc., a defence research company contracted by the US military following World War II, to photograph the enormous range of brightness in nuclear explosions (Figure 2.20) [80]. Upon development each layer was coupled to a specific colour dye for the fast, medium, and slow film speeds and was then printed on colour paper in correspondingly different colours [81]. An HDR image of the scene could then be viewed as a psuedocolour image. After XR film became commercially available it began to be used for other non-military purposes. For example, in one early medical publication XR film was employed in x-ray cardiac imaging to enhance the definition of ventricle walls, allowing wall dynamics of normal and diseased states to be measured successfully [82].

2.4.1.2 Early digital HDR imaging

By the 1990s computers had become powerful enough to make digital image manipulation possible and CCD sensor arrays were commercially available, both of which caused HDR imaging to undergo a rapid evolution. The fundamental form of digital HDR imaging exploits the individuality of pixel responses across the sensor array. The first, and perhaps simplest, approach harnessing this spatial independence was published in a 1993 technical report by Brian Madden who was working in the GRASP laboratory at The University of Pennsylvania: he took several images of a scene using a range of global exposure durations with an early CCD sensor camera, assuming a linear signal response to incident flux [83]. Then, provided

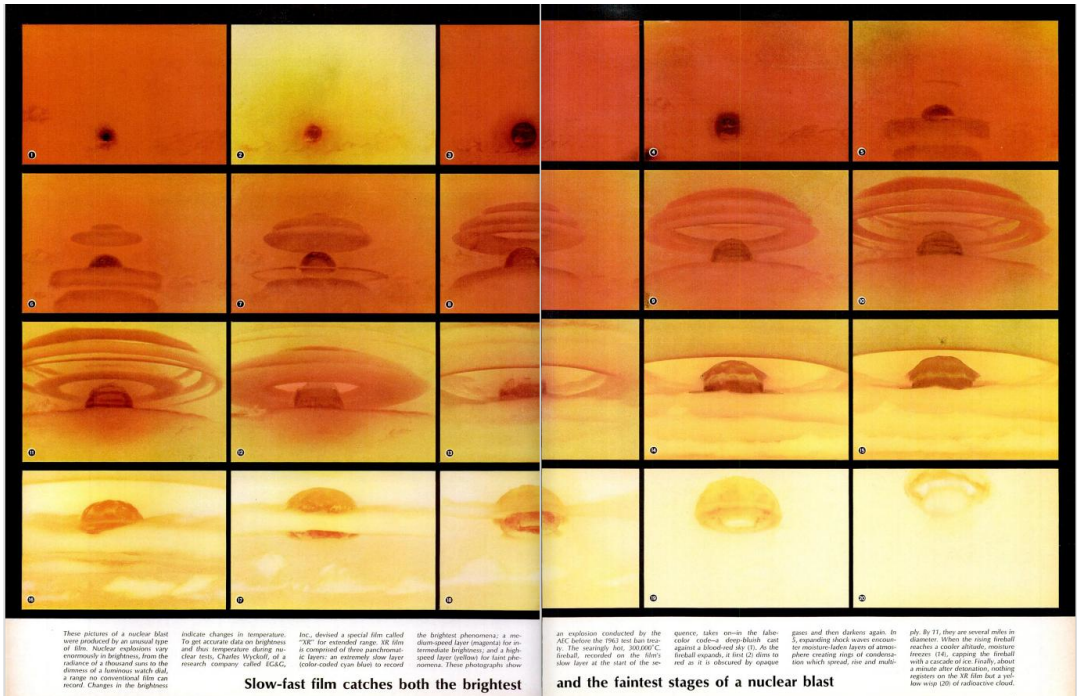

FIGURE 2.20: A double page spread from a 1966 LIFE magazine annual displays a sequence of Charles Wyckoff's XR film photographs of a nuclear explosion. Successive frames run left to right from top left to bottom right. From [80].

there was an overlap in the scene brightness between subsequent exposures, ensuring an exposure where the signal from a region was neither clipped nor saturated, a composite image could be created by fusing the component images together on a pixel-by-pixel basis. Madden noted that the exposure duration controlled the quantisation sensitivity of the sensor to incident light, and that with an increasing number of 'sensitivities' less information was lost due to coarse quantisation as the combined response function of many exposures becomes psuedo-logarithmic. By selecting for each pixel only the highest unsaturated signal (*i.e.* the longest exposure below saturation) information the 'best' intensity resolution is chosen since information loss due to coarse quantisation is reduced as much as possible. These signals are then back-scaled using the known exposure time to obtain an image of the scene with an extended dynamic range having pseudo-logarithmic quantisation levels of the incident light intensity. Figures 2.21 & 2.22 display Madden's explanatory graphs for how the scaling of quantisation with sensitivity for only 3 exposure durations combine to form an extended dynamic range. In Figure 2.23 Madden uses an increased number of exposure durations to demonstrate how the combined response approximates a logarithmic function.

This somewhat rudimentary approach of simply scaling the signal according to the exposure duration falls short of accurately reproducing the scene if the signal response of the sensor to incident light is non-linear. In order to adequately extract the brightness of the scene from multiple images the radiometric response, *i.e.* the signal behaviour of the imaging system to a range of incident light levels, is required. In [84], [85], and [86] this

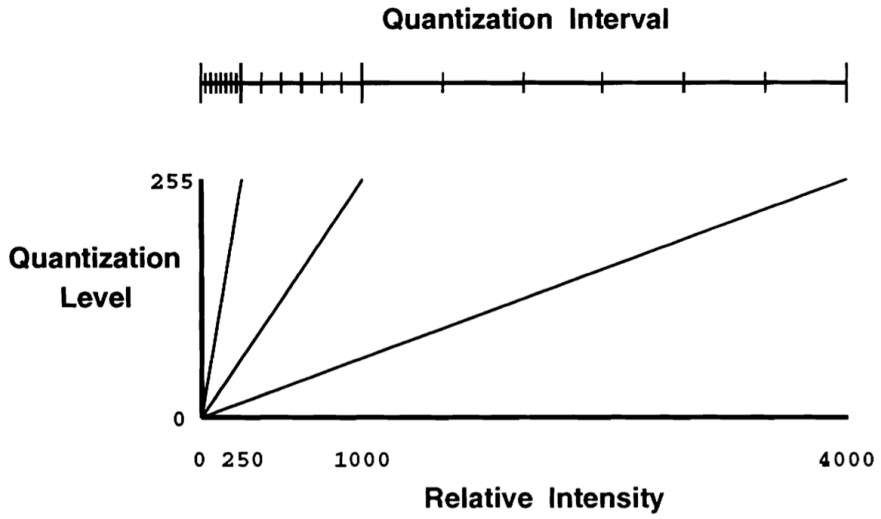

FIGURE 2.21: Madden's depiction of how the quantisation levels of a linear digital sensor change in response to an alteration in sensitivity, achieved by the use of 3 different exposure durations [83]. Sensor saturation occurs at different relative intensities depending on the exposure duration: the longest exposure saturates at the lowest relative intensity (250); the middle exposure saturates at a relative intensity of 1000; and the shortest exposure is saturated by a relative intensity of 4000. The upper scale marks the 'best' intensity resolution: the quantisation scale used when choosing the highest unsaturated signals for each exposure.

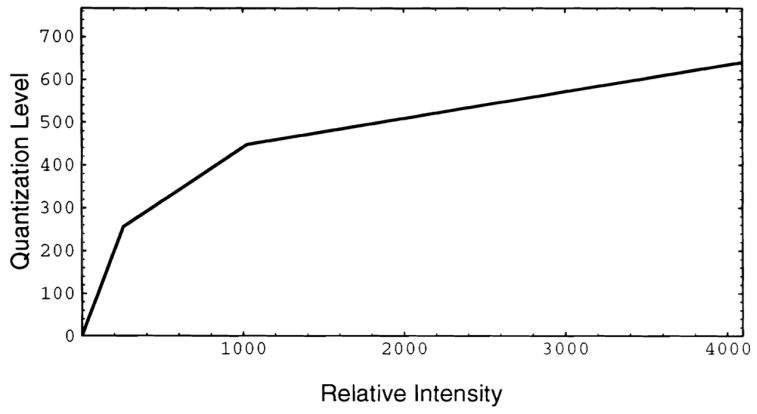

Figure 2.22: The 'best' linear response from the 3 exposures of Figure 2.21 combine piece-wise to form a composite response with extended dynamic range [83]. The intensity resolution is high in dark regions and low in bright regions.

response is recovered directly from the multiple exposure photographs taken of the scene, requiring no calibration of the actual imaging sensor. In [87] the authors perform a calibration of the imaging system first, determining an appropriate function to describe the radiometric response and then use this to extract the scene brightness. All of these methods for HDR imaging are appropriate for static imaging where both the imaging system and the scene stay in the same position and orientation and remain under the same illumination during the recording of each exposure. Primarily due to its low technological requirements, *i.e.* a digital sensor with an electronic shutter, multiple exposure HDR imaging is appropriate for

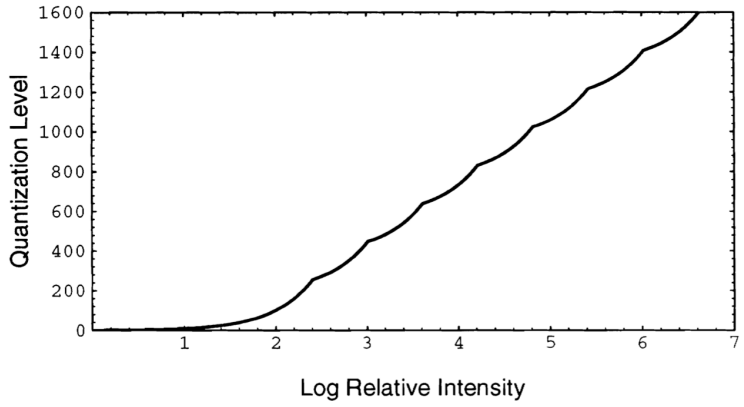

Figure 2.23: By extending the number of sensitivities from 3 to 8 the piece-wise composite response, shown here on a semilogarithmic scale, becomes increasingly pseudo-logarithmic and the intensity resolution becomes more smoothly-varying [83].

the sensor-direct beam profiling device that we develop later in this thesis. Our approach has more parallels with that of the latter paper [87] since we determine the radiometric response of our sensor directly, and then use a mathematical description of this response to extract the incident light levels in the scene.

2.4.1.3 Modern digital HDR imaging

Sequential exposure HDR is technologically-speaking the simplest HDR method to implement. However, the requirement for a static scene during the several exposure imaging duration limits its application to low frame rate photography, rather than high frame rate video. A major influential factor driving the advancement of HDR imaging is a striving towards human visual perception: not just a photographic mimicking of the light response of the eye, but also the ability to register the features of objects within a scene in real-time. Thus, the desire to produce high frame rate HDR cameras has led to numerous innovative technological approaches, briefly reviewed here for the sake of completeness, each with its own drawbacks. The fundamental notion underpinning each of these procedures is the need to make the imaging process much more parallel, *i.e.* where all required image data is acquired simultaneously rather then sequentially, than that of sequential exposure imaging,

The simplest, and perhaps least novel, approach is the use of multiple imaging detectors. Here an individual camera detector is used to record each exposure in a set by controlling the exposure duration electronically or attenuating the light level using neutral density (ND) filters. The light from the scene can be copied or split using one or several beamsplitters and so all the exposures required for a single multiple exposure reconstruction can be acquired simultaneously [88]. Thus, this technique has the advantage of real-time image capture. However, some disadvantages become apparent in the requirement of precision optics and alignment to ensure each copy of the scene is identical at each detector, as well as the cost, and indeed bulk, of multiple imaging detectors. Also, in order to make use of the real-time imaging frame rate additional computer storage capacity and processing power is required to handle the sheer volume of images.

A more novel approach requires the use of a custom image sensor where each detection

pixel is comprised of two (or more) photodiodes of different sensitivities [89]. Thus two measurements of the incident light are measured and combined before read-out. Unfortunately with this technique the down-sides are numerous: First, the sensor requires a custom-made sensor; Second, spatial resolution is sacrificed as the pixel size scales with the number of photodiodes; And third, the signals are simply combined at the pixel on-chip, which may not be radiometrically accurate.

A similar approach which trades off spatial resolution for dynamic range, but can be used with pre-existing detectors, is that of spatially-varying pixel exposures [90]. Here a filter mask of different optical transparencies or, if the electronics allow it, different integration times at neighboring pixels is used to take an image of the scene. The pattern of exposure variation can be periodic or random depending on the application but fundamentally the concept means that if a pixel is clipped then it likely has a neighbor that is not, likewise if a pixel is saturated then it likely has a neighbor that is not. A HDR image can then be constructed by aggregation where the brightness of each pixel is determined via a response function and then averaged between small neighboring set of pixels at the expense of resolution. If, however, the full lateral resolution of sensor is to be retained, dynamic range extension can be achieved at the expense of processing time by interpolating brightness estimates: The clipped and saturated signals are discarded and the remaining pixel values are scaled by their relative exposures to obtain scaled brightness estimates; 2-D interpolation between these estimates produces further estimates at the discarded pixel locations. Then, in order to reduce noise that might be inherent in the initial measurements, the entire array of brightness estimates is 2-D interpolated again and the output array takes values from the surface between each pixel estimate.

An alternative early approach to HDR video imaging inverted the usual temporal integration of flux sensor operation, converting accumulated photo-voltaic charge into an output signal, by instead measuring the time an exposed sensor takes to reach saturation to infer the incident flux. In [91] and [92] a custom solid state sensor that is designed for exactly this is described and tested, allowing the standard video frame rate of 30 Hz to be achieved. However, the novel fabrication of the sensor limited the spatial resolution at which images could be obtained.

A newer HDR technology which was informed by this earlier work is that of adaptive dynamic range imaging (ADRI). In ADRI a controllable optical attenuator (a spatial light modulator (SLM)) is used to change the incident irradiance at each pixel in a feedback loop to completely avoid saturation [93, 94]. Thus the exposures of individual pixels are varied over time in order to ensure effective use of the dynamic range quantisation. The applied transmittance of the attenuator is then used in conjunction with the measured signal to determine the incident radiance. The simple signal processing used in these cameras lends them well to live-feed video purposes. The limitations here concern both how well the pixels of the attenuator array map to the pixels of the imaging sensor and the speed that feedback can be applied. As such, when there is camera motion that changes the sensor irradiance faster than attenuation is fed back to the SLM blurring of the attenuation can be introduced.

However for static camera purposes such as surveillance these cameras can perform with frame rates of 30 Hz and higher.

As a final example to demonstrate the real-world application of HDR we refer the reader to a paper summarising advances in wearable HDR cameras and eye-projectors [95]. Here the authors demonstrate their contribution to the field in terms of extremely high frame rate reconstruction algorithms that allow HDR images to be rendered on-the-fly in real time, projecting the image into the wearer's eye. The investigation of different reconstruction algorithms, known as tone mapping, is a highly active on-going field of research. The primary concern of tone mapping is the construction of HDR images which look as realistic as possible [96]. Wearable eyewear running real-time tone mapping software has been successfully demonstrated in extremely wide dynamic range environments such as tungsten arc welding: a binocular welding mask has recently been created that allows the welder to asses the position of the tungsten electrode with augmented reality overlays that are instantaneously updated [95].

Nevertheless, beneath all of these advances in digital HDR imaging techniques and implementations there lies an unavoidable limit to obtaining information in low light environments: the noise floor. The noise floor can be contributed to in several different ways from a large number of different electronic components. This causes the dynamic range of a sensor to be affected by factors such as temperature, exposure duration, and circuit component uniformity. As such the next section of this chapter is dedicated to the various sources of noise in digital image sensors and the subsequent behaviour of the noise floor.

2.4.2 Overview of digital imaging sensors

2.4.2.1 Charge integration

Reduced to single-pixel operation both CCD and CMOS sensors behave in much the same fashion. Figure 2.24 shows a schematic of pixel as a simplified circuit diagram. A photosite area, typically the location of a silicon semiconductor material, converts the energy from incident photons into conductive valence electrons via the photoelectric effect. The quantum efficiency (QE) of the semiconductor material quantifies the ratio of incident photons to produced photoelectrons and is determined by both the energy, and thus wavelength, of the incoming photons and the energy band-gap of the semiconductor material. A photodiode with 100% QE for any given wavelength will produce 1 photoelectron per 1 incident photon at that wavelength. At 80% QE 8 photoelectrons will be produced on average for every 10 incident photons.

The photoelectrons that are promoted into the conduction band of the photodiode are stored on a capacitor during the specified exposure duration, otherwise known as the integration time. Once the integration time is over either the total charge stored on the capacitor or the voltage signal produced by the photodiode is output and the pixel circuit is reset. This is represented by a switch connecting to a potential of V_{reset} in Figure 2.24.

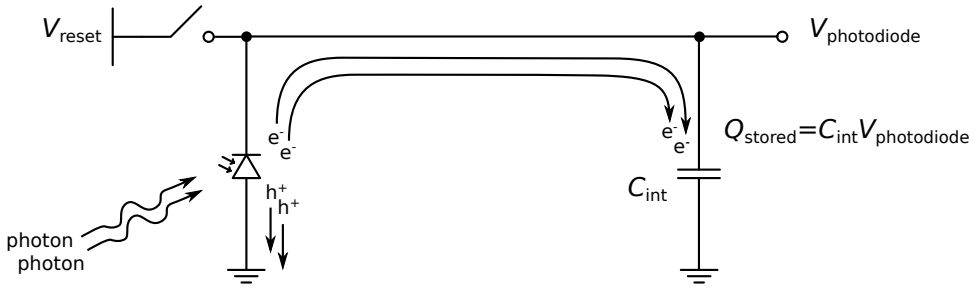

FIGURE 2.24: A simplified depiction of charge integration at a single pixel. Photons incident upon a photodiode produce electron-hole pairs via the photo-electric effect. The holes are transferred to ground whilst the electrons become stored by a capacitor. The total charge stored on the capacitor is equal to the product of the capacitance and voltage signal produced by the photodiode circuit.

2.4.2.2 Pixel read-out

Figure 2.25 shows how the signal produced during charge integration is read-out by a sequence of amplifiers and an analog-to-digital converter (ADC) in order to be represented as a digital signal. One or several amplifiers may be used throughout this signal flow in order to deliver the range of analog signal values produced in the pixel to the ADC. The ADC then digitizes the analog signal according to the quantisation level spacing set by its bit-depth.

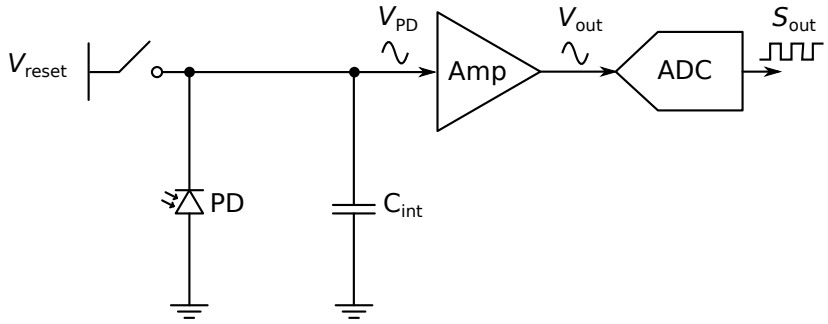

FIGURE 2.25: The signal produced during charge integration is read out using a sequence of amplifiers which apply the gain and offset necessary to match the analog signal range to the input window of an ADC. The output following the ADC is a digital signal.

2.4.2.3 Sensor read-out

The way in which the signal collected by each pixel is amplified and converted across the entire sensor array varies significantly between CCD and CMOS technologies. A comparison of the circuitry in both CCD and CMOS sensors can be made between Figure 2.26 and Figure 2.27, both of which are discussed below.

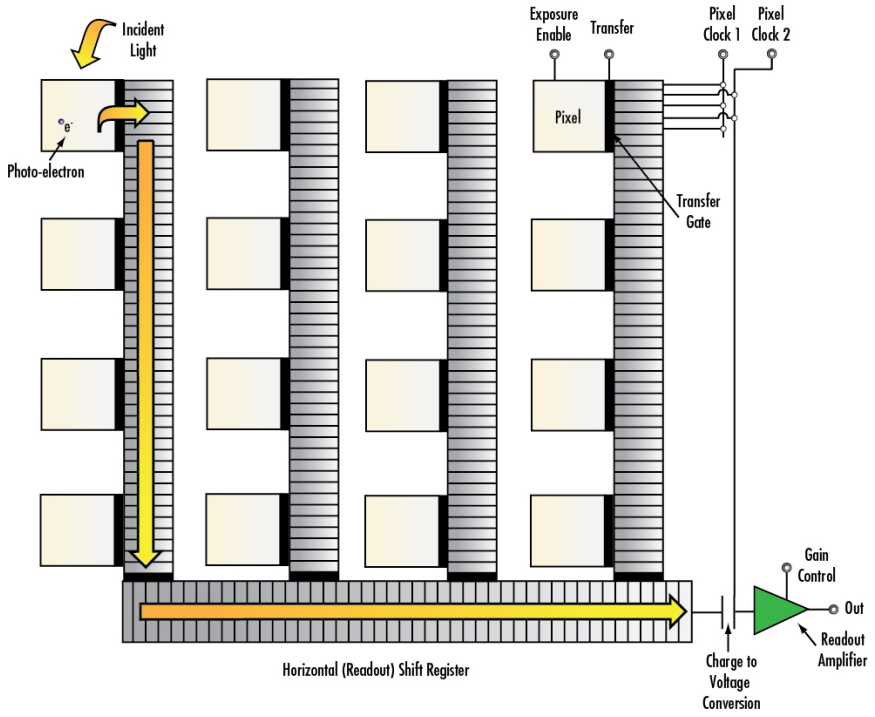

FIGURE 2.26: Signal read-out in a CCD image sensor. In a CCD sensor the electron charge stored at each pixel location is transferred by charge-coupling across the entire array to be read out sequentially. Reproduced from `http://www.edmundoptics.com/technical-resources-center/imaging/understanding-camera-sensors-for-machine-vision-applications/`.

CCD read-out Generally speaking, in a CCD sensor the electron charge stored at the photosite is transferred by charge-coupling from row-to-row down neighboring column pixels until the horizontal readout shift register is reached. This shift register then transfers the charge for each pixel to a single amplifier and ADC. The entire array is read sequentially using clock-timed pulses to move potential wells around the sensor, shifting the charge stored at each photo-site from pixel to pixel. This process consumes large amounts of power for the high potential differences used for the clock signals and the overall read-out duration is large due to it being a serial (pixel-by-pixel) process. More recently, inter-line CCDs have allowed the process to be sped up somewhat by implementing readout shift registers every few rows of pixels, sending the read-out to individual amplifiers and ADCs for each inter-line register.

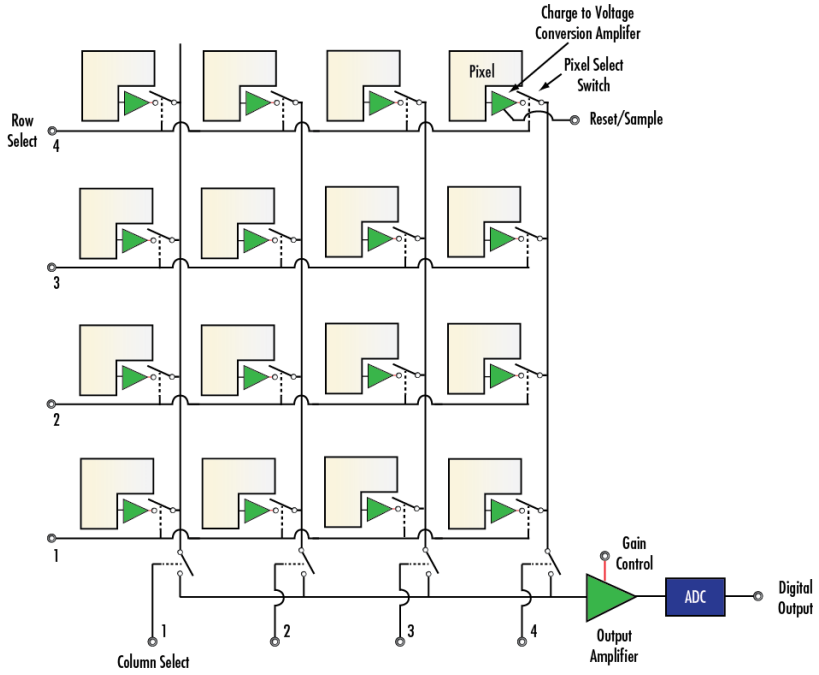

FIGURE 2.27: Signal read-out in a CMOS image sensor. In CMOS sensors MOSFET transistors perform charge transfer and signal amplification at the pixel site. Pixel reset and transfer signals are sent to every pixel along a row simultaneously. The pixel voltages along a particular row are then transferred column-wise to the appropriate ADC before the overall signal can be output. Reproduced from `http://www.edmundoptics.com/technical-resources-center/imaging/understanding-camera-sensors-for-machine-vision-applications/`.

CMOS read-out CMOS sensors allow much faster imaging speeds than CCDs by storing the photosignal as a voltage at each pixel so that charge coupling isn't the necessary form of signal transport. This lack of high voltage clock lines means that power consumption in CMOS sensors is extremely low compared to CCD sensors. Most CMOS sensors amplify the photodiode signal at the pixel site itself, all of which are then read out a row at a time by multiplexing the signals from along each column line together. The pixel circuit format may include ADCs assigned to individual pixels or small groups thereof.

The metal-oxide-semiconductor field-effect-transistor (MOSFET) transistors used to create each of the 'switches' in the CMOS circuit (pixel reset, charge transfer, amplification, row select) tend to be located atop the photodiode semiconductor substrate and thus reduce the overall photosensitive area, also known as the 'fill-factor'. Hence many CMOS sensors constructed in this 'front-illuminated' fashion employ a microlens array above each pixel site to maximise photon absorption efficiency. Extra MOSFET logic gates may be added to the pixel in order to perform even more flexible and complex image processing on-chip, further reducing the fill-factor. Rear-illuminated CMOS sensors have managed to negate this fill-factor issue in many cases, allowing the fabrication of multi-megapixel arrays [97]. However, the requirement for an inversely-doped semiconductor photosite has been a major obstacle in their development and adoption over front-illuminated sensors [98].

2.4.3 Noise sources in digital sensors

2.4.3.1 Noise arising during charge integration

There are two primary sources of noise during charge integration: photon shot noise and dark signal, both of which concern the generation of electrons within the photodiode. Photon shot noise is a by-product of the stochastic nature of photon arrival within a set time-frame and is a fundamental physical effect. Dark signal is the name for the noise signal caused by electrons generated in the photodiode which are not caused by the arrival of an incident photon.

Photon shot noise As the arrival of photons, and thus photoelectron production, is a 'counting' procedure of a discrete random variable the number of photons that are counted within any one time frame varies due to arrival time fluctuations. The number of photoelectrons that are counted is governed by Poisson statistics. This causes the root-mean-squared (RMS) number of photoelectron counts across several successive frames (integration periods) to have a corresponding standard deviation that is associated with the mean counted quantity: for an RMS count of N_{e^-} photoelectrons the associated standard deviation due to shot noise is $\sqrt{N_{e^-}}$.

By averaging the counts from many successive frames the effect of shot noise can be reduced. Figure 2.28 depicts the photon-counting response of a simulated sensor pixel in the presence of shot noise using different numbers of frames. Figure 2.28(a) shows that if only a single image is taken, photon shot noise has a considerable effect on the number of photoelectrons produced. However, if 10 or more successive frames are averaged together, as shown in Figures 2.28(b,c,d), then the RMS photoelectron count tends toward the noise-free linear relationship expected.

Figure 2.28 also demonstrates a by-product of such noise in the presence of full-well saturation that is important to note. With an example full well capacity of 75 photoelectrons the photoelectron signal of the pixel has a hard upper limit which cannot be exceeded. The presence of shot noise, however, causes the counted photon signal to sometimes register below this saturation level. Thus, once frame averaging is employed the RMS photoelectron response close to full-well saturation becomes non-linear and deviates from the noise-free model. Actual full well capacities may be upwards of several orders of magnitude larger than the 75 photoelectrons in our example, causing the effect to become far less noticeable.

It is worth noting that this effective non-linearity only occurs in the presence of photon shot noise at full-well saturation and does not exhibit any effect for low photon counts as a zero count has zero standard deviation and a count of 1 photoelectron has a standard deviation of $\pm\sqrt{1} = 1$ hence the variable signal is rarely clipped at the low end.

Dark signal The dark signal is contributed to during charge integration, predominantly by electrons that are thermally-generated at the locations of energy-level-defects caused by a spread in fabrication consistency across the various components of the pixel circuit. Dark electrons that are generated within the photodiode semiconductor material itself are generated at a constant average rate which depends on the overall temperature. Thus photodiode-generated dark electrons exhibit a notable dependence on the exposure duration.

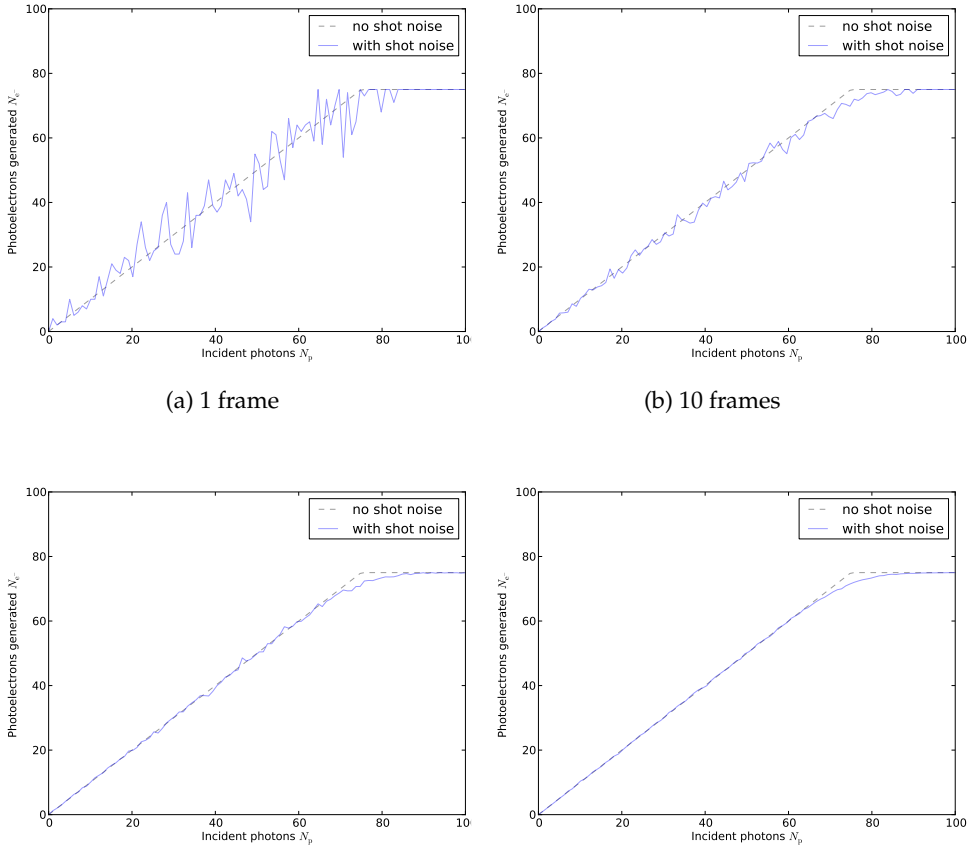

(a) 1 frame

(b) 10 frames

(c) 100 frames

(d) 1000 frames

FIGURE 2.28: Photon shot noise reduction via frame averaging. Each of these 4 graphs presents the simulated photoelectron response of a single pixel demonstrating 100% QE. From (a) to (d) the effect of photon shot noise on the photoelectron count becomes progressively reduced by the averaging of larger numbers of successive frames. This averaging of noise in the presence of signal saturation due to a full well capacity, shown here at 75 photoelectrons, leads to a non-linearity in the averaged pixel response.

The randomly-timed generation of discrete dark electrons within the integration time-frame leads to an additional Poisson statistics-based shot noise contribution to the overall dark signal. A dark current which produces a RMS signal of N_{e^-} dark electrons thus exhibits a standard deviation of $\sqrt{N_{e^-}}$ over time. As with photon shot noise the averaging of many sequential dark frames reduces effect of the temporally-varying shot noise component of the dark signal.

Since the dark signal is stored on the same capacitor as the photosignal for any one integration period, the dark signal behaviour must be identified and subtracted from the output signal in order to determine the pixel photoresponse. By ensuring that several measurements are taken both in the absence of and under illumination, the RMS dark signal (with a reduced shot noise component) can be subtracted from the RMS combined dark

& photo-signal, leaving a calibrated RMS photosignal with a similarly-reduced shot noise component.

2.4.3.2 Noise arising within the signal chain

Outside of the charge integration process there are other sources of noise within the signal chain for an individual pixel. The main additional noise sources within a CMOS pixel circuit are associated with the MOSFET signal gates used in providing reset commands or transferring and amplifying the stored charge/voltage signal. Each of these noise sources contributes to the overall noise associated with signal read-out for any recorded frame, and as such their overall effect is termed 'read noise'.

Reset and thermal (kTC) noise When the reset switch is operated an external potential is connected to the pixel circuit in order to drain any previously-accumulated charge, readying the circuit for photosignal collection. What this essentially causes is the reset voltage V_{reset} to be sampled by the photodiode capacitance. Thus a residual charge is left in the photocircuit as a result of the draining process, affecting the output signal.

However, the actual charge that is accumulated varies each time the circuit is reset. The origin of this phenomenon is random thermal noise. When the reset signal is applied the MOSFET gate acts as a thermally-noisy resistor that ultimately varies the value of V_{reset}. The RMS reset noise signal is given by

$$\langle V_{\text{reset}} \rangle = \sqrt{\frac{\mathrm{k}T}{C}} \ , \tag{2.25}$$

where k is the Boltzmann constant, T is the temperature, and C the photodiode capacitance. The equivalent RMS reset noise signal in terms of the charge stored is

$$\langle Q_{\text{reset}} \rangle = C \langle V_{\text{reset}} \rangle = \sqrt{\mathrm{k}TC} \ , \tag{2.26}$$

which equivalently demonstrates a mean noise electron count of

$$\langle N_{\text{e}^-\text{reset}} \rangle = \langle Q_{\text{reset}} \rangle / \mathrm{q} = \frac{\sqrt{\mathrm{k}TC}}{\mathrm{q}} \ , \tag{2.27}$$

where q is the electron charge. Through the form of these expressions one can see why reset noise is often referred to as kTC noise.

More importantly, these expressions demonstrate that the level of the reset noise in terms of voltage obeys an inverse relationship with the photodiode capacitance, whereas the reset noise in terms of the stored charge exhibits a square-root dependence on C. For low-light signals to be unaffected by reset noise we want $\langle V_{\text{reset}} \rangle$ to be as small as possible, implying a small value of C would be beneficial. However, smaller values of C cause the voltage noise to become larger, and since the signal is read out as a voltage this is highly undesirable. Likewise, if we attempt to reduce the reset noise voltage by using a larger capacitance photodiode we would greatly increase the reset noise electron count, thus masking low-light signals. The required pixel dimensions set an upper limit on the photodiode capacitance.

Since the photodiode capacitance can not be made as large as possible due to fabrication constraints, especially in the case of smaller pixels, efforts have been made to reduce reset noise by other means. The most successful way of reducing the reset noise is by reading out the photodiode signal both before and after charge integration, following the initial reset signal, and then subtracting the second signal from the first. As no other reset signals are sent during this integration period the reset noise contribution in both signals is correlated and the reset noise can be removed completely. This technique, known as correlated-double-sampling (CDS), is more-readily implemented in certain pixel structures and is thus limited by the pixel design [99]. An additional downside to CDS-readout operation is that the noise from non-correlated sources does not cancel and in fact adds together. In the absence of a CDS-readout operation the reset noise can become the dominant temporally-varying noise source between successive frames under uniform illumination, masking low light signals especially.

As kTC noise is a consequence of thermal excitation in the MOSFET gate it applies at all stages of signal transfer in a CMOS pixel circuit. Such noise is often referred to as 'thermal noise', or Johnson-Nyquist noise, to differentiate it from the kTC noise caused solely by the reset switch during charge integration. Thermal noise is a 'white noise' source with a constant power spectrum and as such exhibits no frequency dependency.

Low frequency $1/\nu$ noise Low frequency or 'flicker' noise is a phenomenon associated with the discrete transfer of signal carriers caused by an ensemble of energy level defects at the metal-oxide interface of the MOSFET amplifier [100]. The power spectrum density of this type of noise follows an inverse relationship with frequency in Fourier space, and is commonly abbreviated by $1/f$, though we will use $1/\nu$ to avoid any confusion with the f that represents focal length. A simplified description of the $1/\nu$ noise power spectrum is given by

$$\left\langle V_{\text{flicker}}^2 \right\rangle = \frac{K}{C_{\text{ox}} A} \cdot \frac{1}{\nu} \ , \tag{2.28}$$

where K is a process-dependent constant, C_{ox} is the gate capacitance, and A is the gate area [101]. This inverse relationship of noise power against frequency causes the variation between signals sampled in close succession to be very low, and comparatively high for signals sampled more infrequently [102].

As an interface effect the number of defect locations that contribute to the $1/\nu$ noise is proportional to the metal-oxide transistor gate surface area. With fabrication shrinkage to smaller pixels with smaller transistors less individual contributors to the $1/\nu$ noise are expected. However, Equation 2.28 predicts that as A decreases, the noise power increases. In fact, once the transfer gate area is reduced to a scale where individual traps are hosted then the signal becomes affected by single electron transfer. This process is described by random telegraph signal (RTS) behaviour with the gate signal variation exhibiting random off-on digital pulses. The additional signal processing of CDS for certain CMOS sensors results in RTS causing the overall output signal to take a distinctly Lorentzian form, demonstrating considerable variation between three well-defined output levels [103]. The signal variation

witnessed in these situations has led to such pixels being described as 'blinking pixels'. A predictive model describing the transition between these two behavioural regimes remains an on-going active area of research due to the desire for low-noise small pixels.

A superposition of thermal kTC noise and flicker noise is present at each MOSFET gate. However, as the $1/\nu$ power spectrum reduces steadily with increasing ν whereas the thermal power spectrum remains constant across all ν, there exists some corner frequency ν_c where the two spectra intersect. For signals sampled at frequencies higher than ν_c thermal noise dominates, and for signals sampled at frequencies lower than ν_c flicker noise dominates.

ADC noise I: Quantisation error The final stage of the signal chain involves the conversion of the signal voltage to a digital number by the ADC. A digital number is often expressed as DN or as an analog-to-digital unit (ADU). Here the signal may require a final stage of amplification in order to match the analog signal voltage range (0–V_{max}) to the input signal window of the ADC (V_{ADC1}–V_{ADC2}) and any multiplicative gain applied will thus magnify the random analog noise component within the signal. This amplified analog signal is then converted by the ADC to a range of discretised digital output levels and the effective spacing of these levels is termed the 'least significant bit', which corresponds to an input signal voltage step of magnitude V_{LSB}.

In an ideal linear ADC where the threshold either side of each step is $\pm V_{LSB}/2$ the error in the digital signal output against the analog input range of voltages is a sawtooth function given by

$$S_e(V) = V, \text{ where } -V_{LSB}/2 < V < +V_{LSB}/2 \,. \tag{2.29}$$

The mean-square of this signal error is then found by integrating $S_e^2(V)$ between the limits of V like so:

$$\left\langle S_e^2(V) \right\rangle = \frac{1}{V_{LSB}} \int_{-V_{LSB}/2}^{+V_{LSB}/2} V^2 dV = \frac{1}{V_{LSB}} \left[\frac{V^3}{3} \right]_{-V_{LSB}/2}^{+V_{LSB}/2} = \frac{V_{LSB}^2}{12} \,. \tag{2.30}$$

This leaves us with an RMS quantisation error in terms of the input voltage signal of

$$\langle S_e(V) \rangle = \sqrt{\left\langle S_e^2(V) \right\rangle} = \sqrt{\frac{V_{LSB}^2}{12}} = \frac{V_{LSB}}{\sqrt{12}} \,. \tag{2.31}$$

If this error caused by quantisation is smaller in magnitude than that which is caused by random analog signal variations then the read noise of the system is dominated by analog noise. Conversely, if the quantisation error is larger than the analog signal noise then the read noise of the sensor is quantisation-error-dominated. In this situation an increase in the ADC bit-depth will therefore improve the accuracy to which the analog read noise can be measured.

ADC noise II: Non-linear signal output Additionally the ADC may introduce some unwanted non-linearities into the signal output. The first, and most direct, cause of ADC non-linearities is due to conversion errors caused by fabrication, such that for a linear variation in input signal, the subsequent digital output is not a uniform digital staircase [104]. Such a

performance error may be caused by inconsistencies within a particular ADC technology, or common to all the ADCs across the sensor array.

The second, and perhaps more pertinent, non-linearity effectively caused by the ADC is down to averaging a thresholded/windowed noisy signal. In the case of a signal affected by Gaussian read noise an effect can occur at either end of the input signal window that is similar to that which was seen in Figure 2.28 for the case of photon shot noise in the presence of full-well saturation. Figure 2.29 demonstrates this effect of averaging a windowed read-noise-affected input signal whilst Figure 2.30 demonstrates the consequence of attempting to reduce the presence of these non-linearities via the application of different offsets.

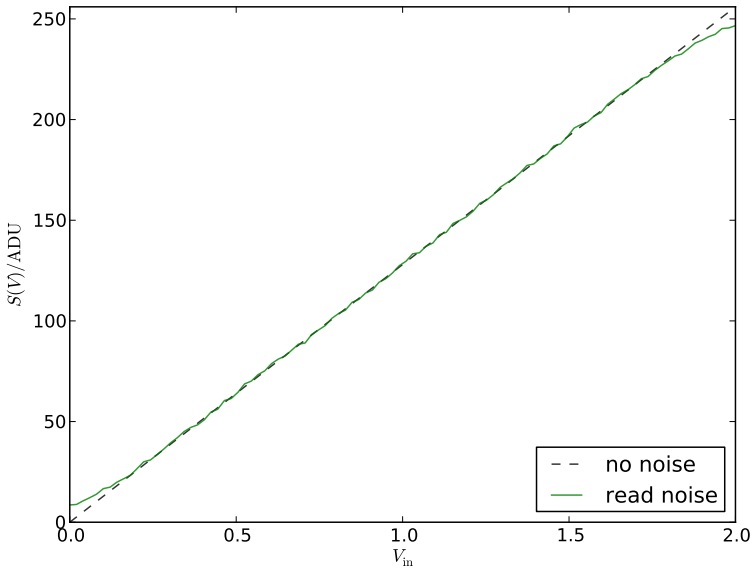

FIGURE 2.29: The limited input window of an ADC can cause non-linear response characteristics in the presence of read noise. This graph describes the average simulated response of an ADC where an input analog voltage signal between the input range of 0–2 V is converted to an 8-bit digital number. The presence of read noise causes a Gaussian spread of the analog input signal either side of the overall mean value, but the conversion window of the ADC causes reference voltages below 0.0 V and above 2.0 V to become clipped. This leads to the mean output signal being larger than expected at the low end and smaller than expected at the high end of the window. This simulation was performed for a large number of data points: 1000 successive frames. These effects are noticeable in the lower-left and upper-right corners of the figure.

Overall consequences of read noise Collectively the combined effect of reset noise, thermal noise, and flicker noise contribute to the overall read noise floor for the signal from an individual CMOS pixel. Provided there is no temperature variation between successive frames the read noise behaves according to predictable statistics with a measurable overall RMS noise signal.

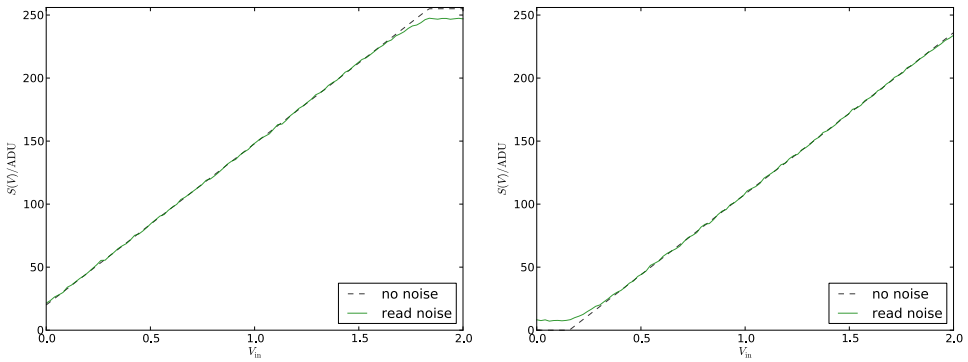

FIGURE 2.30: In (a) the non-linear low end of an ADCs average response has been improved by applying a positive offset to the input signal with the magnitude of the read noise standard deviation. However, this emphasises the non-linearity seen at the top end of the output window. Conversely, in (b) the non-linear top end of the response has been removed through the application of a negative offset of equal magnitude at the expense of an emphasised non-linearity at the low end. Lower gain can be applied in conjunction with a positive offset in order to remove both non-linearities, though this consequently increases the quantisation error in the output signal.

In the case of read-noise dominated by analog signal variation cooling of the sensor will reduce the effect of thermal noise sources, including reset noise, but this may cause flicker noise to dominate, especially in the case of long exposures with a low sampling frequency. However, if flicker noise is small then cooling can cause the read noise to become dominated by the quantisation error.

2.4.3.3 Noise behaviour across a sensor array

Our discussion of noise thus far has attributed the many contributing sources of noise to the various electrical components used within the signal chain for a pixel. Since these components are almost exclusively used by individual sensor pixels in the case of CMOS sensors, the spread of fabrication non-uniformities across all of these components leads to highly non-uniform noise and photo-response behaviour across a CMOS sensor array. Due to the operational layout of transistors and ADCs within CMOS sensors, there is a tendency to exhibit shared noise characteristics along rows and columns of the array that are independent of one another.

Though each various noise source has some dependence on exposure duration (integration time) and device temperature, the noise behaviour for successive frames of the same duration at the same temperature will produce a repeatable average noise signal for each pixel. This repeatable noise non-uniformity across the sensor array is commonly referred to as fixed-pattern-noise (FPN) which can be thought of as the superposition of two noise patterns: dark current non-uniformity (DCNU) and photo-response non-uniformity (PRNU). The former is an offset map of dark signal in the absence of illumination while the latter is a result of gain mis-matches across the array affecting photosignals.

Dark current non-uniformity As several different dark current generation mechanisms are possible within in a CMOS pixel circuit, a large range of dark signal magnitudes are possible across the non-illuminated CMOS array. The dark signal in some pixels may exhibit strong dependencies on exposure duration, whilst other pixels may produce a dark signal that is independent of this [105]. Similarly, the temperature dependence of the dark signal for a single exposure duration may vary largely across the array.

Photoresponse non-uniformity The large numbers of amplifiers and ADCs used to transfer and output signals across the CMOS array are statistically likely to have mis-matches between them. Thus, the voltage signal produced at one pixel circuit may experience a different gain value than that of a neighboring pixel, even when both pixels are under uniform illumination. Being associated with signal gain, this form of non-uniformity scales with the illumination level. Successive frames of low illumination may exhibit good uniformity, whereas under much brighter illumination the non-uniformity can become greatly apparent.

Provided the same exposure duration is used in both cases, and that the device does not undergo heating under the bright illumination, the DCNU can be subtracted from the signal recorded under each illumination. The differing gradient of the photoresponse between the pixels can then be calculated and used to post-process the sensor output to remain uniform under a wide range of illumination levels.

2.4.4 Extending dynamic range

2.4.4.1 Dynamic range: single frame averaging

In the absence of noise The dynamic range of any recording equipment is given by the ratio of the largest recordable signal to the smallest recordable signal. In a perfect environment free of noise the smallest recordable signal is determined by the most minute variation in signal level that can be detected. For a digital device that converts analog signals into digital numbers (DN), or grey levels, the largest signal that can be produced is set by the bit depth of the sensor, and the smallest signal is one bit.

The bit depth of an n-bit digital sensor has 2^n DN available for the output signal, from a zero signal of 0 DN up to $S_{\text{max}} = 2^n - 1$ DN, with a minimum signal error S_{min} corresponding to a least significant bit (LSB) of size $S_{\text{LSB}} = 1$ DN. Thus, the dynamic range (DR) of the sensor is therefore given in terms of gray-levels as

$$\text{DR}_{[\text{DN}]} = \frac{S_{\text{max}}}{S_{\text{min}}} = \frac{2^n - 1}{1} = 2^n - 1 \text{ [DN]}. \tag{2.32}$$

To convert this into decibels we can write the dynamic range as

$$\text{DR}_{[\text{dB}]} = 20 \log_{10}(\text{DR}_{[\text{DN}]}) = 20 \log_{10}(2^n - 1) \text{ [dB]}. \tag{2.33}$$

In the presence of noise If, however, there is noise on the analog signal entering the digital device, then there is an uncertainty associated with the signal that will be converted to a DN

and output by the device. For N digital measurements of the analog input signal there will be a RMS average signal with an associated uncertainty caused by the noise fluctuations.

The output signal in any one measurement can be given as

$$S = \langle S \rangle \pm S_{\mathrm{e}} \,, \tag{2.34}$$

where $\langle S \rangle$ is the RMS signal and S_{e} is the departure from this RMS in any one measurement.

The best possible measure of the signal S is quoted as the RMS signal plus or minus the standard error on the mean (SE). The SE is calculated from the standard deviation (SD) and is given by

$$\mathrm{SE} = \frac{\mathrm{SD}}{\sqrt{N}} \,. \tag{2.35}$$

The signal is therefore

$$S = \langle S \rangle \pm \mathrm{SE} \,. \tag{2.36}$$

The SE of our measurements therefore tells us the smallest output signal that we can reliably measure due to the errors caused by random fluctuations. Hence, the signal corresponding to the SE in our measurements sets the dynamic range of the sensor as it informs us of our measurement accuracy.

Thus, we swap SE for S_{min} in Equation 2.32 to obtain the expression for the *dynamic range in the presence of noise*:

$$\mathrm{DR} = \frac{S_{\mathrm{max}}}{\mathrm{SE}} \,[\mathrm{DN}] \,. \tag{2.37}$$

Substituting Equation 2.35 into Equation 2.37 we then obtain the dynamic range in terms of N and the SD as

$$\mathrm{DR} = \frac{S_{\mathrm{max}}}{\mathrm{SD}/\sqrt{N}} = \sqrt{N}\frac{S_{\mathrm{max}}}{\mathrm{SD}} \,[\mathrm{DN}] \,. \tag{2.38}$$

Since the SD of the noise is typically an inherent property of the noise caused by the operating conditions of the device, the SD can therefore can be approximated as an invariant quantity over any given set of N measurements.

A comparison of Equation 2.38 with Equations 2.32 shows that if we have $\sqrt{N} = \mathrm{SD}$ then the dynamic range of the sensor will return to *noise-free performance*. In other words if the number of successive measurements taken is equal to the square of the standard deviation (in DN) caused by noise, *i.e.* $N = \mathrm{SD}^2$, then the effect of noise is negated as the SE has been reduced to the same value as the least significant bit. We refer to this form of dynamic range extension as successive frame averaging (SFA).

Worked example: SFA of an 8-bit pixel Let's start with a single 8-bit sensor pixel. This pixel is noise-free and has no signal offset. In terms of the output signal there are $2^8 = 256$ DN available for the output signal, from 0–255, with a least significant bit of size 1 DN. There is no noise affecting the signal transfer and so the smallest resolvable signal is the $S_{\mathrm{LSB}} = 1$ and the DR of the sensor is therefore

$$\mathrm{DR}_{\mathrm{ideal}} = \frac{255}{1} = 255 \,[\mathrm{DN}] \,(= 48.1 \,[\mathrm{dB}]) \,. \tag{2.39}$$

Now, if a noise source affects the analog input signal and causes signal fluctuations that obey a standard deviation of SD = 10 DN then the dynamic range for any single image ($N = 1$) becomes

$$\mathrm{DR} = \frac{255}{10} = 25.5 \text{ [DN]} (= 28.1 \text{ [dB]}) . \tag{2.40}$$

The level of detail in the analog signal that can be reliably converted by the device has dropped by a factor of ten.

However if we were to take 10 measurements we would see a slight improvement in the dynamic range:

$$\mathrm{DR} = \frac{255}{10/\sqrt{10}} = \sqrt{10}(25.5) = 80.6 \text{ [DN]} (= 38.1 \text{ [dB]}) . \tag{2.41}$$

And if we took 100 measurements then the dynamic range performance would be restored:

$$\mathrm{DR} = \frac{255}{10/\sqrt{100}} = \sqrt{100}(25.5) = 255 \text{ [DN]} (= 48.1 \text{ [dB]}) . \tag{2.42}$$

We would be able to access a higher dynamic range than that of the pixel itself by taking $N > \mathrm{SD}^2$ measurements. In this example case $N > 100$. If we took $N = 500$ measurements then we would obtain a higher dynamic range of:

$$\mathrm{DR} = \sqrt{500}(25.5) = 570 \text{ [DN]} (= 55.1 \text{ [dB]}) . \tag{2.43}$$

Similarly for $N = 1000$ we would get

$$\mathrm{DR} = \sqrt{1000}(25.5) = 803 \text{ [DN]} (= 58.1 \text{ [dB]}) . \tag{2.44}$$

2.4.4.2 Dynamic range: Multiple exposure imaging

An alternative way of improving the effective dynamic range of a sensor by altering the exposure duration of the sensor is referred to as sequential or multiple exposure imaging (MEI)[3]. By extending the exposure time of a photodiode to longer durations the photosignals generated by lower photon arrival rates produce larger signals. Thus full well saturation occurs at lower incident flux - the sensor effectively becomes more sensitive to the environment to which it is exposed, though signal transfer through the device operates in the exact same way.

Let's assume that the smallest signal measurable by the sensor due to either quantisation (least significant bit), or noise (standard deviation of the measured signal), does not vary when the exposure duration is altered. This means that the measurement error in any given exposure obeys the same statistics. Effectively this means that every individual exposure has the same dynamic range.

The improvement in dynamic range becomes evident when several exposures are used together to observe the overall scene. This allows very large intrascene signals (incident flux,

[3]The MEI acronym is adopted in this section over SEI to avoid confusion with the acronym for the standard error on the mean (SE)

external to the device) to produce $S_{\max}$ in the shortest exposure (labelled A) and very low intrascene signals to produce the smallest measurable signal $S_{\min}$ in the longest exposure (labelled B). Thus the collective benefit of using different exposure durations to measure the brightness of a scene causes the composite intra-scene dynamic range that it is now possible to observe to be set by the ratio between the signals corresponding to these two levels. By scaling the smallest measurable signal in the longest exposure $S_{\min(B)}$ to the range of signals it would correspond to in the shortest exposure, the new extended dynamic range can be found.

In the following we assume that our sensor pixel demonstrates a linear output signal response S to the incident light intensity I; thus, $S \propto I$. The signal output can therefore be modelled as

$$S = \alpha I + \beta = \alpha F \Delta t_i + \beta \ , \tag{2.45}$$

where α and β are constants of proportionality, F is the incident flux, and Δt_i is the exposure duration.

Setting $\alpha = \beta = 1$ we therefore have

$$S = F \Delta t_i \ , \tag{2.46}$$

representing our sensor's linear response to incident flux. The largest signal we can measure in exposure A is given by $S_{\max(A)} = F_{\max(A)} \Delta t_A$ and the smallest signal we can measure in exposure B is $S_{\min(B)} = F_{\min(B)} \Delta t_B$.

Inverting the response equations we can obtain the incident flux from a given signal and exposure time through the following expression:

$$F = \frac{S}{\Delta t_i} \ . \tag{2.47}$$

This now allows us to scale the signals recorded at different exposure times to a common set of units.

Since $S_{\min(i)}$ is constant across all i we can calculate the effective minimum measurable signal (denoted by a prime) in the units of the shortest exposure as

$$S'_{\min} = F'_{\min} \Delta t_A = \frac{S_{\min(i)}}{\Delta t_i} \Delta t_A = \frac{S_{\min}}{\Delta t_i} \Delta t_A \ . \tag{2.48}$$

The improved dynamic range expression for our two exposures is therefore:

$$\mathrm{DR}_{[\mathrm{DN}]} = \frac{S_{\max}}{S'_{\min}} = \frac{S_{\max}}{S_{\min}(\Delta t_A / \Delta t_B)} = \left(\frac{\Delta t_B}{\Delta t_A} \right) \cdot \frac{S_{\max}}{S_{\min}} \ [\mathrm{DN}] \ ; \tag{2.49}$$

Worked example: MEI dynamic range improvement without noise In the absence of noise on an 8-bit sensor $S_{\max} = 255$ DN and $S_{\min} = S_{\mathrm{LSB}} = 1$ DN. Thus if $t_{\mathrm{B}} = 4t_{\mathrm{A}}$ the improved dynamic range is

$$\mathrm{DR}_{[\mathrm{DN}]} = \left(\frac{\Delta t_B}{\Delta t_A} \right) \cdot \frac{S_{\max}}{S_{\min}} = 4 \cdot 255 = 1020 \ [\mathrm{DN}] \ ; \tag{2.50}$$

$$\mathrm{DR}_{[\mathrm{dB}]} = 20 \log_{10}(1020) = 60.2 \ [\mathrm{dB}] \ . \tag{2.51}$$

Worked example: MEI dynamic range improvement with noise If, as before, we have a noise source causing a standard deviation in the recorded signal of SD = 10 DN, then the minimum accuracy of N measurements is set by the standard error as $S_{\text{min}} = \text{SE} = \text{SD}/\sqrt{N} = 10/\sqrt{N}$.

With the same exposure durations as before we then have

$$\text{DR}_{[\text{DN}]} = \left(\frac{\Delta t_B}{\Delta t_A}\right) \cdot \frac{S_{\text{max}}}{S_{\text{min}}} = 4 \cdot \sqrt{N} \cdot \frac{255}{10} = \sqrt{N} \cdot 102 \text{ [DN]} ; \tag{2.52}$$

$$\text{DR}_{[\text{dB}]} = 20 \log(\sqrt{N} \cdot 102) \text{ [dB]} . \tag{2.53}$$

2.4.4.3 HDR comparison: MEI vs. SFA

In theory it is possible to achieve the same extended dynamic range using either MEI or SFA. The difference in the number of images required to achieve the same dynamic range in both cases informs us of the efficiency: the most efficient method requires the lowest number of images to be taken. The maximum resolvable signal on the sensor is given by S_{max}, and the minimum resolvable signal on the sensor is set by the SD of the noise and is given by $S_{\text{min}} = SD$.

Let's consider the dynamic range of a multiple exposure set (MES) of images where N_{MEI} frames are recorded for each exposure so frame averaging also takes place within the set. Here we assume that there are M exposures from the shortest exposure Δt_A to the longest exposure Δt_B in the set that ensure an overlap in the intrascene dynamic range between each exposure. The exposures between A and B do not alter the overall dynamic range, as this is set by the extreme exposures, though they do contribute to the overall number of images taken.

The SFA procedure uses N_{SFA} sequentially recorded frames at an exposure which is equal to the shortest exposure in the MES - *i.e* $\Delta t = \Delta t_A$, thus the maximum recordable signal in both MEI and SFA corresponds to the same intrascene flux.

By setting Equation 2.49 equal to Equation 2.38 we obtain an equal dynamic range in both cases:

$$\begin{aligned} \sqrt{N_{\text{MEI}}}\frac{\Delta t_B}{\Delta t_A} \cdot \frac{S_{\text{max}}}{S_{\text{min}}} &= \sqrt{N_{\text{SFA}}}\frac{S_{\text{max}}}{S_{\text{min}}} \\ \implies \sqrt{N_{\text{MEI}}}\frac{\Delta t_B}{\Delta t_A} &= \sqrt{N_{\text{SFA}}} ; \end{aligned} \tag{2.54}$$

which implies

$$N_{\text{SFA}} = \left(\frac{\Delta t_B}{\Delta t_A}\right)^2 \cdot N_{\text{MEI}} . \tag{2.55}$$

This last expression is important: it tells us that the number of images required in SFA to attain the same extended dynamic range as that of MEI is equal to the *square* of the ratio of the longest exposure to the shortest exposure multiplied by the number of frames used in the MES.

The efficiency of each procedure depends on the total number of images taken. Let's compare both procedures when they are achieving the same dynamic range. The ratio of the

total number of images taken in each procedure is given by

$$\frac{N_{\text{SFA}}}{M \cdot N_{\text{MEI}}} \,. \tag{2.56}$$

Worked example I If we assume that in the MEI procedure $N_{\text{MEI}} = 10$ images are taken at each of $M = 10$ exposures between $\Delta t_A = 1$ ms and $\Delta t_B = 10$ ms then Equation 2.55 tells us that we need to take

$$N_{\text{SFA}} = \left(\frac{10}{1}\right)^2 \cdot 10 = 10^2 \cdot 10 = 10^3 \text{ frames} \tag{2.57}$$

in order to obtain the same dynamic range.

Only $M \cdot N_{\text{MEI}} = 10 \cdot 10 = 10^2$ images have been taken overall in the MEI procedure. This means that the SFA procedure will take

$$\frac{N_{\text{SFA}}}{M \cdot N_{\text{MEI}}} = \frac{10^3}{10^2} = 10 \times \tag{2.58}$$

longer to complete than the MEI procedure.

Worked example II If we input some values that correspond to a similar MEI procedure to that of our HDR technique in Chapter 5: *i.e.* $N_{\text{MEI}} = 10$ images are taken at each of $M = 10$ exposures between $\Delta t_A = 0.1$ ms and $\Delta t_B = 25$ ms. Equation 2.55 then tells us that we would need to take

$$N_{\text{SFA}} = \left(\frac{25}{0.1}\right)^2 \cdot 10 = 250^2 \cdot 10 = 625000 \text{ frames} \tag{2.59}$$

in order to obtain the same extended dynamic range using SFA.

This means that the SFA procedure will take

$$\frac{N_{\text{SFA}}}{M \cdot N_{\text{MEI}}} = \frac{625000}{10 \cdot 10} = 6250 \times \tag{2.60}$$

longer to complete than the MEI procedure.

Adaptive Optics and its application in microscopy 3

3.1 Introduction

This chapter serves as a literature review for the work presented later in Chapter 4, introducing the concept of adaptive optics (AO), giving a general technological overview of the technique in astronomy, and reviewing recent publications incorporating the technique in the context of fluorescence microscopy and in particular single/selective plane illumination microscope (SPIM). AO is an optical compensation technique which was developed to remove aberrations caused by the dynamic effect of atmospheric turbulence from astronomical images taken using ground-based telescopes [106]. The light reaching us from many astronomical objects can be considered to be emitted by a point source at a distance of infinity. However, prior to reaching the telescope aperture the refractive index distributions within the Earth's atmosphere cause these planar wavefronts to become aberrated. Thus, to restore the optical performance of the imaging system the wavefront error imparted by the atmosphere requires correction [107]. The following section gives an overview of the optical components used in, and the operation of, a typical AO system. Following this we describe the more recent incorporation of AO into microscopy.

3.2 Overview of Adaptive Optics

In this section we briefly review the general operation of an AO system. In depth reviews of AO can be found elsewhere and so will not be reproduced here [108]. Instead we give an overview of important system components and the overall optical configuration that is relevant to the AO system presented in Chapter 4.

3.2.1 General AO operation

Figure 3.1 shows a general AO system schematic. The key components are:

1. A *wavefront sensor* that collects information about the shape of the image-forming wavefront;
2. A *corrective device* that corrects for aberrations present in the wavefront gathered by the optical system, typically an adaptive optical element such as a deformable mirror (DM) or a spatial light modulator (SLM);
3. A *control system* that maintains the adaptive operation of the system.

A description of each of these components are given within this overview. The system portrayed in the figure is operating in a closed-loop. This means that the sum of the imaging wavefront error with that which is introduced by the corrective device is measured by the wavefront sensor (WFS). It is worth mentioning that AO systems can also operate in open-loop where the correction element is implemented after the WFS. Despite open-loop AO being preferable for certain astronomical applications, all further discussion is limited to applications of closed-loop AO.

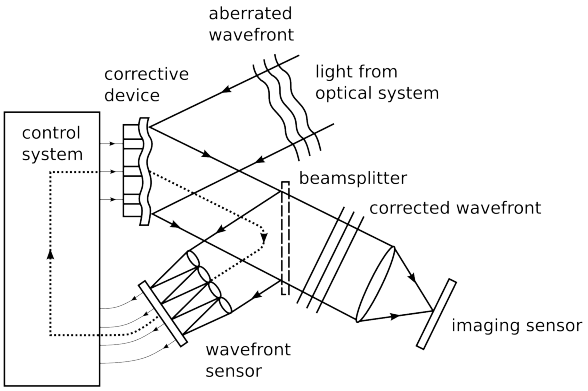

FIGURE 3.1: Schematic of a generic closed-loop AO system.

3.2.2 Aberrations in astronomical AO

For any AO configuration the corrective element and the WFS are optical conjugates of one another. In many AO systems with a single corrective element, the wavefront measurement and correction planes are conjugate to the pupil of the imaging system. In some cases, however, it is preferable to have one or more corrective elements conjugate with different planes in the imaging system. This form of AO is discussed later in the context of microscopy, for now we limit ourselves to pupil-conjugate AO.

For any AO system it is important that the nature of the aberrated wavefronts is understood so that the appropriate key components can be selected to achieve optimal correction. In

astronomy an often-used, and widely-successful, mathematical representation of the refractive index structure of the dynamic atmosphere is 'frozen flow' Kolmogorov turbulence [109], the basic principle of which is thus: refractive index fluctuations vary in spatial scale and magnitude according to an inverse power spectrum [110]. The aberrations which occur due to the atmosphere can thus by simulated by generating, either computationally or via machining, a phase screen that corresponds to a Kolmogorov turbulence refractive index structure and placing this in the appropriate conjugate plane of the system [111, 112].

In order to quantify the types of aberrations encountered in AO systems it is useful to have a mathematical decomposition of the constituent wavefront errors that contribute to the overall wavefront error. This is all the more advantageous if the contributing wavefront errors are formed from a mathematical family of shapes with convenient symmetric properties. The most commonly used mathematical decomposition of the aberrations in systems with circular symmetry are Zernike modes: an infinite set of 2-D orthogonal polynomials defined on the unit circle. Mathematical orthogonality of these polynomials means that each Zernike shape, or 'mode', amplitude can describe an independently-contributing wavefront error to an overall wavefront shape; or, vice-versa, any general wavefront shape can be mathematically decomposed into independent Zernike mode amplitudes. If one was to use a corrective element to only correct for the wavefront shape of a single contributing Zernike mode ampltitude, then that mode alone would be removed; all other contibuting Zernike mode amplitudes would remain [113].

Though other orthogonal sets of polynomials can be defined for the unit circle the majority of the literature for both astronomical and microscopy AO uses Zernike modes; our discussion is thus limited to the latter. Zernike modes are defined in polar coordinates (r, α) according to the two indices n and m as

$$Z_n^m(r,\alpha) = \sqrt{n+1} \begin{cases} R_n^m(r)\sqrt{2}\cos(m\alpha) & \text{for positive } m \\ R_n^m(r) & \text{for } m = 0 \\ R_n^{|m|}(r)\sqrt{2}\sin(|m|\alpha) & \text{for negative } m\,, \end{cases} \tag{3.1}$$

where n is called the radial degree, m is called the azimuthal frequency, and R_n^m are the Zernike polynomials given by

$$R_n^m(r) = \sum_{s=0}^{(n-m)/2} \frac{(-1)^s (n-s)!}{s![(n+m)/2-s]![(n-m)/2-s]!} r^{n-2s}\,. \tag{3.2}$$

The radial degree and the azimuthal frequency can only take values where $|m| \leq n$ and $n - m$ is always even.

Pseudocolour maps of the first 15 Zernike modes are shown in Figure 3.2 and are numbered according to the convention used later in Chapter 4. The first Zernike mode, labeled 'Mode 0' in this figure, is called 'piston' as it describes a completely uniform amplitude. For non-interferometric imaging a wavefront error of this mode shape produces no optical effect. One of the major conveniences of Zernike modes is that the other early modes (1–14) correspond well with classic optical aberrations and as such are named tip, tilt, focus, astigmatism, coma,

and spherical aberration [114]. Such modes are referred to as low-order modes and their corresponding names are specified in Table 4.1 in Chapter 4. Later modes (mode number > 14) are referred to as high-order modes and produce increasingly subtle optical effects.

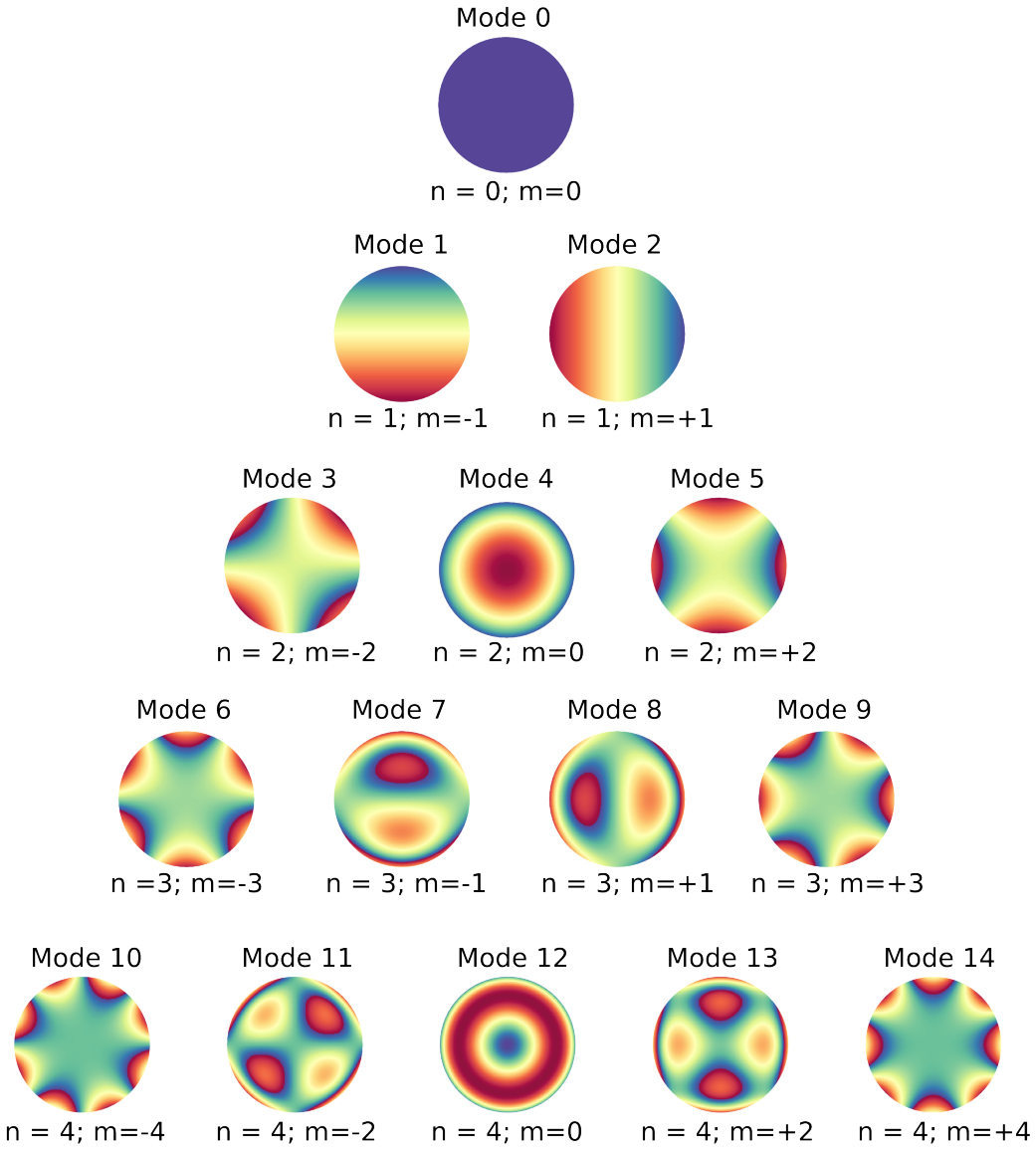

FIGURE 3.2: Pseudocolour maps of the first 15 Zernike mode shapes, numbered according to the convention used in Chapter 4.

3.2.3 Key components of an AO system

3.2.3.1 Wavefront sensor: Operation of a Shack-Hartmann array

Many different WFS technologies now exist. However, we limit our discussion of wavefront errors and their correction to the sensor technology used later in Chapter 4: a Shack-Hartmann wavefront sensor (SHWFS). Figure 3.3 illustrates the general principle of operation for a SHWFS [115]. Imaging wavefronts that are collected by the imaging system after passing through the aberrating medium are incident upon a lenslet array; the lenslet array spatially samples the local tip and tilt of the wavefront shape and focuses each of these regions upon a sensor array. If the spatial scale of the aberrations in the wavefront is much larger than the sub-aperture diameter of each lenslet then the wavefront is over-sampled by the sensor. If, however, the spatial scale of the aberrations is smaller than the sampling diameter of the SHWFS lenslets then the wavefront is under-sampled and the incident wavefront is not being adequately recorded. This spatial scale, called the Fried parameter, is formally defined as the diameter of a circlar area over which the RMS wavefront error is equal to 1 radian, and is typically represented by r_0 [116]. Thus, a convenient way of defining the spatial scale of the wavefront error is the ratio of the imaging system pupil diameter and the size of the Fried parameter at the pupil, D/r_0. When the D/r_0 for an imaging system matches the number of lenslets across the pupil conjugate then the SHWFS is able to adequately measure the wavefront error.

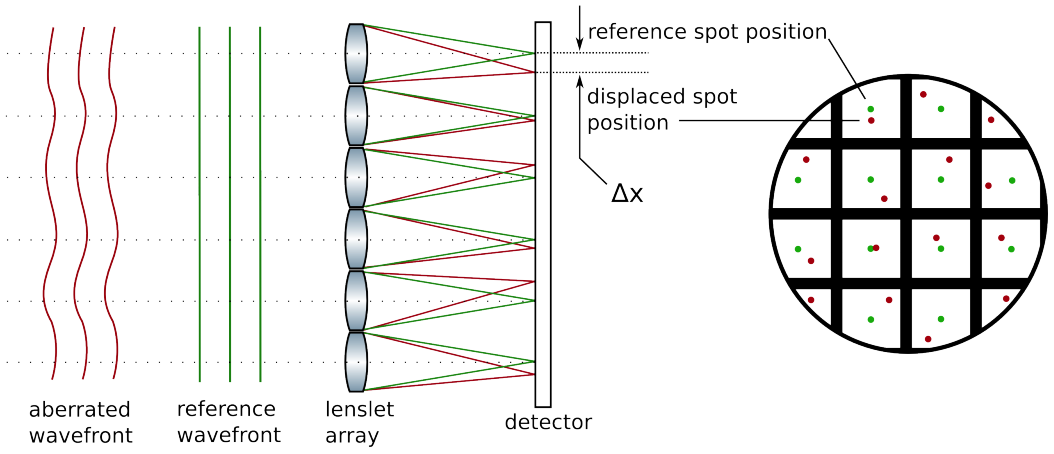

FIGURE 3.3: Principle of operation of a Shack-Hartmann wavefront sensor. Both the aberrated and reference wavefront are traveling to the right and are incident upon the lenslet array. The lenslet sub-apertures focus each region of the wavefront onto an imaging sensor. The displacement between the reference wavefront focal spot position and the focal spots formed by the aberrated wavefront allow the local tip and tilt of the wavefront at each sub-aperture to be measured.

Unfortunately it is only in the occasional circumstance that the light from the science object can be used as the light source for the wavefront sensor. Thus, the effectiveness of the WFS correction is not a simple question of matching the WFS to D/r_0: it is also dependent on how

well the distortions measured by the WFS correspond to the distortions encountered by light from the science object. In the next section we discuss the different light sources used for the WFS and the impact of this choice on the effectiveness of correction.

3.2.3.2 Wavefront sensor: Effectiveness of WFS light sources

The wavefront error is measured by comparing the sub-aperture images produced by the aberrated wavefront with the sub-aperture images produced by a 'perfect', aberration-free, planar wavefront. In the simplest astronomical case of imaging an object which is, or is close to, a single, bright, point-source-like star that is well separated from other bright stars in the telescope field-of-view (FoV), the formed sub-aperture images are diffraction-limited focal spots. The WFS comparison can be made by comparing spot locations across the sensor with those from a planar wavefront through calculating each spot's centre-of-mass via centroid. Since the light from the star passes through the exact same column of the atmosphere that is causing the aberrations, the maximum level of correction can potentially be achieved, restoring diffraction-limited performance. Such light sources used for wavefront sensing are called guide stars, specifically natural guide stars (NGS). Unfortunately this limits AO correction solely to the locations of bright objects in the sky.

In order to extend AO to regions of the sky where there are no NGS available, guide stars were artificially created in the upper atmosphere using high-powered lasers. Such a guide star is thus called a laser guide star (LGS) [117]. Either fluorescence is excited in the high-altitude mesospheric sodium layer of the atmosphere [118], or a highly-scattering laser is used for lower altitudes [119, 120]. The use of a pulsed laser, combined with a temporally-gated WFS shutter, sets the altitude of the LGS light source [121]. On the one hand a LGS is very convenient since they can be directed anywhere in the observable night sky. On the other hand, however, as the light path from the telescope pupil to the science target (effectively at infinity) is essentially a collimated cylindrical beam path through the atmosphere, but a LGS focal spot has a definite altitude making the WFS-sampled region of the atmosphere a conic beam path, atmospheric aberrations caused at higher altitudes are missing from the wavefront error analysis. This problem, termed 'the cone effect', means that full correction is hard to achieve using LGS if there are considerable contributions to the wavefront error from high-altitude atmospheric layers.

In the more complicated astronomical case of solar AO there are no point-like light sources available across the FoV and thus a modified approach to SHWFS operation is required. The lenslet array sub-apertures form similar images of the solar structure; by performing a cross-correlation with a reference image (typically a central subaperture image) an array of Gaussian spots can be produced analagous to those formed when using a guide star. The process is similar from then on: the displacement of every spot position from that of the central reference spot are calculated via centroiding to obtain the local tip and tilt of the aberrated wavefront across each sub-aperture [122].

3.2.3.3 Wavefront correction: deformable mirrors

The next key component to discuss is that of the adaptive optical element. Here we specifically discuss DMs rather than SLMs as the former are more common in modern AO systems since the latter have several undesirable features: two of which are their low optical power efficiency and their polarization dependence. By comparison DMs are incredibly light efficient and responsive, which is extremely important in the case of low light levels and rapid correction. The construction of most DMs consists of a highly-polished mirror surface, the shape of which is controlled by an array of actuators, which is either a continuous membrane or segmented. The signal applied to each actuator controls the extent of the deformation at that position. Many types of DM now exist: electrostatic continuous membrane; magnetic continuous membrane; piezoelectic unimorph or bimorph wafers; and micro-electro-mechanical-systems. Each version has different optical advantages and disadvantages due to the membrane material, the accuracy of the deformation shape, the maximum size of the shape that can be applied (the 'stroke'), diffraction effects caused by segmentation, response speed, and the shape repeatability. As the DM used in our AO system of Chapter 4 is an electrostatic continuous membrane, in particular a push-pull electrostatic membrane deformable mirror (PPDM), we limit our discussion of DMs to this technology.

In a push-pull electrostatic membrane deformable mirror (PPDM) a thin reflective conductive membrane is suspended between two arrays of actuators; the upper layer is transparent to maximise light efficiency and minimise diffraction effects. An attractive force is generated between the actuator and the membrane by the application of a voltage and the membrane is thusly 'pulled' towards the actuator. The spatial distribution of the actuators across the front and back of the membrane along with how the membrane is fixed have an important effect on the applied deformation shapes: the mirror used later on in this thesis is circular and has its actuators distributed in concentric rings across the front and back and the membrane is fixed only at the outer edges. This affords our PPDM a very large stroke, which is advantageous in the case of simulating the large-amplitude, low-order aberrations typically found in microscopy more often than in astronomical imaging. The nature of aberrations encountered in microscopy is described in further detail in Section 3.3.

The method by which the DM is calibrated to produce certain wavefront shapes is detailed for our specific system later on in Section 4.2.3.2 of Chapter 4. In short the 'influence matrix' that transforms DM actuator voltages to WFS signals is generated by sending a voltage to each actuator in turn, measuring the WFS signal induced by the actuator-applied wavefront error [123]. This matrix is then computationally inverted to produce a 'control' matrix which allows calculation of the actuator voltages required to re-produce a given WFS signal. Thus the required correction for a measured wavefront error at the WFS can be calculated and sent to the DM, allowing full operation of the AO system.

3.2.3.4 Overall system performance: the control system

The final key component of the general AO system associated with performance is that of the control system. The aberrations introduced by atmospheric turbulence are dynamic;

the control system has to operate successfully in real-time and so typically relies upon high-performance computers and software to analyse the data from the WFS and apply the appropriate correction to the adaptive optical element. For rapid correction modern and up-coming astronomical AO systems may implement field-programmable gate array (FPGA) acceleration or graphics processing units (GPU) to enable operation at extremely high rates. The acceleration of systems for real-time AO control is currently an on-going field of research [124, 125, 126]. In microscopy, however, the aberrations introduced by biological samples are either static or vary on a very slow time-scale. Thus the control system for a microscope AO system can be a simple PC workstation.

3.3 Adaptive Optics in microscopy

As mentioned in the previous chapter, exotic beam digitally-scanned laser light sheet microscopy (DSLSM), particularly that which uses Bessel beam illumination and confocal slit detection or structured illumination, is particularly effective at reducing the artifacts encountered when imaging highly scattering samples. Scattering aside, refractive index mis-matches between the sample mounting media and inhomogeneities within the sample itself contribute highly to degradation of imaging performance in all types of microscope. In this section we describe how AO has been employed to reduce this degradation in different microscope configurations.

3.3.1 Aberrations in microscopy

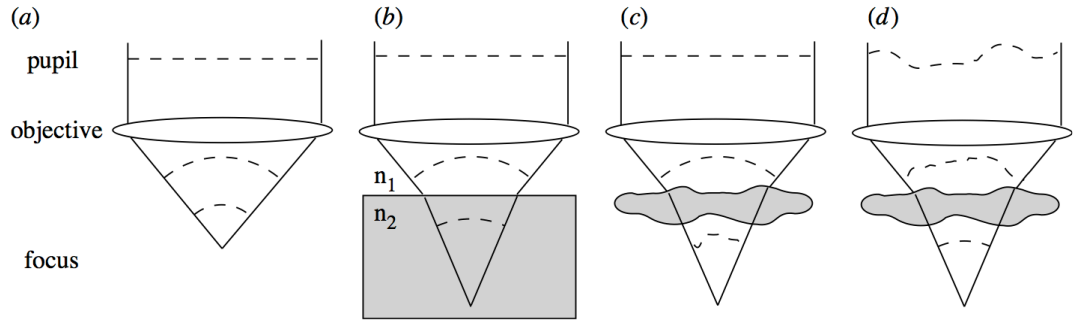

FIGURE 3.4: Aberrations in microscopy arise from imaging or focusing through media with different refractive index distributions. A planar input wavefront is transformed by an objective lens into a spherical wavefront that converges at the focal point (a). Planar interfaces of a refractive index mis-match cause the focal point to deteriorate by introducing spherical aberration in the converging wavefront (b). Inhomogeneous refractive index distributions between the illumination or observation objective front aperture and the intended focal region can distort illumination beam foci (c) and cause the detected fluorophore emission to become distorted (d). Figure reproduced from Martin Booth's 2007 review of AO in microscopy [127].

Figure 3.4 illustrates the presence of aberrations during illumination and observation in microscopy, caused by the refractive index mismatches and distributions of mounting media

and sample tissue. The two primary contributions to aberrations in the microscope are the interfaces of surface refractive index mis-matches between the objective lens front aperture and the sample tissue, introducing spherical aberration [128], and then by different refractive index regions of the sample for the remainder of the beam propagation, producing higher order aberrations. The higher the numerical aperture (NA) of the lens and the more tissue the beam passes through, the more detrimental the aberrations. Mounting interfaces have a far more predictable refractive index geometry than specimen tissue structure, thus specimen-induced aberrations are much more complicated to predict, measure and correct for. Early efforts to survey specimen-induced aberrations employed interferometry to measure aberrations at the imaging pupil point-by-point across thin (sub 100μm) transparent samples [129, 130]. In this paper the authors extracted the wavefront error from the intereference pattern through phase-retrieval and then decomposed the wavefront error into Zernike mode amplitudes, demonstrating the dominance of low-order modes with large standard deviations in amplitude across the sample.

As the nature of the aberrative medium in microscopic biological imaging differs greatly from dynamic atmospheric turbulence different approaches are required between all sample mounting geometries and media, imaging depths, and microscope system optical setups. A wide range of investigations regarding AO in microscopy have been investigated since practical and affordable corrective devices became available in the early 2000s. The widely-varying advances in microscope AO between then and now have so far been reviewed extensively by three publications in 2007 [127], 2009 [131], and 2014 [132]. Only some key techniques and advances will be noted here that are relevant to the work in this thesis; specifically, the wide-field AO system presented in Chapter 4, and, for the sake of completeness in regard to the previous theory chapter concerned with the development of LSM, SPIM systems.

3.3.2 Microscope AO correction strategies

For microscope samples AO correction is typically achieved by assessing the recorded signal from some aberration 'probe', similar to the use of guide stars in astronomical AO. A probe based on fluorescent emission can be assessed through an analysis of either the specimen's inherent fluorescent protein structure or a number of fluorescent beacons which are artifically-introduced into the sample. Successful implementation of the former is beneficial when imaging living biological specimens as the interior of the specimen remains intact. The earliest approach that utilised the inherent fluorescent structure of the specimen was that of 'indirect optimisation'. In indirect optimisation the wavefront error is not measured directly but the specimen-induced aberrations are instead corrected for by analyzing the recorded fluorescent emission (*e.g.* image sharpness or overall signal intensity) whilst different orthogonal mode amplitudes are placed on the corrective element [133]. If the fluorescence image improves when a certain mode is applied the correction algorithm 'learns' the beneficial amplitude of that mode and moves on to the next mode. Once the optimum mode amplitudes have been learned and applied the aberrations have been inherently corrected for without requiring a direct measurement of the wavefront error.

In point-scanning systems such as confocal or multiphoton microscopes the earliest successful AO corrections were achieved by maximising the recorded intensity at a photo-diode 'light bucket', typically a photo-multiplier tube [134, 135]. For wide-field systems an image quality metric can be used to asses a region-of-interest (RoI) within the full-sensor science camera image [136]. The down-side of this technique is the duration required for the search-and-learn mirror optimisation algorithm. Clearly if the correction of sample-based aberrations is required at every scan point in a confocal or multiphoton system then the AO-corrected imaging duration can be far greater than that of a wide-field system.

If, however, correction is needed on a much more rapid time-scale then a more traditional WFS-based AO system may be more appropriate, using a SHWFS in conjunction with some kind of guide star light source. This method typically requires fluorescent beacons to be artificially positioned within the sample [137, 138, 139, 140], though it works just as well in the unusual case where the fluorescent structure of the sample is point-like and well-separated in the FoV [141]. Alternatively a guide star source can be introduced by focusing a laser to a point within the sample. The primary benefit of the 'sensorless' approach is the effectiveness of the correction. Comparatively the sensor-based approach is advantageous in terms of correction speed. A recent publication by Bourgenot *et al* compares both methods of AO aberration correction in an identical microscope system [142].

3.3.2.1 Effectiveness of microscope AO correction regarding the region of interest

As summarised in both [131] and [132], the practicality of full correction point-by-point across a sample is limited by the spatial variations of aberrations across the observation FoV combined with the discrepancy between the response rate of corrective elements compared to the point-scanning speed of the microscope. For the largely-predictable aberrations encountered in two-photon microscopy when imaging a transparent sample sandwiched between a coverslip and microscope slide, a single 'average' correction can improve imaging performance across certain regions by up to 80% [143]. This suggests that 'look-up' tables might be a convenient method of applying specific corrections for certain samples and imaging conditions. However, there may equally be regions where the image becomes worse because the applied correction no longer represents the specimen-based aberrations as the imaging path through the sample has changed. This limitation is not solely associated with point-scanning microscopes: since the aberrations present at all points across a wide FoV are caused by light passing through different refractive index distributions, the application of a single wavefront correction to the imaging pupil of a wide-field microscope will run into the same problem. Figure 3.6(a) illustrates how a single wavefront correction that is conjugate to the imaging pupil can become inappropriate away from a central well-corrected region. The lateral scale across the specimen over which a single pupil-conjugate correction remains valid was described in early investigations as the 'optical memory effect' and is equivalent to the isoplanatic patch size in astronomical AO [77, 144].

As an alternative, and potentially more appropriate, incarnation of AO in microscopy there have been some recent developments regarding AO systems where the correction is

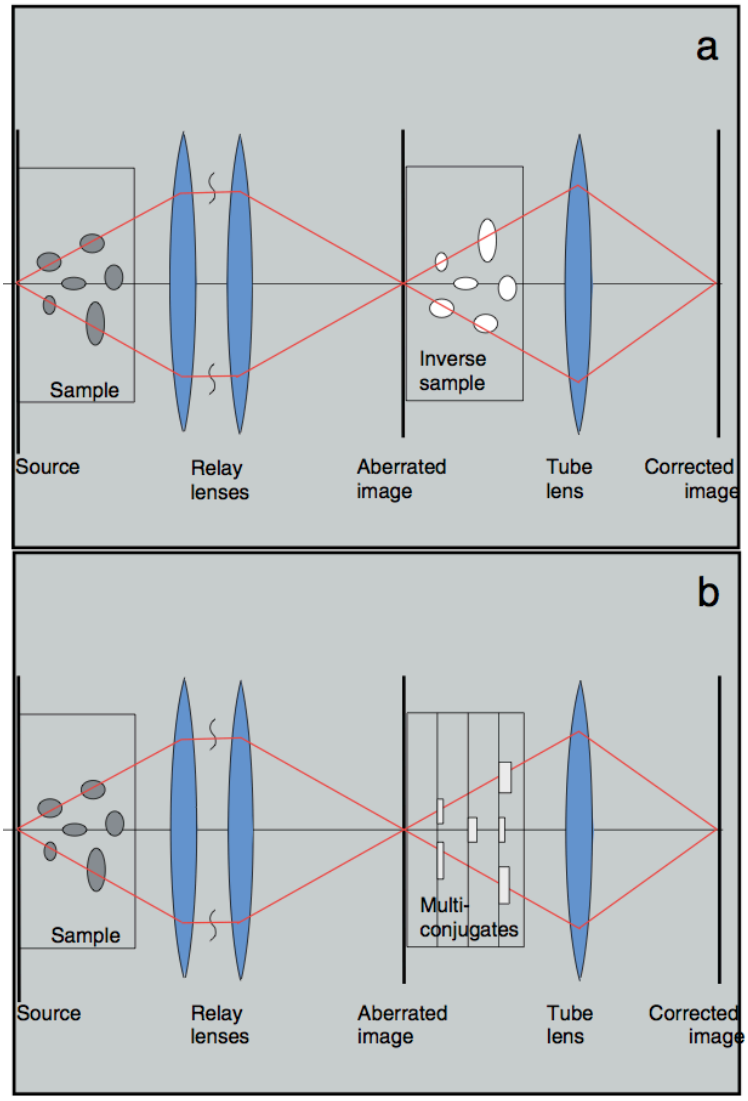

Figure 3.5: Principle of MCAO in microscopy, from [145]. To conduct 'perfect' correction of aberrations encountered when imaging through a thick sample with a inhomogeneous refractive index distribution we need to place an 'inverse sample' with an opposite refractive index gradient in a sample-conjugate plane in order to produce the opposite optical effect (a). By employing multiple corrective elements which are each conjugated to a layer within the sample's refractive index distribution the phase variations imparted by the theoretical inverse sample can be approximated (b).

applied to a different conjugate plane than the pupil of the imaging objective lens. The use of multi-conjugate adaptive optics (MCAO), a technique developed for tomographic wide-field atmosphere correction in astronomy [147, 148, 149, 150], in wide-field microscopy was previously suggested (Figure 3.5) and simulated [145, 151], and an early step towards its experimental demonstration has been published in a very recent paper [146]. Here the corrective elements of the AO system are conjugate with layers of the refractive index distribution within the sample. Conjugation of the corrective elements to layer positions rather than the pupil of the imaging objective allows the correction to be appropriate for much larger FoV region within the sample. Figure 3.6 shows a cartoon depicting the FoV advantage when AO correction is conjugate to a specimen layer position rather than the imaging pupil. This FoV advantage over pupil-corrected AO was recently been demonstrated experimentally using a single adaptive element to compensate for a single conjugate layer

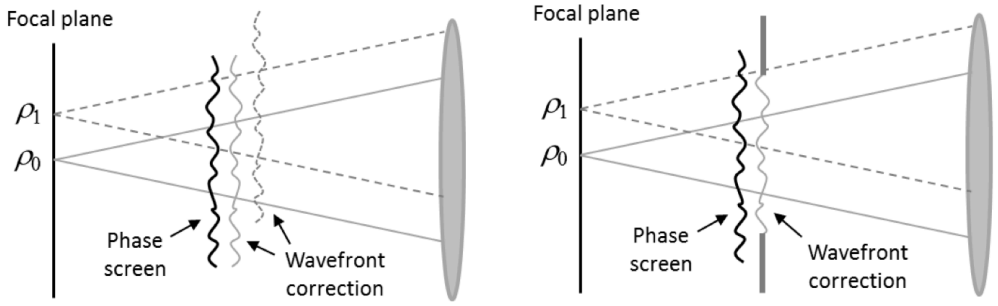

(a) Pupil-conjugate AO

(b) Sample-conjugate AO

FIGURE 3.6: Field-of-view advantage of sample-conjugate AO over pupil-conjugate AO, from [146]. The validity of the correction imparted using pupil-conjugate AO is limited to a small FoV within the sample and becomes inadequate outside of this region, often worsening optical performance (a). The FoV across which correction is valid becomes improved when the correction is imparted in a plane that is conjugate to a position within the aberrative medium, rather than at the lens pupil, since the collected light from two distinct locations in the FoV will pass through the same refractive index distribution (b).

within the sample—simply conjugate adaptive optics (CAO) rather than MCAO—in a recent publication [146]. As a final note regarding the effectiveness of AO correction over a wide FoV, however, it is worth mentioning that despite the AO system of the next chapter being a wide-field imaging system, the simulated aberrations are *introduced* at the pupil plane. Thus sample-conjugate AO is unnecessary in our case; simple pupil-conjugate AO is entirely appropriate.

3.3.3 AO correction in a SPIM

In the final section of this chapter we review recent advances in the incorporation of AO into wide-field SPIM systems. As the propagation of both the illumination beam and the detected emission in SPIM typically propagate through non-planar media, the nature of the system aberrations in a SPIM are different to those encountered in planar, on-axis, epi-configuration imaging systems. In [152] it was shown both through simulation and experimentation that refractive index mis-matches at the cylindrical interface of a mounting pipette used in SPIM (Figure 3.7) cause distortions in both the illumination and emission beam paths, imparting tilt, astigmatism, and defocus in both arms that vary with according to the imaging position within the cylindrical pipette. These effects combine to cause a mis-alignment between the illumination light sheet axis and the focus of the observation optics within the sample mounting pipette. Implementing AO on the emission beam path can re-align these beam paths, thus correcting for the system aberrations, in addition to correcting for the specimen-based aberrations caused by the refractive index distribution within the sample tissue.

It is worth noting that the authors of [152] performed this study with an intentional refractive index mis-match between the capillary sample mount and the mounting/immersion

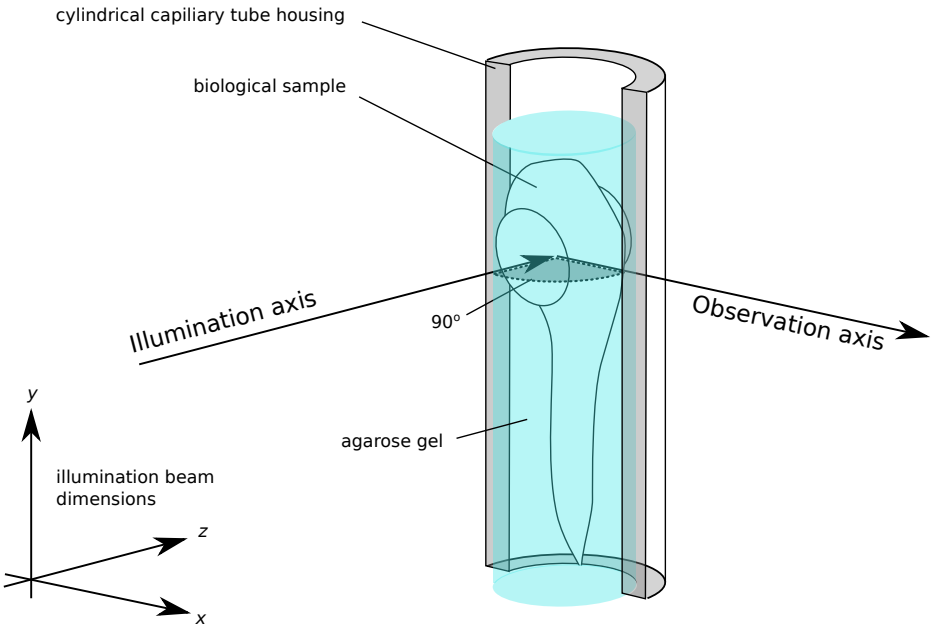

FIGURE 3.7: Cut-away diagram of the typical mounting solution employed for roughly cylindrical samples in a SPIM. The biological sample is held within a cylindrical capillary tube using agarose gel, an aqueous mounting solution. In this diagram the outline of a zebrafish sample has been used to indicate the biological sample. The illumination beam passes from the immersion medium through the cylindrical surfaces of the capillary tube and the agarose gel before reaching the specimen tissue. The fluorescence which is excited by the illumination beam is collected by the observation optics after passing back through the specimen tissue, agarose gel, capillary tube interfaces, and immersion medium.

medium; by matching the refractive index of the the capillary tube and the immersion medium the appearance of these mounting-induced aberrations is greatly reduced and specimen-induced aberrations dominate. In their paper correction was achieved by using sensorless AO, altering the shape of a DM by stepping through an amplitude range of low order Zernike modes, and they compared the effectiveness of different image quality metrics and search-and-learn 'genetic' algorithms. The authors have since combined sensorless AO correction with an optically-gated imaging technique that 'freezes' periodic motion of *in-vivo* specimens [153] to demonstrate aberration correction of a beating zebrafish heart [154], shown in Figure 3.8. The same authors have also demonstrated wavefront sensing in real-time when imaging the optically-gated beating zebrafish heart, using a cross-correlation SHWFS technique without the need for artificially-introduced fluorescent markers [155]: the sub-apertures of the SHWFS lenslet array produce images of the full wide-field fluorescent structure; these images are then cross-correlated to produce an array of Gaussian spots from which the wavefront information can be extracted via centroiding (performed in the same way as mentioned earlier for solar AO [122]). This wavefront sensing technique may prove to be an extremely promising solution for real-time wavefront-sensed AO in future wide-field fluorescence microscopes.

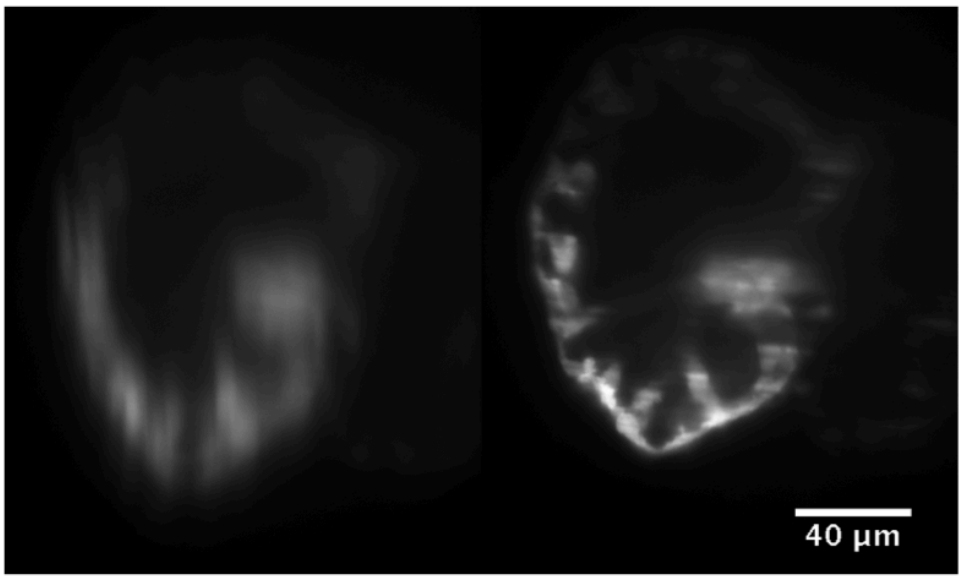

FIGURE 3.8: Demonstration of sensorless aberration correction in an optically-gated SPIM system, allowing clear images of a beating zebrafish heart to be produced, from [154].

A portable Adaptive Optics demonstration system 4

4.1 Introduction

This chapter describes a compact closed-loop adaptive optics (AO) system designed to simulate and demonstrate closed-loop aberration correction in both astronomy and microscopy. The system was conceived as an outreach/teaching aide with three key purposes:

1. To provide a clear and transparent insight into the inner workings of AO.
2. To be informative and educational yet, more fundamentally, intellectually accessible to a wide range of participants; *i.e.* from young members of the general public with no assumed knowledge, up to research-level physicists and astronomers working outside of AO.
3. To demonstrate that small-size, low-cost AO systems could be built according to a simple framework and operated using streamlined and generalized software.

Structurally this chapter is as follows: First, the design considerations, chosen components, and construction of the system are described alongside an outline of the control software; following this, a description of the demonstrative method and the accompanying demonstrative aides employed when using the system at public demonstrations is given; next, the aberration correction resulting from closed-loop operation of the system, alongside some audience participation feedback from a science festival that the system was demonstrated at, are presented and discussed; and finally, conclusions regarding the system are presented.

4.2 Methods & Materials

The following sections each describe some aspect of the AO demonstrator system's design and construction in terms of the hardware, software, and demonstrative method employed.

4.2.1 Optical components

The basic design of our AO system was a transmission microscope adapted to incorporate a transparent turbulence-simulating phase plate (TPP)[1], a large active area push-pull electrostatic membrane deformable mirror (PPDM) (Adaptica, SATURN), and a Shack-Hartmann wavefront sensor (SHWFS), all of which were conjugated to the pupil of the imaging objective lens. All optical components were mounted on a 600 mm × 300 mm optical breadboard to keep the setup portable. An unfolded optical diagram of the system is presented in Figure 4.1. The following sections each describe a particular aspect of the system's design considerations and solutions.

4.2.1.1 Imaging optical system

Sample illumination was provided by a compact LED-based light source. This light source was adapted from an LED-to-optical fiber coupling assembly[2] to provide wide-field illumination. Light from a blue LED was focused by a 5 mm diameter ball lens and collected by a convex lens (focal length $f = 25.4$mm) at $2f$ from the pinhole. At $2f$ on the other side of the collecting lens the samples were placed into the illumination beam. Transmitted light from the illuminated sample was collected by an imaging objective lens, the back pupil of which was conjugate to the TPP and PPDM. Following the PPDM, lens L_6 brought the image of the sample to focus at the imaging camera (Prosilica GC655 by Allied Vision Technologies (AVT) GmbH, Germany). A narrow-band blue filter was placed in front of the camera sensor to avoid image contamination by light sources other than the illumination LED. Magnification of the sample at the imaging camera sensor was given by $M = (f_2/f_1)\cdot(f_4/f_3)\cdot(f_6/f_5) = (100/30)\cdot(50/50)\cdot(300/150) = 20/3 = 6.6\dot{6}\times$.

4.2.1.2 Sample preparation

To simulate both telescopic and microscopic images two types of samples were prepared:

- For astronomical images a 25 micron pinhole was employed as the sample to generate a simple circular star-like image;
- To produce images bearing a resemblance to the highly structured wide-field images typically recorded in microscopy samples were fabricated by mounting either a synthetic substance or sectioned biological sample between circular microscope slides (thickness 1 mm) and glass cover slips (thickness 170 microns) of diameter 25 mm.

[1] Fabricated by Rachel Rampy at the Centre for Adaptive Optics, University of California, Santa Cruz
[2] Constructed by Paul Clark at the CfAI

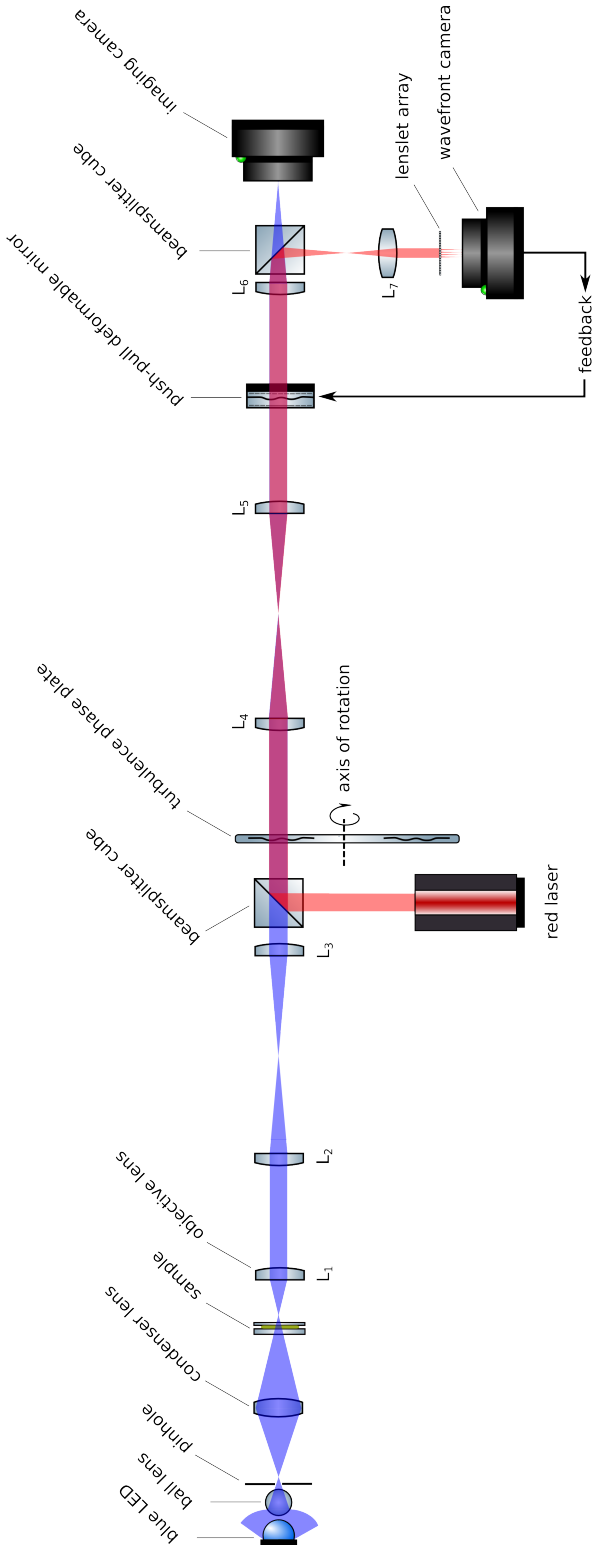

FIGURE 4.1: Schematic of the AO demonstrator system. The optical layout has been unfolded for clarity. The lenslet array and the wavefront camera together comprise the SHWFS referenced in the text. The focal lengths of all lenses, f_i, are 30, 100, 50, 50, 150, 300, and 30 mm for lenses L_{1-7} respectively. The lens pairs of $L_{2,3}$, $L_{4,5}$, and $L_{6,7}$ are all 4-f systems that place the objective lens pupil, turbulence phase plate, push-pull deformable mirror, and wavefront sensor lenslet array in optically-conjugate planes.

All samples were mounted into a filter wheel to improve the ease of switching between individual samples. The thin cover glass surface of the mounted samples was mounted towards the imaging objective lens to reduce the amount of spherical aberration induced by the refractive index mis-match of the air-glass interface. The filter wheel was mounted upon two manual translation stages to allow the system operator to laterally alter the region of the sample being imaged during demonstrations and adjust the sample's position along the optical axis, bringing it into clear focus with the microscope's fixed imaging optics.

4.2.1.3 Introduction of aberrations

To simulate the different types of aberrations affecting both astronomy and microscopy two methods of introducing aberrations into the optical system were employed. Each method altered the phase profile of light within the system at a plane conjugate to the pupil of both the imaging objective lens and the SHWFS.

Simulating atmospheric turbulence: Low amplitude dynamic aberrations, caused by the rapid fluctuations of the Earth's atmosphere, were approximated by allowing the TPP to freely-rotate about its central axis. The TPP was designed to introduce aberrations with a phase spectrum similar to that of Kolmogorov turbulence [156], fabricated with a Fried parameter of r_0 = 700 microns. Note that this is the physical scale of r_0 at the plate itself, rather than the 'on-sky' scale mapped to the imaging pupil.

Lenses L_4 & L_5 provided a TPP magnification of $M = f_5/f_4 = 150/50 = 3\times$, producing an effective Fried parameter of $r_0' = 2.1$ mm at the PPDM. The active area diameter of the PPDM was $D' = 15$ mm, thus $(D'/r_0') = (15/2.1) \approx 7$ at the PPDM.

Further magnification by lenses L_6 & L_7 of $M = f_7/f_6 = 30/300 = 1/10\times$ produced a final effective Fried parameter of $r_0'' = 210$ microns at the SHWFS. The plate was mounted on a manual translation stage to provide lateral motion of the plate through the beam path allowing the same aberrations to be induced into the beam at a slower, more gradual, rate than that of the plate spinning freely.

Simulating static tissue aberrations: Large amplitude static aberrations, experienced when imaging a microscopic biological sample at depth and caused by inhomogeneous refractive index variations throughout the sample tissue, were induced by sending random actuator voltages to the PPDM. Though the PPDM was employed to provide the controlled closed-loop aberration correction described in the following sections, the correction feedback procedure was "blind" to the starting mirror shape; *i.e.* correction was based purely on feedback via the SHWFS - as noted in section 4.2.3.2. The large central actuator of our chosen DM is well-suited to producing, and correcting for, focus and spherical aberration, both of which tend to be dominant in microscopy, alongside astigmatism terms [157].

4.2.1.4 Wavefront sensor & aberration corrector

A red diode laser (Thorlabs, UK) was used as a reference beam to project the introduced aberrations onto the SHWFS. The beam was coupled into the optical train via a beamsplitter cube prior to the TPP. Following lens L_6 another beamsplitter cube was used to send the reference beam through L_7 to the SHWFS, thus placing the TPP, PPDM, and SHWFS pupil at conjugate planes. Magnification of the PPDM active area by lenses L_6 & L_7 of $M = 1/10\times$ produced a reference beam diameter of $D'' = 1500$ microns at the SHWFS. A red optical filter prevented the blue light of the sample imaging system from entering the SHWFS.

The SHWFS in our system was comprised of a micro-lens array (MLA) of effective focal length 6.7 mm and lenslet pitch, r''_{LP}, 150 microns (Thorlabs, UK) mounted at one focal length from a CCD sensor (AVT, Prosilica GC1020). Thus the effective (D/r_0) in the beam that is well-matched to the SHWFS is $(D''/r''_{LP}) = (1500/150) = 10$. This implies that the system should be able to correct for the $(D'/r'_0) \approx 7$ aberration across the PPDM aperture that is induced by the TPP.

4.2.2 Overall design considerations

To keep the system visually attractive, interactive, and well-protected, in order to enhance both the portability and the appeal of the system at public demonstrations, a custom clear perspex housing was machined. The housing, shown in Figure 4.2, was milled to allow access to the components of the system requiring manual interaction during demonstrations, allowing participants to choose the sample and spin or gradually translate the TPP through the beam. The optical breadboard was raised from bench level by three vibration isolated legs covered by a black wooden surround, thus hiding the electrical components, stored underneath the breadboard, from participants whilst retaining operator access from the system rear.

4.2.3 System control software

Control software for the AO demonstrator system was written in the Python programming language and ran on a regular classroom PC running Windows 7. The operation of the software can be broken down into the following categories: wavefront sensor (WFS) monitoring of incident wavefronts; calibration of the feedback system between the WFS and deformable mirror (DM); closed-loop operation of the device; and the graphical user interface (GUI) of the system. These categories are described throughout the following two sections.

4.2.3.1 Wavefront monitoring

The local tip and tilt across wavefronts of the laser beam were monitored by the SHWFS. A square region-of-interest (RoI) was defined for each of the M MLA sub-apertures, bounding each individual focal spot incident on the WFS camera sensor. These are visually represented in Figure 4.3 as a grid bounded by a circle that defines the pupil of the laser beam at the SHWFS. A centroiding algorithm located the centre-of-mass of intensity within each RoI.

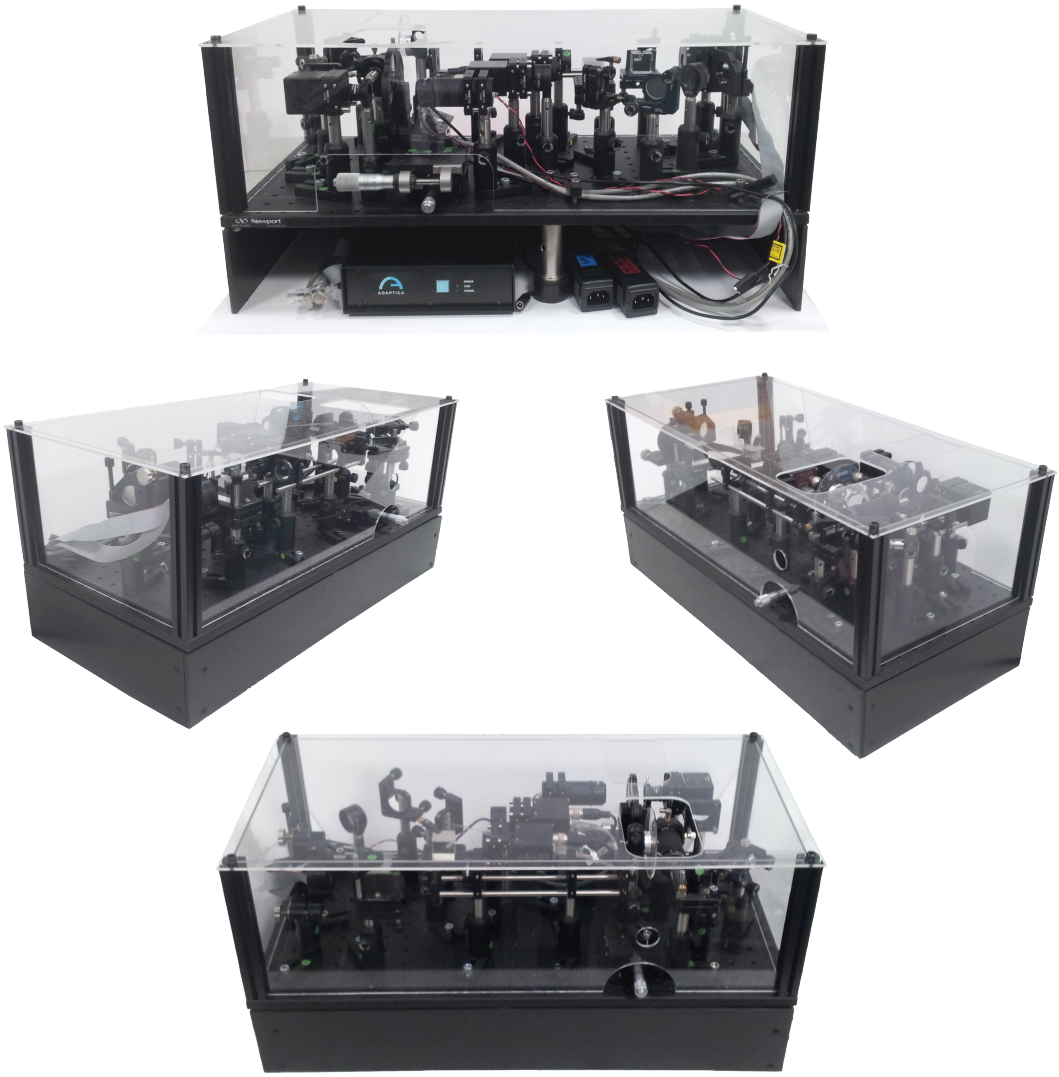

FIGURE 4.2: The clear perspex housing for the AO demonstrator system allows access to key operational components such as the sample filter wheel, the TPP, and their respective translation stages, whilst keeping all optical components completely visible yet protected. The breadboard is raised from bench level by three vibration-isolated legs allowing the power packs and Ethernet connections to be stored underneath. A 3-panel black wooden surround keeps the electrical components out of sight and accessible from the rear of the system (top). The entire system has width × depth × height dimensions of 600 mm × 300 mm × 290 mm.

The centroids, c_x & c_y, along both x and y axes were given by

$$(c_x, c_y) = \left(\frac{\sum_{i,j=1}^{X,Y} i.I(i,j)}{\sum_{i,j=1}^{X,Y} I(i,j)}, \frac{\sum_{i,j=1}^{X,Y} j.I(i,j)}{\sum_{i,j=1}^{X,Y} I(i,j)} \right), \tag{4.1}$$

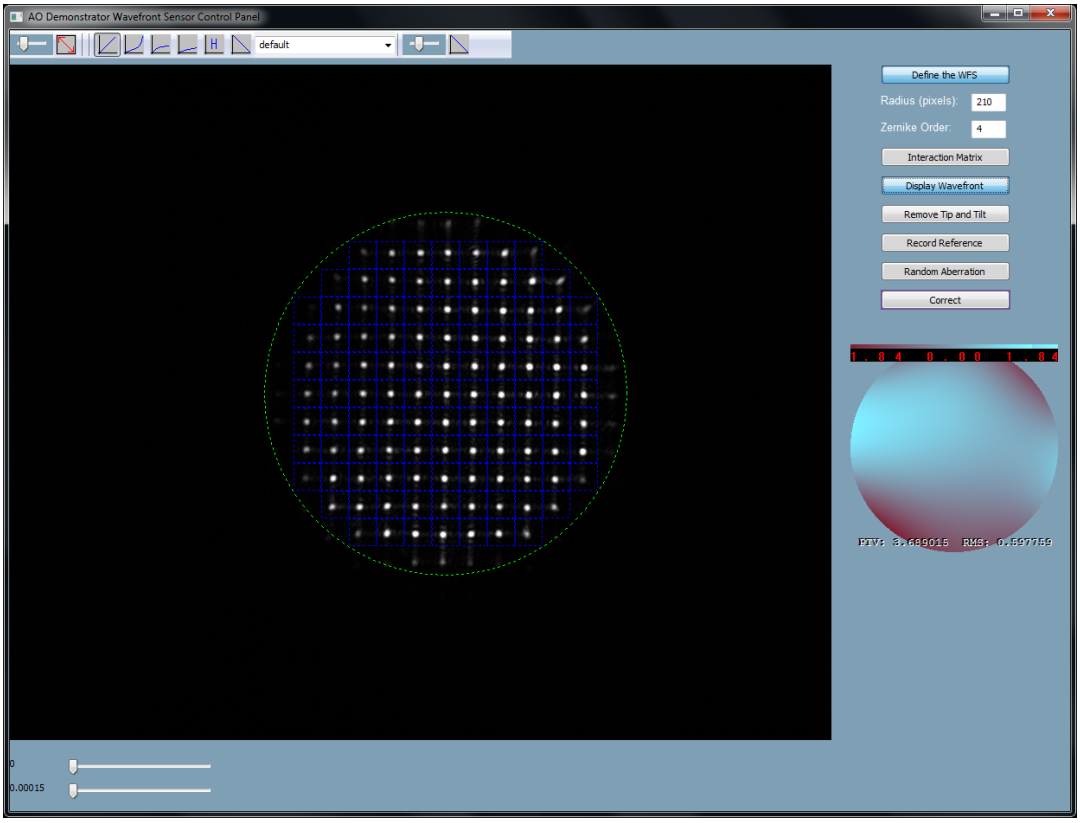

FIGURE 4.3: The wavefront sensor as displayed in the AO demonstrator's GUI. Images from the SHWFS CCD sensor are displayed continuously within the main GUI window to the left of the buttons used to control the system. Two sliders to the bottom left of the CCD feed control the gain (upper) and exposure (lower) of the camera. Controls for the display are situated along the top, allowing the live feed to be presented in other formats than linear monochrome, such as logarithmic; square root; histogram equalised; and inverted. A drop-down menu of alternative colourmaps is also included. The blue grid bounding the spots formed by the MLA defines the centroid RoI for each sub-aperture, within each RoI the local tip-tilt of the incident wavefront is measured.

where X and Y are the number of pixels across the x and y axes of the RoI respectively and $I(i, j)$ is the intensity measured at pixel $(x = i, y = j)$. The local tip and tilt of the wavefront across each sub-aperture is inferred by the displacement of the resulting spot locations from those formed by a *reference* beam in the absence of induced aberrations. Calculated spot displacements within each RoI $(\Delta c_x, \Delta c_y)$ are recorded for all M sub-apertures. Thus the incident wavefront is represented by $2M$-element WFS signal vector $\mathbf{s}$.

4.2.3.2 Closed-loop calibration and operation

Several buttons, denoted by their *"Name"*, in the GUI control the calibration, operation, and other display features of the system. The feedback loop describing the relationship between the SHWFS and PPDM was configured each time the system was set up for demonstration

according to the following steps:

1. The optical train is set to an 'aberration-free' mode by removing the TPP and relaxing the PPDM by setting all actuator voltages to zero;

2. In the GUI the centroid RoIs are centred via centroid onto the MLA focal spots by using the button marked *"Define the WFS"* to define the WFS geometry.

3. The button marked *"Interaction Matrix"* begins the calibration procedure: First, spot locations are recorded for the reference beam; then, a set voltage, a factor of the maximum applicable voltage, is sent to one of the N DM actuators and the resulting WFS signal vector of spot displacements $\mathbf{s}$ is recorded; this is performed for all individual DM actuators to populate each column of the $N \times 2M$ interaction matrix $\mathbf{B}$, thus defining the interaction relationship between DM actuator voltages and WFS signals. The DM returns to a relaxed state.

4. The pseudoinverse of $\mathbf{B}$ is then calculated using a singular value decomposition (SVD) routine to give the control matrix $\mathbf{C}$. This defines the inverse relationship required for closed-loop aberration correction; that is, the actuator voltages $\mathbf{x}$ required to reduce the WFS signal $\mathbf{s}$ can now be calculated.

Closed-loop operation and other features of the system were controlled using the remaining buttons:

- *"Correct"* is an on/off button that initiates and aborts closed-loop operation. While the loop is closed, actuator voltages $\mathbf{x}$ are calculated that reduce the current WFS signal $\mathbf{s}$ and sent to the PPDM with a gain of 0.2.

- *"Display Wavefront"* creates a sub-display within the GUI depicting a live feed of the current wavefront shape. This shape is a composite map of the first 15 Zernike modes with estimated amplitudes. The Zernike mode amplitudes are estimated via the WFS signal vector s by inverting the *response matrix* G, where a, a Zernike mode amplitude vector, is given by $a = G^{-1}s$. G is calculated numerically for the specific WFS geometry by predicting the spot motion caused by unit amplitude Zernike mode wavefronts. This occurs just prior to calculation of the interaction matrix. The colourmap is presented in units of waves, denoted by the colourbar across the top of the sub-display. Also included in this display are the peak-to-valley and root-mean-squared wavefront error.

- *"Remove Tip and Tilt"* concerns this sub-display only; it does not cause any alteration of the mirror shape. Instead, this simply removes the Tip and Tilt Zernike modes bitmap layers from the final displayed wavefront.

- *"Random Aberration"* generates a vector of actuator voltages with a random set of amplitudes, between 0–$V_{\max}/2$ V, and sends this signal to the PPDM.

4.2.4 Demonstrative method

To aid the volunteers demonstrating this system to the public we produced a guide that included a suggested list of actions; an account of which is presented below. The guide was intended to form the skeleton for a flexible yet comprehensive demonstration, allowing the complexity of the explanations to be tailored for the audience present.

Our system has so far been displayed at three science festivals, two of which were completely public, and operated by 10 volunteers in total; 6 of whom had no prior experience of using the system, though 8 of them had a full understanding of AO. Additionally, we produced several posters (see Appendix A) and a video slide-show presentation on AO, shown on a large television screen, to compliment the system and attract participants. Aside from giving an accessible overview of AO in astronomy, microscopy, and ophthalmology, a secondary use of the video presentation was to keep potential participants occupied when a system demonstration was already underway. The suggested list of demonstrative actions described below, under '*Demonstrating Astronomical AO*' and '*Demonstrating AO in Microscopy*', could be presented in either order, though most volunteers preferred to describe AO in the context of astronomy first.

A reproduction of the guide for our volunteers is reproduced here throughout the following subsection.

4.2.4.1 Demonstrative Guide for Volunteers

Stall setup: The stall is arranged as follows (from left to right, or vice versa): the large stand alone poster; the large screen TV showing the video presentation on loop via a laptop; the AO demonstrator system; and a computer screen connected to the control PC, facing the audience. Extra posters explaining AO surround the stall. Prior to the start of the presentation session the system software is booted up and the GUI displayed on the control PC screen, alongside this a live feed from the imaging camera using AVT's proprietary 'GigE Viewer' software is also displayed. Set a suitable exposure for both cameras; check that both the pinhole and microscope samples can be adequately viewed using a single exposure for the imaging camera. When the demonstrator software is initially loaded the PPDM is in a relaxed state.

Initialise the system. Perform the following actions to ready the system for demonstration:

1. Remove the TPP from the beam path using the translation stage beneath it.
2. Click *"Define the WFS"* and make sure the RoI grid bounds all well-formed focal spots from the MLA sub-apertures illuminated by the laser. If necessary change the number of RoI boxes by increasing the pupil radius via the text box below; use the tip and tilt thumb screws on the mirror prior to the SHWFS to adjust the pupil position.
3. Click *"Interaction Matrix"* to record reference spot positions and calibrate the system.

4. Click *"Display Wavefront"* and *"Remove Tip and Tilt"* to display the wavefront reconstructed from the SHWFS signal in the GUI.

Demonstrating astronomical AO:

1. Begin by rotating the sample filter wheel until the pinhole is illuminated. Ensure it is visible in the live feed of the imaging camera. Use the two-axis translation stage beneath the filter wheel to adjust the focus and position of the pinhole image.
2. Explain that this is a simulation of a perfect image of a star; clear and well-defined. There is nothing between the star and the camera to affect our image.
3. Introduce the TPP into the beam using the appropriate translation stage, draw attention to the fact that the image has become distorted and the displayed wavefront has changed.
4. Explain that distortions like this are caused by the atmosphere but constantly alter on a rapid scale rather than remaining static.
5. Demonstrate this effect by spinning the TPP; allow the participants to spin the TPP themselves, noting the changing positions of the WFS spot pattern and the subsequent warping of the simulated star image.
6. Explain that AO allows us to remove this effect by measuring how much the spots have moved and then using a device to produce the opposite spot motion.
7. Show this at a slower speed by using the TPP translation stage to gradually alter the aberrations introduced into the beam.
8. Demonstrate AO by allowing the participants to turn closed-loop correction on and off by clicking *"Correct"* when the plate is static, once correction has been achieved alter the plate position slightly. Point out that they can see the correction happening iteration by iteration for each position of the plate.
9. Inform the participants that this is exactly what happens on a telescope, albeit at a much more rapid rate.
10. End the simulation by translating the TPP out of the beam path and closing the loop to return the mirror to its reference shape.

Demonstrating AO in microscopy:

1. Begin by rotating the sample filter wheel until one of the microscope samples is illuminated. Ensure it is visible in the live feed of the imaging camera. Use the two-axis translation stage beneath the filter wheel to adjust the focus and position of this image.
2. Explain that this is a simulation of a perfect microscope image; clear and well-defined. There is nothing between the layer of tissue we are interested in and the camera that can affect our image.

3. Explain that when imaging larger, more complex, and sometimes even living, specimens there is often a great deal of tissue in between the layer we are interested in and our microscope lenses.

4. Click the *"Random Aberration"* button, draw attention to the distorted image and inform them that this is more similar to what we would see under the microscope. Note how much the WFS spots and the displayed wavefront have changed compared to the astronomy simulation, if it has already been performed.

5. Demonstrate AO by allowing the participants to turn closed-loop correction on by clicking *"Correct"*.

6. Allow the participants to choose different microscope samples and alter the aberrations introduced into the beam using the *"Random Aberration"* button, turning closed-loop correction on and off.

7. Point out that this allows us to see biological features and processes we otherwise would not be able to obtain a clear picture of, if at all, like developing fly embryos or a beating Zebrafish heart.

4.3 Results & Discussion

This section presents the operation of the AO demonstrator system in terms of both closed-loop performance and feedback from participants at a demonstration.

System performance is presented from the point of view of both the imaging camera and wavefront sensor by comparing images and calculated wavefronts from before and after closed-loop correction of aberrations introduced into the optical system, and in the absence of aberrations. After this, the results of an audience participation survey, taken over one day of demonstrating the system to various age groups of school children from the Durham area, are presented and discussed.

4.3.1 Closed-loop correction: Results

Figures 4.4–4.9 all demonstrate closed-loop correction of the typical aberrations introduced into the optical system using both random DM distortions and TPP positions in the exact same way as they are during demonstrations.

The 3-D wire-frame plots on the left column of Figures 4.4–4.6 are surface profiles taken from cropped images of the 25 micron pinhole sample both before and after AO correction, overlaid with a surface profile from a reference image recorded in the absence of induced aberrations. The pixel values have been normalised by the maximum pixel value of the reference image to present the variation in intensity between the three images as a Strehl ratio, a common method of describing the imaging improvement facilitated by AO [158, 159, 160]. The bar charts to the right of the wire-frame profiles present the average Zernike mode amplitudes both before and after AO correction, and have been reconstructed from the wavefront sensor

Mode #	n	m	Name
0	0	0	Piston
1	1	-1	Tilt
2	1	+1	Tip
3	2	-2	Astigmatism
4	2	0	Defocus
5	2	+2	Astigmatism
6	3	-3	Trefoil
7	3	-1	Coma
8	3	+1	Coma
9	3	+3	Trefoil
10	4	-4	Tetrafoil
11	4	-2	5th-order Astigmatism
12	4	0	3rd-order Spherical
13	4	+2	5th-order Astigmatism
14	4	+4	Tetrafoil

Table 4.1: Naming convention for the first 15 Zernike modes as used in this thesis.

signal. The Zernike modes are labelled according to the convention described in Table 4.1 and the amplitude of Mode 0, or 'Piston', has been omitted from the bar charts as it has no effect on the image intensity.

Figure 4.7 presents the same pinhole images as used for the wire-frame surface profiles in Figures 4.5 & 4.6 as basic grayscale images, as shown to participants via the imaging camera live display, and inverted for clarity. This is a visual example of how astronomical AO is demonstrated using the system. Similarly, Figure 4.8 is a visual example of how AO in microscopy is demonstrated using the system. Line sections across these images for both the reference, before AO, and after AO correction situations are presented in Figure 4.9.

4.3.2 Closed-loop correction: Discussion

The wavefront decomposition charts shown in Figure 4.4 show that the random mirror shape aberrations are dominated by defocus (Zernike mode 4) terms with mode amplitudes of over 0.5 wave RMS. Closed-loop correction of these aberrations is highly successful, with the focus term being completely removed and all residual mode amplitudes reduced below 0.05 wave RMS. As can be seen on the 3-D wire-frame profiles, the corrected pinhole image returns to a Strehl ratio of 1.0; nearly indistinguishable from the reference pinhole image. Thus, the system achieves full correction of these aberrations.

Closed-loop correction of the aberrations introduced into the system using the TPP returns

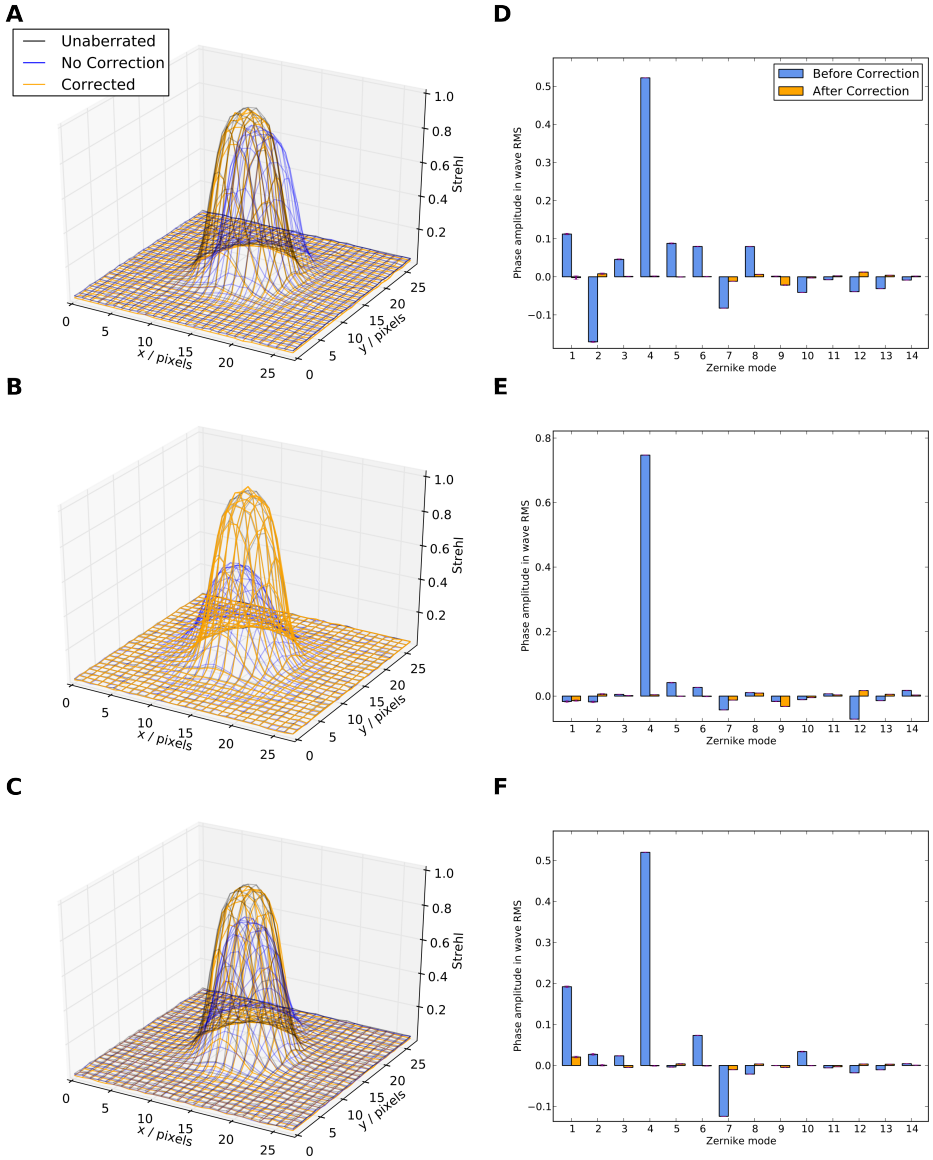

FIGURE 4.4: Closed-loop correction of three random mirror shapes **A**&**D**, **B**&**E**, and **C**&**F** by the AO demonstrator system. In **A**, **B**, and **C** monochrome images of a 25 micron diameter pinhole have been normalized by the maximum pixel value of the unaberrated reference image and plotted as wire-frame Strehl ratio surface profiles. The unaberrated reference (gray) and corrected (orange) wire-frame profiles are virtually indistinguishable from each other as they overlap very closely. In **D**, **E**, and **F** the reconstructed wavefronts at each stage of the AO process are presented as the arithmetic average of 30 Zernike mode amplitudes reconstructed from WFS signals. The standard deviations of these average mode amplitudes are presented as purple error bars on each of the bars. The Zernike mode numbers correspond to those detailed in Table 4.1.

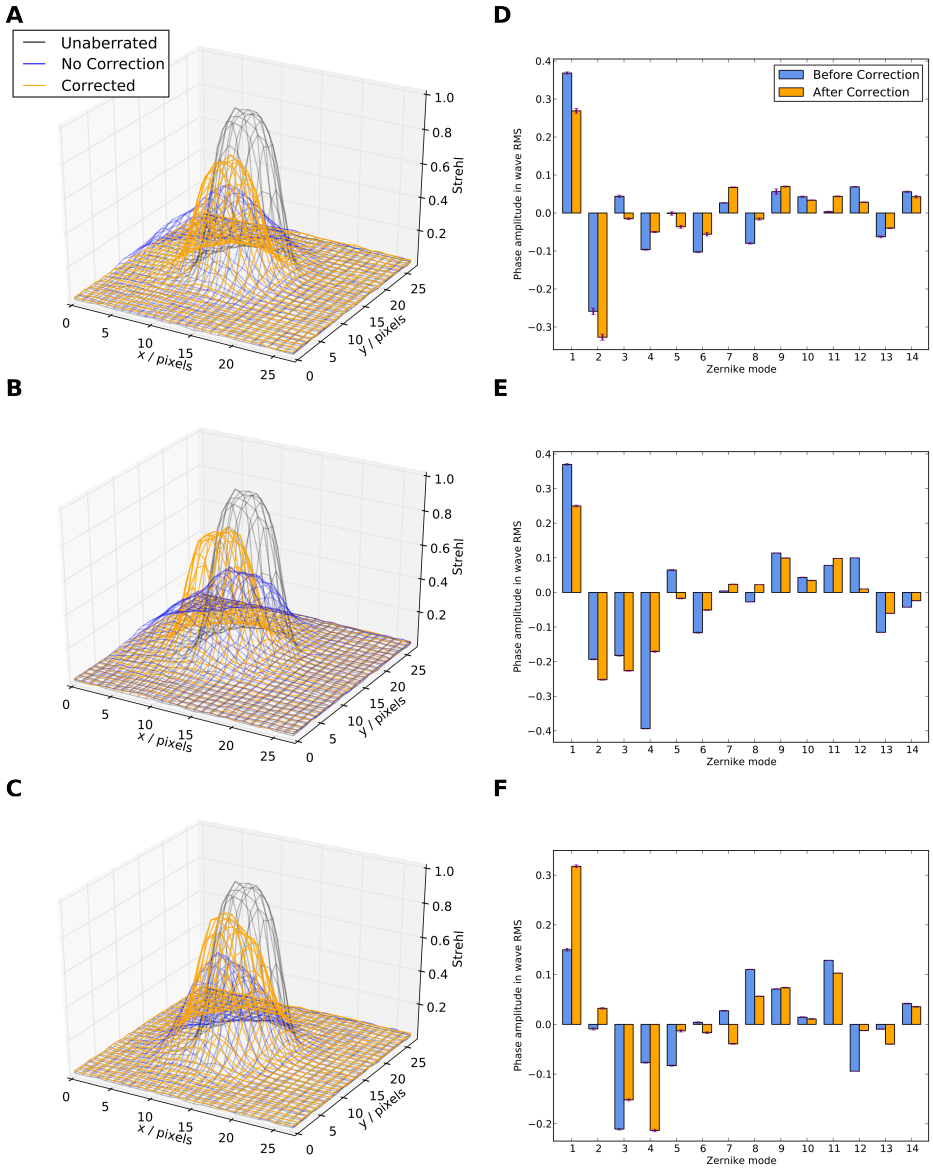

FIGURE 4.5: Closed-loop correction of three random TPP positions **A**&**D**, **B**&**E**, and **C**&**F** by the AO demonstrator system presented in the same format as Figure 4.4. Closed-loop correction of three further aberrations induced by random positions of the TPP are presented next in Figure 4.6.

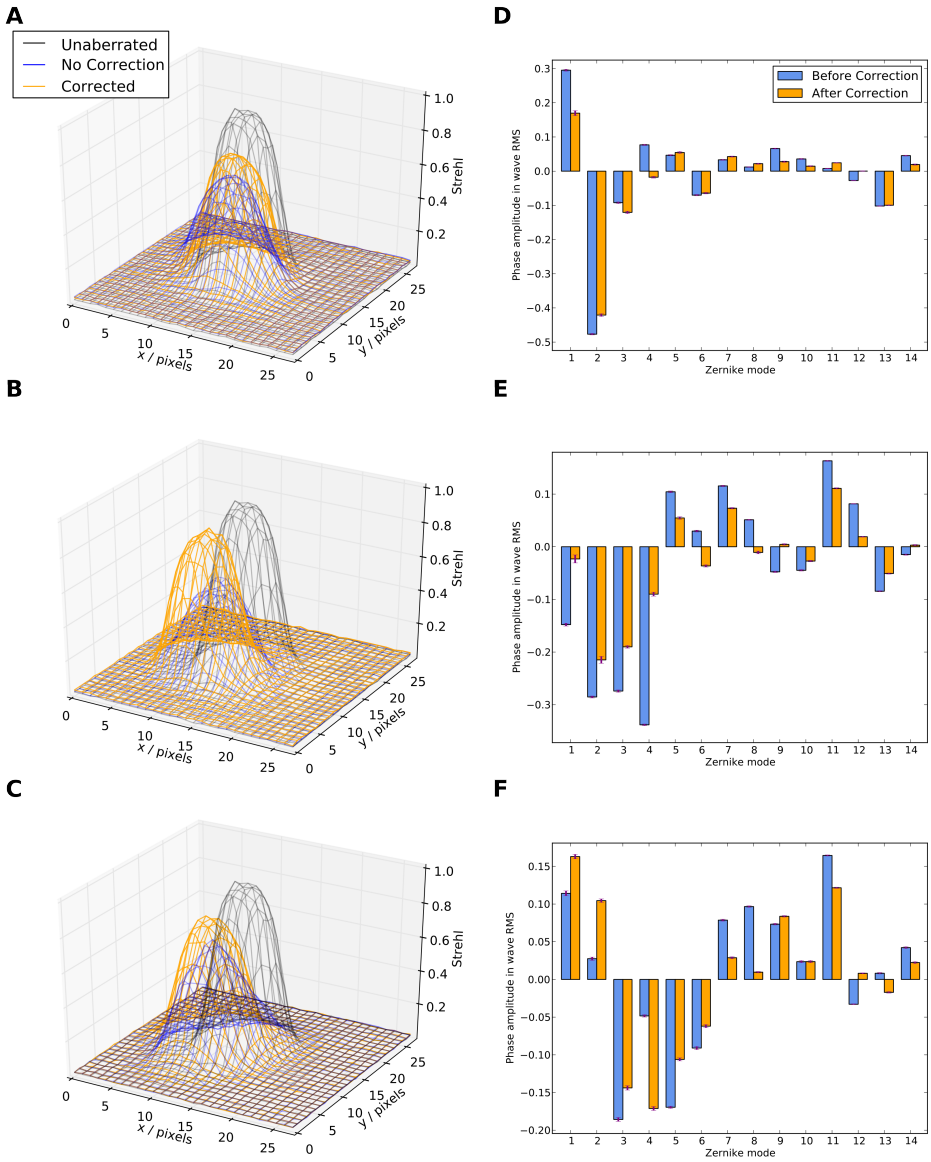

FIGURE 4.6: Closed-loop correction of three further random TPP positions **A**&**D**, **B**&**E**, and **C**&**F** by the AO demonstrator system additional to those presented in Figure 4.5.

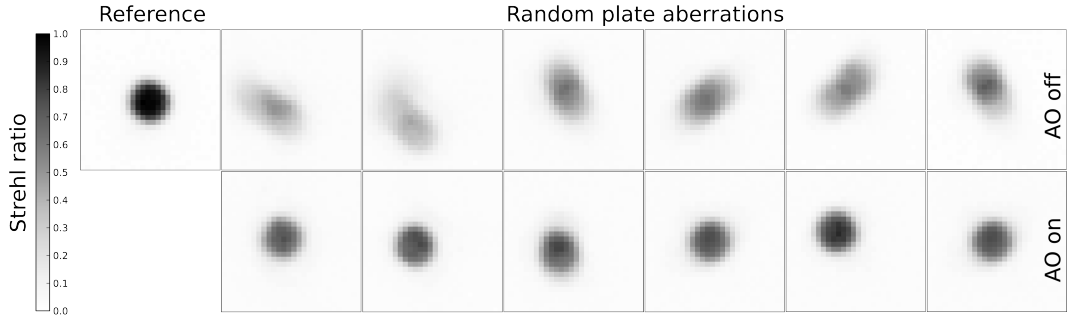

FIGURE 4.7: Simulation of astronomical AO. Closed loop correction of six random phase plate positions, as seen by the participant of a demonstration. These images are an alternative presentation of Figures 4.5(A,B,C), & 4.6(A,B,C); the pinhole images are the same as are used for the 2-D wire-frames of the previous figures but instead are presented 2-D in inverted grayscaleThe Strehl ratio colorbar again refers to the pixel values normalised by the maximum pixel value of the reference image.

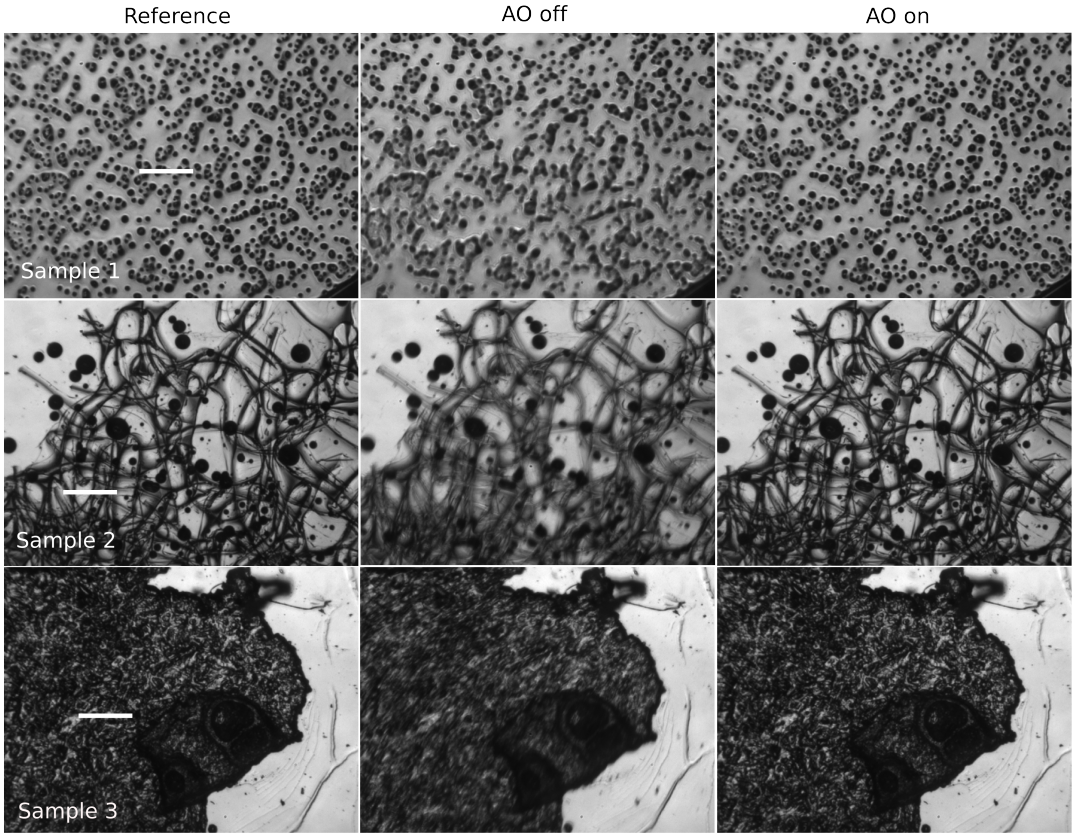

FIGURE 4.8: Simulation of AO correction in microscopy. Reference images of three microscope samples are presented alongside images of the same samples affected by a random mirror aberration both before AO correction, and after. The scale bar on each image is 1 mm. Line sections of these scale bars for all three samples in all three situations are presented in Figure 4.9

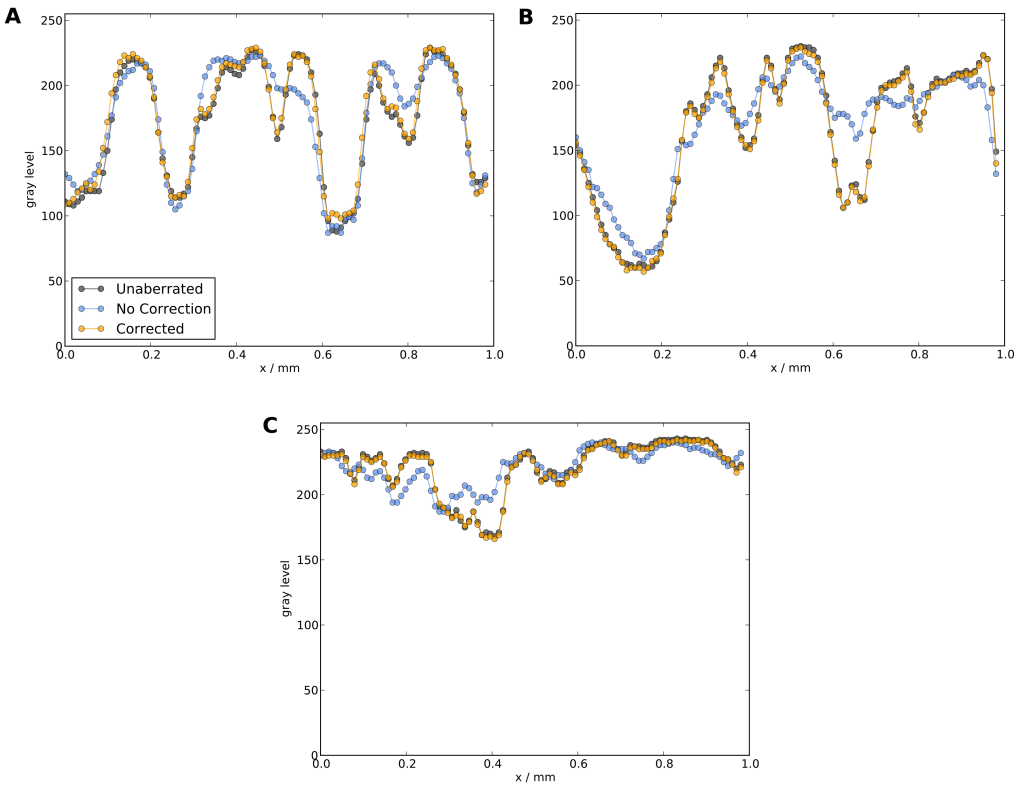

FIGURE 4.9: Line sections along the scale bars shown on the images of Sample 1 (**A**), Sample 2 (**B**), and Sample 3 (**C**) in Figure 4.8.

the pinhole images to a Strehl ratio of between 0.6–0.8, as shown in the 3-D wire-frame profiles in Figures 4.5 & 4.6 The wavefront decomposition charts in these figures show that in many cases the modal amplitudes of the reconstructed wavefront in fact increase following correction. Despite this, the two-dimensional (2-D) grayscale counterparts to these wire-frame plots shown in Figure 4.7 demonstrate that the correction is visible enough for demonstrative purposes.

As discussed earlier, the substantial defocus amplitude term of aberrations introduced using random mirror deformations causes the distinct appearance of wide-field aberrations affecting the pre–AO correction images of the three microscope samples in Figure 4.8. This successfully emulates the wide-field aberrations often encountered during deep imaging of sample tissues in microscopy. Additionally, since the system is capable of fully correcting mirror-induced aberrations, the correction is highly visible: The *'AO on'* images in the right column of the figure are virtually indistinguishable from the *'Reference'* images in the left column. This is emphasised in Figure 4.9 where line sections along the scale bar coordinates on the *'Reference'* images of Figure 4.8 are plotted with same-coordinate sections across the *'AO off'* and *'AO on'* images. Clearly the AO correction has returned each image to its original

form.

Overall, the system both imparts and corrects for aberrations in a manner which is appropriate for the simulation of astronomical AO and AO in microscopy.

4.3.3 Participation feedback

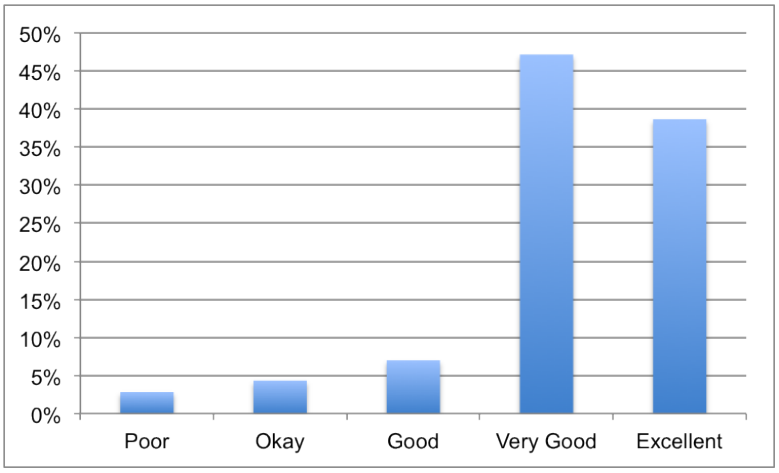

FIGURE 4.10: Feedback on the AO demonstrator from a short questionnaire that was completed by participants during a science festival for school children from Durham and the surrounding area.

Six different school groups of different ages and ability were presented the AO demonstration system during a science festival held at Durham University for children from the surrounding area. Following the presentation each participant was asked to fill out a questionnaire indicating their enjoyment of the presentation. The questionnaire was only devised to generate simple participant feedback, rather than an exhaustive evaluation of their understanding of the various theoretical components of AO. As shown in Figure 4.10, 86% of those that answered the questionnaire rated the demonstration either 'Excellent' (39%) or 'Very Good' (47%) while 11% selected either 'Good' (7%) or 'Okay' (4%); 3% described the demonstration as poor. This data shows that the majority of participants responded positively to the demonstration.

4.4 Conclusions

The main issues affecting the construction of most AO systems are the cost of the high performance cameras, powerful lasers, and the subsequent bulk and size of the system. These systems are also typically very sensitive to vibrations and mis-alignments and can easily be rendered into an inoperable state when not carefully monitored within a contained

environment. By choosing to perform AO on simulated astronomical and microscope environments these factors are significantly reduced to the point where our system was robust enough to withstand days of continuous operation at public science festivals where there were large numbers of participants. As the aim of the system was to visibly demonstrate AO to a participant in real-time there was no need for high frame rate cameras, expensive simulated LGS spots within atmospheric chambers, expensive microscope objectives and illuminator/condensor lenses. The light sources used were low cost, the control computer was a regular classroom PC, and the lenses, lenslet array, mirrors, beamsplitters, filters and breadboard can easily be purchased *off-the-shelf* from online opto-mechanical component retailers. The most expensive component was the PPDM, costing €5000 (currently £4000), below that the two Prosilica cameras cost £600 each, the TPP $700USD (currently £464), and the lenslet array £300.

The performance of the instrument has been quantified and analysed in a manner in-line with it's pedagogical aims: A system performance in terms of Strehl ratio has not been performed for a point-source, but rather for the system operating in point-source-simulation mode, using a pinhole. Though the 3-D wire-frames and modal wavefront decomposition charts show that the closed-loop correction of the TPP aberrations achieved with the system are far from perfect, observation of the before and after images presented to participants show that the level of correction is visually clear enough for demonstration purposes. Similarly, though the large-amplitude aberrations simulating those found in microscopy are created by the corrective element itself, heavily influenced by the large central actuator, these aberrations affect and are corrected fully across the entire wide-field sample image. Plus, the stages of the iterative correction occur on a timescale of seconds, making visible to the participant/observer what could easily be overlooked with a faster system.

HDR beam profiling camera probe 5

5.1 Introduction

In this chapter we describe a beam profiling system that was developed in order to directly image the laser illumination beams used in fluorescence microscopes. In particular we use our system to profile the illumination beam of an operational single/selective plane illumination microscope (SPIM), obtaining images from directly within the small volume of the specimen chamber in-between the orthogonally-mounted objective lenses. The beam profiling system itself is comprised of a minimally-invasive camera probe which is used in conjunction with a high dynamic range (HDR) imaging procedure and image reconstruction algorithm in order to measure the wide range of flux levels present in focused laser illumination. The reconstructed beam profile images are quantitative 2-D maps of the flux incident on the camera sensor and can be extended to 3-D by scanning the probe along the optical axis of the beam.

This chapter opens with an explanation of how sequential exposure HDR imaging can be used to extend the dynamic range of a camera sensor. Following this, we present the experimental development of our beam profiling system, starting with the camera probe design. We explain the beneficial features of the selected sensor and the custom-manufactured sensor housing in regard to using the device directly at the illumination beam focus of operational microscope systems. Next, we explore the performance of our camera probe and give details of the sensor calibration required for our quantitative sequential exposure HDR imaging procedure. The full experimental HDR imaging and reconstruction procedure is then explained and verified by comparing a 2-D flux map with the theoretical profile for a test beam. The device is then demonstrated within three operational fluorescence microscope configurations. 3-D illumination beam profiles from these microscope systems are presented that allow us to make conclusions regarding microscope optical alignment and performance alongside further comments regarding our beam profiling method. Lastly, we discuss the limitations of our imaging approach in terms of the profile resolution, the speed of the HDR

imaging and reconstruction procedure, and the reliability of the reconstructed flux maps.

5.2 Quantitative sequential exposure HDR imaging

Here we present the theoretical framework for our HDR imaging and reconstruction procedure. The overall intention of this work was to create a compact camera device that could be used to record the full intensity profile of a beam directly. Due to the nature of beam foci, namely the high flux concentrated within the focal volume and the comparatively low flux outside of that, our system was required to quantify a wide range of incident flux. However, there is a limit on the range of intensities that any camera sensor can adequately reproduce in a single image which is set by the sensor's dynamic range. In this section we first explain how the dynamic range of a sensor can be extended by sequential exposure imaging (SEI) to allow a wider range of incident flux to be recorded. We then explain how quantitative HDR images can be composed from the recorded data.

5.2.1 Dynamic range of a sensor

Each pixel on a sensor array responds to an incident flux by collecting the charge induced by the photo-electric effect over a time period called the exposure duration. The maximum amount of charge that can be collected by a single pixel is referred to as the analogue well depth. If the well becomes full then signal saturation occurs. Thus, the signal saturation level set by the well depth and the exposure duration determines the maximum incident flux that can be measured. Once the exposure duration ends the stored charge is released and an analogue measure of the photoelectric signal is converted from an analogue input signal into a digital output signal by an analog-to-digital converter (ADC). Gain and offset controls are used to set the scaling factor relationship between the analogue input and digital output signal ranges. The relationship between the analogue input and digital output signal ranges determines the flux range that can be measured by the sensor. The bit-depth of the sensor determines the number of digital signal levels the analogue charge signal can be converted to. For a linear n-bit sensor, the ADC maps the input signal range of analogue charge to a discrete range of 2^n equally-spaced digital signal levels. This sets the quantisation resolution of the signal. The saturation level and quantisation resolution together set the maximum output dynamic range of the sensor, depicted for a single pixel in Figure 5.1(a).

5.2.2 Sequential exposure extension of dynamic range

Figure 5.1(b) depicts how the saturation level across a sequence of exposure durations alters the measurable range and quantisation resolution of the incident flux, thereby extending the intrascene dynamic range. The saturation level can be made to correspond to larger flux levels by reducing the exposure duration, allowing flux that was above the saturation level of a longer exposure to become measurable. However, low signals produced by low incident flux can be greatly affected by either read noise in the sensor circuitry, coarse quantization in the digital conversion, or both. This masks the input analogue signal and reduces the accuracy of

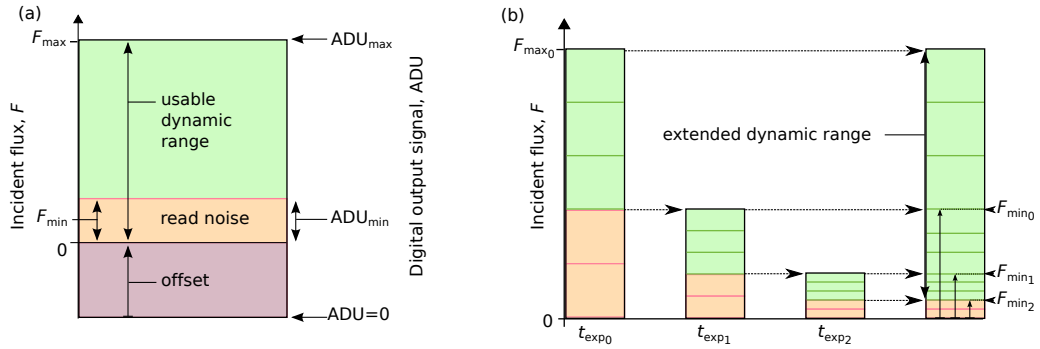

FIGURE 5.1: The dynamic range of a sensor pixel is represented here by a vertical rectangular bar corresponding to the full ADU output signal bit-depth (a). The usable region of the dynamic range is affected by offset and read noise, shown as different colored portions of the vertical bar and scaled for emphasis. When a dark image (F=0) results in a digital output signal above 0 ADU the dynamic range has been reduced by the offset applied between the analogue input signal and the digital output signal (purple shading). Above this offset there is a region where there is poor resolution between the low flux signals and the analogue input signal is a similar magnitude to, and therefore masked by, the read noise (orange shading). The extent of the orange region effectively sets the minimum resolvable signal within the usable dynamic range as ADU_{min}. The upper limit on the output signal is set by saturation at ADU_{max}. Within this usable dynamic range there is a distinct range of incident flux that produces signals which are resolvable at the scale of ADU_{min} at a given exposure. This range can be extended by sequential exposure imaging (b). For illustrative purposes the dynamic range reduction due to the applied offset has been omitted in (b). The range of signals affected adversely by read noise is shown to take up two fifths of the pixel's dynamic range. The three successively longer exposure durations shown in the figure demonstrate how the highest flux that produces signals which are masked by read noise successfully produce a quantifiable signal in the usable dynamic range of the next longest exposure duration. The dynamic range of these three exposures combines to form an extended dynamic range, allowing signals produced by a wide range of incident flux to be quantified more accurately.

the output signal. In either case these noise sources may behave approximately uniformly across different exposure durations, thus corresponding to much smaller uncertainties in the incident intrascene flux at longer exposures. Therefore, by combining the output signals from images taken with different exposure durations a wide range of incident flux can be measured more accurately. Such images are referred to as HDR images, the procedural composition of which is explained in the following section.

5.2.3 Composition of quantitative HDR images

The exposure durations used in sequential exposure HDR imaging have to be chosen such that there is an overlap in the flux range between the lowest measurable signal and the saturation level between successive exposures, otherwise there will be a gap in the range of flux that can be measured. Once a set of images have been taken using a sequence of exposure durations each pixel then has several measurements of the incident flux associated with it that are

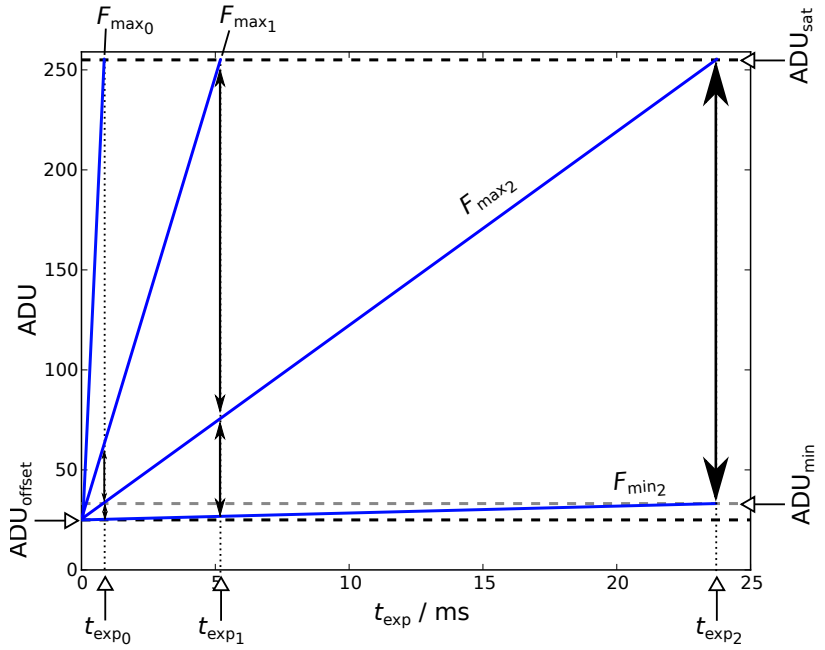

FIGURE 5.2: The hypothetical flux response of an 8-bit sensor pixel in ADU vs. t_{exp} parameter space. This pixel is shown to exhibit a linear response to incident flux. The response to 4 incident flux levels is presented as 4 solid blue lines diverging from a common offset of ADU_{offset} at $t_{exp} = 0$. Three exposure durations are noted in the diagram: t_{exp0}, t_{exp1}, and t_{exp2}. For the entire range of exposure durations the output signal of the sensor may range from ADU_{offset} up to the output saturation signal, ADU_{sat}. Both limits are shown as horizontal black dashed lines. Additionally, the presence of read noise dominates low signal levels and limits the accuracy of the output signal to ADU_{min}, which extends from ADU_{offset} up to the horizontal gray dashed line. The signals induced by low incident flux that are not well sampled by the dynamic range of the sensor at the shortest exposure duration, t_{exp0}, can be better quantified by taking images at longer exposure durations. This improves the signal-to-noise ratio and provides greater distinction between low flux signals. This in turn allows the flux signals that were previously indistinguishable from noise to be recovered: the signals from flux between F_{max2} and F_{min2} that were lost to read noise at t_{exp0} are fully resolved by the dynamic range of the sensor at t_{exp2}.

represented by both the output signal and that signal's corresponding exposure duration.

In order to extract a quantifiable measure of the flux incident at each pixel we need to determine the relationship between the output signal and the exposure durations in response to a range of known incident flux. Such a relationship is referred to hereafter as the *flux response* of the sensor and determines the output signal, measured in ADU, when recording a flux of F over an exposure duration of t_{exp}. Figure 5.2 depicts the flux response of a linear 8-bit sensor pixel to 4 incident flux levels. We refer to the mathematical form of the flux response as the *flux response equation*. This equation describes a family of curves in ADU versus t_{exp} parameter space where a value of the incident flux can be calculated by using a pair of ADU and t_{exp} co-ordinates, effectively solving the flux response equation. To obtain the best estimate of the incident flux we select the pair of ADU and t_{exp} values where the

output ADU signal is as high as possible without being affected by saturation. This selects the best quantisation resolution and the highest SNR for the signal in order to obtain the best estimate of F. Composition of the quantitative HDR image is complete once F has been calculated for each sensor pixel. The uncertainty in F, caused by noise, limits the intrascene dynamic range of flux that can be reproduced. A quantitative assessment of the dynamic range improvement invoked by sequential exposure imaging is discussed more thoroughly in the following section.

5.2.4 HDR sensor technology

The fact that signal saturation is an inherent part of sequential exposure HDR imaging informs our choice of sensor technology for a HDR camera. As mentioned earlier, high beam intensities cause signal saturation once the analogue well depth has been filled. Thus, when taking sequential exposure images of a 'scene' containing a wide range of incident flux magnitudes, there will be exposure durations where a particular flux may cause saturation of some pixels, whilst the lower flux incident upon neighboring pixels does not cause saturation. As an example we consider two neighboring pixels on a sensor array, pixels A & B, where the incident flux is higher at pixel A than at pixel B. Three sequential exposures of the scene are taken using the sensor: $t_{\text{exp}0}$, $t_{\text{exp}1}$, and $t_{\text{exp}2}$, where $t_{\text{exp}0} < t_{\text{exp}1} < t_{\text{exp}2}$. These result in three corresponding recorded signals for each pixel: $\text{ADU}_{\text{A}\,0,1,2}$ and $\text{ADU}_{\text{B}\,0,1,2}$. In this example sequence of three images saturation of pixel A occurs during $t_{\text{exp}1}$, and saturation of pixel B occurs during $t_{\text{exp}2}$. Hence, when the HDR image of the scene is composed the saturated signals are ignored and our best estimate of the flux incident at pixel A is calculated using $\text{ADU}_{\text{A}\,0}$ and $t_{\text{exp}0}$ and at pixel B using $\text{ADU}_{\text{B}\,1}$ and $t_{\text{exp}1}$. A problem common to some sensors is an inability to retain charge within the confines of a single pixel well once saturation has been reached. The excess charge induced can flow into the wells of neighboring pixels, producing an erroneous signal. For our example sensor this would cause the saturation of pixel A to affect the readout signal from pixel B during exposure $t_{\text{exp}1}$, thus affecting the HDR image which uses the $\text{ADU}_{\text{B}\,1}$ signal to calculate the incident flux at pixel B. This unwanted process is called blooming and occurs predominantly in CCD sensors due to the readout signal path running through entire rows of pixels on the sensor array. Blooming does not, however, occur in CMOS sensor chip architectures as the readout circuitry is fabricated on an individual pixel by pixel basis. This makes CMOS the ideal sensor choice for HDR imaging.

5.3 Camera probe design and operation

5.3.1 Intra-microscope camera probe design & construction

5.3.1.1 Sensor selection

Use of the device directly within an operational microscope system restricts the maximum overall dimensions of the camera probe to sub-centimetre scales. A minimal-dimensions CMOS sensor (NanEye 2b [161] by Awaiba, Madeira, Portugal), originally designed as a

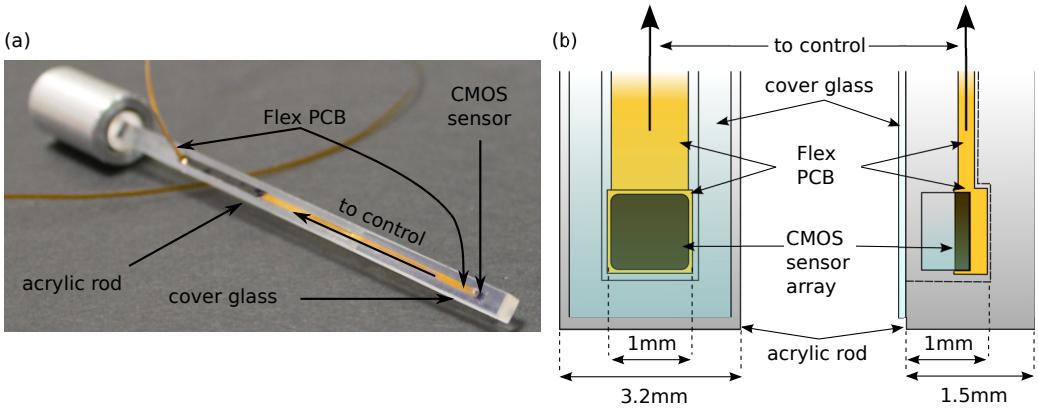

FIGURE 5.3: Photograph (a) and schematic (b) of the compact waterproof mounting solution for the Awaiba NanEye 2b CMOS sensor comprising our beam profiling camera probe.

compact endoscope, was selected for its compact sensor size and long read-out cable; it was the smallest stand-alone sensor on the market at the time of this research. The re-purposed 8-bit CMOS sensor has a footprint of only 1 mm × 1 mm and the read-out cable, 55 cm long, feeds into a separate USB-to-PC control interface away from the active sensor array. The glass-fronted array of the sensor, comprised of 3 μm × 3 μm pitch pixels over a 250 pixel × 250 pixel array, spans an active area of 750 μm × 750 μm.

5.3.1.2 Probe construction

As the probe was intended for use within specimen chambers a waterproof housing was devised to contain the sensor, shown in Figure 5.3. A glass microscope cover slip of thickness 170 μm was cut to the dimensions of the housing face and glued in place using a UV-cured optical adhesive (Norland, New Jersey, USA) to seal the sensor within the housing. Such cover slips are regularly used in microscopy to seal samples to microscope slides. The optical adhesive was refractive index matched to both the cover glass and the glass front of the sensor array. The dimensions of the device were minimised to reduce the distance between the sensor pixels and the outer surface of the cover slip, allowing the device to operate in close proximity to short-working-distance optical components.

5.3.2 Camera operation and settings

Awaiba's proprietry 'Viewer' software was used to control the gain and exposure for the sensor, and subsequently to take images, as there was no software developer kit (SDK) available for the device. This resulted in the gain and offset settings for the sensor being limited to four discrete values each: '0', '1', '2', and '3'. The gain and offset were chosen so that the usable dynamic range of the sensor was maximised. In the complete absence of incident light an offset of '3' ensured the dark voltage produced a signal above 0 ADUs for all pixels so no signals were lost at the low end. The minimum output signal for all pixels across the sensor array was between 50–100 ADUs using this setting. A gain of '3' scaled the average analogue

well saturation signal level up to the maximum output signal of 255 ADU. These settings therefore caused the usable dynamic range for each pixel to be between 155–205 ADUs.

5.4 Camera probe calibration

As mentioned earlier in Section 5.2 a mathematical description of the sensor's flux response is required in order to generate quantitative HDR images. To determine the sensor's flux response we recorded the output signal of the sensor in response to a range of known incident flux using a range of exposure durations. We then devised a general mathematical equation to describe the properties of the flux response shown in our calibration data. In the next section we describe the full calibration procedure undertaken and derive the mathematical form of the flux response equation and comment on its limitations.

5.4.1 Determining the flux response equation

The sensor was uniformly illuminated using an integrating sphere (AvaSphere-50 by Avantes, Apeldoorn, The Netherlands) fed by a light emitting diode (LED) light source. A range of absorptive ND filters were used to set the relative flux that was incident on the sensor. The transmission of each ND filter was used as our measure of the flux incident on the sensor, F. This F was adopted as our numerical quantity of flux in this work and is referred to throughout this chapter and the next as the *relative incident flux*, in arbitrary units.

To roughly match the 488 nm excitation wavelength of many commonly used fluorophores, *e.g.* green fluorescent protein (GFP), a blue LED (wavelength 470 nm, linewidth 10 nm) was selected as the calibration light source. Light from this LED was collected by a plano-convex lens (focal length 35 mm), coupled through a microscope objective lens (40×, 0.65NA) into the core of a multi-mode fiber (diameter 200μm, 0.22NA), and then fed into the integrating sphere. Prior to the objective lens a filter mount was installed to house the ND filters. Care was taken to ensure the sensor and integrating sphere were completely shrouded in black-out cloth, in addition to all calibration images being taken in a lightless room. Thus all light incident on the sensor array was solely controlled by the LED-ND filter fiber coupling system. The optical densities, OD, of the ND filters used were 0.2, 0.4, 0.6, 0.8, 1.0, 1.2, 1.5, and 2.0. The transmission of these filters gave us a specific range of calibration flux values of 0.63, 0.40, 0.25, 0.16, 0.10, 0.06, 0.03, and 0.01 respectively. For each incident flux, including $F = 1$ where no ND filter was present and $F = 0$ in the complete absence of light, images were taken using a range of 14 exposure durations, linearly spaced along the horizontal axis of the ADU vs. t_{exp} parameter space between 90 μs and 22.3 ms. Exposure durations outside of this range were inaccessible using the Awaiba 'Viewer' software. For each exposure duration 25 images were taken and the ADU count for each pixel was taken as the corresponding arithmetic mean in order to reduce the effect of signal variations caused by shot noise and read noise. The $F = 0$ flux response was used as the dark frame for each exposure duration and was subtracted from each of the recorded data sets in the following calibration procedure.

The flux response of each pixel was determined in a two-step manner: First, we determined a general function which described what we refer to as the *ensemble* flux response across the entire chip by spatially averaging the signals from all pixels at each exposure duration; Second, we fitted this function to the flux response of each pixel individually. The sensor's ensemble flux response to a range of incident flux is shown in Figure 5.4.

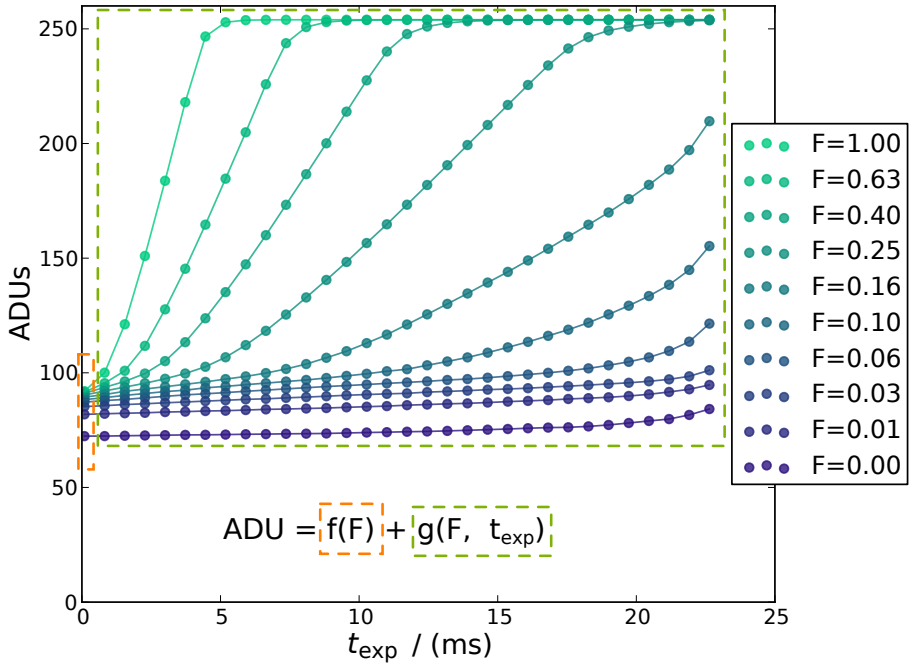

FIGURE 5.4: Ensemble flux response of the Awaiba NanEye 2b CMOS sensor to a range of incident flux, F, using a range of exposure durations t_{exp}. In this figure the flux response data has not undergone dark subtraction. The general flux response equation, and the regions of the data set which it is used to describe, is labeled as Equation 5.1 and is explained in the main text.

The response was distinctly non-linear and displayed two key features: a non-linear flux-dependent offset at low exposures that transitioned into a linear region, and a soft-knee transition of this linear region up to saturation level. We therefore needed to develop a mathematical form of the flux response equation that took these two response features into account. We began with the following general flux response equation:

$$\mathrm{ADU} = \mathrm{f}(F) + \mathrm{g}(F, t_{exp}), \tag{5.1}$$

where the function $\mathrm{f}(F)$ is a function solely in terms of the incident flux, F, and is used to describe the flux-dependent offset at the shortest recorded exposure duration; the function $\mathrm{g}(F, t_{exp})$ is a function in terms of both F and the exposure duration t_{exp} that describes the

response data across the range of longer exposure durations. We refer to this latter feature of the flux response as the *remainder* of the flux response. Both response features are highlighted on Figure 5.4 by dashed-line rectangles in orange and green for $\mathrm{f}(F)$ and $\mathrm{g}(F, t_{\mathrm{exp}})$ respectively.

The non-linear flux-dependent offset witnessed in our sensor response is highly unusual and may have been caused by excessive noise sources within the CMOS circuitry. The various noise sources within a CMOS sensor were discussed earlier in Chapter 2. There are two key points that need to be reinforced regarding this witnessed behaviour: First, this behaviour becomes manifest only at the shortest exposures; Second, extrapolation of the sensor response curves back to an exposure duration of zero exhibits no common offset, *i.e.* there appears to be a definite flux dependency. The first point suggests the presence of a noise source that dominates the noise power spectrum at the high sampling frequencies of short exposures. At high frequencies we expect flicker $(1/\nu)$ noise to be masked by the uniform power spectrum of thermal kTC noise. As a Gaussian white noise source thermal kTC has a zero-mean and thus its impact will be reduced by the successive frame averaging (SFA) that takes place in our procedure. However, if the use of an input signal window in the ADC causes signals below a threshold level to become clipped then SFA results in a response exhibiting non-linear behaviour. Unfortunately this does not directly explain the witnessed flux-dependency.

This flux-dependency implies that either the thermal noise level is larger for higher incident flux, or that there is a flux-dependent residual signal stored during these short charge integration periods. If the higher incident flux used in this calibration was bright enough to cause heating of the sensor then the thermal noise would indeed be increased with brighter illumination. However, the calibration light source was an LED and the sensor was illuminated using an integrating sphere, hence excessive noise generated by heating is unlikely to be the case. Alternatively, the overall room temperature of the lab may have changed between datasets. The lab was not temperature controlled and the duration required to take each dataset was around 10 minutes each. Over the 80+ minutes required to take all of the calibration data any variation in the lab temperature could have been taken into account by re-recording a new set of dark frames for each dataset. The second suggestion is that there is an additional photoelectric signal generated even during the reset operation. We already know that CMOS sensors suffer from kTC noise being sampled onto the storage capacitor via the reset transistor, causing there to be a random offset for any single frame, but such reset noise is only caused by the device temperature and the storage capacitance and therefore cannot cause the flux dependency.

If, however, the reset operation is failing to flush out the stored charge at very short exposures then we could expect there to be some behaviour akin to a flux-dependent offset. That is, at a hypothetical zero exposure, where the pixel is meant to be held in reset such that there is no exposure duration and all photo signals are diverted to ground, if there is an error in the timing of the reset signal then there may actually be a small duration of exposure when there was not meant to be one. This reset signal timing error may only be substantial in the shortest exposures and as such the shortest exposures are effectively made longer than they are meant to be. If we expected this timing error to be constant for a given exposure

then we would expect the flux-dependency to be linear which unfortunately does not explain the logarithmic spacing of the signals that is witnessed. Such logarithmic spacing may in fact be caused by conversion errors in the ADC. Without knowledge of the sensor's circuit design, sampling operation, and ADC conversion it is difficult to obtain a working model for this behaviour. The lack of this knowledge is the reason for proceeding with a general mathematical model that describes the witnessed effects, rather than by modelling the noise characteristics.

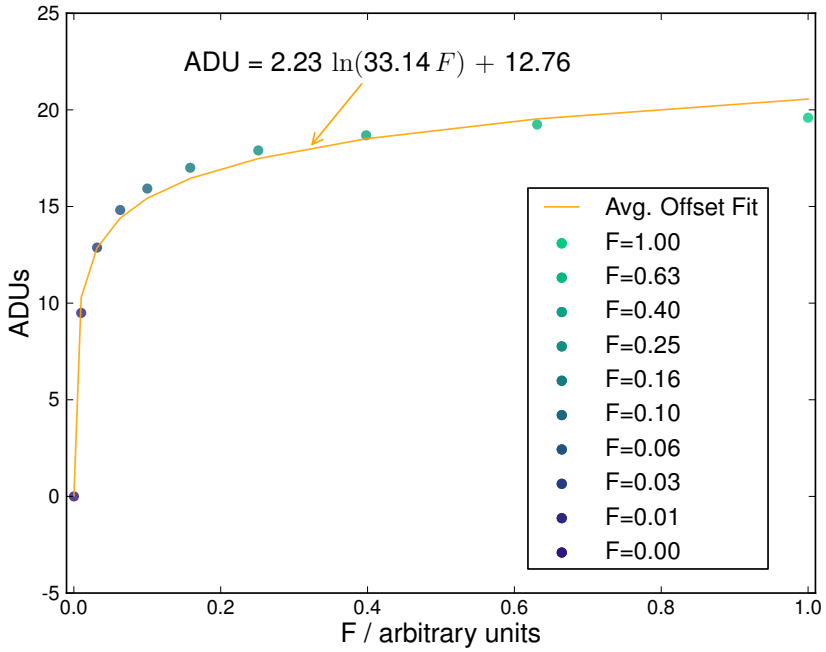

FIGURE 5.5: Form of the flux response offset. Data representing the ensemble flux response of the sensor was examined at the shortest exposure alone. A logarithmic function of the form $f(F) = C_\alpha \ln(C_\beta F) + C_\delta$ was fitted to this data, parameter values of $C_{\alpha,\beta,\delta} = 2.23, 33.14, 12.76$ respectively.

The form of $f(F)$ was devised through empirical analysis of the flux response at the shortest exposure alone. Figure 5.5 shows the non-linear flux-dependent offset to take a logarithmic form, represented by the function

$$f(F) \;=\; C_\alpha \ln(C_\beta F) \;+\; C_\delta \,, \tag{5.2}$$

where the constants $C_{\alpha,\beta,\delta}$ were fitted parameters.

We found the remainder of the flux response could be described by a function of the flux scaled by the exposure duration after noting the agreement of the calibration data ADUs plotted against $F \times t_{\text{exp}}$, as shown in Figure 5.6.

As such we described the remainder of the response as a general polynomial in terms of

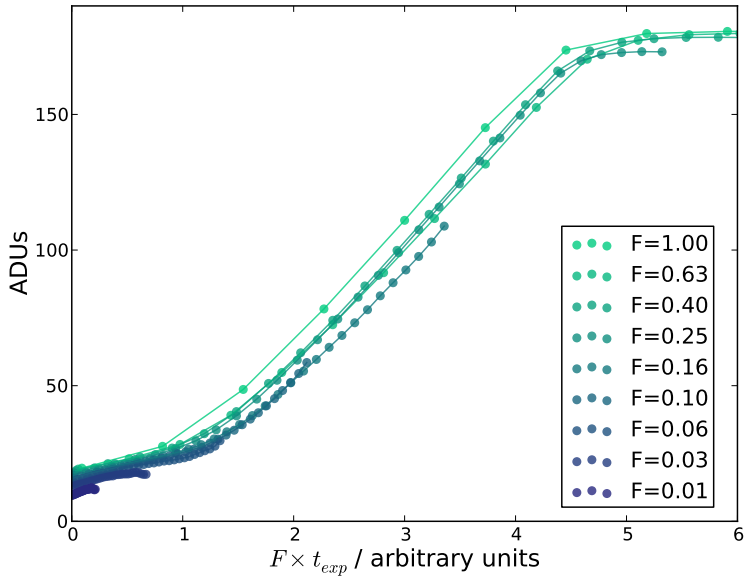

FIGURE 5.6: Investigation of the remainder of the flux response. Data representing the ensemble response of the sensor to incident flux was examined by plotting the recorded output signal in ADUs against the flux scaled by the exposure duration, $F \times t_{\text{exp}}$. The overlap of the recorded data for all incident flux suggested that the response could be described by some general polynomial function $g(F, t_{\text{exp}}) = \sum_k C_k (F \times t_{\text{exp}})^k$.

$F \times t_{\text{exp}}$, given by

$$g(F, t_{\text{exp}}) \;=\; \sum_{k=1}^{8} C_k \; (F \times t_{\text{exp}})^k \;, \tag{5.3}$$

where the constants C_k are again fitted parameters and the t_{exp} is the exposure duration. The maximum order of $k = 8$ was selected after testing a range of maximum orders. Maximum orders of $k > 8$ exhibited no noticeable improvement of the fit, whereas for maximum orders of $k < 8$ the fit became worse.

The combined description of the general flux response thus took the following form:

$$\text{ADU} \;=\; C_\alpha \ln(C_\beta F) \;+\; \sum_{k=0}^{8} C_k \; (F \times t_{\text{exp}})^k \;, \tag{5.4}$$

where the previous constant parameter C_δ has become the initial term C_0 of the polynomial.

The PYTHON function `scipy.optimize.curve_fit()` was used to fit Equation 5.4 to the ensemble flux response of the sensor first and then for individual pixels second. The fitted ensemble flux response of the sensor is shown in Figure 5.7. All 10 $C_{\alpha,\beta,0\text{–}8}$ fit parameters were given a starting value of 1.0. The fit parameters found when investigating the ensemble response were then used as the starting values of $C_{\alpha,\beta,0\text{–}8}$ when fitting the equation to the individual responses of each pixel to reduce the fit parameter space.

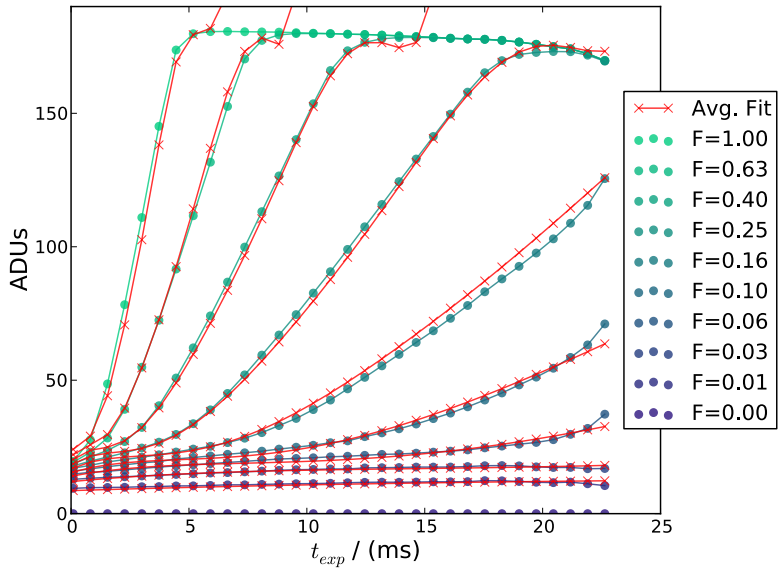

(a)

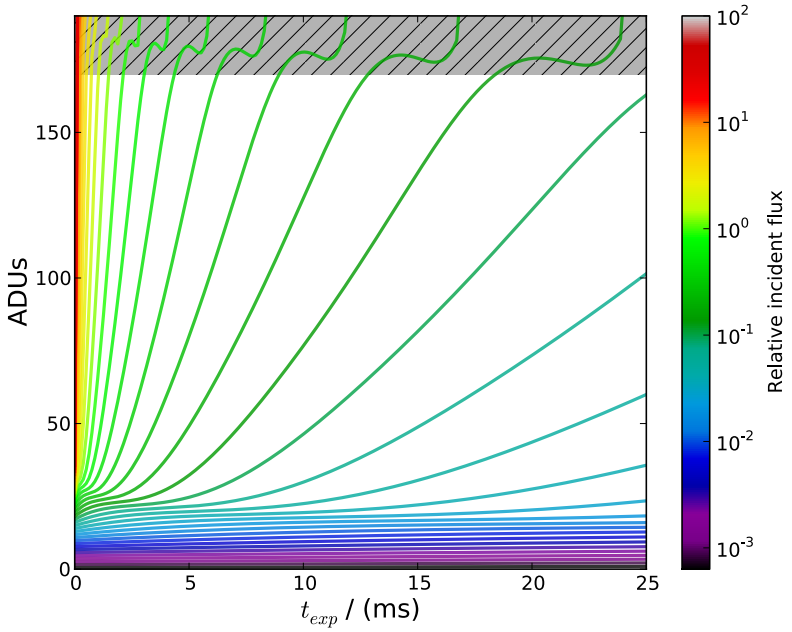

(b)

FIGURE 5.7: Fit to the ensemble flux response of the camera probe sensor. In (a) the fit of the flux response equation, Equation 5.4, to the ensemble flux response data for the sensor is shown. The fitted form of this equation determines a continuum of curves in ADU vs. t_{exp} parameter space (b) describing the values of F that can be quantified, relative to the calibration flux magnitudes, using a pair of ADU and t_{exp} coordinates. The gray shaded region across the top of (b) illustrates an example range of ADU values that would be omitted from HDR reconstructions due to their proximity to the dark-subtracted saturation threshold.

5.4.2 Approach limitations

Though the polynomial flux response equation performed well when fitting to the ensemble flux response of the sensor, the general polynomial equation was not an ideal description of the flux response for some pixels. Figures 5.8 & 5.9 shows the fitted flux response equation for two different pixels. The fitted flux response equation for the pixel shown in Figure 5.8 is in good agreement with the flux response data across the entire parameter space. However, the fit for a different pixel on the sensor is in a less good agreement with the flux response data, as demonstrated by the pixel response in Figure 5.9. In the case of the latter pixel the flux equation fits well to the flux response at higher flux where $F \geq 0.25$. However, for flux lower than this the flux response is not well described by the fitted flux equation. Low incident flux levels at this pixel would therefore be erroneously assigned a considerably higher value of F when reconstructing a HDR image using the parameter space described by the form of Equation 5.4.

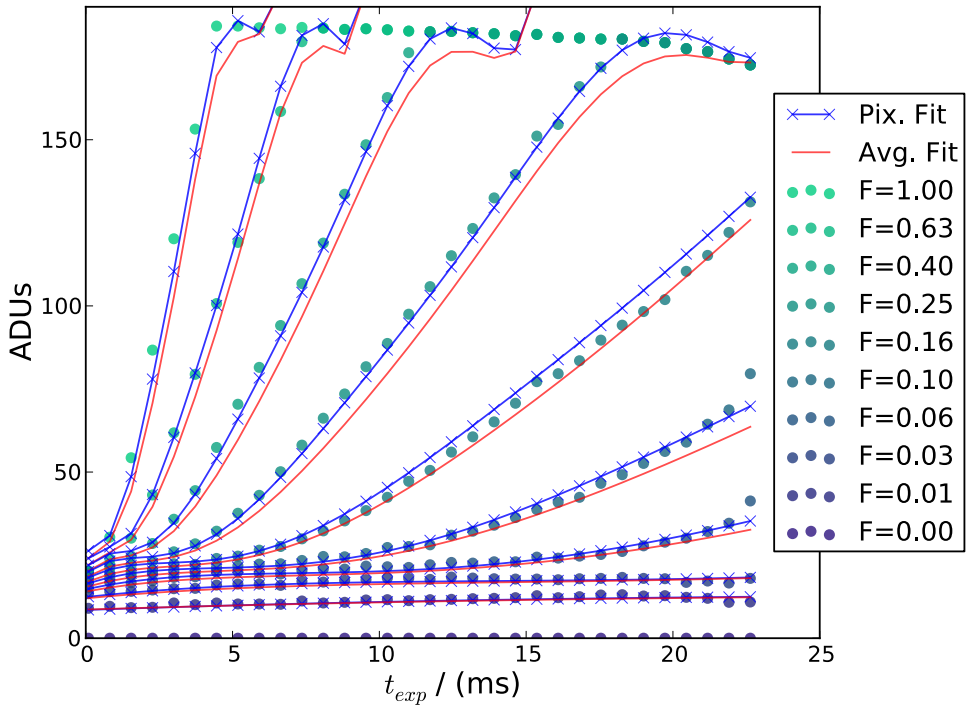

FIGURE 5.8: A pixel with a flux response that is well-described by the fitted general polynomial flux response equation in ADU vs. t_{exp} parameter space.

This demonstrates the limitations associated with the application of a general polynomial flux response equation to describe the behaviour of a miniature CMOS sensor with inherently non-uniform (pixel-specific) noise characteristics. Wide distributions of both photo-response non-uniformity (PRNU) variations and dark signal output are typically associated with such non-scientific CMOS sensors. In order to take these features into account it would be beneficial to examine the flux response of the sensor at each individual exposure duration, rather than

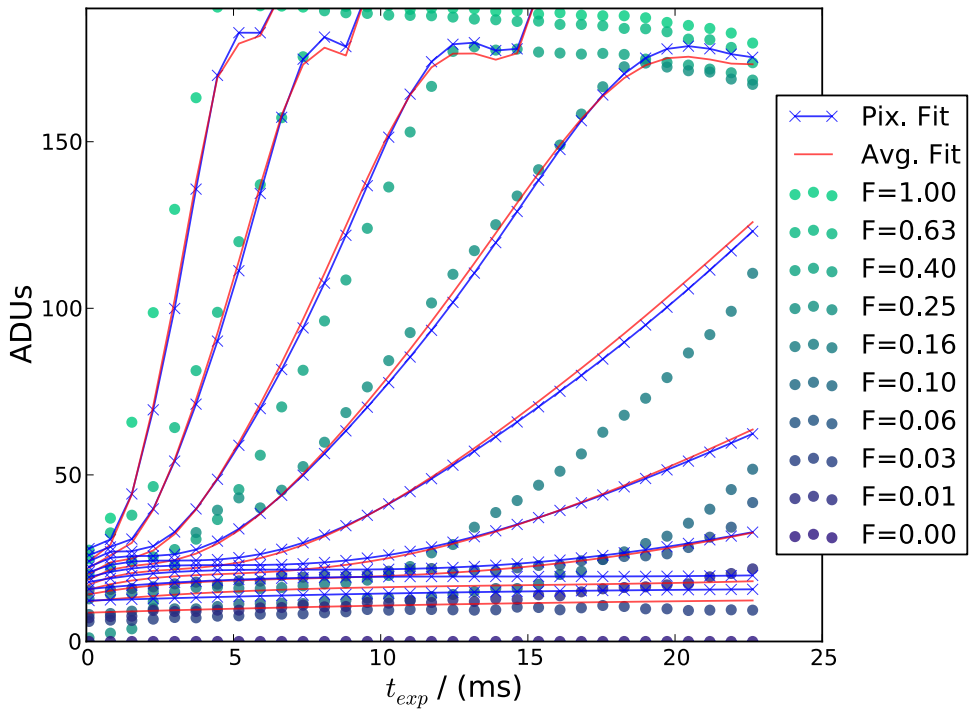

FIGURE 5.9: A pixel with a flux response that is not well-described by fitted general polynomial flux response equation in ADU vs. t_{exp} parameter space.

across all exposure durations as was performed here. Thus the reduced headroom caused by a large dark signal at longer exposures for some pixels would become de-coupled from the overall flux response. As the response of each pixel is dealt with individually the PRNU will inherently be taken into account and thusly removed during the HDR reconstruction. Therefore we suggest that in future work the flux calibration of the sensor be examined in ADU vs. F parameter space for each individual t_{exp} in order to obtain a better calibration across all pixels.

5.5 HDR imaging procedure

In this section we explain how our flux response equation was used to reconstruct flux values for each pixel, allowing HDR flux maps to be composed. As mentioned earlier in Section 5.2, the best estimate of incident flux was reconstructed from multiple exposures of a scene. First, the longest unsaturated exposure for each individual pixel was selected prior to dark subtraction. Then, following dark frame subtraction, the fitted flux response equation for every pixel was solved using the recorded ADU and corresponding exposure duration, t_{exp}, pixel to numerically obtain F.

This can be visualised as using a pair of ADU and t_{exp} coordinates to determine F within the ADU vs. t_{exp} parameter space, according to the continuum of flux response curves described by the fitted flux response equation for each pixel. These curves are shown in

Figure 5.7b for the example of the ensemble response of the entire sensor array. We used the Python function `scipy.optimize.brentq()` to solve Equation 5.4, finding F for each individual pixel. This numerical method is based on Brent's root finding method [162] and was selected over other root-finding functions for its robustness and generality. The function accepted a wide range of input bounds between which it iterated to locate a root of the given function. In order to allow our reconstruction of F to explore a large area of the ADU vs. t_{exp} parameter space we set an upper bound of $F = 10^2$ and a lower bound at $F = 10^{-30}$, effectively $F = 0$. In the case where a root could not be found the pixel was assigned a relative incident flux of zero.

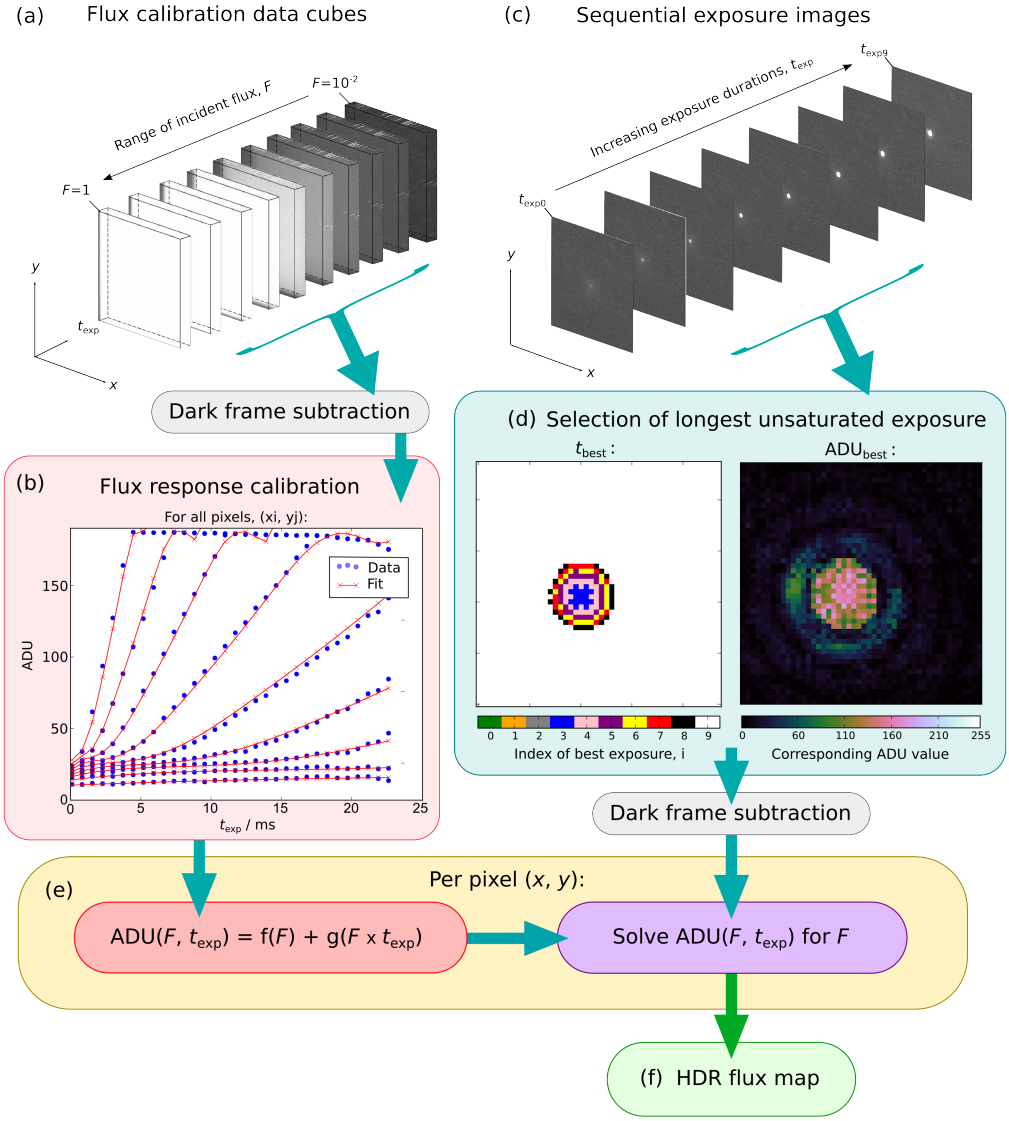

Figure 5.10: Flow chart depicting the component processes involved in calibrating our device and composing our HDR flux profiles. All component processes (a–f) are explained in the main text.

Figure 5.10 depicts a flow chart describing the component processes (a–f) within the overall calibration and flux reconstruction process. Images of uniform illumination are taken over the available range of exposures for a number of different incident fluxes; these form the flux calibration data cubes (a). Following dark frame subtraction a custom polynomial equation is fitted to the calibration data. These fit parameters describe the general polynomial fit to the time-integrated flux response of each particular pixel and are stored computationally for later access. The flux calibration data and fitted response equation are plotted in (b) as blue circles and red curves respectively.

Separately, images are taken of the beam of interest using a sequential range of 10 exposures (c); the index of these exposures runs from 0 for the shortest exposure up to 9 for the longest exposure. Dark frames are recorded at for each of the exposure durations being used. This is performed in the same conditions as during beam profiling but with the light source switched off. The longest exposure duration resulting in an ADU signal below the saturation threshold is selected as the appropriate dataset for each pixel. The leftmost map within box (d) represents the selected index of best exposure, *i.e.* the exposure time index having the highest unsaturated ADU signal, for a central region of the input images shown in (c). The rightmost map in (d) shows that the ADU signals corresponding to the longest unsaturated exposure of each pixel within the same region are below saturation.

Following subtraction of the appropriate dark frame the best exposure, t_{best}, and signal, ADU_{best}, are then used along with the stored fit parameters to solve the polynomial response equation for the best estimate of the incident flux at each pixel, $F(x_{\text{i}}, y_{\text{j}})$ (e). Once this process has been followed for all pixels the full flux map is compiled (f).

5.5.1 Quoting the dynamic range of our technique

It is clear from the earlier discussion in Section 2.4.4 that dynamic range can be discussed for our instrument in several ways: in terms of the sensor itself; images created using the sensor in conjuction with successive-exposure-imaging; and indeed the overall output intrascene dynamic range of our HDR imaging procedure. In all cases a specific noise characteristic of the sensor needs to be quantified in order to proceed. The particular noise characteristic of our sensor that is required for such calculations falls into one of two categories. These categories differ in terms of the particular standard deviation (SD) of the output signal which is used to define the minimum resolvable signal S_{min} in our dynamic range calculations. The first option is to assess the SD of the temporal noise associated with both read-out (reset & thermal kTC, $1/\nu$ flicker) and shot noise (photon and dark signal) in each individual pixel. The second option is to attribute a SD to the spatial non-uniformities of the fixed pattern noise (FPN) signal across the sensor array.

The first option, *i.e.* assessing the temporal noise on our measurements, tells us of the reliability of our quoted mean signal when taken from measurements obtained using a single pixel and thus tells us only of the dynamic range for that pixel. To extend this description across the entire sensor array we would be required to determine the dynamic range for all pixels individually, and then quote the improved overall sensor dynamic range as an

average of these calculations. The large variations in noise behaviour across a CMOS sensor array could potentially cause the dynamic range between neighboring pixels to be significant, resulting in a wide standard deviation from the quoted average dynamic range across the sensor.

The second option effectively assesses the spread of the maximal dynamic range across the sensor. That is to say, the variation in signal headroom across the sensor in the absence of temporal fluctuations while taking the applied offsets and saturation levels into account. This could be assessed using dark frames taken at the shortest and the longest exposures used in our HDR imaging procedure. It is important to note that as this option does not take the temporal noise into account, taking a S_{min} as the SD of the offset signal in each pixel's output, the dynamic range calculated using this option is a somewhat over-simplified description of the sensor and our procedure's performance. Indeed, it would be erroneous to attribute this form of SD to the minimum resolvable signal S_{min}. Thus the first option is our preferred option for determining the dynamic range of both our sensor and our SEI procedure.

A full investigation of our HDR imaging procedure needs to take into account the entire sequence of signal manipulation: the recording and averaging of successive frames at each exposure duration and the subtraction of a mean dark signal from each of these exposures (both with associated errors due to temporal fluctuations which must be added in quadrature) and also errors in the flux value attributed to a digital signal recorded at a given exposure time due to imperfect calibration (where our mathematical description of the sensor's photoresponse deviates significantly from the calibration data, *i.e.* the residual error). This latter point ultimately imposes its own FPN upon our reconstructed HDR flux maps which is distinctly different from the inherent FPN associated with the sensor's signal output which was taken into account during calibration (*i.e.* calibration was performed on a dark-subtracted signal for each pixel).

The final consideration is whether or not to calculate and quote the dynamic range in terms of interscene brightness as reconstructed relative flux, or in terms only of the signal output in digital numbers. The most simplistic way to take the several noise sources and the errors invoked through calibration of our full HDR procedure is to simply quote the dynamic range (DR) in terms of this reconstructed flux:

$$\text{DR} = \frac{F_{\text{max}}}{F_{\text{min}}} \text{ [DN/s] (arbitrary linear flux scale) ;} \tag{5.5}$$

$$\text{DR} = 20 \log_{10} \left(\frac{F_{\text{max}}}{F_{\text{min}}} \right) \text{ [dB] .} \tag{5.6}$$

F_{min} can be taken as the standard error on our mean flux values calculated from the variation in our measured ADU signals. Unlike calculating the dynamic range in terms of signal output, the maximum signal here is somewhat arbitrary, unlike the hard limit on S_{max} set by the usable bit-depth of the sensor ADC. The maximum value of flux F_{max} used in the dynamic range calculation can take a number of values: we could use the upper limit imposed during our reconstructions of $F = 100$; we could use the highest flux value used during calibration of $F = 1$; or we could quantify the dynamic range of every individual reconstructed image by using the highest flux value in that particular flux map.

5.6 Results & Discussion

In this section the results of using our device and imaging/reconstruction procedure to profile various beam foci are presented. The first optical system profiled is a test bench setup. This was designed to assess the performance of our technique in reproducing a wide range of incident flux in terms of both magnitude and spatial distribution. We verify the ability of our imaging/reconstruction procedure to reproduce a wide range of incident flux with high accuracy and demonstrate the performance of our technique when applied to 3-D imaging. Following this, we present some 3-D profiles of microscope illumination beams taken using the device. First, orthographic sections of a 3-D SPIM beam profile are presented and conclusions regarding the limitations of our profiling device are made. Next, we present several 3-D beam profiles to illustrate the use of the device within operational LSM systems with various illumination beam geometries. A brief discussion follows each of the presented results; overall discussion of the limitations of, and improvements to, the probe and imaging/reconstruction procedure is left until the end of the section.

5.6.1 Test bench verification of performance

5.6.1.1 Verification of HDR flux reconstruction

The ability of our procedure to reliably construct HDR flux profiles was examined by comparing with theory the beam profile of a test-bench optical setup. A blue Gaussian laser beam (wavelength 488 nm) was fed through a single-mode fiber, then collimated and passed through an iris aperture, which was in turn demagnified by 3× using a telescopic 4-f relay and focused by a 5 mm diameter achromat lens (AC050-015-A-ML by Thorlabs, UK), of focal length of 15 mm, onto the camera probe. The iris was used to stop down the beam to enhance the effects of diffraction and increase the beam's focal waist diameter and Rayleigh length. An effective aperture diameter of D = 370μm, produced by an iris of diameter 1.1 mm, caused the achromat lens to produce a beam focus with a waist of w_0 = 13μm and a Rayleigh length of z_R = 1020μm. A sequence of 10 exposures ranging between 0.18–20.91 ms were taken of the beam: 0.18, 0.27, 0.45, 0.73, 1.09, 1.82, 3.27, 6.18, 11.82, and 20.91 ms. For each pixel the ADU signal for each exposure was taken from the arithmetic mean of 20 images.

Figure 5.11(a) presents the flux map resulting from our HDR procedure. The reconstructed HDR image demonstrates additional structure effects in the beam profile: the subsequent intensity maxima and minima of the diffraction pattern which stretch away from the central maxima appear along a discrete number of arms. In addition the so-called rings of the diffraction pattern appear to have a structure that tends more towards a polygonal shape than a circle. We attributed these features to the beam itself rather than as artifacts of the HDR reconstruction due to their appearance when monitoring the beam and in the single-exposure non-HDR images that were taken as part of the HDR dataset.

This presents the first limitation in our approach to verify the HDR performance using this particular test bench optical setup. The reduction in circularity can be attributed to the polygonal aperture shape formed by the blades of the iris aperture. Here we note that the

actual 2-D shape of the iris aperture was not recorded directly. The diffraction pattern formed at a lens focus represents the Fourier transform of the pupil aperture shape, thus the increased appearance of such arms is therefore expected when the pupil aperture shape tends towards a polygon rather than a perfect circle. If HDR verification were to be performed again using a similar setup it would be beneficial to use a fixed aperture of a known shape, preferably perfectly circular, in place of the iris.

It can be seen that some residual FPN remains in the background of the HDR reconstruction in two forms. These effects can be attributed to the limitations in our flux calibration that were discussed previously at the end of Section 5.4.2, specifically relating to the non-uniform noise characteristics of our CMOS sensor. Though it would be ideal to discuss these effects using a HDR reconstruction of a uniformly illuminated scene, their presence can be noted in Figure 5.11(a). It is important to note that the exposure duration which was chosen for HDR reconstruction in these background, low-signal, regions was that of the longest exposure duration, where the dark signal non-uniformity across the sensor becomes more apparent than at shorter exposures.

The first effect to be noted is the sequential horizontal regions down the sensor array where the background region displaying on average a higher signal than others. This distribution of fixed pattern noise is associated with the row/column circuitry on the CMOS sensor, depending on the orientation, caused by fabrication inconsistencies in the transistors common to each row/column used to deliver reset signals or provide read-out. The second effect to be noted is the variation in signal within these regions; there are a number of punctate bright pixels throughout the background which seem to be randomly distributed. This less-uniform source of noise is attributable to the fabrication inconsistencies between pixel-specific transistors which contribute to the PRNU across the sensor. In both cases the reason for the HDR reconstruction procedure failing to remove such FPN is down to the erroneous assignment of F at the longest exposure. As discussed in Section 5.4.2 this may be a direct limitation of our general mathematical description of the response in ADU vs. t_{exp} parameter space and may be remedied by an alternative, exposure-specific, calibration.

In Figure 5.11(b) a typical radial line profile outward from the focus is presented alongside a profile of the theoretical Airy diffraction pattern for this setup. The theoretical Airy profile was generated with a high spatial resolution and then sampled according to the 3 micron pixel pitch of the sensor array. This form of spatial sampling causes the theoretical Airy profile to take a mean value at every 3 micron interval along the radial coordinate r, thus demonstrating as an example the flux profile we would expect to see if the beam had been generated using a perfect circular aperture rather than an iris. Specifically we see that although the minima of our reconstructed beam profile do not reach down to negligible values of flux, such low values of flux may not necessarily be recorded due to the spatial sampling of the diffraction pattern by the dimensions of the pixel array. Though our comparison of the reconstructed HDR line profile with that of the theoretical Airy pattern utilises a familiar subject matter (the Airy pattern) to demonstrate the range of flux which was reconstructed using our HDR procedure, any direct comparison between the spatial structure of the theoretical beam profile

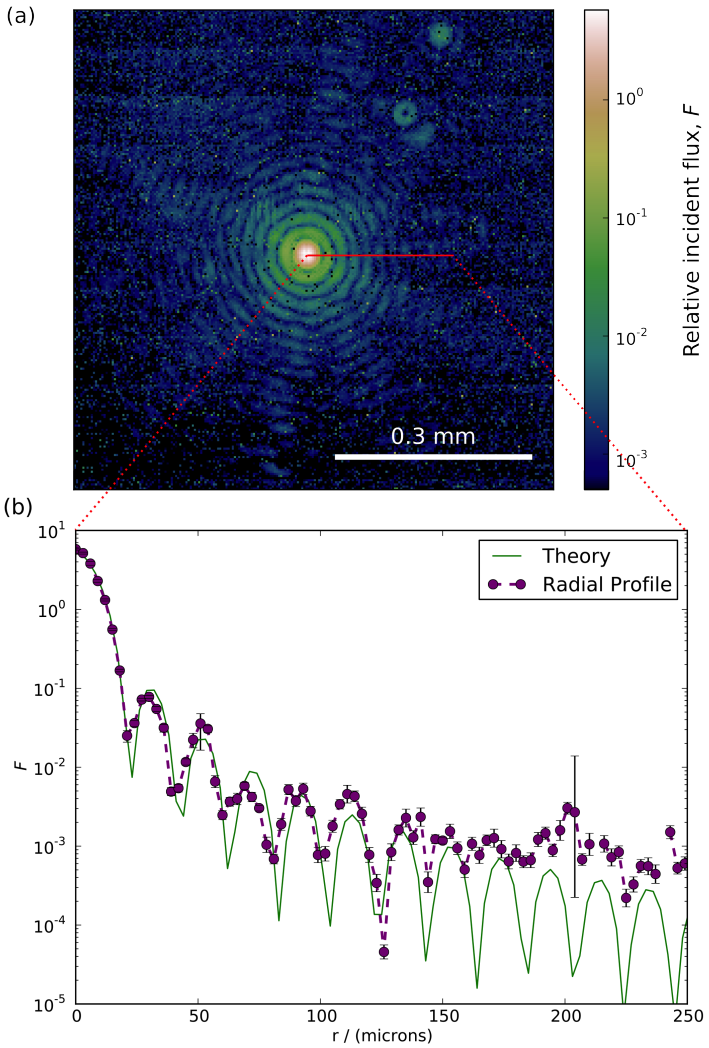

FIGURE 5.11: Verification of our HDR flux reconstruction procedure. The HDR flux map of a laser beam focus (presented in false-color, (a)) from a test bench setup is presented alongside the theoretical Airy diffraction pattern for the setup (b). Logarithmic scales are used to present the calculated flux on both the colourmap in (a) and the vertical axis in (b). The radial line profile in (b) demonstrates the capacity of our procedure to resolve a wide and continuous range of fluxes that are several orders of magnitude below the maximum recorded incident flux. Error bars correspond to the standard error on the ADUs used to determine incident flux.

against our own remains relatively arbitrary due to the spatial sampling of the full-resolution Airy pattern.

A better subject matter, or scene, that would allow a more thorough HDR verification would be one with controlled overall spatial variations in flux according to a well-known variation. This could be achieved through the use of graduated ND filters, linear interference gradients, or sinusoidal interference fringes. The benefit of using interference fringes is

that complete cancellation is expected to occur at the interference minima, so the maximum brightness can be made very large and thus HDR performance can be examined over a very large inter-scene dynamic range. However, a wide spacing of fringes would be desirable in order to avoid the dark interference minima being recorded as a higher mean flux due to spatial sampling by the pixel array, as emphasised above in our discussion of the test bench Airy beam.

5.6.1.2 Dynamic range: test bench

In order to test the accuracy of our HDR procedure we calculated the flux values corresponding to the standard error on the signal mean (in ADU) used in the creation of our reconstructed flux map image. This distribution of standard errors on the mean flux value were then used to calculate the dynamic range of the sensor across the array.

The interscene dynamic range has been calculated using the largest value of flux in the output reconstructed image, *i.e.* $F_{\max} = 5.80$. We took a 40×40 square area of pixels in one corner of the sensor as our sample, omitting any pixels where the reconstruction had been unable to assign a flux value where a value of $F = 0$ was returned, leaving a sample size of 1588 individual pixels. This particular area size was selected in order to span two of the row/column noise variations were present in the distribution.

Figure 5.12 shows the distribution of the interscene dynamic range across the sensor. The median interscene dynamic range in our reconstructed flux map sample is 91.3 dB. By selecting a sample area of our image that corresponds to background light rather than the incident beam we have chosen to investigate the smallest present standard errors on the mean flux. This stems from the fact that the longest exposure in the MES has been selected in these background regions and therefore the standard error on the mean ADU signal corresponds to a smaller range of flux than that which would correspond to the ADU error at shorter exposures.

As mentioned above, the choice of $F_{\min}$ is somewhat arbitrary. If we used our maximum allowed value of $F = 100$ then we shift the distribution of dynamic range up to a median value of 116 dB, and if we instead used the upper calibration value of $F = 1$ the distribution shifts leftwards to a median DR of 76.0 dB. We will use the most modest DR quantity, that of 76.0 dB, in a comparison of our HDR technique against that of a perfect 8-bit sensor, operated using SFA.

5.6.1.3 Comparison with single-frame-averaging (SFA)

We know from Equations 2.38 & 2.33 that the DR of a noise-free 8-bit linear-response sensor pixel with zero offset and operated using a N exposures is

$$\mathrm{DR} = 20 \log_{10} \left(\sqrt{N} \cdot 255 \right) \ \mathrm{dB} \, . \tag{5.7}$$

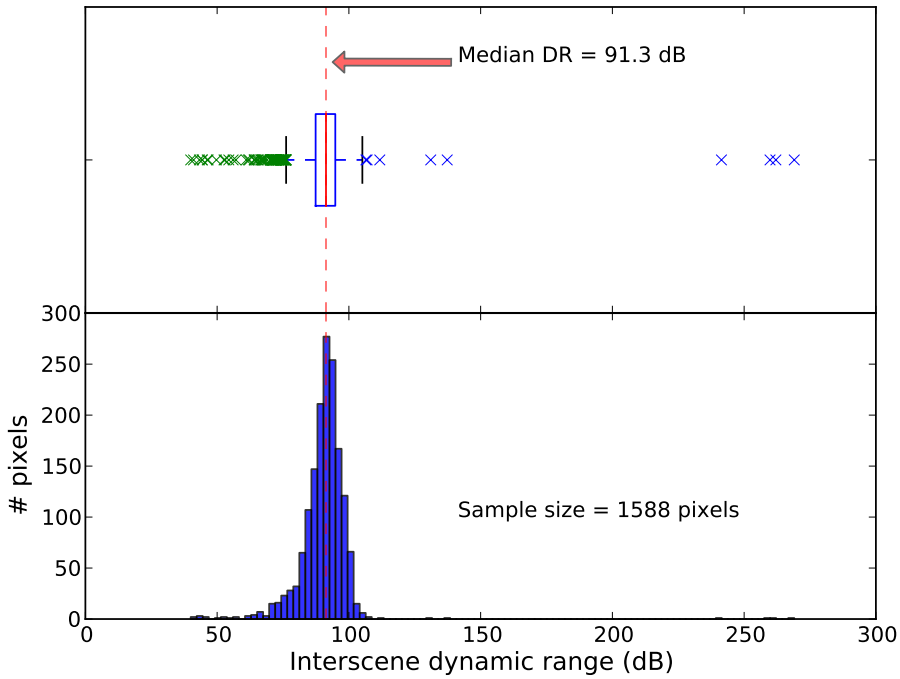

FIGURE 5.12: Interscene dynamic range of test bench beam flux map. The lower plot is a histogram showing the distribution of calculated interscene dynamic range values in units of decibels while the upper plot displays a box-and-whisker plot of the same data. The leftmost and rightmost limits of the box represent the lower and upper quartiles of the data and the red line between these represents the data median.

Comparing this with the most modest DR for our sensor we can calculate the number of SFA frames N required for averaging at the shortest exposure in order to achieve the same DR:

$$\begin{aligned} 76.0\ \text{dB} &= 20\log_{10}\left(\sqrt{N}\cdot 255\right)\ \text{dB} \\ \implies \sqrt{N}\cdot 255 &= 10^{\left(\frac{76}{20}\right)} \\ \implies N &= \left(\frac{10^{3.8}}{255}\right)^2 = 24.7^2 \\ &= 612 \text{ successive frames.} \end{aligned} \tag{5.8}$$

Our HDR imaging procedure took 10 successive frames at each of 10 exposure durations and thus took an overall number of 100 images. Therefore, successive frame averaging would have taken at least six times longer to achieve a DR equal to our most conservative DR of our HDR imaging procedure. However, a caveat exists here in that the output of the SFA procedure can be calculated rapidly using simple computational array calculations which is much faster than the pixel-by-pixel numerical flux reconstruction required by our HDR procedure.

5.6.1.4 Comparison with noise-free sequential-exposure-imaging (SEI)

Let's now compare the interscene DR of our technique with that of a noise-free linear-response 8-bit sensor, this time operated using SEI, taking images at the same exposure durations as our HDR procedure, and taking into account the same average number of usable bits as our sensor. The median offset across our sensor was 70 ADU, leaving us with a headroom of 255-70=185. In our HDR procedure we used a shortest exposure of $\Delta t_A = 0.18$ ms and a longest exposure of $\Delta t_B = 20.91$ ms. The ratio of these two end exposures is $\Delta t_B / \Delta t_A = 20.91$ ms$/0.18$ ms $= 116.17$. Thus, for a perfect 8-bit linear-response sensor, the dynamic range would be

$$\mathrm{DR} = 20 \log_{10} \left(\sqrt{N} \cdot 116.17 \cdot 185 \right) \text{ dB} . \tag{5.9}$$

Therefore, in order to achieve the same interscene DR:

$$\begin{aligned} 91.3 \text{ dB} &= 20 \log_{10} \left(\sqrt{N} \cdot 116.17 \cdot 185 \right) \text{ dB} \\ \implies \sqrt{N} \cdot 116.17 \cdot 185 &= 10^{\left(\frac{116}{20}\right)} \\ \implies N &= \left(\frac{10^{4.57}}{116.17 \cdot 185} \right)^2 = 1.71^2 \\ &= 2.92 \text{ successive frames.} \end{aligned} \tag{5.10}$$

Now, as mentioned before, our HDR technique takes 10 successive frames at each exposure. Thus the above calculation suggests that fewer frames would be required for the same DR using a linear-response 8-bit sensor in the absence of noise.

It is important to emphasise here that the behaviour of our particular sensor is quite far removed from that of a perfect sensor: there is indeed a substantial amount of read noise present when using the sensor and this read noise is highly non-uniform across the sensor array; and the photoresponse of the sensor is non-linear, exhibiting an unusual flux-dependent offset at the shortest exposures. As such, the above similarity between N for our technique with both our sensor and a hypothetical sensor demonstrates that the overall performance of our HDR system is not dissimilar to that of a noise-free sensor. That is to say, our flux calibration and reconstruction using averaged signals restores the performance of our noisy sensor.

5.6.1.5 Verification of 3-D beam profiling

To allow 3-D profiling the mounted sensor was affixed to a compact micro-translation stage (M111.1 [163] by Physik Instrumente (PI), Karlsruhe, Germany) and scanned along the optical (z) axis of the beam being imaged. The z=0 plane corresponded to images taken at the closest proximity to the focusing lens. Using the same test bench setup as before the sensor was scanned through a 1.0 mm axial extent of the beam focus, taking images using the same 10 exposure durations at each of 90 z-positions throughout the focal volume. The 3D profile was thus comprised of volume elements of uneven dimensions (anisotropic voxels) of $3\mu\text{m} \times 3\mu\text{m} \times 11.11\mu\text{m}$. To speed up image acquisition only one image was taken for each exposure: no arithmetic averaging of the recorded ADUs took place. Orthographic sections through the central axes of the reconstructed 3-D beam profile are presented in Figure 5.13.

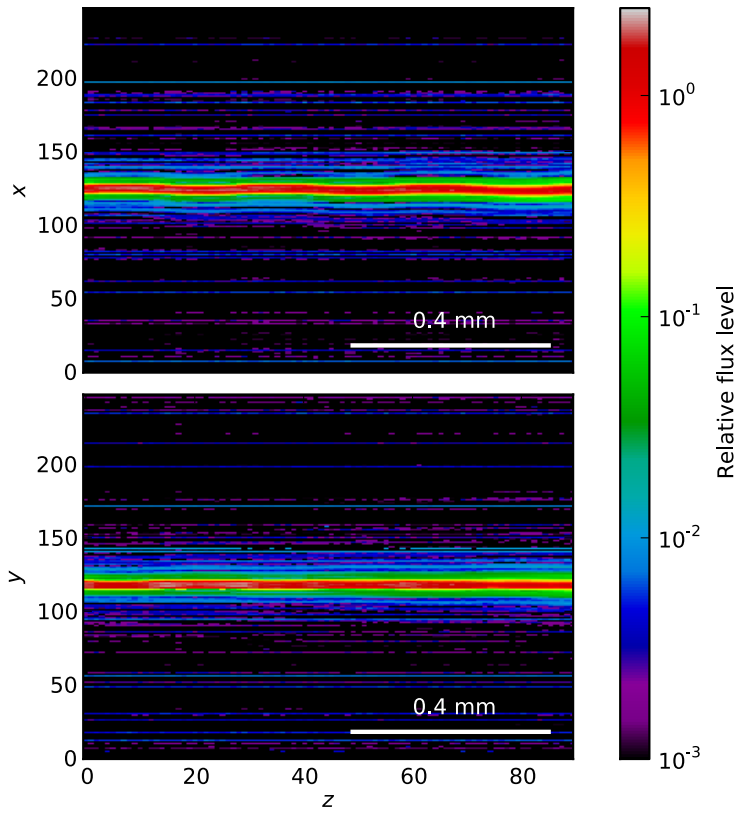

FIGURE 5.13: Orthographic x-z and y-z sections along the optical axis of the test bench beam focus. The colourmap corresponds to the reconstructed flux for each voxel and is presented on a logarithmic scale. The x, y, and z coordinates correspond to the voxel coordinates of the beam profile. The scale bar is 0.4 mm and both sections are presented with a 1:1 aspect ratio. In the x-z section a periodic lateral oscillation of the order of one pixel is apparent.

The long Rayleigh length of the stopped-down beam caused the focal profile to resemble a small-diameter pencil beam, *i.e.* a collimated beam exhibiting low-divergence. The upper section displayed in Figure 5.13 demonstrates a small lateral 'wobble' in the x-z plane. To investigate this effect further the centroid of the reconstructed flux was calculated for each slice in this plane and then plotted against z, as shown in Figure 5.14. Two features became apparent:

1. The wobble of the beam appeared to be periodic, potentially sinusoidal;
2. The beam had an overall linear mis-alignment between the z-axis of the translation stage and the optical axis of the test bench beam.

A function taking these two features into account, $x = a\sin(2\pi z/Z) + m\,z + c$, was then fitted to the centroid graph where a describes the spatial amplitude of the periodic wobble, m describes the linear gradient or 'tilt' of the beam across the profile, Z is the spatial period of

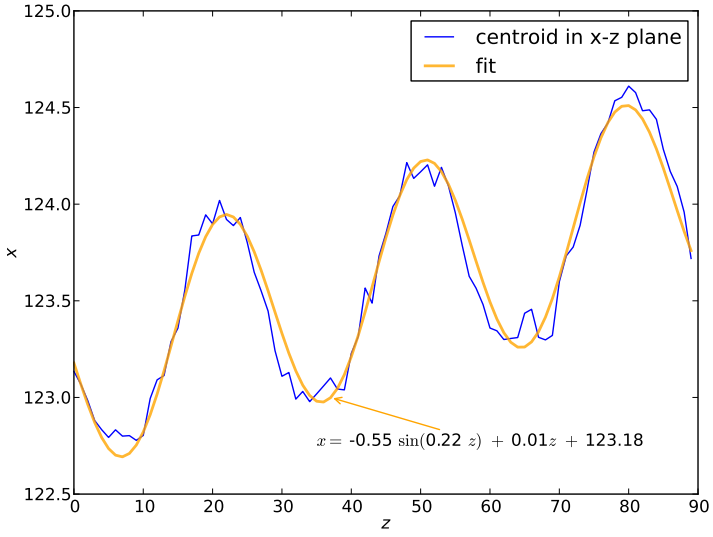

FIGURE 5.14: The central intensity oscillation across the x-z orthographic beam profile slice presented in Figure 5.13, calculated via centroid. Both a linear and an sinusoidal motion were found to be present. The mathematical form of this function is annotated on the graph and described in the main text. The x and z coordinates correspond to the voxel coordinates of the beam profile.

the function, and c is a sensor array coordinate offset. A least squares fit to these centroids was given by $x = -0.55\sin(0.22\,z) + 0.01\,z + 123.18$. The spatial period was thus calculated as $Z = 2\pi/0.22 = 28.6$ in units of the z-coordinates of the beam profile, corresponding to a physical distance of 317μm. As the pitch of the leadscrew was given as 0.4 mm to 1 decimal point by the manufacturer we attributed this periodic motion to a defect in the leadscrew driving the translation stage.

5.6.2 Device operation within operational microscope systems

An optical layout describing all three of the microscope systems in this section is profiled in this section is presented in Figure 5.15. Labels of (a), (b), and (c) have been used to annotate the optical components that differ between the illumination optics and refer to the SPIM, dual-wavelength SPIM, and beam-switched Bessel vs. Top Hat microscope systems respectively. In the following reconstructions the beam profiles were recorded using the same range of 10 exposures between 0.18–20.91 ms used for performance verification.

Figure 5.16 shows orthographic sections through the 3-D profile of a water-submerged SPIM illumination beam. Only one image was taken per exposure in order to speed up the overall profiling duration, as was also performed in the verification of 3-D beam profiling in Section 5.6.1.5. The combined device and translation stage were mounted over the SPIM water tank with the illumination laser beam (wavelength 488 nm) incident on the face of the sensor

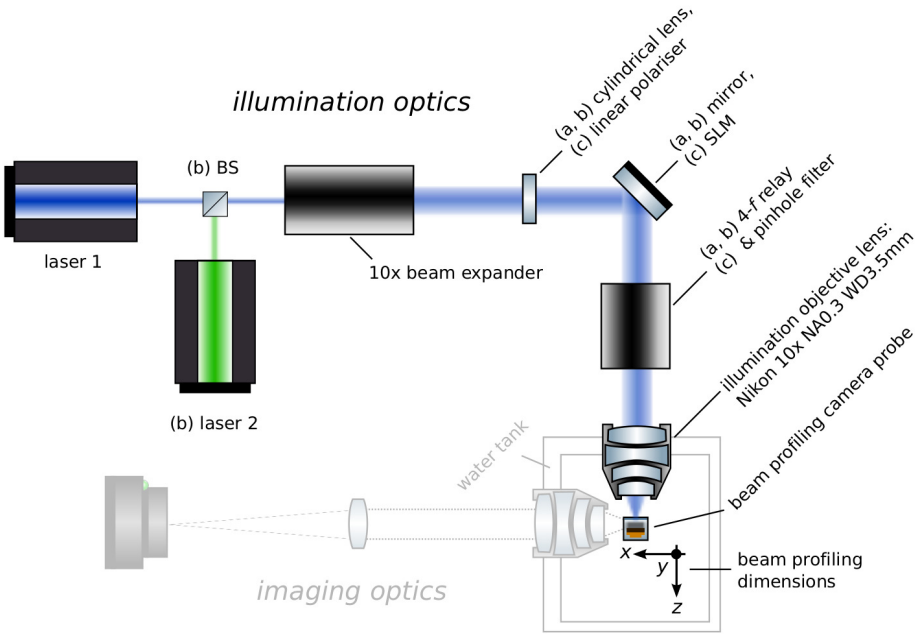

FIGURE 5.15: Illumination arm optical layout for the microscope systems profiled in this section. The imaging optics have been included as a watermark to demonstrate their relative position to the illumination optics. Labels of (a), (b), and (c) have been used to annotate the optical components that differ between the microscopes profiled in this chapter. These refer to a SPIM, dual-wavelength SPIM, and beam-switched Bessel vs. Top Hat microscope systems respectively. For both SPIM systems the cylindrical lens forms a light sheet focus at the mirror which is conjugated via a 4-*f* relay to the rear aperture of a water-dipping microscope objective lens. For the beam-switched microscope system a linear polariser is used in place of the cylindrical lens and a spatial light modulator (SLM) is used in place of the mirror. A 400 micron pinhole was placed at the focus of the 4-*f* relay to block unwanted diffracted orders from the SLM for system (c).

and images were taken at 90 z–positions over a range of 1.0 mm along the optical axis of the illumination beam. The reconstruced beam profile thus had anisotropic voxel dimensions of $3\mu\text{m} \times 3\mu\text{m} \times 11.11\mu\text{m}$.

The logarithmic spectral colourbar with which the orthographic sections in Figure 5.16 are presented allows a number of conclusions to be made regarding both our profiling system and the SPIM itself. Our results demonstrate the success of our beam profiler in reconstructing a wide range of fluxes over a volume much larger than the focal region of the beam from a relative flux magnitude of 10 down to 10^{-3}. Low relative flux from 10^{-2} down to 10^{-3} is constrained to the regions outside of the beam focus in the x-z plane and is visibly affected by noise. Fixed pattern noise is clearly present throughout the entire x-z plane at flux levels of around 10^{-2}, represented as light blue down to navy blue on the colourbar. Below this, flux

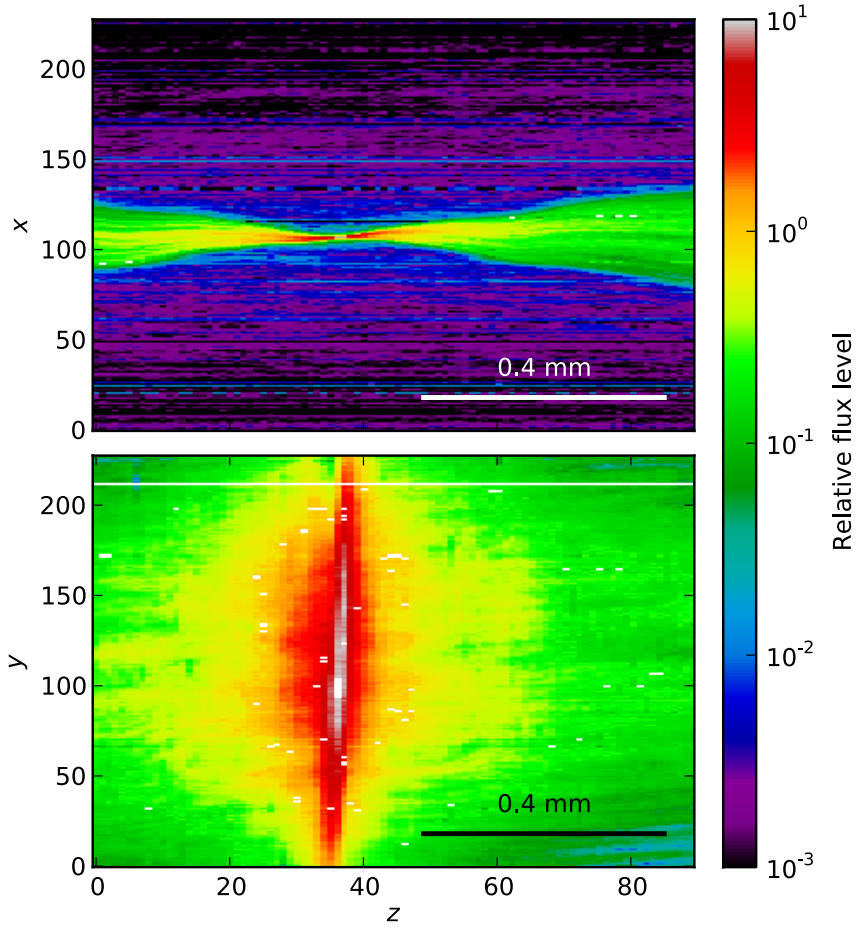

FIGURE 5.16: Logarithmic false color x-z (upper), and y-z (lower) sections through a 3-D HDR flux profile of a SPIM illumination beam within a water tank. The full 3-D profile is presented in Figure 5.17. The x and y scales correspond to pixel coordinates across the sensor; the z scale refers to the coordinates of each slice within the image stack along the optical axis – the closest plane to the focusing objective lens is at $z = 0$.

levels of around $10^{-2.5}$ and lower are present in the form of a general background surrounding the beam, represented as purple on the colourbar. Also visible in the y-z plane are a number of individual "hot" voxels outside of the beam focus that are shown in white. Apparent in both x-z and y-z sections are lateral amplitude variations within the beam between relative flux levels of 10^{-1}–10^{0} that suggest diffraction within the illumination optical train produces a considerable contribution to the beam profile. In addition to this there is an asymmetric transfer of flux across the focus in the x-z plane suggesting that the illumination beam may not be perfectly aligned to the optical axis of the lenses used. Also in the x-z plane is a small periodic lateral transit of the beam in x as the beam propagates along z. This was attributed to the lateral motion of the translation stage caused by the rotating leadscrew pitch, identified in the previous section as a non-optical effect.

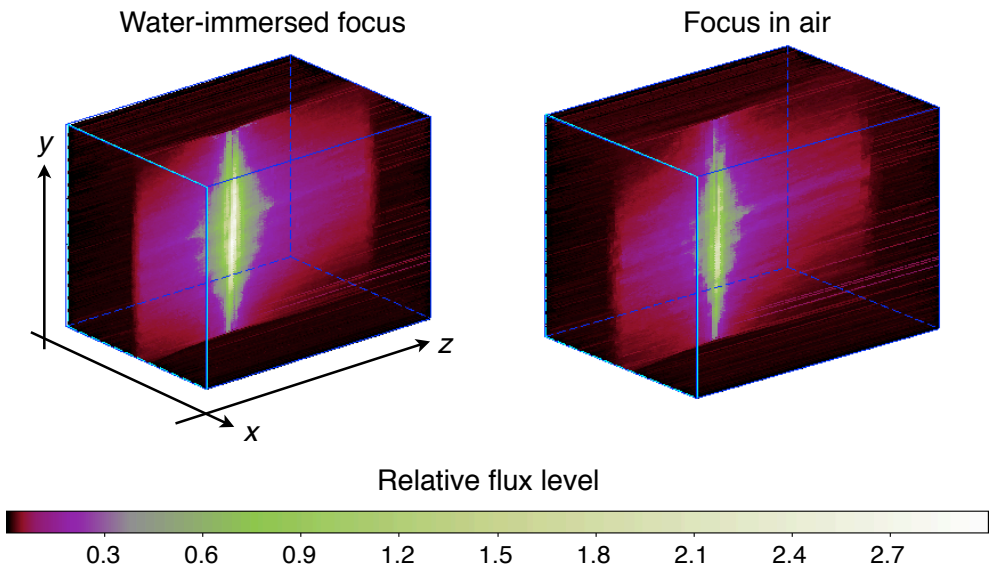

FIGURE 5.17: 3-D beam profiles of a SPIM system illumination beam in both water and air. The overall profiled volume has dimensions of 0.74 mm × 0.74 mm × 1.0 mm ($x \times y \times z$ respectively). The observation imaging plane of the SPIM witness fluorescence excited by the illumination beam as it is shown here in the y-z plane of these beam profiles.

Figure 5.17 presents the full 3-D profile of the previous SPIM beam alongside a beam profile from the same microscope but with the water tank drained. The beam profiled in air does not have as smoothly-fluctuating a beam profile as the water beam. As planar refractive index mis-matches typically introduce spherical aberration, artifacts that are visible within the beam profile when using water-dipping lenses in air, instead of water, are expected.

Figure 5.18 shows 60-slice beam profiles taken within the water tank of a dual-wavelength SPIM microscope over a 1.0 mm axial range. Again, only one image was taken per exposure to reduce the overall profiling duration. The anisotropic voxel dimensions of these profiles was $3\mu\text{m} \times 3\mu\text{m} \times 16.67\mu\text{m}$. In this system two separate laser light sources were directed through the same illumination optics to provide illumination that could excite two types of fluorophore at once or switch between the two. Thus, for the microscope performance to be matched at both wavelengths, the illumination beam profiles required alignment and similar focal dimensions. The illumination beam wavelength was 488 nm in the leftmost reconstruction and 532 nm in the rightmost reconstruction. The beam profiles of both beams share the same overall dimensions and focal location, though there are visible differences in their flux profiles in the centre of the sheet along z and down the focus of the sheet along y, both in the y-z-plane.

In Figure 5.19 the profiles of two illumination beam geometries are presented for comparison both with (leftmost profiles) and without (rightmost profiles) water immersion of the beam. In this microscope system a SLM was conjugated to the pupil of the illumination

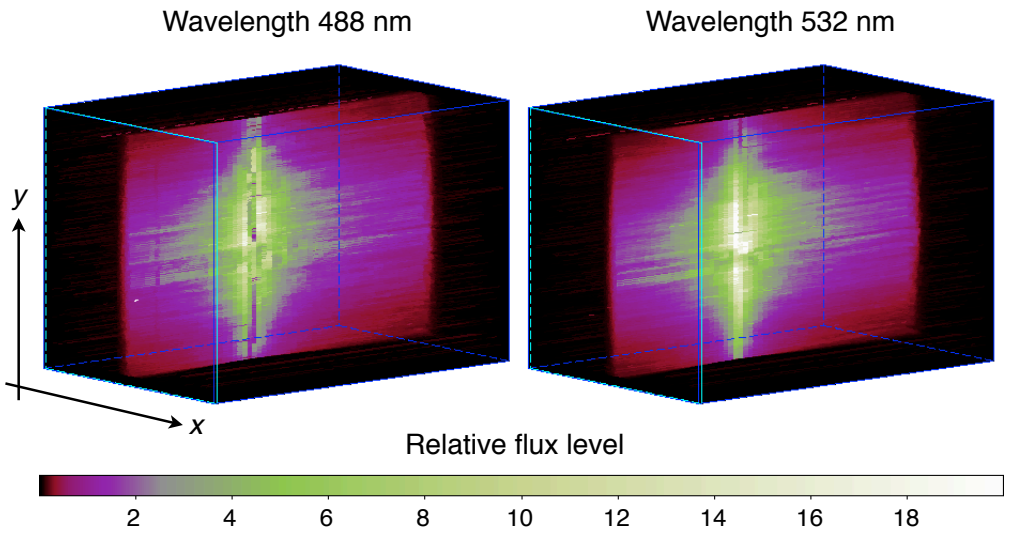

FIGURE 5.18: Reconstructed beam profiles taken within a dual-wavelength SPIM system. The colourbar represents the incident flux level, relative to the uniform fluxes used in the calibration of the sensor. The left profile was taken with the blue laser illumination (wavelength 488 nm) and the right profile was taken with the green laser illumination (wavelength 532 nm). The light sheets are well-aligned within the focal volume and have the same height, thickness, and length dimensions. The overall profiled volume has dimensions of $(x \times y \times z)$ are 0.74 mm $\times$ 0.74 mm $\times$ 1.0 mm.

objective and switched between axicon and uniform phase patterns to alter the illumination between Bessel and top hat beams. A phase slope was added to the desired phase profile and a 400 μm pinhole was used within the 4-f relay to filter out unwanted orders of diffraction from the SLM. The phase slope was only applied to a circular region of the SLM array. Hence, the light reflected from the SLM outside of this circular region was blocked by the pinhole. Thus, a circular aperture was effectively applied to the applied phase maps. A wavelength of 532 nm was used - the design wavelength of the chosen SLM. These beam profiles were taken over a 4.0 mm axial range, four times larger than the axial ranges used for the previous beam profiles. 60 z-slices were taken, producing anisotropic beam profile voxels with dimensions of 3μm $\times$ 3μm $\times$ 66.67μm. In this case five images were taken and arithmetically averaged to produce a mean ADU value for each exposure. The reconstructions clearly demonstrate the extended focal depth of the Bessel beam illumination compared with that of the top hat illumination beam. Additionally, the profiles taken without water immersion demonstrate a distinct deviation of the beam direction and relative flux magnitude when compared with the water-immersed beam profiles.

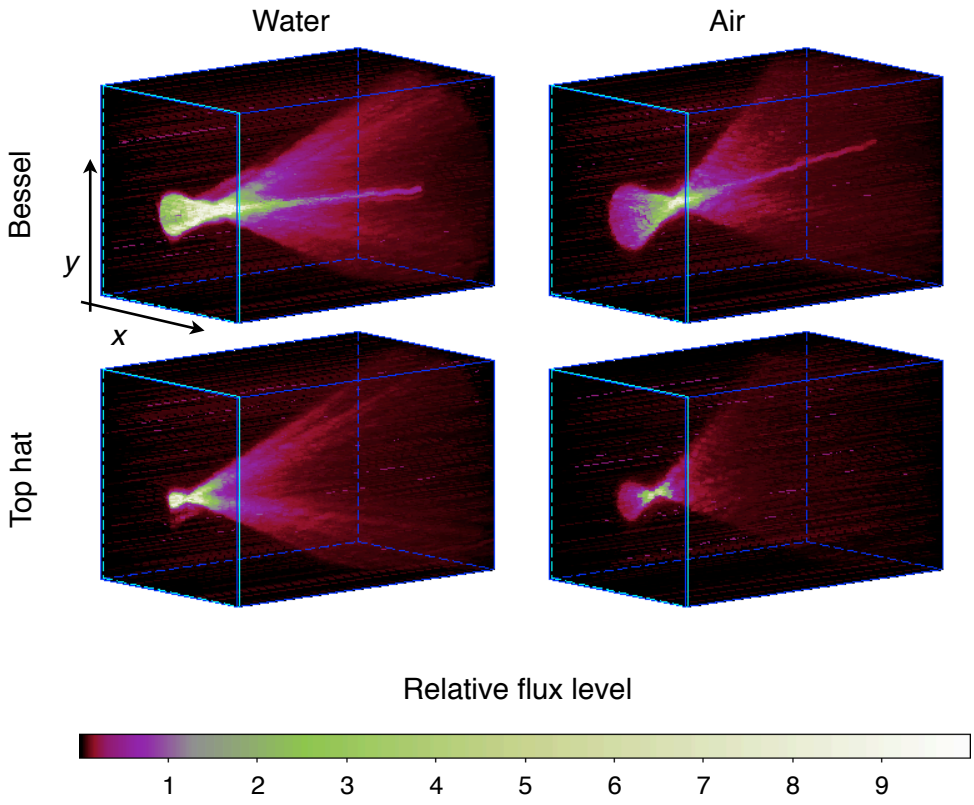

FIGURE 5.19: Reconstructed beam profiles taken within a microscope with switchable illumination beam geometry. The Bessel beams (top) feature a bright focal region which is greatly extended along z compared to the top hat beams (bottom). The overall profiled volume has a larger axial extent than the other results, with dimensions of ($x \times y \times z$) are 0.74 mm $\times$ 0.74 mm $\times$ 4.0 mm.

5.6.3 Overall Discussion

The discussion in this section contains comments upon three key areas: the limitations placed on our beam profiles by our chosen sensor; the imaging rate limitations imposed by our software and imaging procedure; and final remarks concerning our system in regard to other profiling methods.

5.6.3.1 Comments on the sensor technology

The sensor that comprised our beam profiling probe had several drawbacks, in addition to the benefits we cited for its selection in Section 5.3.1. One set of limitations concern the physical limitations of the device itself in profiling small-volume foci, the second set concern the overall quality of the 3-D beam profiles taken with our HDR technique.

Sensor resolution The lateral resolution of our system is limited by the 3μm lateral pitch of the sensor array. As such, small diameter foci below 3μm are not well-resolved. The direct profile resolution could therefore be improved by using a sensor with a smaller pixel pitch, though at the time of writing there appears to be no miniature CMOS sensors commercially available having considerably smaller pixels than those of our chosen sensor; as such the lateral resolution of our direct beam profiling method is limited by the available technology to the order of around 3 microns. Although the axial resolution of our resulting 3-D reconstructions was intentionally coarse in order to demonstrate the wide range of fluxes across the beam focus that could be reconstructed by our system, a simple reduction of the axial z-scan range and an increase in the number of imaged slices can easily produce beam profiles with isotropic reconstructed voxel dimensions of $3\mu\text{m} \times 3\mu\text{m} \times 3\mu\text{m}$. Additionally, replacement of the translation stage used with one exhibiting less lateral motion would immediately improve the quality of the reproduced beam profiles, allowing the attribution of all apparent flux variations solely to optical effects within the beam itself.

Sensor performance The success of our HDR procedure was limited in two ways by the electronic behaviour of the 8-bit sensor used for the camera probe. First, in order to avoid clipping of low signals a high offset was applied between the analogue input signal and the digital output signal. This reduced the full dynamic range of some pixels to 150 ADUs. Second, the unusual non-linear performance of the chip required our custom flux response equation to describe the sensor response in ADU vs. t_{exp} parameter space. Pixels where this did not adequately describe the performance were therefore assigned a flux value of zero when a solution could not be found or unintentionally assigned an erroneous flux value, especially in the case of low incident flux. Both points come down to the quality of the sensor chip itself, and are therefore issues which will remain for similarly-constructed devices until sensors with a more homogeneous and predictable performance are manufactured with a similarly long read-out cable and miniature footprint. We predict that the use of such a sensor in accordance with our HDR methodology would produce beam profiles with even less fixed-pattern noise and fewer "hot" voxels. A sensor with a greater bit-depth inherently possesses a far greater dynamic range than that which was available when using an 8-bit sensor.

5.6.3.2 Comments on sensor calibration and HDR flux reconstruction

An overall improvement of the 'quantitative' aspect of our HDR procedure remains based in the calibration of the sensor. A wider range of incident uniform flux, from high levels causing saturation at even the shortest exposures down to a very controlled range of low-light levels, which is associated with measured beam powers rather than our 'relative incident flux' arbitrary units, could allow a more reliable fit for our flux response equation.

It is worth noting that there is an uncertainty associated with the flux values used during calibration as the calibration flux values were calculated using the quoted optical density (OD) of the ND filters. Therefore one might expect this uncertainty to have an impact upon the

quality of our calibration. For our ND filters the manufacturer's quoted error on the optical density ranges from ±0.01 for the lowest optical density of 0.2 up to ±0.1 for the highest optical density of 2.0.

For a function $z = f(x)$ the error in z caused by the error in x is given by

$$\delta z = \left| \frac{d}{dx} f(x) \right| \delta x \ . \tag{5.11}$$

Transmission is given by $T = 10^{-\mathrm{OD}}$, so for the above equation we assess the function $f(x) = 10^{-x}$. The absolute value of the derivative of $f(x)$ is $|f'(x)| = x \cdot 10^{-(x+1)}$. Therefore we have

$$\delta z = x \cdot 10^{-(x+1)} \delta x \ . \tag{5.12}$$

The relative error in z is given by

$$\begin{aligned} \frac{\delta z}{z} &= \frac{x \cdot 10^{-(x+1)} \delta x}{10^{-x}} \\ &= 0.1 \cdot x \cdot \delta x \end{aligned} \tag{5.13}$$

Using the manufacturers quoted errors for our ND filters, the relative error in our calculated transmission, and thus flux, values ranges from 0.02% for the lowest OD of 0.2 ± 0.01 up to 2% for the highest OD of 2.0 ± 0.1. The corresponding transmissions and their calculated uncertainties are therefore $6.3 \times 10^{-1} \pm 1.3 \times 10^{-4}$ and $1.0 \times 10^{-2} \pm 2.0 \times 10^{-4}$ respectively. In both cases the errors in T are at least two orders of magnitude smaller than the values of T and are therefore unlikely to negatively impact upon our calibration accuracy.

Here it is worth noting that the manufacturer's quoted errors are specified for a wavelength of 633 nm. The transmission of all ND filters exhibits spectral variation and therefore the quoted ODs may be different in our calibration setup using a 470 nm light source. However, our set of ND filters are designed to provide the same relative transmission between them across the visible spectrum. That is, use of the filters at a different wavelength than 633 nm will globally shift all transmittance by the same amount, *i.e.* all transmissions are affected equally. Thus, while the calculated transmissions may overall be wrong, the validity of their use as a calibration set remains true.

If, however, this spectral behavioural uniformity was somehow not the case then the calibration would need to be made more thorough by experimentally measuring the transmission of each ND filter at the appropriate wavelength. If there was indeed a filter that was assigned an erroneous transmission value then this may affect the reliability of the flux calibration. However this could be combated by making the filter transmission values variables in the calibration and first calibrating each to one another. The calibration could indeed be made more thorough by experimentally measuring the transmission of each ND filter, though this may not improve the overall outcome of our HDR procedure as we are only interested in relative measurements of the incident flux.

As an alternative to assessing the sensor's flux response across ADU vs. t_{exp} parameter space, where the combined effect of PRNU and increased dark signal on the CMOS chip at long exposures can cause difficulties in obtaining a general solution, the sensor response

could instead be assessed for each individual exposure duration. This re-calibration might provide a more adequate mathematical description of the sensor's flux response, further improving the accuracy of reconstructing very high fluxes at short exposure durations and very low fluxes at long exposure durations.

Whatever calibration parameters are chosen to describe the flux response, any future quantitative HDR beam profiles can be re-calculated using the same image data already taken. Overall though, our performance verification demonstrates the general success of our polynomial flux response equation in reconstructing a wide range of incident flux, despite the limitation to 'well-behaved' pixels. To truly determine the accuracy of our HDR calibration and reconstruction algorithm we suggest further analysis using several known intensity patterns projected directly onto the sensor array, such as a lateral wedge, or sinusoidal intensity fringes, having a large inter-scene dynamic range.

5.6.3.3 Comments on the imaging rate

The main obstacles to using our device and procedure in real-time, as would be required for either live-feed or 'snapshot' beam profiling, are both the image acquisition speed and the reconstruction procedure. Limitations were imposed upon both by our software. For the different SPIM beam profiles presented in Section 5.6.2 only one image was taken per exposure in order to speed up the image acquisition time. Due to our use of Awaiba's proprietary imaging software, the maximum rate that images could be acquired was 1 Hz due to their time-stamp convention. The automation software we developed to control the Awaiba imaging software also had an adverse effect on the imaging rate. To acquire a single image at each of our ten chosen exposures took an overall duration of 25 seconds. Thus, a total imaging duration of around 25 minutes was required to capture the data for a 60 slice beam profile when recording only one image for each exposure duration. With custom software communicating with the sensor image acquisition could potentially be pushed to much higher frame rates. Thus many more images could be acquired within a given time frame to provide reconstructions with the arithmetic mean of several images for a given exposure duration, reducing noise artifacts and increasing the reliability of reconstructions. However, both live-feed or snapshot beam profiling would still be inhibited by the numerical root-finding reconstruction procedure required for each pixel.

It is worth noting that the software for the presented reconstructions was written in Python 2.7 and compiled using a dual-core 2.3 GHz Intel Core i5 Apple MacBook Pro with 4 GB of 1333 MHz DDR3 RAM. The code itself was in no way optimised for speed. As such, the inverse numerical determination of F for each pixel took around 2 minutes for each pixel of the 250×250 sensor array, about 2 ms per pixel. This meant the full-sensor-array 60 slice reconstructions presented earlier required a reconstruction time of around 2 hours. For beams with a smaller cross-section the reconstruction could be restricted to a specific area of the sensor array. This would reduce the reconstruction time linearly with the number of pixels for which a solution for F is being found. If the reconstructed cross section was only across one third of the sensor array a 60-slice reconstruction duration could therefore be reduced

down from 2 hours for the full array down to around 13 minutes. A 'real-time' reconstruction of the order of 2 seconds would require there to be only 1000 pixels in the region of interest. Hence a limit on the number of voxels in the reconstruction would need to be combined with optimised code performance to allow beam profiles with a reasonable number of voxels to be created on short time scales.

5.6.3.4 Final remarks

Whilst the previously mentioned drawbacks certainly apply to quantitative beam profiles recorded and reconstructed using the device, a major benefit of having a camera probe that is small enough to sit directly within the beam is the ability to *monitor* the beam in real-time with a live-feed, regardless of quantitative 3-D reconstructions. Parts of the optical train can be adjusted and replaced whilst the beam focus, or different parts of the beam entirely, are monitored using the probe. The device could also be used in conjunction with adaptive optical elements and rapid image acquisition software to allow adaptive correction of aberrations or focal shaping of the illumination beam.

The benefit of recording the beam profile directly is that limitations imposed by additional optics, for example the imaging arm of a SPIM, are removed. For example, the volume of a SPIM illumination beam profile recorded using fluorescent beads is limited by both the field of view and depth of field of the imaging optics, setting the observation volume. The ability to monitor the beam focus over a much larger volume than this allows detection of stray light, diffractive effects, and distortions, that might otherwise have been overlooked. Though the imaging capabilities of the system will predominantly be affected by artifacts present in the illumination beam solely within the observation volume, the ability to image the beam throughout a wider volume allows the propagation of these artifacts to be examined.

Additional to the camera probe itself, the quantitative HDR imaging procedure presented in this chapter can be used with any CMOS camera. Thus, the HDR imaging procedure could also be implemented separately on the detection camera system to extend the dynamic range of a fluorescent bead profile. Coupling this with a large-volume profile taken using the camera probe and composite HDR beam profiles could be constructed with improved spatial resolution at the beam focus.

Finally, as the components of our profiling system are simple and compact, and the calibration and HDR imaging solution presented are general and flexible, devices similar to ours could be constructed and implemented with ease by those wishing to directly profile beams within any similar optical system. As the technique allows accurate amplitude profiles either side of a beam focus to be constructed, the technique may be well-suited to phase diversity techniques to determine the aberrations present in the illumination beam or to resolve the beam shape at the focus through complex field propagation from either plane back to the focus. Of course, this is not solely limited to microscope beam profiles since the device is capable of profiling any low-power visible-wavelength beam within a small focal volume. As a final example, the system may find alternative uses in profiling the foci of fiber-coupling assemblies or animal ocular lenses.

5.7 Conclusions

Numerous fluorescence microscopy techniques rely on specific illumination beam shapes to create high resolution, optically sectioned images. As the performance of these techniques is directly affected by the illumination beam shape, it is desirable to create 3-D profiles of the beam's focal intensity for both alignment purposes and the assessment of optical performance. Though fluorescent beads are typically used to produce illumination beam profiles by recording fluorescent emission along the microscope system's imaging arm, such profiles are limited by the detection optics. We have developed a camera beam probe and HDR imaging/reconstruction procedure that allows the full intensity profile of illumination beams to be recorded directly within the microscope without the need for any additional optics. This device is comprised of a miniature endoscopic sensor encased in a waterproof housing; the HDR imaging procedure allows quantitative measurement of the incident flux over several orders of magnitude on a pixel by pixel basis. The accuracy of this HDR reconstruction procedure has been examined by profiling a low NA test bench beam and the device has been used to profile the illumination beams of several operational microscope systems.

The most modest calculation of the interscene dynamic range that can be resolved by our HDR technique has a median of 76.0 dB across the sensor, far greater than the 48.1 dB dynamic range of a noise-free 8-bit sensor. 612 images would need to be taken using such a sensor in order to achieve the same dynamic range through successive-frame-averaging, whereas our technique only requires 100. Thus our HDR technique can achieve a large dynamic range whilst remaining data-efficient. The maximum interscene dynamic range that can be resolved using our HDR procedure is 116 dB.

Though the performance of the device is limited by presently available technology, our HDR flux reconstruction procedure is highly general and thus not limited to our specific hardware. Camera probe beam profiles could potentially compliment HDR fluorescent bead profiles to allow composite 3-D beam profiles to be created that possess both large volumetric dimensions and increased spatial resolution at the beam focus over a wide quantified range of flux. A thorough optimisation of the computational reconstruction procedure could potentially allow HDR beam profiles to be created in real-time for an instant assessment of microscope performance during alignment or optical component alteration. The application of our device and procedure is not limited to fluorescence microscopy and could be beneficial in determining the performance of other optical systems with short focal length beam foci.

Light sheet illumination with a curved focus 6

6.1 Introduction

In this chapter we demonstrate the use of a spatial light modulator (SLM) to produce a custom-shaped illumination beam with a focal geometry appropriate for use in a single/selective plane illumination microscope (SPIM). First, we present a short theory section that outlines the potential benefits of using an adaptive optical element rather than a cylindrical lens to produce a line focus. After deriving the phase profile required to produce such a focus we describe the alterations that can be applied to it in order to introduce and exploit an intentional one-dimensional (1-D) field curvature to produce a non-planar SPIM illumination beam.

Second, we present our methodology. The initial portion of the methodology investigates the focus formed directly by a SLM. We begin by describing the operation of a SLM as a phase control device and describe the appropriate conversion procedure from the calculated phase profile to the digital pixel values sent to the SLM. Following this we present images of a line focus produced by a SLM alone and demonstrate how the the application of an additional phase slope or blazed grating can spatially separate the line focus from the unwanted optical throughput caused by reflection off the SLM array. Next, we demonstrate use of the SLM to produce a simple alteration to the focal length of the light sheet in only a specific region across its height.

In the latter portion of the methodology we investigate the use of a 4-f telescope system to re-image the focus formed directly by the SLM in order to produce a light sheet with an adaptable 1-D focal curvature at the scale appropriate for a SPIM. We refer to a SPIM system having an illumination beam with an adaptable focal curvature as an adaptively-curved SPIM (A-SPIM) system. To verify that the focal geometry of such a beam is adequate for use in a SPIM we examine beam profiles of the focus taken using our camera probe, discussed

earlier in Chapter 5. These beam profiles exhibit some visible artifacts that we attribute to unwanted lateral movement of the camera probe, the majority of which are reduced by laterally re-aligning the voxel coordinates of the beam profile data-sets.

We then assess the dimensions of our A-SPIM light sheet illumination where the focal length has been altered spatially along the height of the light sheet according to a Gaussian amplitude variation. These light sheets possess focal region dimensions which promise enhanced optical sectioning of cellular features with curved surfaces. Finally we discuss potential improvements to the technique and summarise our results.

6.2 Theory

6.2.1 Optical sectioning in a SPIM

The optical layout for a SPIM has been presented earlier in Chapters 2 & 5. In summary, fluorescence is excited within the sample by an illumination beam which propagates perpendicular to the axis of detection. A cylindrical lens is used to focus a collimated illumination laser beam in one lateral dimension, producing a sheet of light at the beam focus that excites only a thin plane within the sample. Alignment of this excitation region with the focal depth of the orthogonal detection objective lens allows optical sections of the sample to be recorded. A 3-D image of the sample can be produced by scanning the sample through the beam along the detection optical axis.

As presented earlier in Chapter 2, Gaussian beam optics dictate that the waist and Rayleigh length of a focused Gaussian laser beam are inextricably linked. These parameters are both given in terms of the focusing lens numerical aperture (NA) by

$$w_0 = \frac{\lambda}{\pi \mathrm{NA}} , \tag{6.1}$$

and

$$z_\mathrm{R} = \frac{\lambda}{\pi \mathrm{NA}^2} , \tag{6.2}$$

where the beam waist at the focus, w_0, is measured laterally from the optical axis, the Rayleigh length, z_R, is the propagation distance from the focus at which the beam waist has increased to $\sqrt{2}w_0$, and λ is the wavelength of the focused light.

In a SPIM system this results in the volume of the illumination light sheet region having a length of $2z_\mathrm{R}$ and a width of $2w_0$ that are set by the NA of the focused beam. A reduction in the Rayleigh length of the illumination light sheet reduces the length across the detection field-of-view (FoV) in which excitation by the narrowest part of the light sheet occurs. This also reduces the thickness of the light sheet, resulting in the excitation of a narrower planar region, akin to a vertical stripe, within the sample. Figure 6.1 portrays a 3-D optical schematic of a SPIM illumination beam with both a low NA and a high NA to visually demonstrate the difference in light sheet dimensions within an example sample volume. Typically SPIM systems are operated using a reduced NA in the illumination path in order to image a wide FoV across a sample. Though the depth-of-focus (DoF) of the detection optics may be as

small as 0.5 microns, the light sheet may have a thickness of up to 3 microns. As such the light sheet may cause some excitation outside of the detected volume within the sample. If, instead, a larger NA in the illumination path is used, excitation outside of the detected volume within the sample is minimised, thus maximising the sectioning capability of the light sheet. Although consequently this enhanced section is restricted to features within a small, vertical, planar region within the detection FoV.

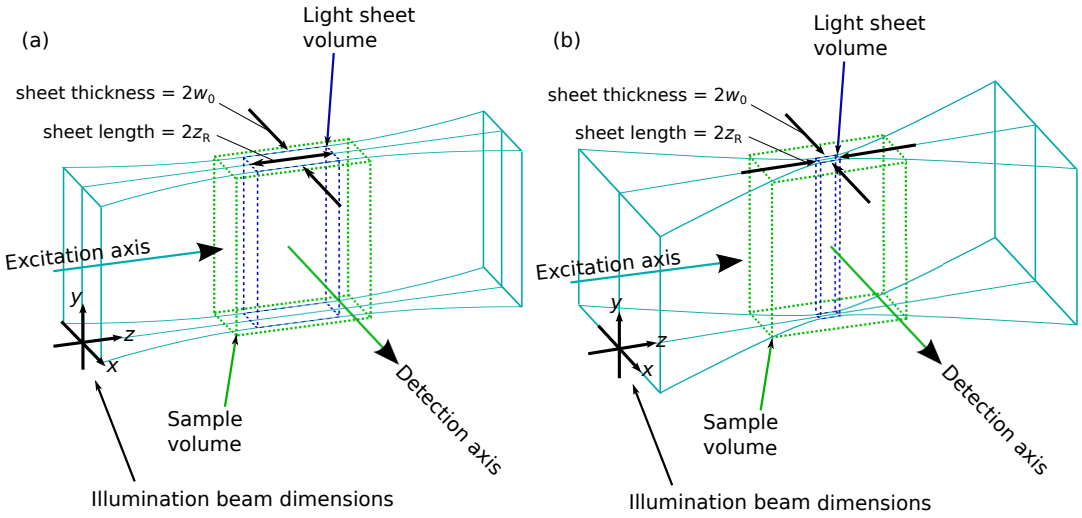

FIGURE 6.1: 3-D schematic of a SPIM illumination beam with both a low NA (a) and a high NA (b). Drawn in green dashed lines is an example volume within a fluorescent sample. The volume of the light sheet region within the sample, bordered with navy dashed lines, has dimensions of length along the excitation axis (along z) and thickness orthogonal to this (along x) which are associated with the Rayleigh length z_R and the beam waist w_0 of the illumination beam respectively. As $w_0 \propto \mathrm{NA}^{-1}$ a high NA beam produces a smaller light sheet thickness than a low NA beam, potentially improving the optical sectioning of images taken along the detection axis. However, as $z_R \propto \mathrm{NA}^{-2}$, this high NA greatly reduces the lateral extent of the light sheet across the detection field-of-view.

6.2.2 Enhanced optical sectioning of curved biological features

Biological specimens typically consist of many cellular surfaces and regions that can have very distinct curvatures over the detection FoV. Similarly, since samples are typically mounted using restricted orientations within a SPIM, features of interest may span the detection FoV in an orientation which is non-vertical. Therefore, by using the full NA of the illumination objective to improve the sectioning capability of the light sheet, portions of these curved, or non-vertical, features may exist outside of the optimum vertical light sheet region. Hence we would not be able to image these features simultaneously when utilising the improved optical sectioning offered by a light sheet with a high NA.

For example, in the eye of a zebrafish embryo one particular region of interest is the *lens epithelium*, which constitutes the outer surface of the eye lens. The cells that comprise the lens

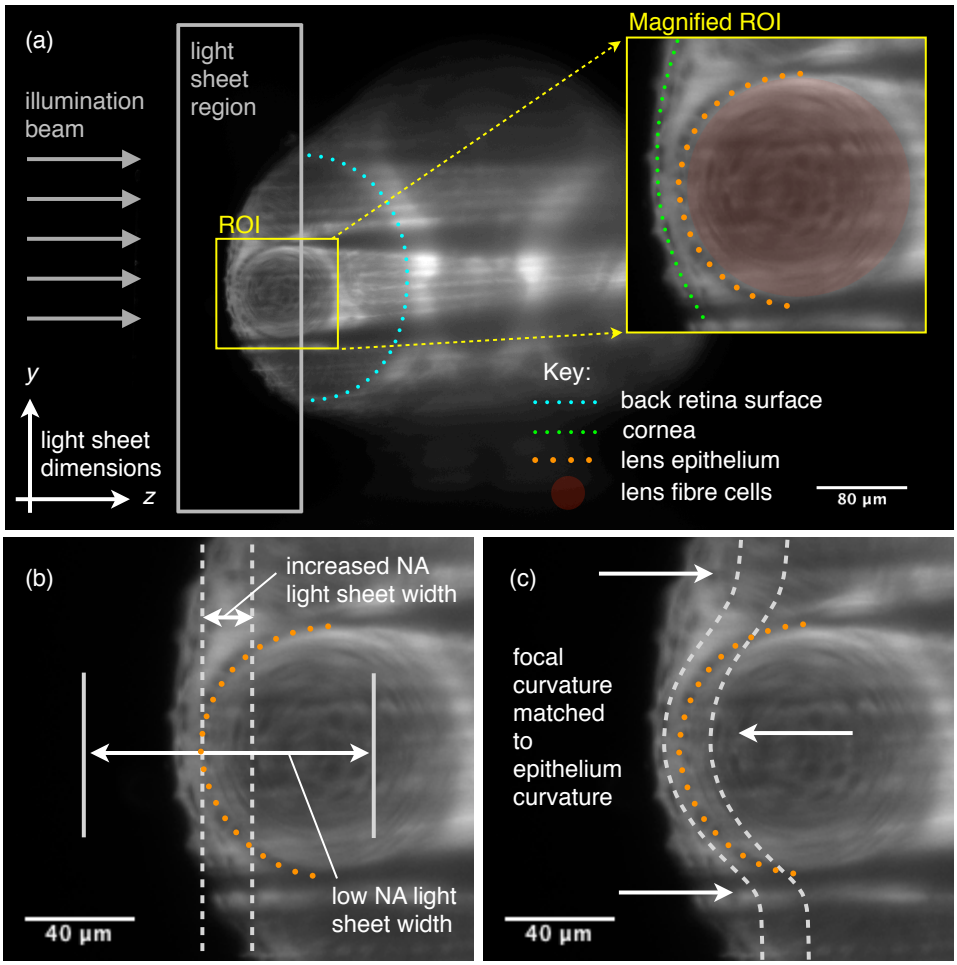

FIGURE 6.2: Example light sheet dimensions in relation to the features of a zebrafish eye. The light sheet region produced by a typical SPIM illumination beam optically sections several component features across a large region-of-interest (RoI) at once. In this example image the sample is a zebrafish embryo at 2 d.p.f and the RoI surrounds the eye lens (a). Within this RoI are several cellular regions, each with a distinct curvature (inset). By increasing the NA of the illumination beam the length of the light sheet region is reduced to the extent of one specific feature, though the curvature of this feature may cause part of the cellular structure to lie outside of this region (b). Combining this increase in NA with a variation in focal length across the height of the light sheet allows the entire curved feature to be optically sectioned (c).

derive entirely from this single layer of epithelial cells, the behaviour of which under-pins the development and continued biological function of the lens. As the eye lens of a zebrafish can be treated as spherical, a section through the eye can be treated as circular. The lens epithelium can therefore be treated as a circularly-curved region with a particular radius of curvature. The radius of curvature of the lens epithelium for zebrafish embryo eye lenses varies from 45 μm at 2 days post-fertilisation (d.p.f.) up to 60 μm at 4 days post-fertilisation (d.p.f.). Similarly, the

radius of curvature of the retina varies from 135 μm at 2 d.p.f. up to 160 μm at 4 d.p.f.. Thus, to obtain images of either of these cellular surfaces with improved optical sectioning not only does the full NA of illumination objective need to be used, but also the focal length has to be locally altered throughout the height of the light sheet. The alteration of the light sheet focal length to locally match the position and topology of different features in the observation plane can therefore result in highly *feature-specific* SPIM images with optimised optical sectioning. Figure 6.2 illustrates the effect of increasing the NA and applying a focal curvature to an illumination light sheet in relation to the observed features of a zebrafish eye[1].

Clearly, in order to introduce focal length alterations within an illumination beam that are specifically-adapted to a variety of different features and curvatures, an adaptive optical element is required in the beam path. We investigated the use of a SLM to introduce a focal power across one lateral axis in the beam path, similar to the use of a cylindrical lens in a typical SPIM system.

6.2.3 Calculation of the phase profile required to form a line focus

To use an adaptive optical element to introduce a focal power in only one lateral axis, *i.e.* to produce a line focus, we first need to derive the form of the phase profile required to produce a 1-D focus. Considering the adaptive optical element as a rectangular array of phase-modulating pixels, and the desired line focus as being parallel to the columns of the array, we start by considering the phase profile required by only one row of this array. The calculated phase profile can then be applied to every row on the sensor to create the line focus.

For a 1-D beam geometry we begin by considering a 'height' coordinate, h, relative to the centre of a planar surface, S. To bring light of a given wavelength, λ, to focus at one focal length, f, from the centre of S (where $h = 0$), the optical path length (OPL) vectors, $p(\vec{h})$, from all points of origin across S to the focal point must arrive with equal phase. The following equation describes a curved surface, C, from which all emanated rays begin in-phase, and subsequently arrive in-phase at the focus:

$$|p(\vec{h})| + \Delta p(h) = \text{const}, \tag{6.3}$$

where $\Delta p(h)$ denotes the OPL difference between surface C and surface S, as shown in Figure 6.3.

As the planar surface S bisects this converging bundle of OPL vectors, a spatially dependent variation in phase, $\phi(h)$, is present across S. By determining the phases advanced along each OPL between these two surfaces a map of $\phi(h)$ can be calculated. The phases advanced along each OPL, in units of waves, are found by substituting $\Delta p(h) = \lambda\phi(h)$ into Equation 6.3 and re-arranging for $\phi(h)$. Thus,

$$\frac{|p(\vec{h})|}{\lambda} + \phi(h) = k, \tag{6.4}$$

[1]Image credit: Zebrafish SPIM image courtesy of Dr. L. K. Young at the CfAI.

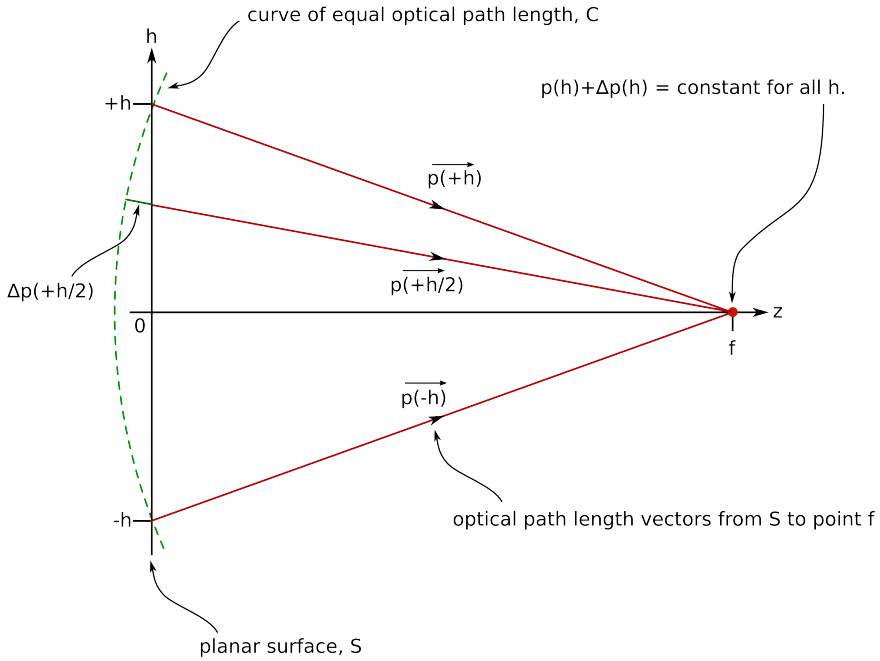

FIGURE 6.3: A plane wave emanating from surface S at z = 0 can be brought to a focus at z = f by altering the OPL vectors across the surface. By altering all OPL vectors to arrive at (z=f, h=0) with the same constant phase, a focus is formed. Alteration of the OPL vectors across S describes a virtual curved surface of equal OPL. This surface can be constrained to S through the use of phase retardation. The corresponding mathematics are derived in section 6.2.3.

where k is some arbitrary constant. By simple trigonometry this can be written in terms of f and h as

$$\phi(h) = k - \frac{\sqrt{f^2 + h^2}}{\lambda}. \tag{6.5}$$

This is equivalent to the phase that needs to imparted by the optical array elements of a SLM at S in order to produce the desired focus.

Applying a boundary condition that the phase has advanced by half a wavelength at $h = 0$, *i.e* $\phi(h = 0) = 0.5$ waves, we determine the arbitrary constant k as

$$k = 0.5 + \frac{f}{\lambda}, \tag{6.6}$$

thus giving the phase across S required to produce a focus at f as

$$\phi(h) = 0.5 + \frac{f - \sqrt{f^2 + h^2}}{\lambda}. \tag{6.7}$$

This choice of boundary condition ensures that phase wrapping is avoided either side of this central region when applying the phase profile to an optical device such as a SLM. Applying this phase profile to each row on the SLM array thus produces a line focus at f.

Now, by varying the value of f that is used when calculating the phase profile for each row of array elements the position of the line focus can undergo a continuous variation along the height of the light sheet.

6.3 Method

6.3.1 Forming a line focus using a SLM

This section describes the use of a SLM to produce a line focus in lieu of any additional optics. We begin with an overview of how a SLM can be used to modulate the phase of an incident wavefront of light. Following this, we demonstrate the application of such phase profile to an actual SLM.

6.3.1.1 Phase modulation by a SLM

Each pixel on a nematic SLM is fabricated with a homogenous liquid crystal (LC) layer between the cover glass face of the SLM and a reflective mirror-coated very-large-scale integration (VLSI) silicon printed circuit board (PCB) backplane. An applied voltage causes the LCs to rotate about an axis, known as the ordinary axis, to align themselves with the applied electric field. The longest dimension of the LC crystal determines the extraordinary axis, orthogonal to the ordinary axis and, in the case of an applied voltage, to the VLSI backplane and cover glass surfaces. When no voltage is applied to a SLM pixel both the extraordinary and ordinary axes of the corresponding LC crystals remain in a parallel plane to the backplane. This is depicted in Figure 6.4.

The plane of polarization of light which is incident upon the LC medium determines the refractive index which is experienced. In the following we restrict the description of SLM–light interaction to incoming beams that are plane-polarised parallel to the rotation plane of the extraordinary axis. This polarized light experiences the SLM as a pixellated material where each cell has a variable refractive index, n_e, that is controlled by the applied voltage. Because the extraordinary axis of the LC is completely aligned with the backplane in the absence of an applied voltage, incoming light experiences the maximum refractive index n_e along the extraordinary axis and thus is reflected having undergone a maximum retardation of phase. However, when the applied voltage causes the LC to rotate 90 degrees about the ordinary axis, becoming completely orthogonal to the backplane, a minimum value of n_e is experienced and the phase retardation present in the output light is effectively zero.

For a reflective 8-bit SLM each pixel can be sent any one of 256 discrete voltages, calibrated to linearly impart a phase retardation of between 0 and 1 waves of the design wavelength in the reflected wavefront. A signal level of 0 thus leaves the pixel with zero voltage across it and imparts one full wave of phase retardation, whereas a signal level of 255 applies the maximum voltage to the pixel, thereby imparting no phase retardation to the output light. As such the signal values sent to a SLM are inverted with respect to the calculated phase map.

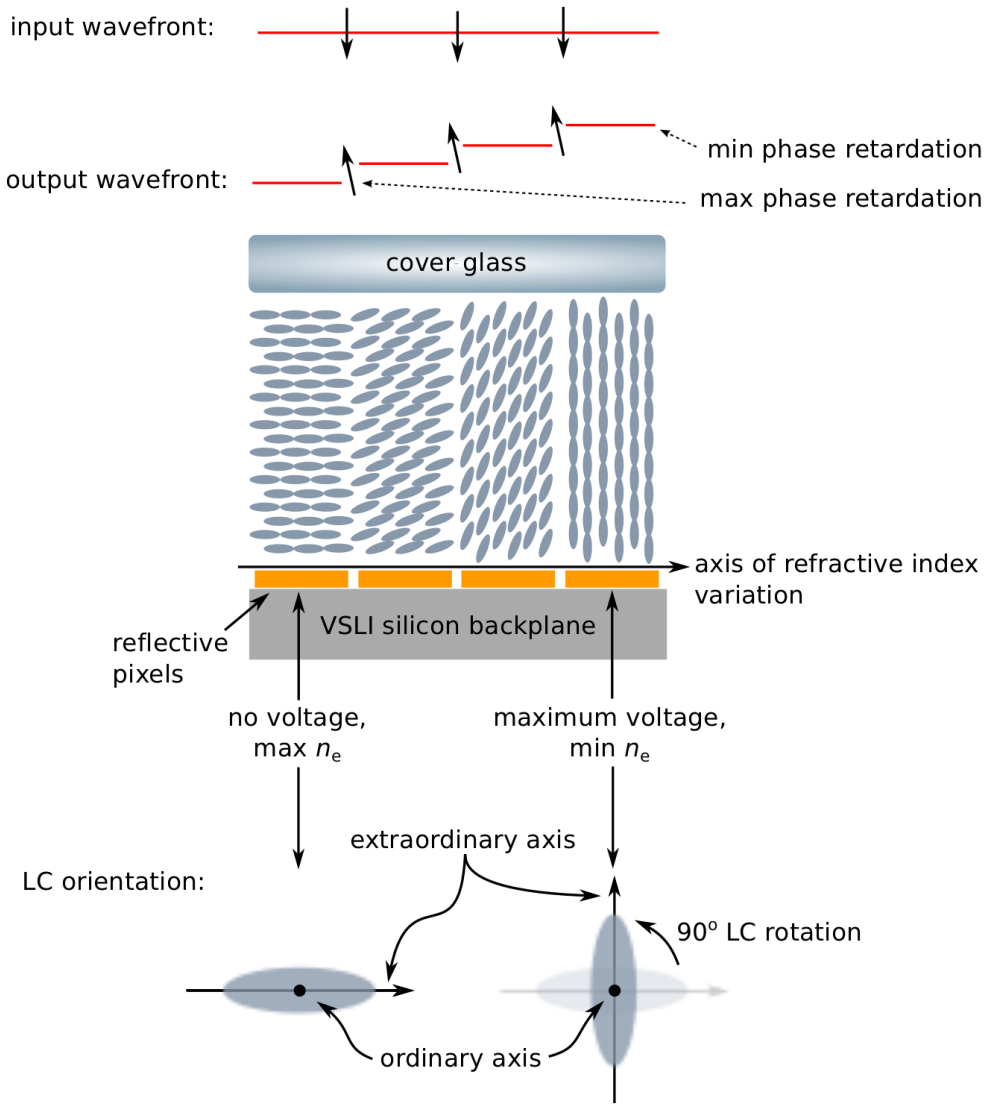

FIGURE 6.4: Schematic describing SLM operation. An input wavefront passes through the cover glass and LC layer of each pixel before being reflected back through these media and exiting the system as an output wavefront. A controlled voltage can be applied between the coverglass and each individual pixel by the VSLI silicon backplane to alter to orientation of the LCs. An increase in voltage rotates the LC orientation about the ordinary axis so that its extraordinary axis is orthogonal to both the backplane and coverglass. An input wavefront that is plane polarised 90˙ to the ordinary axis can thus experience a controllable phase retardation depending on the orientation of the extraordinary axis, with maximum retardation arising from the minimum applied voltage and vice versa.

6.3.1.2 Appropriate conversion of a phase profile to a SLM format

The phase profile required to create a cylindrical focus of λ = 532 nm light at f = 60 cm from a 256 x 256 element SLM array with a 24 micron pixel pitch (active area area of 6.14 mm × 6.14 mm) is shown in Figure 6.5a. Since a SLM can only impart phase retardation between 0 and 1 waves at the optimised design wavelength the calculated phase profile must be modulo divided by 1 wave. Figure 6.5b shows the calculated phase profile of Figure 6.5a phase wrapped between 0 and 1 waves. The boundary condition that we specified earlier to ensure that $\phi(h = 0) = 0.5$ waves avoids phase wrapping either side of the central pixel strip once the phase map has been sent to the SLM.

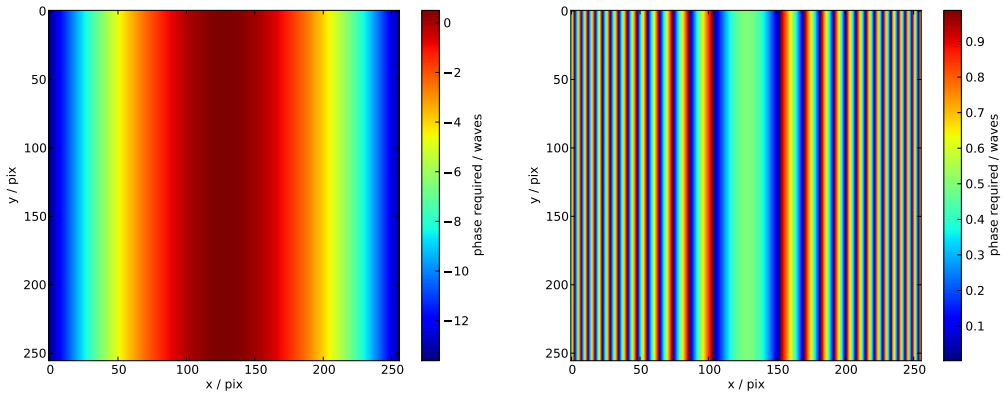

(a) Unwrapped phase

(b) Wrapped phase

FIGURE 6.5: Phase map calculated to produce a line focus at a focal length of f = 60 cm from the phase surface with the phase left unwrapped (a), and with the phase wrapped between 0 and 1 waves of retardation (b). The phase surface has an area of 6.14 mm × 6.14 mm and is comprised of 256×256 pixel elements to match to the SLM that (b) is converted for. Both colourbars represent the phase retardation in units of waves.

The line focus formed by sending the phase pattern in Figure 6.5b to a nematic SLM (XY Phase Series by Boulder Non-linear Systems (BNS), Colorado USA) is shown in Figure 6.6b. Clearly visible outside of the line focus is a large portion of the overall beam intensity that has not been focused, due to both the flat reflective surfaces of the SLM and the number of phase wrap boundaries [164]. The images were taken using a CCD camera (Retiga 4000R by QImaging, Canada) at the line focus position, one focal length of f_{SLM} = 60 cm from the SLM. As our goal was to use the SLM to directly shape the illumination beam for an optimised SPIM the obstruction of any extraneous light emanating from the SLM is important for preventing the excitation of undesirable fluorophores. We demonstrate how to filter the beam appropriately in the following section.

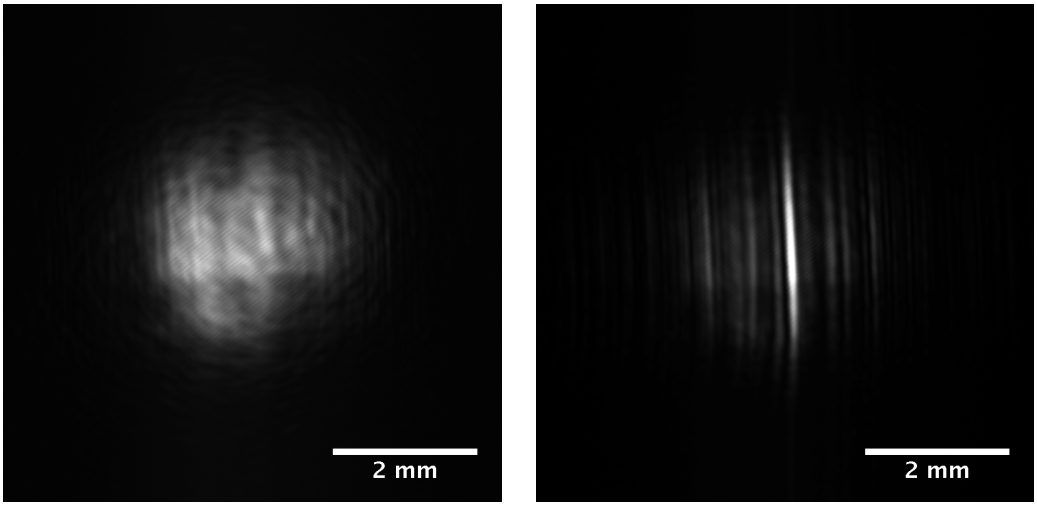

(a) Blank SLM (b) Phase applied

FIGURE 6.6: Image of the SLM output beam with no phase map (a) and with the phase map in Figure 6.5b applied (b). The phase map has no control over a portion of the beam intensity that is simply reflected by the flat SLM components, seen in (b) as the region outside of the line focus.

6.3.1.3 Spatial removal of SLM artifacts

The spatial separation of unwanted optical artifacts, caused by the reflectivity of a SLM's optical structure, from the intended, controlled, beam can be achieved through the addition of either a phase slope or a blazed grating to the applied phase pattern. The intended diffraction pattern which is controlled by the phase map sent to the SLM is convolved with the multiple-order diffraction pattern caused by the SLM's reflective pixel array, as illustrated in Figure 6.7(a). This 'intended diffraction pattern' can refer to the Fourier transform of the applied 'ideal' phase map, formed either at the focal length of a subsequent lens or in the far-field, or can refer to our SLM-produced line focus. Though the first orders of this convolved pattern can be blocked using apertures, the central zeroth order remains a combination of the reflected SLM throughput and the intended diffraction pattern. Arithmetic combination of the ideal phase map with a phase slope - a separate phase map having some linear slope across the SLM array - spatially separates the intended diffraction pattern from the reflected SLM throughput. An aperture can then be used to isolate the zeroth order of the intended diffraction pattern. This aperture can either be a pinhole at the centre of a 4-f relay, as shown in Figure 6.7(b), or could be a simple rectangular slit surrounding our SLM-produced line focus, for example. Combining the phase map in Figure 6.5b with a diagonal phase slope of $2\pi/4$ waves per pixel across both x and y resulted in the phase map shown in Figure 6.8a. Sending this phase map to the SLM results in the image displayed in Figure 6.8b. It is clear that the line focus has been spatially separated from the unwanted background which surrounded the line focus in Figure 6.6.

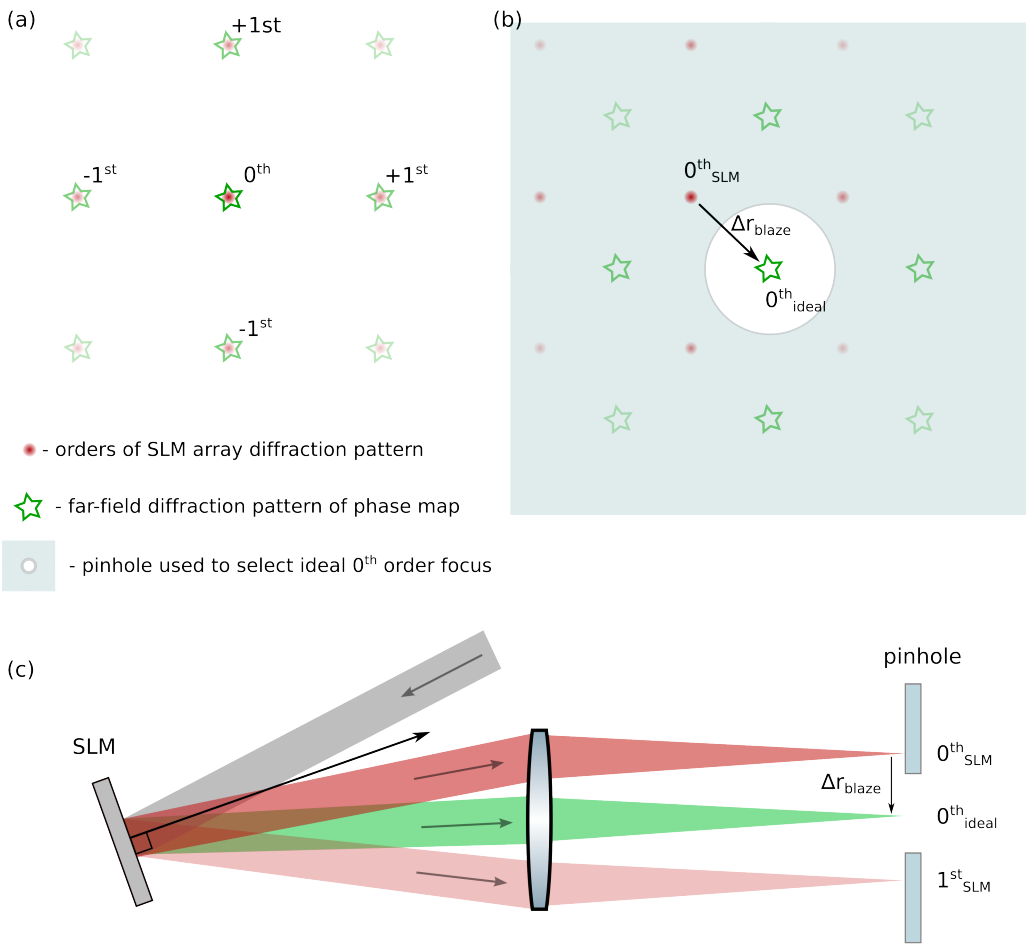

FIGURE 6.7: Use of a phase slope to spatially separate the different components of the diffraction pattern from a SLM. (a) Without an additional phase slope the far-field diffraction pattern of the SLM is a convolution of the intended far-field pattern (green stars), formed by the ideal phase pattern sent to the SLM, with the multiple-order diffraction pattern caused by the reflective pixelated array of the SLM (red spots). (b) By combining the phase pattern sent to the SLM with a phase slope or blazed grating the ideal far-field pattern becomes displaced by Δr_{blaze} from the pattern caused by the reflective structure of the SLM. An aperture or pinhole can then be used to obstruct everything other than the desired order of the ideal-phase focus to eliminate any background light from the system. (c) This method can be used within a 4-*f* system to filter out the unwanted diffraction pattern of the SLM formed at the Fourier plane of an intermediate lens.

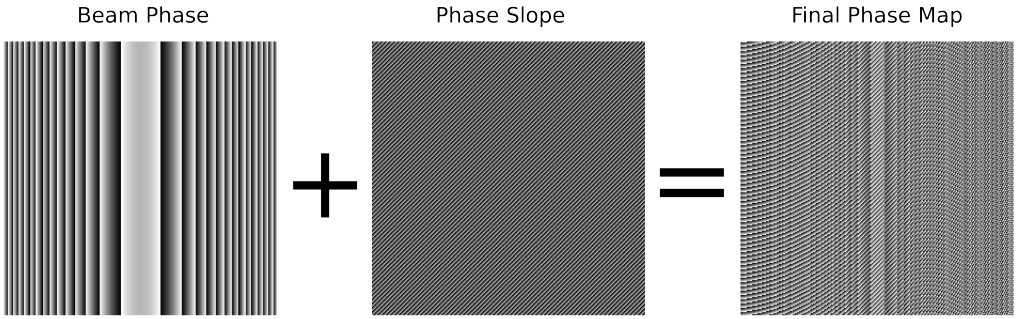

(a) Phase map composition

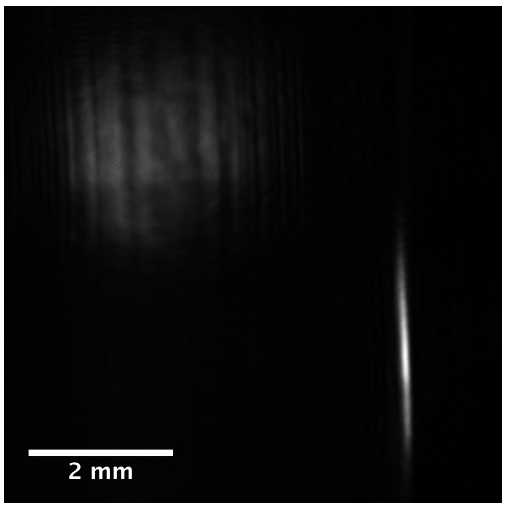

(b) Formed line focus

FIGURE 6.8: Separation of a line focus from unwanted SLM artifacts by applying an additional phase slope. When the phase map in Figure 6.5b is combined with a diagonal phase slope the resulting phase map (a) forms a line focus at f_{SLM} = 60 cm that is spatially separated in both x and y dimensions from the reflective SLM artifacts (b).

6.3.2 Discrete regional variation in SLM focal length

To investigate localised alterations in the light sheet focal length we imaged the SLM focus at two separate locations, which coincided with the focal planes of different regions of the SLM phase pattern. The SLM array was segmented into three horizontal bands across the height of the array and a line-focus-producing phase map was calculated using an associated focal length for each region and sent to the SLM. Figure 6.9 presents two pairs of camera images taken at 50 cm (a, c) and 55 cm (b, d) from the SLM. The leftmost pair of images show a uniform light sheet with a focal length of 50 cm from the SLM. In the rightmost pair of images the light sheet focal length has been increased to 55 cm in the central region of the light sheet only; we see that the central region of the light sheet has been brought to focus at 55 cm from the SLM.

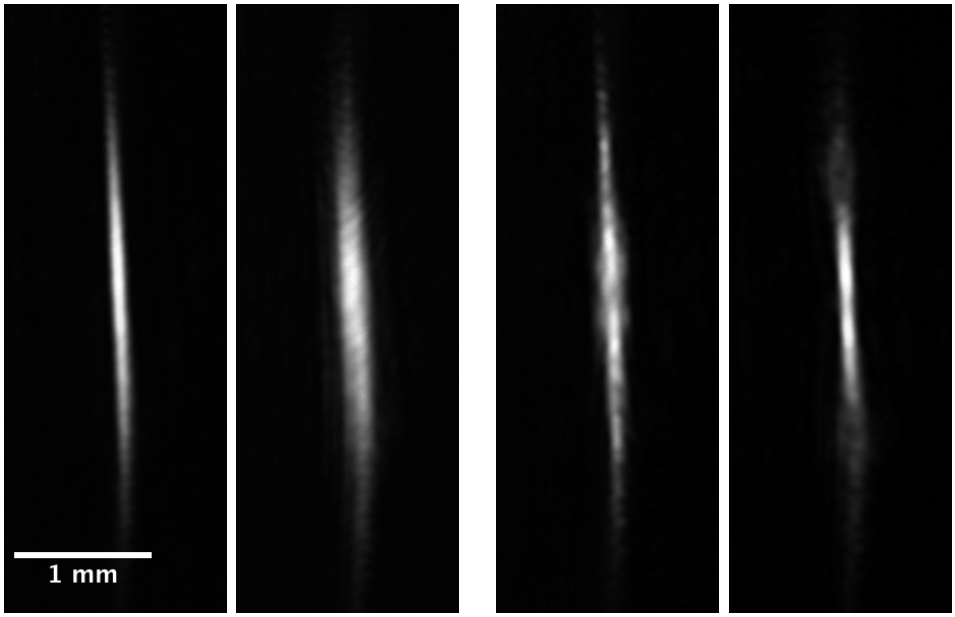

(a) ϕ_1 at 50 cm. (b) ϕ_1 at 55 cm. (c) ϕ_2 at 50 cm. (d) ϕ_2 at 55 cm.

FIGURE 6.9: The resulting beam shapes from two phase profiles ϕ_1 and ϕ_2 imaged at two distances, 50 cm and 55 cm from the SLM. The phase profile used for the left two images, ϕ_1, produces a regular line focus of focal length 50 cm. The phase profile used for the right two images, ϕ_2, was a modified version of ϕ_1 where the central third of the light sheet had the focal length extended from 50 cm to 55 cm. The latter pair of images (c, d) show a line focus with a discrete variation in focal length from 50 cm in the upper and lower regions to 55 cm in the central region.

6.3.3 Continuous variation in SLM focal length

Following our verification of discrete regional variations in focal length we investigated continuous variations in the light sheet focal length. We opted to use our beam profiling device from Chapter 5 in order to take 3-D beam profiles of the A-SPIM light sheet focus. In

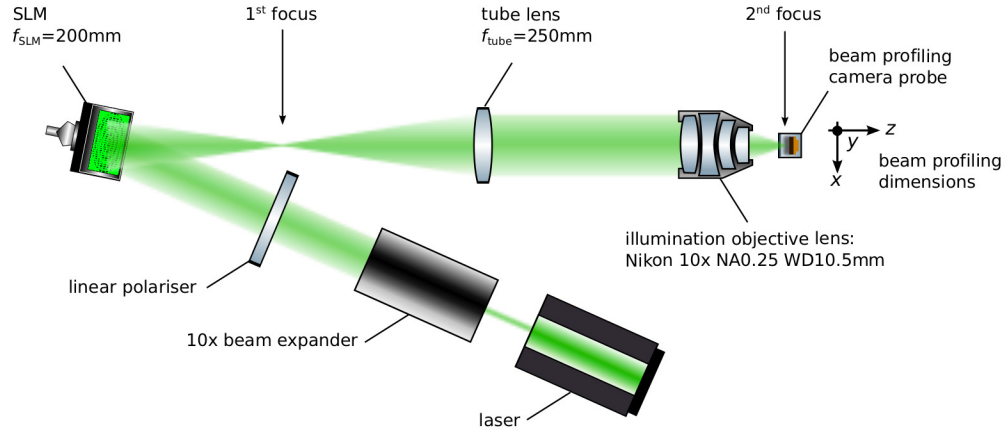

FIGURE 6.10: Top-down optical layout used for the SLM-produced SPIM light sheet. A 4-*f* relay is used to re-image the 1st line focus produced by the SLM at dimensions appropriate for use within a SPIM system.

the following sections we describe the A-SPIM optical system, the theoretical dimensions of the A-SPIM light sheet, and the continuous variation in the light sheet focal length that was applied.

6.3.3.1 Optical layout

Figure 6.10 shows the optical diagram of our proposed A-SPIM illumination beam. The line focus produced by the SLM, referred to hereafter as the first focus, was re-imaged down to the dimensions appropriate for a SPIM illumination beam using a 4-*f* telescope system comprised of a tube lens of focal length f_{tube} = 250 mm and an infinity-corrected microscope objective lens designed for use in air (Transverse magnification given on the barrel as M_{b} = 10×, numerical aperture NA_{obj} = 0.25, working distance WD_{obj} = 10.5 mm, Nikon, Japan). Following the first focus, the tube lens re-collimates the light sheet in one axis and forms a line focus in the opposing axis (along x) across the back focal plane of the objective lens. We used a smaller focal length for the SLM-produced light sheet, f_{SLM} = 200 mm, in order to fill the 10 mm diameter rear aperture of the illumination objective lens, producing a light sheet at the second focus with the full 0.25 NA of the objective lens.

6.3.3.2 Theoretical beam dimensions and camera probe limitations

The thickness of the light sheet according to Equation 6.1 was $2w_0 = 2 \times 0.532\mu\text{m}/\pi \times 0.25 = 1.35\mu\text{m}$ and the sheet length along the optical axis according to Equation 6.2 was $2z_{\text{R}} = 2 \times 0.532\mu\text{m}/\pi \times 0.25^2 = 5.42\mu\text{m}$. Even when taking camera probe beam profiles of the focus using the smallest possible isotropic voxels of 3 μm × 3 μm × 3 μm the light sheet focal dimensions would therefore be impossible to measure accurately. However, a maximum

estimate of these dimensions can be made, in addition to the profile providing an image of the overall shape of the light sheet.

6.3.3.3 Application of focal curvature

To produce a continuously-curved light sheet we altered the focal length across the height of the SLM array using a Gaussian amplitude function. The equation describing this variation in the SLM focal length, Δf_{SLM}, took the form

$$\Delta f_{\mathrm{SLM}} = a_{\mathrm{SLM}} \exp\left(\frac{-(y_{\mathrm{SLM}} - b_{\mathrm{SLM}})^2}{2c_{\mathrm{SLM}}^2}\right), \tag{6.8}$$

where a_{SLM} is the maximum amplitude of the axial focal variation at the first focus, y_{SLM} is the vertical row coordinate across the height of the SLM array, b_{SLM} is the central coordinate of the Gaussian curve, and c_{SLM} denotes the half-width of the Gaussian bell: the inflection points of the Gaussian curve occur at $y_{\mathrm{SLM}} = b_{\mathrm{SLM}} \pm c_{\mathrm{SLM}}$, so $2c_{\mathrm{SLM}}$ determines the bell width.

The maximum focal variation amplitude was calculated at the first focus by specifying the amplitude variation at the second focus. That is, $a_{\mathrm{SLM}} = M_{\mathrm{L}}\, a$, where a was the desired maximum amplitude at the objective lens focus and M_{L} is the longitudinal magnification produced by the objective lens-tube lens 4-f relay. This magnification is related to the transverse magnification produced by the 4-f relay, M_{T}, through $|M_{\mathrm{L}}| = {M_{\mathrm{T}}}^2$. The bell half-width at the first focus was given by $c_{\mathrm{SLM}} = M_{\mathrm{T}}\, c$, where c is the bell half-width specified at the second focus.

For our setup $M_{\mathrm{T}} = 12.5\times$ rather than the objective lens barrel magnification of $M_{\mathrm{b}} = 10\times$ due to the tube lens focal length of $f_{\mathrm{tube}} = 250$ mm rather than the $f_{\mathrm{tube}} = 200$ mm typically used for Nikon objective lenses. Hence, the longitudinal magnification of our 4-f relay was $M_{\mathrm{L}} = 12.5^2 = 156.25$. Thus an example focal variation amplitude of $a = 48$ μm at the second focus would require $a_{\mathrm{SLM}} = 7.5$ mm at the first focus. The Gaussian bell width was set at 120 μm at the second focus, thus $c_{\mathrm{SLM}} = 12.5 \times 120/2$ μm $= 750$ μm. The entire active area of the SLM was used, thus the height of the light sheet at the second focus was 6.14 mm/12.5$\times$ = 492 μm. The points of inflection of the Gaussian focal variation were fixed in z at $f_{\mathrm{SLM}} = 200$ mm so that the Gaussian bell of the focal variation was brought closer to the objective lens and the top and bottom edges of the light sheet were pushed farther away. The focal variations were applied with amplitudes of 20 μm, 40 μm, and 60 μm at the second focus.

6.4 Results

6.4.1 Initial assessment of adaptively-curved illumination beam

Figure 6.11 shows orthographic sections through beam profiles taken of our A-SPIM illumination beam with different amplitudes of continuous Gaussian variation applied to the sheet focal length. In these results there was no spatial separation or filtering of the SLM throughput at the first focus following the SLM. Five images were taken at each exposure in

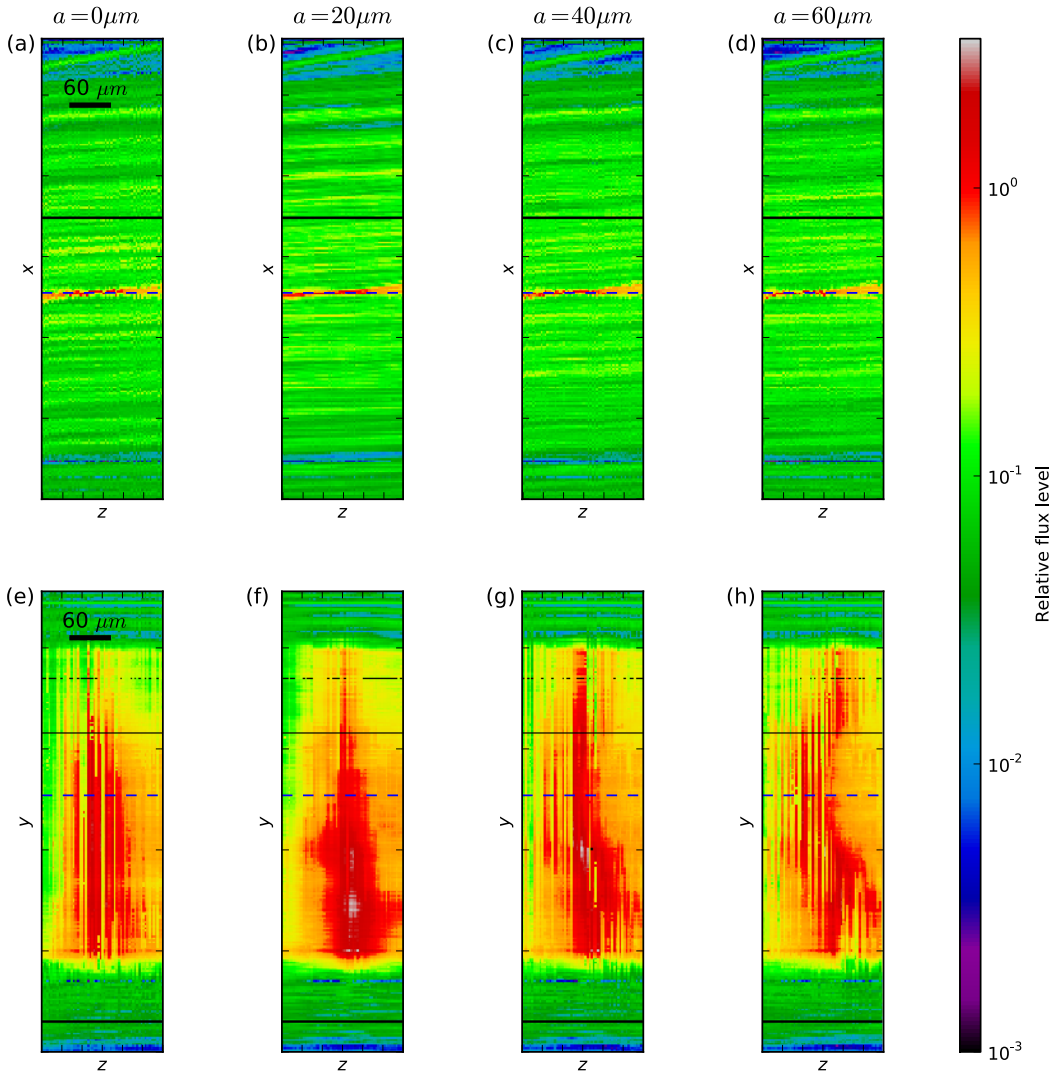

FIGURE 6.11: Orthographic x-z (a–d) and y-z (e–h) sections through beam profiles taken of our A-SPIM illumination beam. The amplitudes, a, of the applied Gaussian focal variation are given above each of the x-z and y-z pairs of sections. The horizontal dashed blue line across the centre of each section denotes the location of the corresponding orthogonal section shown either above or below. The beam profiles were taken with isotropic voxel dimensions of 3 μm $\times$ 3 μm $\times$ 3 μm.

the HDR imaging procedure for the sake of noise reduction. The focal curvature applied to three of the light sheets was difficult to determine in these sections due to the appearance of very bright reconstructed slices next to much darker reconstructed slices along the z-axis of each beam profile. Clearly visible in the x-z section are small noisy lateral shifts of the profiled beam by one or two pixels across the camera probe sensor array. We therefore investigated orthogonal sections through these beam profiles to determine if this was an optical effect present in the illumination beam itself, or an imaging artifact that could be removed with

post-processing.

In Chapter 5 we associated the cause of a sinusoidal lateral variation with a spatial period of around 400μm with the lead screw of the translation stage. However, the beam profiles presented here were taken over a much smaller axial range of 180μm and the lateral shifts exhibited no distinct periodicity. Since the unfiltered and collimated SLM throughput was also visible in the beam profile, this demonstrated that the noisy lateral variation affected the profile as a whole. We therefore attributed the relative lateral motion between successive slices again to the translation stage, rather than to an optical effect. A lateral motion between successive planes of the reconstructed profile, coupled with the low NA of the beam itself, potentially explains the appearance of the vertical stripes in the y-z sections of Figure 6.11: Any y-z section taken along a single x-coordinate of the beam profile will show a drop in intensity if the lateral motion of the sensor in the x-dimension is of a similar magnitude to both the beam width and the sensor array pixel pitch. We attempted to remove this effect by using post-processing to laterally shift the voxel coordinates of successive slices. This procedure is explained fully in the next section.

6.4.2 Reduction of artifacts by voxel coordinate shifting

To investigate if these artifacts were caused by lateral sensor motion we recorded the coordinate position of the centroided centre-of-mass (CoM) for the flux values in each z-slice of the beam profile and then reconfigured the voxel coordinates for that slice accordingly. The light sheet was oriented such that the line focus was parallel to a single column of pixels on the camera probe sensor and the unwanted lateral sensor motion throughout the recorded beam profiles appeared to be predominantly constrained to the x-z plane, along the x axis. As such, we averaged the pixel values across the height of the light sheet along y, flattening each slice of the beam profile to a single strip of pixels along x in the x-z plane, and calculated the CoM coordinate for each of these pixel strips. A threshold was applied to remove the lowest 50% of flux values from the CoM calculation. The difference between the CoM for each flattened slice and the mean CoM coordinate gave us the required magnitude for the lateral shift along x of each beam profile slice. Figure 6.12 shows the calculated CoM coordinates (a) and the result of the lateral shift (b) for each flattened slice of the line focus output by the tube-objective lens 4-f system. Each slice of the beam profile was up-sampled by a factor of 5 prior to the calculation of the CoM and the lateral re-shifting. A comparison of Figure 6.12(a) and (b) shows the success of laterally re-shifting the z-slices to align the central maximum reconstructed flux of the beam within the profiled volume, removing the overall tilt of the beam by shifting some stray slices back by as much as two pixels, or 6 μm. Figure 6.13 shows the effect that this lateral re-shifting has on the central y-z plane section of the unaltered line focus light sheet.

Figure 6.14 shows orthographic sections of the beam profiles presented earlier in Figure 6.11 after applying the centroid-based lateral slice re-shifting. For all beam profiles in Figure 6.14 the vertical stripes apparent in the central y-z plane sections before re-shifting in Figure 6.11 have been greatly reduced following centroid re-shifting, though there are still a noticeable number present. Also, the x-z plane sections demonstrate that although the central reconstructed

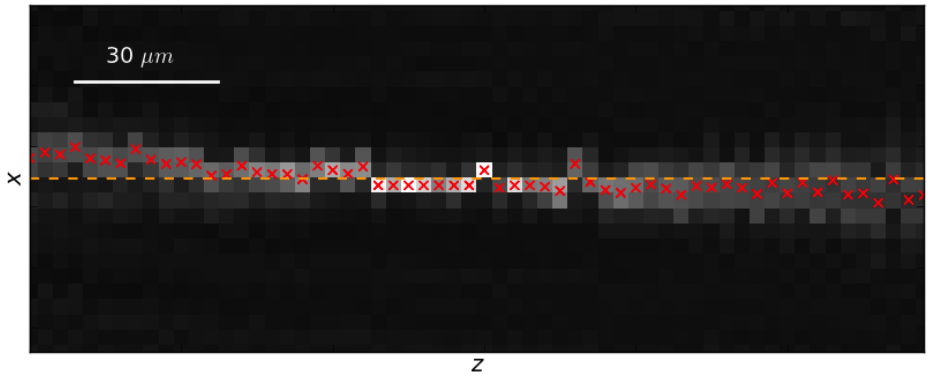

(a) Without slice re-adjustment

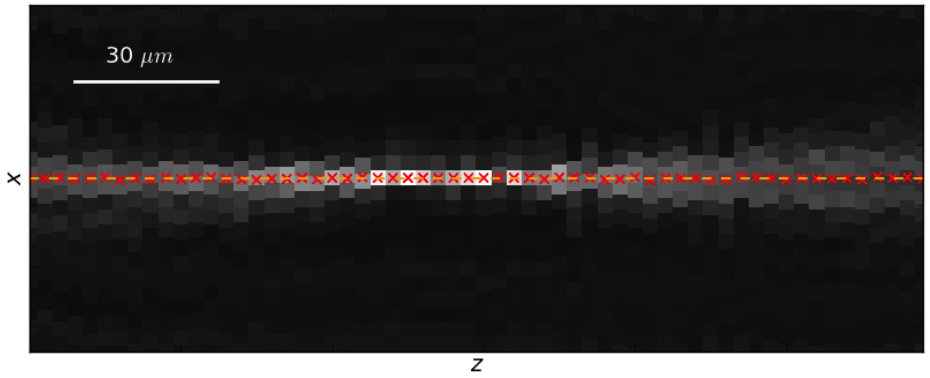

(b) With slice re-adjustment

FIGURE 6.12: Zoomed-in x-z plane sections through the un-altered A-SPIM light sheet focus are presented before (a) and after (b) centre-of-mass centroid re-adjustement of the beam profile slices. For each slice along z the red crosses show the x coordinate location of the CoM. The mean CoM is displayed in orange as a horizontal dashed line.

flux maxima were successfully aligned along the profile z-depth, the structures outside of this caused by the un-filtered SLM throughput still exhibit some noisy lateral mis-alignment. Hence, in order to comment any further on the overall 'quality' of our SLM-produced A-SPIM light sheet we require further removal of any artifacts introduced by the beam profiling system. It is important to re-iterate that our centroid realignment was only performed along a vector parallel to the x axis, though there is a small y component to the lateral shift vector. We suggest that by aligning the beam to something other than the locations of the coarsely-sampled, and thus poorly-quantised, central peak pixel values, the data sets could be re-aligned more successfully. This could take the SLM throughput into account, which is a collimated projection of the SLM array pixel structure. Such a re-alignment could be achieved

by assessing the centroided peak of the cross-correlation map between successive z slices.

6.4.3 Optical sectioning of curved features

We now move on from discussion of the beam quality and discuss the applied continuous focal variation and its relation to the dimensions of curved sample features. In Figure 6.15 the four amplitudes of applied Gaussian focal curvature are overlaid on top of the centroid re-adjusted y-z sections of Figure 6.14. Dashed lines have been drawn either side of the central Gaussian line shape to indicate an example light sheet length of 30 μm. This light sheet length is roughly 5.5× longer than that which was calculated earlier in Section 6.3.3.2 for the maximum NA of our illumination optics and represents the axial extent over which the thickness of the unaltered light sheet in Figure 6.12 is within the lateral dimensions of two camera probe sensor pixels, 6 μm. Optimum optical sectioning occurs close to the centre of the focal variation between the two dashed lines. The position of the unaltered focus and the points of inflection of the Gaussian variation are noted on the figure to indicate the scale of the applied variation. To illustrate the interaction of our applied focal variation with a curved feature a shaded circle with a radius of r = 90 μm is also present. This circle is centered with regards to the Gaussian variation. The radial centre of the curved surface is aligned with the lateral centre of the light sheet, a distance of r along z from the centre of the focus. As the Gaussian amplitude increases, the 30 μm long focal region becomes better suited to illumination of the curved circular surface. A Gaussian amplitude of 60 μm displays the maximum potential optical sectioning of the curved surface compared with the unaltered light sheet. Since the surface of the circle lines up well with the Gaussian bell, the sectioning provided by a thinner focal region that is therefore shorter in length will still be successful for this curvature radius.

Figure 6.16 demonstrates a number of potential feature curvature radii that the light sheet with a 60 μm Gaussian focal variation can section with varying degrees of success. Both the r = 90 μm and r = 120 μm curvatures match well to the centre of the focal variation as a wide arc of the curved surface remains well within the 30 μm sheet length. The curvature radii of r = 60 μm and r = 150 μm demonstrate the limits where this focal variation becomes less well matched to the curvature radii. For $r < 60$ μm the sectioning provided by the focal variation becomes similar to that which would be provided by the simple unaltered light sheet. Thus to match the focal variation for curvatures with smaller radii of $r < 60$ μm the distance between the points of inflection of the Gaussian focal variation, $2c$, needs to be smaller than 120 μm. Similarly, for curvatures with $r > 150$ μm the curved surface begins to extend outside of the central Gaussian profile, so an increase in the Gaussian bell width, making $2c > 120$ μm, is required. To maintain the same overall Gaussian shape whilst altering the distance between the points of inflection we suggest that the ratio of the Gaussian amplitude and the bell half-width at the 2nd focus be kept at the current value of a/c = 60 μm/60 μm = 1. At the 1st focus this changes from 1 to M_T since $a_{SLM}/c_{SLM} = M_T^2 a/M_T c$. This would ensure the Gaussian focal variation is well-matched to a range of circular feature curvatures.

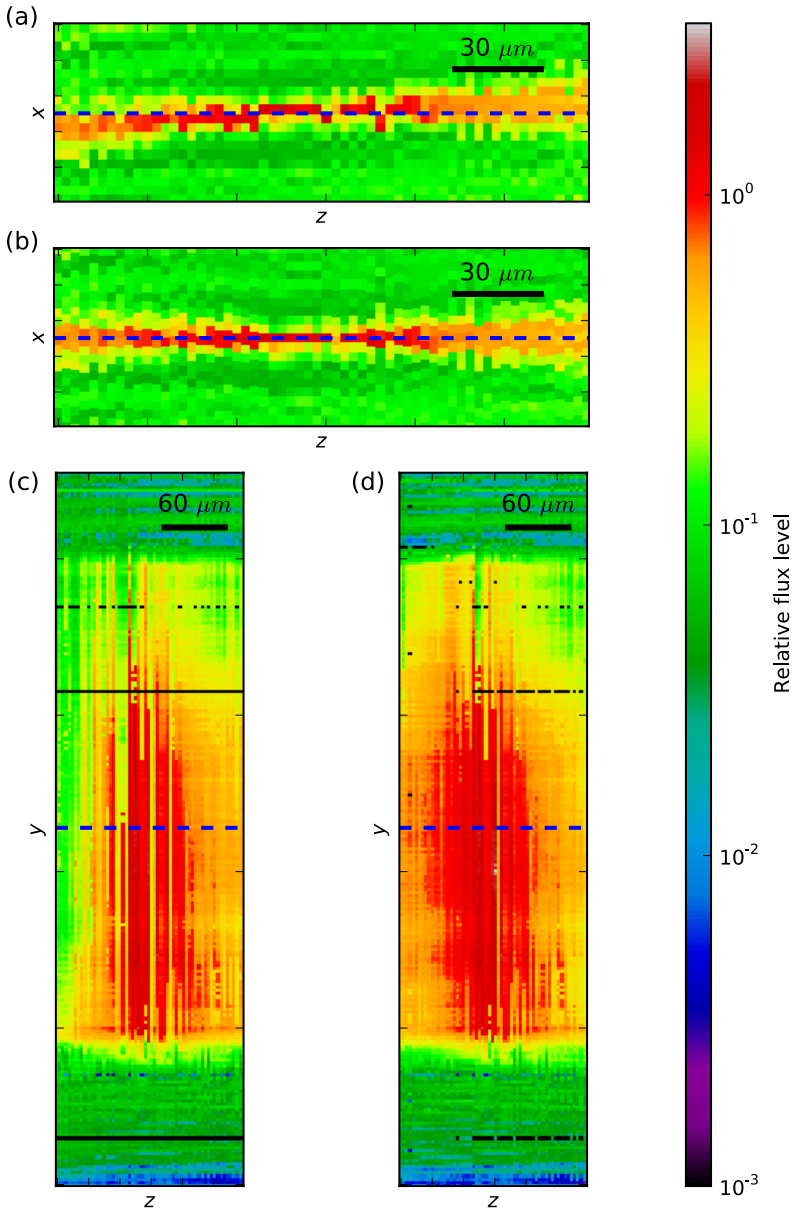

FIGURE 6.13: Orthogonal sections through a beam profile of the SLM-produced line focus before (a, c) and after (b, d) a centroid-based re-shifting of voxel coordinates along x in order to line up the central intensity maximum along the profile. The dashed blue lines along the centre of each x-z section (a, b) represent the position of the corresponding orthographic y-z sections (c, d), and vice versa.

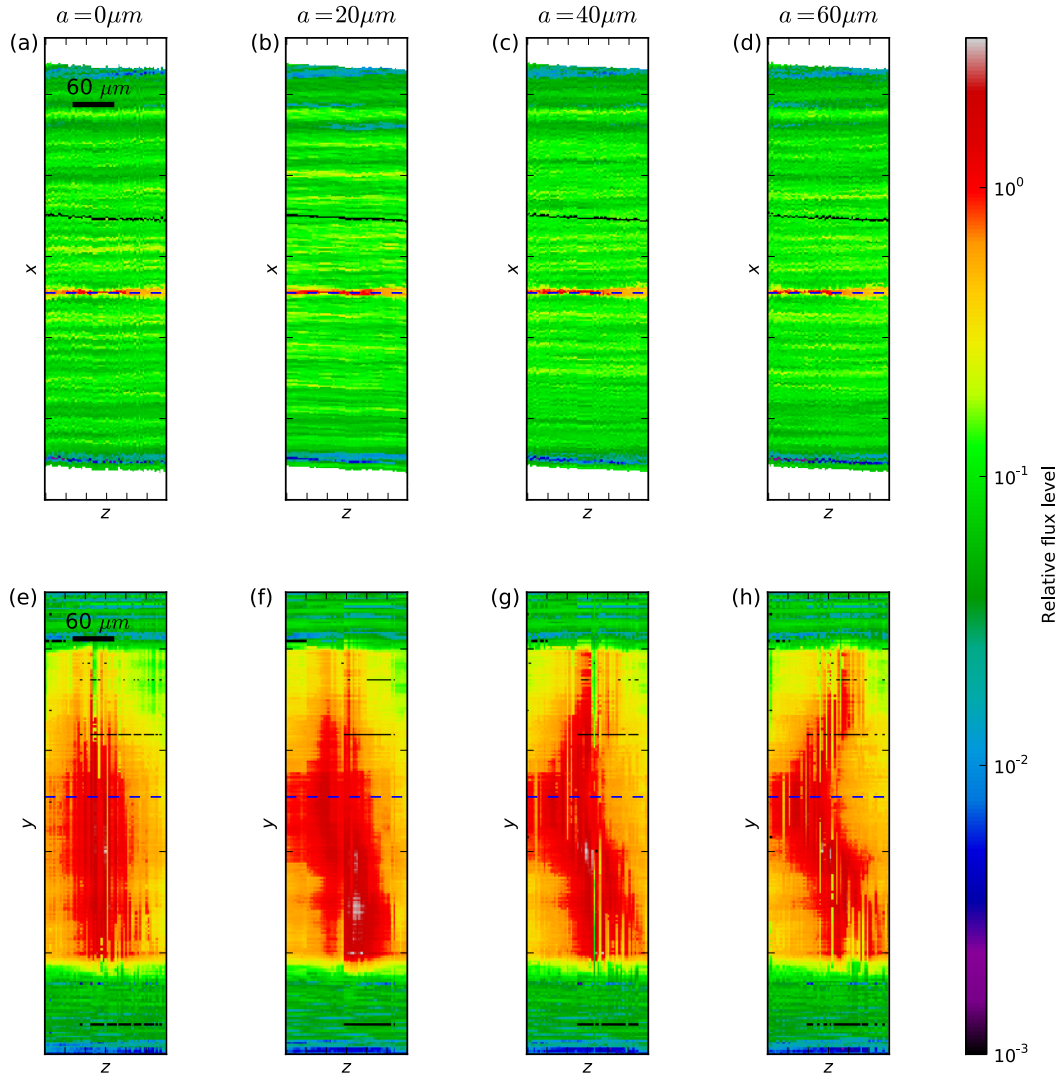

FIGURE 6.14: Orthographic sections through the same beam profiles presented in Figure 6.11 following centroid-based lateral re-shifting of voxel coordinates. The dashed blue lines along the centre of each *x*-*z* section (a, b) represent the position of the corresponding orthographic *y*-*z* sections (c, d), and vice versa.

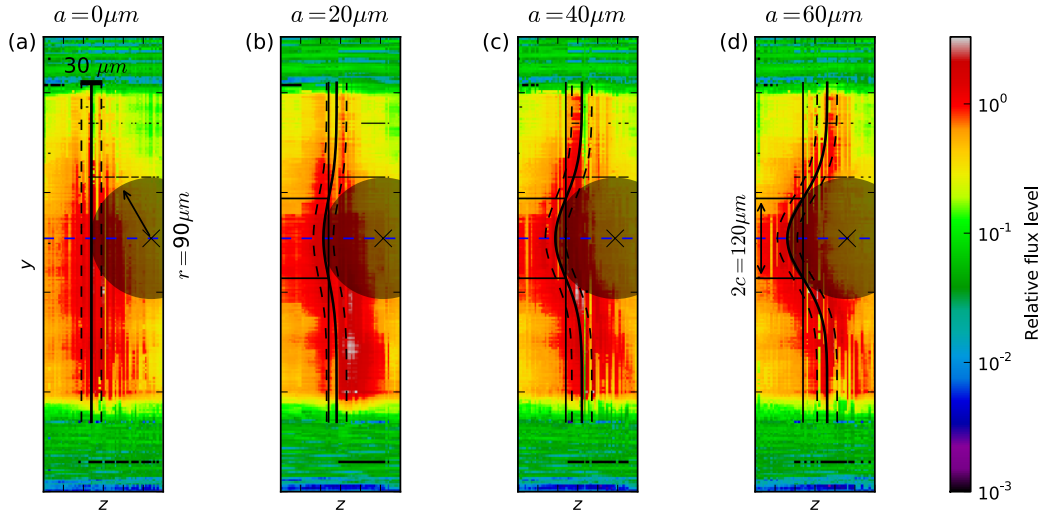

FIGURE 6.15: Increasing the amplitude a of the Gaussian focal variation applied to the A-SPIM light sheet, whilst keeping the separation of the points of inflection the same, improves the alignment of the central light sheet focus with a circularly-curved surface.

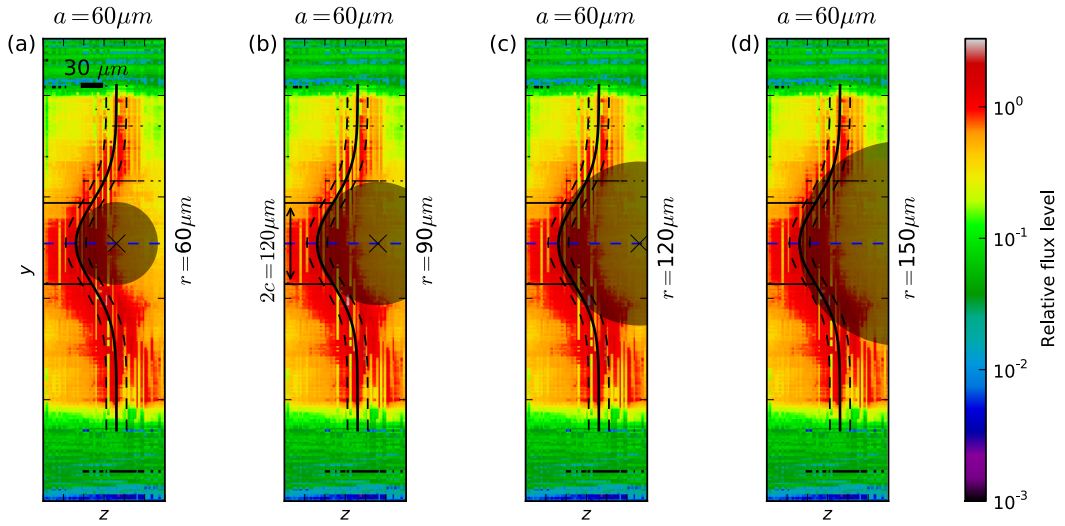

FIGURE 6.16: Relationship between the optical sectioning region of the A-SPIM light sheet curved focus with curved features of different radii.

6.4.4 Discussion

As mentioned previously the ability to accurately quantify the focal dimensions of these beams is limited by the 3 μm pixel pitch of the sensor array. We can only infer approximate limits on the light sheet dimensions: 3 μm and 30 μm for the sheet thickness and length respectively.

Any further conclusions regarding the overall quality of the A-SPIM light sheet are inhibited by the operation and construction of the camera probe sensor. Either a more involved post-processing procedure, a more stable translation stage, or a smaller sensor array pixel pitch are required. As noted previously in Chapter 5, the beam profiling camera probe is better suited to large volume beam profiles that allow the overall 3-D shape of the beam focus to be assessed, rather than direct assessment of the beam focal dimensions.

Limitations aside, the presented results demonstrate the application of a continuous lateral variation in the light sheet focal length, producing a light sheet with a Gaussian focal curvature that is well-matched to circularly-curved features. The focal variation is well matched to circularly-curved features when the ratio of the amplitude a and Gaussian bell half-width c is 1 in the sample plane. A focal variation with $a, c = 60$ μm produces a light sheet that can improve the sectioning of circular surface features with a range of curvature radii between 60–150 μm. The width of the Gaussian bell and the amplitude of the focal variation can then be altered to adapt the shape of the light sheet focus to a wider range of circular curvature radii.

6.4.5 Suggestions for future work

In this final part of the discussion we describe several 'next steps' in the the completion of the A-SPIM system and suggest some potential further investigations which can be made using this system. The first step required to complete the A-SPIM system is the construction of an orthogonal imaging arm with a sub-micron resolution. High-resolution beam profiles of the focus can then be taken using either a fluorescent sea or a suspension of fluorescent beads in the sample plane, resulting in a more accurate representation of the beam focus than those presented earlier that were taken with our HDR beam profiler. This will allow us to determine whether the quality of a light sheet produced by the SLM alone is high enough to be used within a SPIM by examining the beam for vertical striping artifacts similar to those in the beam profiles presented earlier. Additionally, this will allow us to accurately measure the thickness and length of the light sheet dimensions, and see if these match the theoretical dimensions calculated in Section 6.3.3.2. If the measured dimensions are larger than expected then this suggests that the full NA of the objective lens has not been used. This may be due to a reduced effective lateral beam width across the SLM during formation of the 1st line focus, caused by excessive phase wrapping in the applied phase pattern. In regions where the phase 'curvature' on the SLM causes a phase wrap of one wave between 4 successive pixels or less, these pixels may not efficiently contribute to the line focus formed. Since the phase gradient increases away from the central vertical coordinate of the phase map, these

regions can effectively set a boundary on the beam width and thus the NA of the 1st focus. To increase the NA of the beam at the second focus there are two options: One, simply switch the objective lens to one with a NA higher than 0.25; Two, reduce the amount of phase wrapping on the SLM. In the case of point one, a higher NA objective lens will typically possess a higher barrel magnification and so the height of the light sheet at the 2nd focus will be reduced. Provided the height of the light sheet remains larger than the curvature radius of the feature being imaged, the height reduction should not adversely affect the feature-specific optical sectioning of the A-SPIM system. In the case of point two, although an increase in f_{SLM} will reduce phase wrapping at the edges of the phase pattern, an improvement across the entire array width requires a large increase in f_{SLM}. Hence there will be no improvement in the NA of the 1st focus, and consequently no improvement in the NA of the 2nd. However, we could modify the optical setup so that the SLM is not required to impart such a large focal power. The focal power could be introduced using a cylindrical lens to produce the 1st line focus and the SLM could instead be used to apply much smaller 1-D focus terms, conjugated to the surface of the cylindrical lens via an additional 4-f relay. Tangential to these points we suggest removal of the SLM throughput through the implementation of either an aperture-filtered additional phase slope (in the case of the SLM-produced line focus) or a pinhole-filtered blazed grating (in the case of the SLM conjugated to the cylindrical lens surface). All of these steps would collectively ensure the beam is fit-for-purpose as an A-SPIM illumination beam.

Following this, we could begin imaging of tissue phantoms or biological samples and produce our proposed feature-specific optically sectioned images. With custom SLM control software operating in a closed loop with an imaging camera, the focal curvature could be controlled 'live' in the sample, adapting to different sample curvatures in real-time. The edges of the SLM array could be 'switched off' by removing the phase slope or blazed grating in that region in order to reduce the width and thus the NA of the beam to control the sectioning ability and the sheet extent in the sample plane.

Once feature-specific optical sectioning has been demonstrated we suggest using the A-SPIM system for sample-based focal compensation. Premature focusing of local regions of the light sheet can be caused by optical features within a biological sample. In the example of a zebrafish eye we may want to image the retina down-stream of the eye lens rather than the epithelium which instead is on the lens surface. The A-SPIM illumination beam could be used to introduce a focal power that opposes the focal power introduced in the light sheet by the eye lens, allowing the light sheet part of the illumination beam to be at the desired retinal location. We also suggest a further incarnation of the A-SPIM system where alternate rows of the SLM are switched off in order to introduce a periodic striped structure into the light sheet illumination. This would allow images to be obtained with a higher lateral resolution than that achievable by conventional SPIM imaging through post-processing by using HiLo or, if the stripes are uniform enough, structured illumination microscopy (SIM) techniques. Both techniques have previously been demonstrated in LSM elsewhere [165, 166, 167].

6.5 Conclusions

Individual features-of-interest within biological specimens can often possess a distinct topological curvature in the observation plane of a microscope system. A fluorescence microscope system widely-adopted for rapid 3-D imaging of biological specimens is the SPIM. In SPIM the fluorescent excitation is provided by optics which introduce the illumination beam into the sample along an excitation axis which is perpendicular to the axis of fluorescence detection. A cylindrical lens is used within the illumination optics to focus the beam in one axis, whilst keeping the beam collimated in the other. This produces a light 'sheet' at the focus of the illumination beam which typically has dimensions that span several cellular features of a sample at once, across the observation plane. As the excitation at the focus is restricted to a thin plane which intersects the orthogonal observation axis, the system can produce optically-sectioned images of the sample. Gaussian optics dictates that as the length of the light sheet along the illumination axis becomes shorter, the thinner the focal waist of the sheet becomes. The use of a higher NA illumination beam therefore provides an improvement in optical sectioning across a smaller region of the observation plane. Thus, fewer cellular features can be better optically-sectioned by using an illumination beam with a higher NA. However, since many features-of-interest are typically curved, the focal region of the light sheet must spatially coincide with this feature in order to take advantage of this improvement in imaging across the entirety of a single curved feature. We refer to such a SPIM with an adaptively-curved illumination beam as an A-SPIM system.

In this work we have designed and tested an A-SPIM illumination beam. We have explained the necessity of using an adaptive optical element to produce light sheet illumination with a customisable and continuous focal curvature, adopting a SLM as our chosen adaptive optical element. The shape of the overall light sheet has been recorded using the beam profiling camera probe presented earlier in Chapter 5, and we have demonstrated how the applied focal curvature shape can be matched to the dimensions of circularly-curved features with a range of different radii. Our ability to examine the overall quality of the A-SPIM light sheet was limited by the mechanical dimensions of the beam profiling camera sensor array, though we were able to determine maximum limits on the dimensions of the light sheet: a focal extent length of 30 μm and a sectioning thickness of 3 μm at most. We have made several suggestions for future work with a completed A-SPIM system, including a thorough assessment of the A-SPIM beam's illumination quality, an alternative optical layout in the case of poor performance of our current system, and further improvements to the system's imaging capabilities by periodically modulating the beam intensity throughout the height of the light sheet.

Conclusions 7

This final chapter summarises the three optical instruments presented in this thesis: Namely,

1. an adaptive optics (AO) demonstration system;
2. a camera probe used in conjunction with a high dynamic range (HDR) imaging/reconstruction procedure; and
3. a beam shaping optical setup that can match the focal region of light sheet illumination to a curved surface.

A summary of each is given in the sections below.

7.1 Summary: An AO demonstration system

In Chapter 4 we presented a closed-loop AO system that performed aberration correction for a simulated telescope and microscope. The system was built to be visually attractive, portable, sturdy, and light efficient to ensure successful continuous operation at day-long public science demonstrations. Additionally, the system was built almost entirely out of off-the-shelf components such that the design could be reproduced by other research groups within the AO community wishing to improve their public outreach potential.

The system performed wavefront sensing via a Shack-Hartmann wavefront sensor (SHWFS), using a reference laser beam that was coupled into the beam path of the imaging optics as the wavefront sensor (WFS) light source. A push-pull electrostatic membrane deformable mirror (PPDM) with a large circular aperture was used as the corrective optical element in the closed loop system and was also used to introduce large-stroke aberrations into the beam using randomly-generated actuator voltages. These randomly generated aberrations were intended to simulate the high-amplitude low-Zernike-mode order wavefront errors typically encountered in microscopy, whilst also allowing step-by-step AO correction to be witnessed by participants. A freely-rotating phase screen (TPP) which approximated the

effect of frozen-flow Kolmogorov turbulence was used to impart dynamic aberrations into the imaging system to simulate atmospheric degradation of ground-based telescopes. The TPP, PPDM, and WFS were all located in optical planes conjugate to the imaging lens pupil.

The system has so far been used for demonstration at several science festivals, at one of which the participants were presented with a feedback questionnaire. The feedback that was collected demonstrates the success of our system in bringing AO to a wider audience in an engaging and digestible fashion. We regard the instrument in this project as completed; future work may be undertaken to publish the software, component list, optical layout and instructions for construction and system operation as an online web resource, allowing other groups to build a similar system in both a time and cost efficient way.

7.2 Summary: HDR camera probe

In Chapter 5 we presented the development of a minimally-invasive camera probe that allowed the 3-D intensity profiles of fluorescence microscope illumination beams to be reproduced with a high dynamic range over spatial scales that were previously difficult to observe. A sequential exposure HDR imaging procedure was used in conjunction with a flux reconstruction algorithm we developed to extend the imaging capabilities of the miniature camera sensor (a re-purposed low-cost endoscope) used in our device. This flux reconstruction algorithm was developed in order to obtain a quantified measure of the incident flux at the sensor array, reproducing a wider range of flux values with highly-reduced quantization noise than was available when using the sensor in standard operation.

We calibrated the camera sensor to a wide quantified range of incident flux in order to determine the radiometric response of the device. We found that the response of the camera sensor could be described by a general polynomial equation. The parameters of this equation took different values for each of the pixels across the sensor array due to the inhomogeneous sensor performance, presumably due to the extremely small (1 mm by 1 mm) dimensions of the fabricated sensor array (250 pixels by 250 pixels). These calibration parameters were then used to computationally determine the best quantified estimate of the flux incident at a single pixel from a set of sequential exposure images.

The success of beam profiles taken using our device is limited by both the sensor itself and the software we used. In terms of the sensor itself: lateral resolution was limited by the pitch of the pixel array of the sensor and the radiometric response of some pixels was not well described by our general polynomial approach, thus causing unreliable flux values to be reconstructed at these pixels. Both of these effects are direct consequences of the sensor's manufacturing; a sensor with smaller pixels and a more homogeneous response would cause a direct improvement in resolution and beam profile quality, though such a sensor is not currently commercially available with the minimal dimensions we require. The software caused the imaging and reconstruction processes to extend over long durations which limited the usability of the procedure for rapid beam analysis. Custom control software with speed optimisation would immediately improve the device's prospect in this regard as the software

we used was not optimised for rapid performance. The imaging duration could in theory be reduced down to approximately the sum of all of the sequential exposure durations. Fewer exposure durations could be used in order to reduce the overall imaging duration further at the expense of the signal-to-noise ratio (SNR) for certain flux levels and a coarser quantisation resolution. The reconstruction duration is limited by the computing time required by the numerical procedure that determines the flux value at each pixel. Improved reconstruction speed could be achieved by using a less accurate and computationally simpler estimate of the flux by simply scaling the recorded signal at each pixel by the corresponding exposure duration in parallel and summing this over the entire sequence of exposures. Such an estimate would not take the response of the sensor into account and thus would be far less accurate than our procedure, but could be performed on a much shorter time scale. Nonetheless the beam profiles taken using our device and HDR procedure can reproduce the incident flux with a continuous dynamic range of over $10^4 : 1$ and a pseudo-logarithmic quantisation resolution and the device has been used to observe the illumination beam geometry in several operational microscope configurations.

7.3 Summary: SLM-shaped light sheets with focal curvature

In Chapter 6 we presented a method of alteration to the focal geometry of static light sheet illumination through the use of a spatial light modulator (SLM). The main aim of this investigation was to enhance the optical sectioning of specific specimen features within a single/selective plane illumination microscope (SPIM) by matching the thinnest possible light sheet to the specific position of curved surfaces of interest within a specimen. As an example we illustrated this for the lens epithelium of a zebrafish eye. We used the SLM to produce the phase profile of a cylindrical lens to create a static light sheet focus; this was in turn re-imaged by a 4-f configuration of a tube lens and microscope objective lens to create a light sheet at the appropriate dimensions for use in a SPIM. To introduce a 1-D curvature in what would be the observation plane according to the orthogonal axis of observation in a SPIM we altered the focal length of the cylindrical lens phase profile across the vertical axis of the SLM phase array. We used the term A-SPIM to define such a SPIM system having an adaptively-curved illumination beam. The focal length was altered in order to produce a vertical variation in the light sheet focal position according to a Gaussian curve, the dimensions of which were specified at the re-imaged focus so that the curvature could be applied according to the known scale of curved features within the specimen. We determined the amplitude and span of the Gaussian curve to match well to surfaces with specific curvature radii.

We used the HDR beam profiling camera probe developed in Chapter 5 in order to investigate the quality of the beam at the re-imaged focus and ascertain the appropriateness of the applied curvature. However, as the width of the beam at the focus was below the camera pixel pitch (< 3 μm), coupled with a lateral imprecision of the mechanical translation stage position used to axially scan the beam profiler, in our initial results the beam quality and the applied curvature were difficult to determine. An examination of the SLM throughput,

i.e. the still-collimated portion of the beam power simply reflected by the SLM, within our beam profiles suggested that re-assignment of the beam profile voxel positions to laterally re-shift each slice by a small displacement could allow the artifacts caused by imprecision in the translation stage position to be reduced. We thus performed a centroid-based re-shifting of each 2-D slice in the beam profiles and noted an immediate improvement in the clarity of our recorded data. The curvatures of the resulting beams formed using different Gaussian focal shift amplitudes were then investigated using the voxel-shifted beam profiles. We demonstrated the appropriateness of a single applied curvature, producing a Gaussian focal shift at the re-imaged focus with an overall amplitude of 60 μm and span of 120 μm, at following the surface of circular features with radii of curvature from 60 μm up to 150 μm. Though our results were limited by the pixel pitch of the camera sensor we estimated the A-SPIM illumination beam to have a maximum focal thickness of 3 μm and length (along the propagation axis) of 30 μm.

We suggest that future work for this project be concerned with demonstrating the enhanced optical sectioning of curved features using this technique. The first step is the construction of an orthogonal axis observation arm, completing the SPIM setup, and a higher resolution examination of the beam quality and focal dimensions by imaging point-scanned fluorescent beads or a fluorescent sea. If the quality of the beam is poor then modifications to the optical setup of the A-SPIM illumination arm may be required: Excess phase wrapping on the SLM may have contributed to optical artifacts in the beam; a smaller overall phase variation across the SLM could be used whilst keeping the focal dimensions the same by using a cylindrical lens in the setup to form the line focus and using the SLM to only adjust its focal length rather than forming the focus entirely. Different test specimens with pre-defined curvature radii, *e.g.* fluorescent spheres or glass beads in agarose, could be illuminated using the A-SPIM beam and the appropriate Gaussian focal shift can be applied in order to examine how well the focal curvature matches to the curved features within the specimen. Following a successful demonstration of the light sheet curvature in test specimens we would then investigate the improved sectioning of biological features using our A-SPIM system. A final remark regarding the use of an SLM rather than a DM is the added benefit of potential light sheet structuring. Alternating rows of the SLM can be 'switched off' to remove their contribution to the overall light sheet profile. A HiLo or structured illumination imaging and post-processing procedure can then be used to computationally reduce the effect of scattered light and improve the overall quality of images taken using the system.

Supplemental Material A

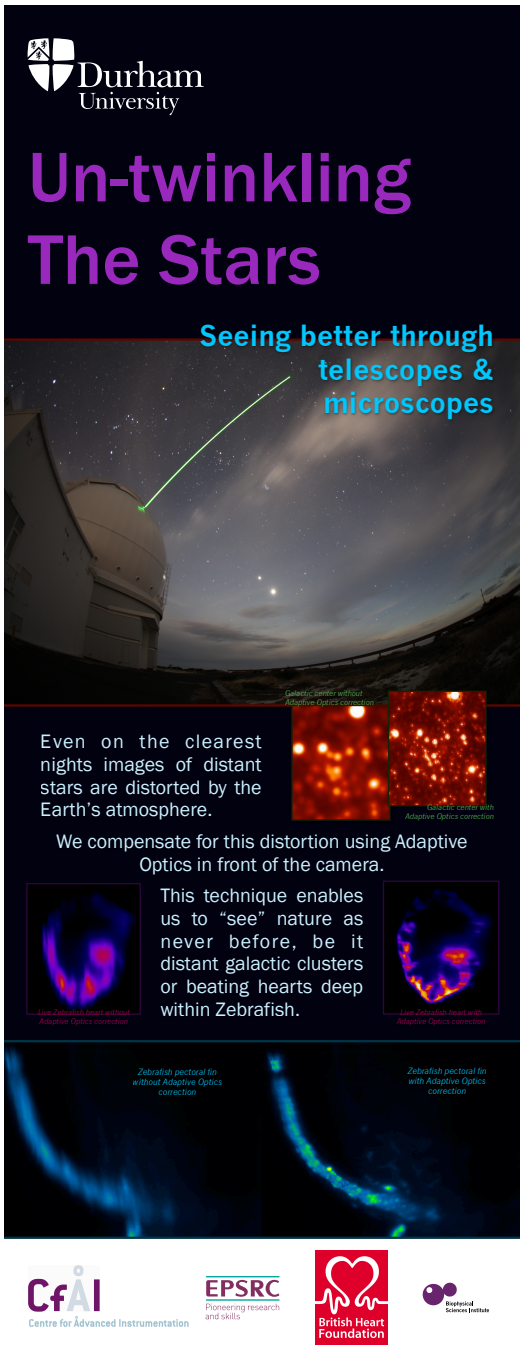

Figure A.1: Stand-alone poster for the AO demonstration system. The poster stands 2 metres tall and is typically placed in an eye-catching location; intended to initiate an engaging encounter with the demonstration at our stall.

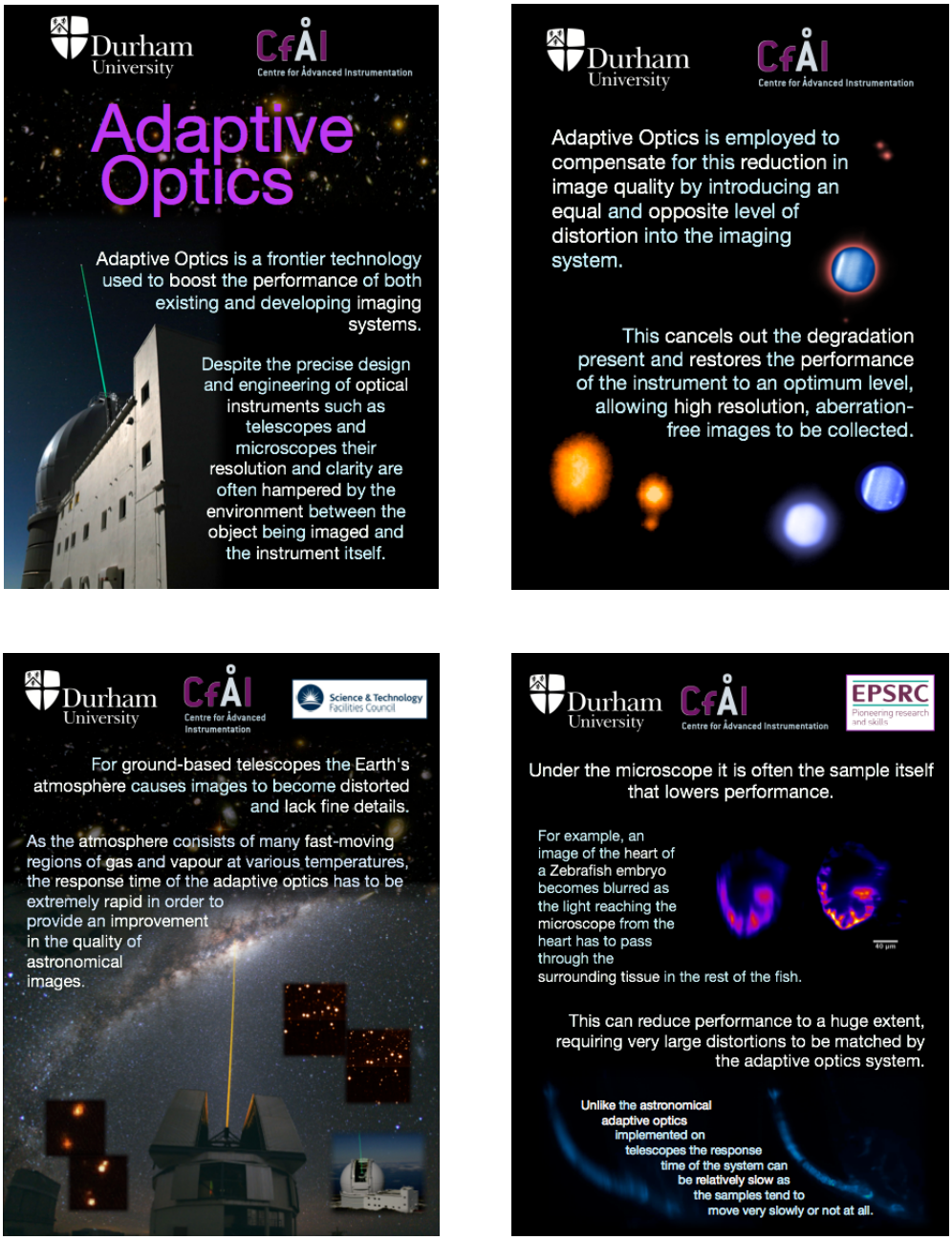

FIGURE A.2: Four 'surround' panel posters for the AO demonstrator system. Each of these posters decorate the panels surrounding our system, provided such poster panels are available. These four posters describe what AO can achieve and how it is implemented in both astronomy and microscopy. The general intention of these posters is to use language appropriate for participants wanting to learn more about the context of AO technology away from the volunteer-led demonstration.

(a)

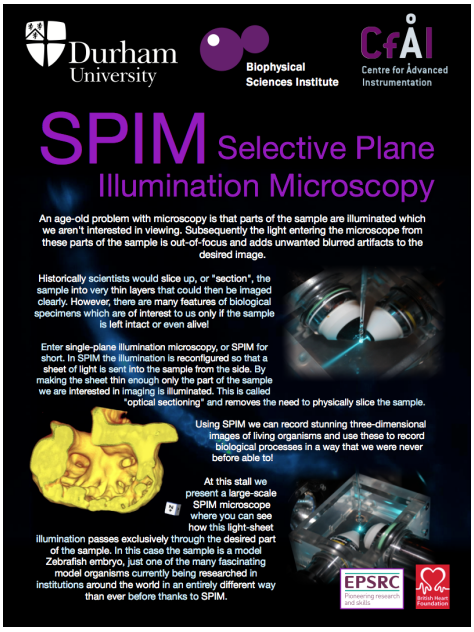

(b)

FIGURE A.3: Additional surrounding posters for public demonstrations of AO and SPIM. These relate specifically to the demonstration instruments and were used together at a science fair where the AO demonstrator was used alongside a model SPIM system made by John Girkin.

FIGURE A.4: Photograph of the AO demonstrator stall at the British Science Festival 2013 at Newcastle University. The central television screen was set up to play an informative video presentation about AO. To the right of this is the AO demonstrator and a computer screen which was connected to the control PC (not pictured). The systems on the left hand side of the television screen were used to demonstrate fluorescence imaging in SPIM, and were constructed by John Girkin. The computer screen on the left presented an interactive z-stack of real zebrafish eye images, taken using our group's research SPIM system. The small black box to the right of this contained model fish composed of a fluorescin-epoxy solution which were illuminated by an LED at the excitation wavelength. A filter gel was affixed to the viewing window to block light from the illumination LED and allow participants to see the fluorescent structure within the model fish appear and disappear by switching this light source on and off. The laptop screen atop the black box behind this shows a webcam image of a fluorescent epoxy zebrafish model illuminated orthogonally by a light sheet and contained within the box below.

Bibliography

[1] G. Rousset, J. C. Fontanella, P. Kern, P. Gigan, and F. Rigaut. First diffraction-limited astronomical images with adaptive optics. *Astronomy & Astrophysics*, 230:L29–L32, 1990. (Cited on page 1.)

[2] C. Paterson, I. Munro, and J. C. Dainty. A low cost adaptive optics system using a membrane mirror. *Optics Express*, 6(9):175–85, April 2000. (Cited on page 1.)

[3] H. Siedentopf and R. Zsigmondy. Uber Sichtbarmachung und Größenbestimmung ultramikoskopischer Teilchen, mit besonderer Anwendung auf Goldrubingläser. *Annalen der Physik*, 315(1):1–39, 1902. (Cited on page 5.)

[4] R. Zsigmondy. Colloids and the ultra microscope. *Journal of the American Chemical Society*, 31(8):951–952, 1909. (Cited on page 5.)

[5] Nobelprize.org. Richard zsigmondy - biographical. `http://www.nobelprize.org/nobel_prizes/chemistry/laureates/1925/zsigmondy-bio.html`, 2014. Accessed: 19 May 2015. (Cited on page 5.)

[6] P. Santi. Light sheet fluorescence microscopy: a review. *The Journal of Histochemistry and Cytochemistry: Official Journal of The Histochemistry Society*, 59(2):129–38, February 2011. (Cited on pages 5 and 7.)

[7] C. J. R. Sheppard and A. Choudhury. Image Formation in the Scanning Microscope. *Optica Acta: International Journal of Optics*, 24(10):1051–1073, 1977. (Cited on page 5.)

[8] K. Carlsson and N. Aslund. Confocal imaging for 3-D digital microscopy. *Applied Optics*, 26(16):3232–3238, 1987. (Cited on page 5.)

[9] M. Laurent, G. Johannin, H. Guyader, and A. Fleury. Confocal scanning optical microscopy and three-dimensional imaging. *Biology of the Cell*, 76(1):113–124, 1992. (Cited on page 5.)

[10] G. J. Brakenhoff, P. Blom, and P. Barends. Confocal scanning light microscopy with high aperture immersion lenses. *Journal of Microscopy*, 117:219–232, 1979. (Cited on page 6.)

[11] E. Stelzer and S. Lindek. Fundamental reduction of the observation volume in far-field light microscopy by detection orthogonal to the illumination axis: confocal theta microscopy. *Optics Communications*, 111:536–547, 1994. (Cited on page 6.)

[12] A. H. Voie, D. H. Burns, and F. A. Spelman. Orthogonal-plane fluorescence optical sectioning: Three-dimensional imaging of macroscopic biological specimens. *Journal of Microscopy*, 170(3):229–236, 1993. (Cited on page 6.)

[13] E. Fuchs, J. Jaffe, R. Long, and F. Azam. Thin laser light sheet microscope for microbial oceanography. *Optics Express*, 10:145–154, 2002. (Cited on page 6.)

[14] J. Huisken, J. Swoger, F. Del Bene, J. Wittbrodt, and E. Stelzer. Optical sectioning deep inside live embryos by selective plane illumination microscopy. *Science*, 305(5686):1007–9, August 2004. (Cited on pages 6, 7 and 8.)

[15] J. Huisken and D. Stainier. Selective plane illumination microscopy techniques in developmental biology. *Development*, 136(12):1963–75, 2009. (Cited on pages 7 and 8.)

[16] J. Ritter, R. Veith, J. Siebrasse, and U. Kubitscheck. High-contrast single-particle tracking by selective focal plane illumination microscopy. *Optics Express*, 16(10):7142, May 2008. (Cited on pages 7 and 26.)

[17] T. A. Planchon, L. Gao, D. E. Milkie, M. W. Davidson, J. A. Galbraith, C. G. Galbraith, and E. Betzig. Rapid three-dimensional isotropic imaging of living cells using Bessel beam plane illumination. *Nature Methods*, 8:417–423, 2011. (Cited on pages 7 and 20.)

[18] P. Keller and M. Ahrens. Visualizing Whole-Brain Activity and Development at the Single-Cell Level Using Light-Sheet Microscopy. *Neuron*, 85(3):462–483, 2015. (Cited on page 7.)

[19] M. Weber and J. Huisken. Light sheet microscopy for real-time developmental biology. *Current Opinion in Genetics & Development*, 21(5):566–72, October 2011. (Cited on pages 7 and 9.)

[20] K. Khairy and P. Keller. Reconstructing embryonic development. *Genesis*, 49(7):488–513, July 2011. (Cited on page 7.)

[21] R. Tomer, K. Khairy, and P. Keller. Shedding light on the system: studying embryonic development with light sheet microscopy. *Current Opinion in Genetics & Development*, 21(5):558–65, October 2011. (Cited on page 7.)

[22] P. J. Keller, F. Pampaloni, and E. Stelzer. Life sciences require the third dimension. *Current Opinion in Cell Biology*, 18:117–124, 2006. (Cited on page 7.)

[23] J. Lin, O. G. Rodríguez-Herrera, F. Kenny, D. Lara, and J. C. Dainty. Fast vectorial calculation of the volumetric focused field distribution by using a three-dimensional Fourier transform. *Optics Express*, 20(2):1060, 2012. (Cited on page 11.)

[24] E. Hecht. *Optics*. Addison-Wesley, 4th edition, 1998. (Cited on pages 12 and 13.)

[25] G. Brooker. *Modern Classical Optics*. Oxford master series in atomic, optical and laser physics. Oxford Univ. Press, Oxford, 2003. (Cited on pages 12 and 15.)

[26] J. Ritter, J-H. Spille, T. Kaminski, and U. Kubitscheck. A cylindrical zoom lens unit for adjustable optical sectioning in light sheet microscopy. *Biomedical Optics Express*, 2(1):185–93, January 2010. (Cited on page 17.)

[27] K. Greger, J. Swoger, and E. Stelzer. Basic building units and properties of a fluorescence single plane illumination microscope. *Review of Scientific Instruments*, 78(2):023705, 2007. (Cited on page 17.)

[28] J. Durnin, J. J. Miceli, and J. H. Eberly. Diffraction-free beams. *Physics Review Letters*, 58:1499–1501, Apr 1987. (Cited on page 17.)

[29] J. Arlt and K. Dholakia. Generation of high-order Bessel beams by use of an axicon. *Optics Communications*, 177(April):297–301, 2000. (Cited on page 17.)

[30] R. Arimoto, C. Saloma, T. Tanaka, and S. Kawata. Imaging properties of axicon in a scanning optical system. *Applied Optics*, 31(31):6653–7, November 1992. (Cited on pages 17 and 18.)

[31] N. Chattrapiban, E. Rogers, D. Cofield, W. Hill III, and R. Roy. Generation of nondiffracting Bessel beams by use of a spatial light modulator. *Optics Letters*, 28(22):2183, November 2003. (Cited on page 17.)

[32] B. Yalizay, B. Soylu, and S. Akturk. Optical element for generation of accelerating airy beams. *Journal of the Optical Society of America A*, 27(10):2344–2346, 2010. (Cited on page 17.)

[33] G. Siviloglou, J. Broky, A. Dogariu, and D. Christodoulides. Observation of Accelerating Airy Beams. *Physical Review Letters*, 99(21):213901, November 2007. (Cited on page 17.)

[34] G. Porat, I. Dolev, O. Barlev, and A. Arie. Airy beam laser. *Optics Letters*, 36:4119, 2011. (Cited on page 17.)

[35] P. Zhang, Y. Hu, T. Li, D. Cannan, X. Yin, R. Morandotti, Z. Chen, and X. Zhang. Nonparaxial Mathieu and Weber Accelerating Beams. *Physical Review Letters*, 109(19):193901, November 2012. (Cited on page 18.)

[36] J. Broky, G. Siviloglou, A. Dogariu, and D. N. Christodoulides. Self-healing properties of optical Airy beams. *Optics Express*, 16(17):12880–12891, 2008. (Cited on page 19.)

[37] F. O. Fahrbach, P. Simon, and A. Rohrbach. Microscopy with self-reconstructing beams. *Nature Photonics*, 4(November):780–785, 2010. (Cited on page 19.)

[38] F. O. Fahrbach and A. Rohrbach. A line scanned light-sheet microscope with phase shaped self-reconstructing beams. *Optics Express*, 18(23):2608–2610, 2010. (Cited on page 19.)

[39] T. Vettenburg, H. Dalgarno, J. Nylk, C. Coll-Lladó, D. Ferrier, T. Čižmár, F. Gunn-Moore, and K. Dholakia. Light-sheet microscopy using an Airy beam. *Nature Methods*, 11(5):541–4, May 2014. (Cited on pages 19 and 21.)

[40] Z. Yang, M. Prokopas, J. Nylk, C. Coll-Lladó, F. Gunn-Moore, D. Ferrier, T. Vettenburg, and K. Dholakia. A compact Airy beam light sheet microscope with a tilted cylindrical lens. *Biomedical Optics Express*, 5(10):3434–42, October 2014. (Cited on pages 19 and 21.)

[41] J. Durnin. Exact solutions for nondiffracting beam. I . The scalar theory. *Journal of the Optical Society of America A*, 4(4):651–654, 1987. (Cited on page 19.)

[42] G. A. Siviloglou and D. N. Christodoulides. Accelerating finite energy Airy beams. *Optics Letters*, 32(8):979, 2007. (Cited on pages 19 and 20.)

[43] D. McGloin and K. Dholakia. Bessel beams: Diffraction in a new light. *Contemporary Physics*, 46(1):15–28, January 2005. (Cited on page 19.)

[44] Y. Hu, G. Siviloglou, P. Zhang, N. Efremidis, D. Christodoulides, and Z. Chen. *Nonlinear Photonics and Novel Optical Phenomena*, volume 170 of *Springer Series in Optical Sciences*. Springer New York, New York, NY, 2012. (Cited on page 19.)

[45] Z. Bouchal, J. Wagner, and M. Chlup. Self-reconstruction of a distorted nondiffracting beam. *Optics Communications*, 151(4–6):207–211, 1998. (Cited on page 20.)

[46] M. Neil, R. Juskaitis, and T. Wilson. Method of obtaining optical sectioning by using structured light in a conventional microscope. *Optics Letters*, 22(24):1905–1907, December 1997. (Cited on page 20.)

[47] M. Gustafsson. Surpassing the lateral resolution limit by a factor of two using structured illumination microscopy. *Journal of Microscopy*, 198:82–87, 2000. (Cited on page 20.)

[48] P. So. Two-photon Fluorescence Light Microscopy. *Encyclopedia Of Life Sciences*, pages 1–5, 2002. (Cited on page 20.)

[49] O. Olarte, J. Licea-Rodriguez, J. Palero, E. Gualda, D. Artigas, J. Mayer, J. Swoger, J. Sharpe, I. Rocha-Mendoza, R. Rangel-Rojo, and P. Loza-Alvarez. Image formation by linear and nonlinear digital scanned light-sheet fluorescence microscopy with Gaussian and Bessel beam profiles. *Biomedical Optics Express*, 3(7):1492–505, July 2012. (Cited on page 21.)

[50] F. O. Fahrbach and A. Rohrbach. Propagation stability of self-reconstructing Bessel beams enables contrast-enhanced imaging in thick media. *Nature Communications*, 3:632, January 2012. (Cited on page 21.)

[51] L. Silvestri, A. Bria, L. Sacconi, G. Iannello, and F. S. Pavone. Confocal light sheet microscopy: micron-scale neuroanatomy of the entire mouse brain. *Optics Express*, 20(18):20582, 2012. (Cited on page 21.)

[52] P. Zhang, M. E. Phipps, P. M. Goodwin, and J. H. Werner. Confocal line scanning of a Bessel beam for fast 3D imaging. *Optics Letters*, 39(12):3682–5, June 2014. (Cited on page 21.)

[53] E. Baumgart and U. Kubitscheck. Scanned light sheet microscopy with confocal slit detection. *Optics Express*, 20(19):21805–14, September 2012. (Cited on page 21.)

[54] F. O. Fahrbach, V. Gurchenkov, K. Alessandri, P. Nassoy, and A. Rohrbach. Light-sheet microscopy in thick media using scanned Bessel beams and two-photon fluorescence excitation. *Optics Express*, 21(11):13824–39, June 2013. (Cited on page 21.)

[55] L. Gao. Optimization of the excitation light sheet in selective plane illumination microscopy. *Biomedical Optics Express*, 6(3):881, 2015. (Cited on page 21.)

[56] A. E. Siegman. How to (Maybe) Measure Laser Beam Quality - OSA Trends in Optics and Photonics. In M. Dowley, editor, *DPSS (Diode Pumped Solid State) Lasers: Applications and Issues*, volume 17, page MQ1, Washington D.C., 1998. Optical Society of America. (Cited on page 23.)

[57] ISO. Lasers and laser-related equipment—Test methods for laser beam widths, divergence angles and beam propagation ratios—Part 1: Stigmatic and simple astigmatic beams. ISO 11146– 1:2005, International Organization for Standardization, Geneva, Switzerland, 2005. (Cited on page 24.)

[58] ISO. Lasers and laser-related equipment—Test methods for laser beam widths, divergence angles and beam propagation ratios—Part 2: General astigmatic beams. ISO 11146– 2:2005, International Organization for Standardization, Geneva, Switzerland, 2005. (Cited on page 24.)

[59] ISO. Lasers and laser-related equipment—Test methods for laser beam widths, divergence angles and beam propagation ratios—Part 3: Intrinsic and geometrical laser beam classification, propagation and details of test methods. ISO 11146– 3:2005, International Organization for Standardization, Geneva, Switzerland, 2005. (Cited on page 24.)

[60] M. Gentili and N. A. Riza. Wide-aperture no-moving-parts optical beam profiler using liquid-crystal displays. *Applied Optics*, 46(4):506–512, Feb 2007. (Cited on page 24.)

[61] J. Alda. Laser and Gaussian Beam Propagation and Transformation. *Optical Engineering*, 110:999–1013, 2003. (Cited on page 24.)

[62] L. I. Green, C. B. Roundy, J. Reingruber, and SPIRICON GmBH. Camera-based systems for modern laser beam diagnostics. *Photonik International*, 2006. (Cited on page 24.)

[63] D. F. Grosjean, R. A. Olson, B. Sarka, and D. C. Rabe. High-power CO(2) laser-beam monitor. *Review of Scientific Instruments*, 49(6):778, June 1978. (Cited on page 24.)

[64] G. Brost, P. D. Horn, and A. Abtahi. Convenient spatial profiling of pulsed laser beams. *Applied Optics*, 24:38–40, 1985. (Cited on page 24.)

[65] W. Plass, R. Maestle, K. Wittig, A. Voss, and A. Giesen. High-resolution knife-edge laser beam profiling. *Optics Communications*, 134:21–24, 1997. (Cited on page 24.)

[66] N. Riza and D. Jorgesen. Minimally invasive optical beam profiler. *Optics Express*, 12(9):1892–1901, May 2004. (Cited on pages 24 and 26.)

[67] N. A. Riza and M. J. Mughal. Optical power independent optical beam profiler. *Optical Engineering*, 43(4):793–797, 2004. (Cited on page 24.)

[68] M. Sheikh and N. A. Riza. Demonstration of Pinhole Laser Beam Profiling Using a Digital Micromirror Device. *IEEE Photonics Technology Letters*, 21, 2009. (Cited on page 24.)

[69] M. Sheikh and N. A. Riza. Motion-free hybrid design laser beam propagation analyzer using a digital micromirror device and a variable focus liquid lens. *Applied Optics*, 49(16):D6–D11, Jun 2010. (Cited on pages 24 and 25.)

[70] P. J. Marraccini and N. A. Riza. Multimode laser beam analyzer instrument using electrically programmable optics. *Review of Scientific Instruments*, 82(12):–, 2011. (Cited on pages 24 and 25.)

[71] R. D. Niederriter, J. T. Gopinath, and M. E. Siemens. Measurement of the m^2 beam propagation factor using a focus-tunable liquid lens. *Applied Optics*, 52(8):1591–1598, Mar 2013. (Cited on page 24.)

[72] P. J. Shaw and D. J. Rawlins. The point-spread function of a confocal microscope: its measurement and use in deconvolution of 3-D data. *Journal of Microscopy*, 163(2):151–165, 1991. (Cited on page 26.)

[73] H. Yoo, I. Song, and D. G. Gweon. Measurement and restoration of the point spread function of fluorescence confocal microscopy. *Journal of Microscopy*, 221:172–176, 2006. (Cited on page 26.)

[74] M. J. Nasse, J. C. Woehl, and S. Huant. High-resolution mapping of the three-dimensional point spread function in the near-focus region of a confocal microscope. *Applied Physics Letters*, 90, 2007. (Cited on page 26.)

[75] R. W. Cole, T. Jinadasa, and C. M. Brown. Measuring and interpreting point spread functions to determine confocal microscope resolution and ensure quality control. *Nature Protocols*, 6:1929–41, 2011. (Cited on page 26.)

[76] J. Ritter, R. Veith, A. Veenendaal, J. Siebrasse, and U. Kubitscheck. Light sheet microscopy for single molecule tracking in living tissue. *PLoS ONE*, 5(7), 2010. (Cited on page 26.)

[77] H. Dalgarno, T. Čižmár, T. Vettenburg, J. Nylk, F. Gunn-Moore, and K. Dholakia. Wavefront corrected light sheet microscopy in turbid media. *Applied Physics Letters*, 100(19):191108, 2012. (Cited on pages 27 and 60.)

[78] H. R. Blackwell. Contrast threshold of the human eye. *Journal of the Optical Society of America*, (36):624–643, November 1946. (Cited on page 28.)

[79] C. W. Wyckoff. Experimental extended exposure response film. *Society of Photographic Instrumentation Engineers Newsletter*, page 16, June 1962. (Cited on page 29.)

[80] 30th anniversary: Photography. *LIFE*, 61(26):112–113, December 1966. (Cited on pages 29 and 30.)

[81] C. W. Wyckoff. Silver halide photographic film having increased exposure-response characteristics, June 1969. US Patent 3,450,536. (Cited on page 29.)

[82] L. M. Eber, H. M. Greenberg, J. M. Cooke, and R. Gorlin. Dynamic changes in left ventricular free wall thickness in the human heart. *Circulation*, 39(4):455–464, 1969. (Cited on page 29.)

[83] B. C. Madden. Extended Intensity Range Imaging. Technical Report December, Grasp Laboratory, University of Pennsylvania, 1993. (Cited on pages 29, 31 and 32.)

[84] S. Mann and R. W. Picard. On Being 'undigital' With Digital Cameras: Extending Dynamic Range By Combining Differently Exposed Pictures. Technical Report 323, M.I.T. Media Lab Perceptual Computing Section, Boston, Massachusetts, 1994. Also appears, IS&T's 48th annual conference, Cambridge, Massachusetts, May 1995. (Cited on page 30.)

[85] P. E. Debevec and J. Malik. Recovering High Dynamic Range Radiance Maps from Photographs. In *Proceedings of ACM SIGGRAPH*, SIGGRAPH '08, pages 369–378, New York, NY, USA, 1997. ACM. (Cited on page 30.)

[86] T. Mitsunaga and S. K. Nayar. Radiometric self calibration. In *IEEE Computer Society Conference on Computer Vision and Pattern Recognition*, volume 1, pages 374–380. IEEE Computer Society, 1999. (Cited on page 30.)

[87] M. A. Robertson, S. Borman, and R. L. Stevenson. Dynamic range improvement through multiple exposures. In *International Conference on Image Processing*, volume 3, pages 159–163. IEEE Computer Society, 1999. (Cited on pages 31 and 32.)

[88] M. Aggarwal and N. Ahuja. Split aperture imaging for high dynamic range. *International Journal of Computer Vision*, 58(1):7–17, 2004. (Cited on page 32.)

[89] M. Konishi, M. Tsugita, M. Inuiya, and K. Masukane. Video camera, imaging method using video camera, image processing apparatus and method, and solid-state electronic imaging device, May 1995. US Patent 5,420,635. (Cited on page 33.)

[90] S. K. Nayar and T. Mitsunaga. High dynamic range imaging: spatially varying pixel exposures. In *IEEE Conference on Computer Vision and Pattern Recognition*, volume 1, pages 472–479. IEEE Computer Society, 2000. (Cited on page 33.)

[91] V. Brajovic and T. Kanade. A sorting image sensor: an example of massively parallel intensity-to-time processing for low-latency computational sensors. In *IEEE International Conference on Robotics and Automation*, volume 2, pages 1638–1643. IEEE Computer Society, 1996. (Cited on page 33.)

[92] V. M. Brajovic, R. Miyagawa, and T. Kanade. Temporal photoreception for adaptive dynamic range image sensing and encoding. *Neural Networks*, 11(7-8):1149–1158, 1998. (Cited on page 33.)

[93] S. K. Nayar and V. Branzoi. Adaptive Dynamic Range Imaging: Optical Control of PixelExposures over Space and Time. In *IEEE International Conference on Computer Vision (ICCV)*, volume 2, pages 1168–1175. IEEE Computer Society, 2003. (Cited on page 33.)

[94] H. Mannami, R. Sagawa, Y. Mukaigawa, T. Echigo, and Y. Yagi. Adaptive dynamic range camera with reflective liquid crystal. *Journal of Visual Communication and Image Representation*, 18(5):359–365, 2007. (Cited on page 33.)

[95] R. Lo, S. Mann, J. Huang, V. Rampersad, and T. Ai. High dynamic range (HDR) video image processing for digital glass. *Proceedings of the 20th ACM international conference on Multimedia - MM '12*, page 1477, 2012. (Cited on page 34.)

[96] J. Duan, M. Bressan, C. Dance, and G. Qiu. Tone-mapping high dynamic range images by novel histogram adjustment. *Pattern Recognition*, 43(5):1847–1862, 2010. (Cited on page 34.)

[97] N. Waltham, M. Prydderch, H. Mapson-Menard, M. Clapp, P. Pool, and A. Harris. Development of a thinned back-illuminated CMOS active pixel sensor for extreme ultraviolet spectroscopy and imaging in space science. *Proc. SPIE*, 6690(1-2):669007–669014, 2007. (Cited on page 37.)

[98] M. E. Hoenk, T. J. Jones, M. R. Dickie, F. Greer, T. J. Cunningham, E. R. Blazejewski, and S. Nikzad. Delta-doped back-illuminated CMOS imaging arrays: progress and prospects. *Proc. SPIE*, 7419:74190T–74190T–15, 2009. (Cited on page 37.)

[99] E. R. Fossum. Cmos image sensors: Electronic camera-on-a-chip. *IEEE Transactions on Electron Devices*, 44(10):1689, 1997. (Cited on page 41.)

[100] F. Wang and Z. Çelik-Butler. An improved physics-based 1/f noise model for deep sub-micron MOSFETs. *Solid-State Electronics*, 45(2):351–357, 2001. (Cited on page 41.)

[101] B. Razavi. *Design of Analog CMOS Integrated Circuits*. McGraw-Hill, Singapore, international edition, 2001. (Cited on page 41.)

[102] M. S. Keshner and F. N. Hooge. 1/f Noise. *Proceedings of the IEEE*, 70(3):212–218, 1982. (Cited on page 41.)

[103] X. Wang. *Noise in Sub-Micron CMOS Image Sensors*. PhD thesis, Technische Universiteit Delft, 2008. (Cited on page 41.)

[104] R. Jacob Baker. *CMOS Circuit Design, Layout, and Simulation*. Wiley-IEEE Press, New Jersey, third edition, 2010. (Cited on page 42.)

[105] W. C. Porter, B. Kopp, J. C. Dunlap, R. Widenhorn, and E. Bodegom. Dark current measurements in a CMOS imager. *SPIE-IS&T Electronic Imaging*, 6816:1–8, 2008. (Cited on page 45.)

[106] J. W. Hardy. *Adaptive Optics for Astronomical Telescopes*. Oxford series in optical and imaging sciences. Oxford University Press, 1998. (Cited on page 51.)

[107] H. W. Babcock. The possibility of compensating astronomical seeing. *Publications of the Astronomical Society of the Pacific*, pages 229–236, 1953. (Cited on page 51.)

[108] M. Hart. Recent advances in astronomical adaptive optics. *Applied Optics*, 49(16):D17–D29, 2010. (Cited on page 51.)

[109] A. N. Kolmogorov. The local structure of turbulence in incompressible viscous fluid for very large Reynolds numbers. In *Dokl. Akad. Nauk SSSR*, volume 30, pages 299–303, 1941. (Cited on page 53.)

[110] F. Roddier. The Effects of Atmospheric Turbulence in Optical Astronomy. *Progress in Optics*, 19:281–376, 1981. (Cited on page 53.)

[111] A. Reeves, R. Myers, T. Morris, A. Basden, and N. Bharmal. Real-Time Laser Guide Star Elongation and Uplink Turbulence in the Lab. In *Proceedings of the Third AO4ELT Conference*, volume 1, page 35, 2013. (Cited on page 53.)

[112] A. P. Reeves, R. M. Myers, T. J. Morris, A. G. Basden, N. A. Bharmal, S. Rolt, D. G. Bramall, N. A. Dipper, and E. J. Younger. DRAGON, the durham real-time, tomographic adaptive optics test bench: progress and results. In *SPIE Astronomical Telescopes + Instrumentation*, pages 91485U–91485U. International Society for Optics and Photonics, 2014. (Cited on page 53.)

[113] Robert J Noll. Zernike polynomials and atmospheric turbulence. *Journal of the Optical Society of America*, 66(3):207–211, 1976. (Cited on page 53.)

[114] M. Born and E. Wolf. *Principles of Optics*. Cambridge University Press, 7th edition, 1999. (Cited on page 54.)

[115] B. Platt and R. Shack. History and Principles of Shack-Hartmann Wavefront Sensing. *Journal of Refractive Surgery*, 17(Sept/Oct):S573–S577, 2001. (Cited on page 55.)

[116] D. Fried. Statistics of a Geometric Representation of Wavefront Distortion. *Journal of the Optical Society of America*, 55(11):1427, 1965. (Cited on page 55.)

[117] R. Foy and A. Labeyrie. Letter to the Editor Feasibility of adaptive telescope with laser probe. *Astronomy & Astrophysics*, 152:L29–L31, 1985. (Cited on page 56.)

[118] L. A. Thompson and C. S. Gardner. Experiments on laser guide stars at Mauna Kea Observatory for adaptive imaging in astronomy. *Nature*, 328:229–231, 1987. (Cited on page 56.)

[119] C. A. Primmerman, D. V. Murphy, D. A. Page, B. G. Zollars, and H. T. Barclay. Compensation of atmospheric optical distortion using a synthetic beacon. *Nature*, 353(6340):141–143, 1991. (Cited on page 56.)

[120] R. Q. Fugate, L. M. Wopat, D. L. Fried, G. A. Ameer, S. L. Browne, P. H. Roberts, G. A. Tyler, B. R. Boeke, and R. E. Ruane. Measurement of atmospheric wavefront distortion using scattered light from a laser guide-star. *Nature*, 353:144–146, 1991. (Cited on page 56.)

[121] L. Zhang, H. Jiang, S. Cui, J. Hu, and Y. Feng. Versatile Raman fiber laser for sodium laser guide star. *Laser & Photonics Reviews*, 8(6):889–895, 2014. (Cited on page 56.)

[122] M. G. Löfdahl. Evaluation of image-shift measurement algorithms for solar Shack-Hartmann wavefront sensors. *Astronomy & Astrophysics*, 524:A90, 2010. (Cited on pages 56 and 63.)

[123] J. E. Pearson and S. Hansen. Experimental studies of a deformable-mirror adaptive optical system. *Journal of the Optical Society of America*, 67(3):325–332, 1977. (Cited on page 57.)

[124] A. Basden, D. Geng, R. Myers, and E. Younger. Durham adaptive optics real-time controller. *Applied Optics*, 49(32):6354–6363, 2010. (Cited on page 58.)

[125] T. N. Truong, A. H. Bouchez, R. S. Burruss, R. G. Dekany, S. R. Guiwits, J. E. Roberts, J. C. Shelton, and M. Troy. Design and implementation of the PALM-3000 real-time control system. In *SPIE Astronomical Telescopes + Instrumentation*, pages 84472F–84472F. International Society for Optics and Photonics, 2012. (Cited on page 58.)

[126] N. Dipper, A. Basden, U. Bitenc, R. Myers, A. Richards, and E. Younger. Adaptive Optics Real-time Control Systems for the E-ELT. In *Proceedings of the Third AO4ELT Conference*, volume 1, page 41, 2013. (Cited on page 58.)

[127] M. Booth. Adaptive optics in microscopy. *Phil. Trans. R. Soc. A*, 365:2829–2843, 2007. (Cited on pages 58 and 59.)

[128] S. Hell, G. Reiner, C. Cremer, and E. Stelzer. Aberrations in confocal fluorescence microscopy induced by mismatches in refractive index. *Journal of Microscopy*, 169(3):391–405, 1993. (Cited on page 59.)

[129] M. Schwertner, M. Booth, M. Neil, and T. Wilson. Measurement of specimen-induced aberrations of biological samples using phase stepping interferometry. *Journal of Microscopy*, 213(Pt 1):11–9, January 2004. (Cited on page 59.)

[130] M. Schwertner, M. Booth, and T. Wilson. Characterizing specimen induced aberrations for high NA adaptive optical microscopy. *Optics Express*, 12(26):6540–52, December 2004. (Cited on page 59.)

[131] J. M. Girkin, S. Poland, and A. J. Wright. Adaptive optics for deeper imaging of biological samples. *Current Opinion in Biotechnology*, 20(1):106–10, February 2009. (Cited on pages 59 and 60.)

[132] M. Booth. Adaptive optical microscopy: the ongoing quest for a perfect image. *Light: Science & Applications*, 3(4):e165, April 2014. (Cited on pages 59 and 60.)

[133] O. Albert, L. Sherman, G. Mourou, T. Norris, and G. Vdovin. Smart microscope: an adaptive optics learning system for aberration correction in multiphoton confocal microscopy. *Optics Letters*, 25(1):52–4, January 2000. (Cited on page 59.)

[134] M. Booth, M. Neil, R. Juskaitis, and T. Wilson. Adaptive aberration correction in a confocal microscope. *Proceedings of the National Academy of Sciences of the United States of America*, 99(9):5788–92, April 2002. (Cited on page 60.)

[135] L. Sherman, J. Y. Ye, O. Albert, and T. B. Norris. Adaptive correction of depth-induced aberrations in multiphoton scanning microscopy using a deformable mirror. *Journal of Microscopy*, 206(1):65–71, 2002. (Cited on page 60.)

[136] D. Debarre, M. Booth, and T. Wilson. Image based adaptive optics through optimisation of low spatial frequencies. *Optics Express*, 15(13):8176, 2007. (Cited on page 60.)

[137] O. Azucena, J. Crest, J. Cao, W. Sullivan, P. Kner, D. Dillon, S. Olivier, and J. Kubby. Wavefront aberration measurements and corrections through thick tissue using fluorescent microsphere reference beacons. *Optics Express*, 18(16):17521, 2010. (Cited on page 60.)

[138] P. Vermeulen, E. Muro, T. Pons, V. Loriette, and A. Fragola. Adaptive optics for fluorescence wide-field microscopy using spectrally independent guide star and markers. *Journal of biomedical optics*, 16(7):076019, 2011. (Cited on page 60.)

[139] O. Azucena, X. Tao, J. Crest, S. Kotadia, W. Sullivan, D. Gavel, M. Reinig, S. Olivier, and J. Kubby. Adaptive optics wide-field microscope corrections using a MEMS DM and Shack-Hartmann wavefront sensor. volume 7931, MEMS Adaptive Optics V, pages 79310J–79310J–6, 2011. (Cited on page 60.)

[140] X. Tao, B. Fernandez, O. Azucena, M. Fu, D. Garcia, Y. Zuo, D. Chen, and J. Kubby. Adaptive optics confocal microscopy using direct wavefront sensing. *Optics Letters*, 36(7):1062–1064, 2011. (Cited on page 60.)

[141] X. Tao, J. Crest, S. Kotadia, O. Azucena, D. Chen, W. Sullivan, and J. Kubby. Live imaging using adaptive optics with fluorescent protein guide-stars. *Optics Express*, 20(14):3389–3391, 2012. (Cited on page 60.)

[142] C. Bourgenot, C. D. Saunter, J. M. Girkin, G. D. Love, and J. M. Girkin. Comparison of closed loop and sensorless adaptive optics in widefield optical microscopy. *Journal of the European Optical Society - Rapid publications*, 8:13027, 2013. (Cited on page 60.)

[143] S. Poland, A. J. Wright, S. Cobb, J. Vijverberg, and J. M. Girkin. A demonstration of the effectiveness of a single aberration correction per optical slice in beam scanned optically sectioning microscopes. *Micron*, 42(4):318–323, 2011. (Cited on page 60.)

[144] I. Freund, M. Rosenbluh, and S. Feng. Memory effects in propagation of optical waves through disordered media. *Physical Review Letters*, 61(20):2328–2331, 1988. (Cited on page 60.)

[145] Z. Kam, P. Kner, D. Agard, and J. Sedat. Modelling the application of adaptive optics to wide-field microscope live imaging. *Journal of Microscopy*, 226(Pt 1):33–42, April 2007. (Cited on page 61.)

[146] J. Mertz, H. Paudel, and T. Bifano. Field of view advantage of conjugate adaptive optics in microscopy applications. *Applied Optics*, 54(11):3498–3506, April 2015. (Cited on pages 61 and 62.)

[147] J. M. Beckers. Detailed compensation of atmospheric seeing using multiconjugate adaptive optics. In *1989 Orlando Symposium*, pages 215–219. International Society for Optics and Photonics, 1989. (Cited on page 61.)

[148] R. Ragazzoni, E. Marchetti, and F. Rigaut. Modal tomography for adaptive optics. *Astronomy & Astrophysics*, 342:L53–L56, 1999. (Cited on page 61.)

[149] E. Marchetti, N. N. Hubin, E. Fedrigo, J. Brynnel, B. Delabre, R. Donaldson, F. Franza, R. Conan, M. Le Louarn, C. Cavadore, et al. MAD the ESO multi-conjugate adaptive optics demonstrator. In *Astronomical Telescopes and Instrumentation*, pages 317–328. International Society for Optics and Photonics, 2003. (Cited on page 61.)

[150] F. Rigaut, B. Neichel, M. Boccas, C. d'Orgeville, G. Arriagada, V. Fesquet, S. J. Diggs, C. Marchant, G. Gausach, W. N. Rambold, et al. GeMS: first on-sky results. In *SPIE Astronomical Telescopes + Instrumentation*, pages 84470I–84470I. International Society for Optics and Photonics, 2012. (Cited on page 61.)

[151] R. Simmonds and M. Booth. Modelling of multi-conjugate adaptive optics for spatially variant aberrations in microscopy. *Journal of Optics*, 15(9):094010, 2013. (Cited on page 61.)

[152] C. Bourgenot, C. D. Saunter, J. M. Taylor, J. M. Girkin, and G. D. Love. 3D adaptive optics in a light sheet microscope. *Optics Express*, 20(12):13252, May 2012. (Cited on page 62.)

[153] J. M. Taylor, J. M. Girkin, and G. D. Love. High-resolution 3D optical microscopy inside the beating zebrafish heart using prospective optical gating. *Biomedical Optics Express*, 3(12):3043–53, December 2012. (Cited on page 63.)

[154] J. M. Girkin, J. M. Taylor, C. Bourgenot, C. D. Saunter, and G. D. Love. Adaptive optical methods for in vivo imaging in developing Zebra fish. *2012 International Symposium on Optomechatronic Technologies (ISOT 2012)*, pages 1–2, October 2012. (Cited on pages 63 and 64.)

[155] J. M. Taylor, C. D. Saunter, C. Bourgenot, J. M. Girkin, and G. D. Love. Realtime wavefront sensing in a SPIM microscope, and active aberration tracking. In *Proc. SPIE*, volume 9335, Adaptive Optics and Wavefront Control for Biological Systems, pages 93350A–93350A–6, 2015. (Cited on page 63.)

[156] R. Rampy, D. Gavel, D. Dillon, and S. Thomas. New method of fabricating phase screens for simulated atmospheric turbulence. In B. L. Ellerbroek, M. Hart, N. Hubin, and P. L. Wizinowich, editors, *Proc. SPIE*, volume 7736, Adaptive Optics Systems II, pages 77362Y–1–77362Y–10, July 2010. (Cited on page 68.)

[157] I. Capraro, A. Acciari, S. Bonora, C. Trestino, T. Occhipinti, and G. Meneghini. PushPull deformable mirror: performances in closed loop operation and comparison with membrane mirror. Technical report, Adaptica, Padova, Italy, 2012. (Cited on page 68.)

[158] K. Strehl. *Theorie des fernrohrs: auf grund der beugung des Lichts*. JA Barth (A. Meiner), 1894. (Cited on page 75.)

[159] K. Strehl. Über luftschlieren und zonenfehler. *Zeitschrift für Instrumentenkunde*, 22:213–217, 1902. (Cited on page 75.)

[160] F. Roddier. *Adaptive optics in astronomy*. Cambridge university press, 1999. (Cited on page 75.)

[161] M. Wäny and S. Voltz. Awaiba NanEye Camera System specifications. `http://www.awaiba.com/v2/wp-content/uploads/2010/01/NanEye_Camera_system_Spec_v_1.06.pdf`. Accessed: 2014-06-29. (Cited on page 88.)

[162] G. E. Forsythe, M. A. Malcolm, and C. B. Moler. In *Computer Methods for Mathematical Computations*, chapter 7.2. Prentice-Hall, Englewood Cliffs, NJ, 1977. (Cited on page 98.)

[163] Gmbh & Co. KG. Physik instrument Compact Micro-Translation Stage specifications. `http://www.physikinstrumente.com/en/pdf/M110_Datasheet.pdf`. Accessed: 2014-06-29. (Cited on page 106.)

[164] P. Salter, Z. Iqbal, and M. Booth. Analysis of the Three-Dimensional Focal Positioning Capability of Adaptive Optic Elements. *International Journal of Optomechatronics*, 7(1):1–14, 2013. (Cited on page 127.)

[165] T. Breuninger, K. Greger, and E. Stelzer. Lateral modulation boosts image quality in single plane illumination fluorescence microscopy. *Optics Letters*, 32:1938–1940, 2007. (Cited on page 142.)

[166] J. Mertz and J. Kim. Scanning light-sheet microscopy in the whole mouse brain with HiLo background rejection. *Journal of Biomedical Optics*, 15(1):016027, 2010. (Cited on page 142.)

[167] T. J. Schröter, S. B. Johnson, K. John, and P. A. Santi. Scanning thin-sheet laser imaging microscopy (sTSLIM) with structured illumination and HiLo background rejection. *Biomedical Optics Express*, 3(1):170, 2012. (Cited on page 142.)

Colophon

This document was prepared with the LaTeX typesetting system using a template (adapted by the author) based on the Maggi Memoir Thesis Template originally authored by Federico Maggi (fede@maggi.cc) with extensive modifications by Vel (vel@latextemplates.com) available at `http://www.latextemplates.com/template/maggi-memoir-thesis`.
The aforementioned template is distributed for use and adaptation under Creative Commons License CC BY-NC-SA 3.0 (`http://creativecommons.org/licenses/by-nc-sa/3.0/`).
The main fonts used are the newpxtext and newpxmath font packages: modified forms of the Palatino typeface originally designed by Hermann Zapf and released by the Linotype foundry in 1948.